

Modelling ionised and photodissociated regions

Magda Vasta

Thesis submitted for the Degree of Doctor of Philosophy
of University College London

Department of Physics & Astronomy
UNIVERSITY COLLEGE LONDON

March 2010

I, Magda Vasta, confirm that the work presented in this thesis is my own. Where information has been derived from other sources, I confirm that this has been indicated in the thesis.

*To my parents, my brother and my husband,
who always supported and encouraged me no matter what.*

I tell people I am too stupid to know what is impossible.

*I have ridiculously large dreams, and
half the time they come true.*

— Thomas D.

ACKNOWLEDGEMENTS

Some people come into our lives and quickly go. Some stay for a while and leave footprints on our hearts. And we are never, ever the same. I made it, I still cannot believe it, but I finally made it. However, it would have been almost impossible to reach this target without the constant scientific support from some people.

My first big THANKS go to my supervisor Serena Viti. Thanks for being the supportive person you are, for giving me the possibility to be independent in my research, but being always present when I needed you. Thanks for all the times that you did not talk to me in Italian, for encouraging me to not give up and for being the lovely person you are. Thanks to Mike Barlow for the amazing scientific suggestions and for tolerating ALL my silly questions (most of them grammatically incorrect!). Thanks to Barbara Ercolano for her patience when answering my emails “HELP, PLEASE!!” about MOCASSIN. Thanks to Tom Bell for replying to all my UCL.PDR questions and for all his encouraging emails. Thanks to Jeremy Yates for having listen to me vent out and for helping me constantly. Thanks to Dugan Witherick and John Deacon for having helped during all the computational problems.

Lately I was thinking that my experience in London was the biggest failure of my life, from a friendship point of view, but maybe I was wrong because I have had the possibility to share a bit of my life with some of you. Thanks to my G16 officemates: Oskar, Helen, Julia, Fotini, Farah. Thanks to Zainab for her support. Thanks to DR WESSON for having tolerated me with all my english questions and Mikako Matsuura for her advise and suggestions. Thanks to Mark Westmoquette for having given me a piece of himself and for his constant support. Thanks to Estelle Bayet for her scientific support, all the toto and tata and all the bananas she did not throw at me. Thanks to Will Whyatt, Nick Wright and Iraklis (Greek boy) for all your hugs, smiles, chats, support and best friendship ever. Thanks to Filipe Abdalla for having been there when

I needed him, for his friendship and support. Thanks to Edu Cypriano for his initial support. Thanks to Silvia C. for her friendship, and for all the hamburgers and cookies we shared together. Thanks to Pierandrea D.F. for having always been the best “big brother” I could possibly desire. Thanks to Agnese D.M for her friendship over the past years and for all the visits to London to try to cheer me up. Thanks to Daniele F. for having tolerated all the WD films, all my venting out, for your amazing energy and joy of life and for being one of the best friends I could ask for. Thanks to my sardinian friends: Alessandro O., Luca P., Ste S. and Fabio L. that followed me all over the place with their love and friendship. Thanks to Simone G., Moris B. and Andrea P. for all the emails, calls, chats, friendship and support. Thanks to Mirko S. who in the last 10 years NEVER stopped to tell me that I COULD make it. Thanks to Andrea U, for all the chats in the “crying corner” and thanks to Simone S. that NEVER abandoned me, and always supported and loved me for the past 25 years. Thanks to my easyjet friends: Maurizio V., Efen A. and Francesco R. for having been the best commuters ever, thanks to having helped me not to sleep on monday morning :-). Last but not least, Thanks to my “adopted” father, Stephen F., for his unconditional love and all his good sunday food. Thanks to Samuel F. because he brought the sun into my life in London just when I thought I would never have had seen the sun in this country, thanks for our SPECIAL FRIENDSHIP, for having tolerated me in these last months of writing up and for having proof read EVERYTHING I wrote (also the acknowledgements). Thanks to Diego, because you were beside me when I started, when I wanted to quit and now that I made it. Thanks for all the times that, at the airport, you told me “do not worry as 2 week-ends pass quickly, 3 years pass quickly too..” and for having went along with my wishes and all my crazy decisions. Thanks because you never stopped to believe in me while showing your love to me every day. Thanks to Cippi for being my lovely brother.

Grazie a mamma e papà per aver assecondato i miei sogni sempre e con sacrificio in questi lunghi 10 anni, grazie per essere stati sempre lì, dall'altra parte del telefono, in qualunque paese io fossi: le parole non bastano per esprimere tutto il mio amore e la mia gratitudine.

Grazie a Don e nonna, perchè se sono così e anche merito vostro.

ABSTRACT

The bulk of the mass in star-forming environments is contained in photodissociated regions (PDRs) where the chemistry is controlled by the far ultraviolet radiation field coming from nearby ionizing sources. H II regions can be found throughout active star forming galaxies as they are also controlled by the presence of a nearby ionizing source. In fact, H II regions, PDRs, and molecular clouds are not distinct physical regions, but rather a series of layers that are unified by the transport of radiation from hot stars into cold gas and the flow of cold molecular gas into hot ionized regions. The relative contributions of the ultraviolet radiation field from different gas phases can be estimated from observations of several far infrared forbidden lines such as [C II]158 μm , [O I]145 μm and 63 μm . Fine structure emission line studies provide valuable information on H II and PDR regions and it is well known that they originate in the outer part of both H II and PDR regions. The only exception are the nitrogen lines that clearly come exclusively from ionized regions. With the launch of ISO the far infrared properties of galaxies were observed with greater sensitivity than ever before. This thesis deals with the study of [C II]158 μm , [O I]145 μm , 63 μm and partly CO in external galaxies. In Chapter 3 we investigate the [C II]158 μm , [O I]145 μm and 63 μm emission lines in a sample of external galaxies in order to use them as diagnostics to infer the physical conditions in the gas, such as temperatures, densities and radiation fields. This study was carried out using the photodissociation UCL.PDR code, testing PDR model results against ISO LWS observations. In addition, a detailed study of the oxygen self absorption, computed by modelling the emission line profiles with the radiative transfer SMMOL code, was conducted. In Chapter 4 a detailed study of the starburst NGC 4038 has been performed by using both MOCASSIN and UCL.PDR. The contribution of [C II] 158 μm , [O I] 63 μm and 145 μm lines coming from the H II region was studied using the 3D ionization MOCASSIN code. We then used the computed radiation field at the ionization front

as an input for the photodissociation UCL_PDR code and an examination of the oxygen self absorption and a comparison of the CO rotational emission lines with CSO observations, were also presented. Finally, to improve the interpretation of future observations such as those from ALMA and HERSCHEL, a feasibility test on the coupling of the two codes (MOCASSIN and UCL_PDR) was performed and the results are presented in Chapter 5. Conclusion and ideas for future work are presented in Chapter 6.



An image of the extragalactic source, Andromeda, in the infrared.

CONTENTS

Acknowledgements	5
Abstract	7
Table of Contents	10
List of Figures	13
List of Tables	25
1 Introduction	28
1.1 The physics of photoionization regions	31
1.1.1 Photoionization	33
1.1.2 Nebular continuum emission	34
1.1.3 Charge transfer	35
1.2 The Physics of PDRs	36
1.3 The Chemistry of PDRs	38
1.3.1 H ₂ photodissociation	39
1.3.2 CO photodissociation	41
1.3.3 Hydrogen recombination on grain surfaces	42
1.3.4 The H/H ₂ layer	44
1.3.5 The C II/C I/CO layer	46
1.3.6 The S II layer	47
1.4 The importance of the thermal balance	47
1.4.1 Thermal Equilibrium in H II region	48

1.4.2	Heating Mechanisms in PDRs	54
1.4.3	General cooling mechanisms in PDRs	56
1.5	Far Infrared fine structure emission lines	59
1.5.1	Infrared Space Observatory	61
1.6	Extragalactic sources and their Infrared emission	62
1.6.1	Starburst galaxies	63
1.6.2	Active galactic nuclei	64
1.6.3	Radio galaxies and Quasi stellar objects	65
1.7	A unified region: H II/PDR	65
2	The UCL models	67
2.1	The Photodissociation code UCL_PDR	67
2.2	The Photoionization code MOCASSIN	69
2.3	The Radiative Transfer code SMMOL	72
3	Testing PDR models against extragalactic ISO data for fine structure emission lines	75
3.1	The ISO data	76
3.1.1	Data Reduction	76
3.1.2	Extragalactic ISO data for fine structure emission lines	77
3.2	The UCL_PDR models	83
3.3	Sensitivity of model results to parameter variations	87
3.3.1	Visual Extinction	88
3.3.2	Radiation field	91
3.3.3	Metallicity	92
3.3.4	Density	94
3.3.5	Cosmic ray ionization rate	96
3.4	Using [N II] fluxes to estimate the ionized gas contribution to [C II] fluxes	97
3.5	Fitting the observations	102
3.5.1	[O I] 63- μ m self-absorption	105
3.6	Conclusions	112
4	Modelling NGC 4038: an attempt at a unified model.	114
4.1	Starburst galaxy sample	114

4.1.1	Oxygen emission lines as diagnostic of the electron density	117
4.2	Antennae galaxy	119
4.3	Modelling the nucleus of NGC 4038	122
4.3.1	Modelling with STARBURST 99	124
4.3.2	Modelling gas and dust in the ionized region with the MOCASSIN code	124
4.3.3	Modelling the chemistry in PDRs with the UCL_PDR code	127
4.3.4	Modelling the oxygen emission line profiles with the radiative transfer SMMOL code	132
4.4	Results	132
4.5	Comparison of CO and [CI] observations	147
4.6	Conclusions and future work	148
5	Coupling of the UCL_PDR and MOCASSIN codes	151
5.1	The UCL_PDR code	152
5.2	The MOCASSIN code	153
5.3	The Feasibility of the coupling	154
5.3.1	Escape probability formalism	155
5.3.2	Adaptive grid and H ₂ self shielding	158
5.3.3	Chemical Network and Ordinary Differential Equations	165
5.3.4	Steady state vs time dependent with the reduced chemical network . . .	167
5.3.5	The dimensionality of the cells	183
5.4	Conclusion and future work	183
6	Concluding remarks and proposals for future work	186
	Bibliography	189

LIST OF FIGURES

1.1	Cross section of a characteristic small cloud. The crosshatched region shows the cold core, which gives the usual optical absorption lines. The following region is the WNM with ionization produced by soft X-ray background. The outer layer, WIM, is gas largely ionized by stellar UV background (McKee & Ostriker 1977).	29
1.2	The [C II] emission of the galaxy observed by the FIRAS instrument of COBE (Bennett <i>et al.</i> 1994). The galactic plane is horizontal with the galactic centre at the centre.	30
1.3	The [N II] emission of the galaxy observed by the FIRAS instrument of COBE (Bennett <i>et al.</i> 1994). The galactic plane is horizontal with the galactic centre at the centre.	31
1.4	The most important reactions in the chemistry of carbon and oxygen compounds. Oxygen-bearing radicals are formed through reactions of O with H ₂ , whereas most of OH produced is photodissociated again, but a small fraction reacts with C ⁺ to form CO ⁺ and so on (Sternberg & Dalgarno 1995).	39
1.5	A schematic diagram of a photon-dominated region. The PDR is illuminated from the left and extends from the predominantly atomic surface region to the point where O ₂ is not appreciably photodissociated ($A_V > 10$) (Hollenbach & Tielens 1997).	44

1.6	Experimental and theoretical recombination rate coefficients as a function of temperature for recombination to produce Fe^{17} . The heavy line gives the experimental dielectronic recombination (DR) rate coefficient, and dotted/dashed lines are the results of various theories. The light solid line is the contribution from radiative recombination. The points-with-error bars are previous experimental measurements, and the error bar on the curve indicates the uncertainty in the heavy line. The collisionally ionized zone marks the temperature range where the kinetic temperature is roughly equal to the ionization potential, whereas the photoionized zone is the range where the temperature is a small percentage of the ionization potential, as is typical of a photoionized gas (Savin <i>et al.</i> 2002).	51
1.7	Simplified energy-level diagram for O^+ (left) and O^{2+} (right). Unlabelled O^+ and O^{2+} wavelengths are in nm.	52
1.8	The photoelectric heating mechanism: FUV photons are absorbed by interstellar grains and PAHs and energetic electrons are ejected into the gas with excess kinetic energy (Hollenbach & Tielens 1997)	55
1.9	The two step photodissociation of H_2 : absorption of FUV photons ($912 \text{ \AA} < \lambda < 1118 \text{ \AA}$) in the Lyman and Werner bands, followed by radiative decay to the vibrational continuum of the ground electronic state. This occurs in 10 – 15% of the cases, the majority of decays leading to a vibrationally excited molecule in the ground electronic state (Hollenbach & Tielens 1997).	57
1.10	A schematic depiction of the Infrared Space Observatory.	62
3.1	$[\text{C II}]_{158} / [\text{O I}]_{63}$ and $[\text{O I}]_{63} / [\text{O I}]_{145}$ ratios. Filled triangles represent the ratio of the literature value of $[\text{O I}]_{63} / [\text{O I}]_{145}$ over our own measured $[\text{O I}]_{63} / [\text{O I}]_{145}$ ratio, with respective error bars. Open triangles represent the ratio of the literature value of $[\text{C II}]_{158} / [\text{O I}]_{63}$ over our own measured $[\text{C II}]_{158} / [\text{O I}]_{63}$ ratio with respective error bars. The horizontal line represents the case in which literature ratios and our own measured ratios are perfectly matched. The source index numbers and galaxy identifications are listed in Table 3.1.	88
3.2	The observed $[\text{C II}]_{158} / [\text{O I}]_{63}$ ratios versus the $[\text{O I}]_{63} / [\text{O I}]_{145}$ ratios for detections $\geq 4\sigma$, with error bars.	90

-
- 3.3 [C II]₁₅₈ / [O I]₆₃ versus [O I]₆₃ / [O I]₁₄₅ ratios with error bars, compared with models of varying visual extinctions. The insert shows a zoomed-in region of the overlapping coloured circles corresponding to differing visual extinction values. 91
- 3.4 [C II]₁₅₈ / [O I]₁₄₅ versus [O I]₁₄₅ / [O I]₆₃ ratios (right), with error bars, compared with models of varying visual extinctions. 92
- 3.5 The observed [C II]₁₅₈ / [O I]₆₃ versus [O I]₆₃ / [O I]₁₄₅ ratios, with uncertainties. The coloured points represent models with radiation field strengths in the range $10^4 \leq G_0 \leq 2 \times 10^4$ 93
- 3.6 The observed [C II]₁₅₈ / [O I]₆₃ versus [O I]₆₃ / [O I]₁₄₅ ratios, with uncertainties. The coloured points represent models with radiation field strengths in the range $10^3 \leq G_0 \leq 8 \times 10^3$ 94
- 3.7 The observed [C II]₁₅₈ / [O I]₆₃ versus [O I]₆₃ / [O I]₁₄₅ ratios, with uncertainties. The coloured points represent models with radiation field strengths in the range $10^2 \leq G_0 \leq 8 \times 10^2$ 95
- 3.8 The observed [C II]₁₅₈ / [O I]₆₃ versus [O I]₆₃ / [O I]₁₄₅ ratios, with uncertainties. The coloured points represent models with radiation field strengths in the range $10 \leq G_0 \leq 80$ 96
- 3.9 Observed [C II]₁₅₈ / [O I]₆₃ versus [O I]₆₃ / [O I]₁₄₅ ratios, with uncertainties, compared to models of differing metallicity. The coloured circles represent models with different values of metallicity, ranging from 0.01 (light green circle), 0.25 (claret circle) and 0.5 (light blue circle) up to 5 times solar metallicity. 97
- 3.10 Observed [C II]₁₅₈ / [O I]₆₃ versus [O I]₆₃ / [O I]₁₄₅ ratios, with uncertainties, compared to models of differing metallicity, with the C/O ratio adopted to be 0.53 for metallicities of 0.25 and above, but dropping to 0.16 as metallicities decrease to 0.03. The coloured circles represent models with different values of metallicity, ranging from 0.03 (light green circle), 0.25 (claret circle) and 0.5 (light blue circle) up to twice solar metallicity. 98
- 3.11 Observed [C II]₁₅₈ / [O I]₆₃ versus [O I]₆₃ / [O I]₁₄₅ ratios, with uncertainties, compared to models of differing densities. The colored points represent models with densities in the range $10^5 \leq n_H \leq 2 \times 10^5 \text{ cm}^{-3}$ decreasing from left to right. 99

- 3.12 Observed $[C II]_{158} / [O I]_{63}$ versus $[O I]_{63} / [O I]_{145}$ ratios, with uncertainties, compared to models of differing densities. The colored points represent models with densities values in the range $10^4 \leq n_H \leq 9 \times 10^4 \text{ cm}^{-3}$, decreasing from left to right. 100
- 3.13 Observed $[C II]_{158} / [O I]_{63}$ versus $[O I]_{63} / [O I]_{145}$ ratios, with uncertainties, compared to models of differing densities. The colored points represent models with densities in the range $10^3 \leq n_H \leq 9 \times 10^3 \text{ cm}^{-3}$ decreasing from left to right. 101
- 3.14 Observed $[C II]_{158} / [O I]_{63}$ versus $[O I]_{63} / [O I]_{145}$ ratios, with uncertainties, compared to models of differing densities. The colored points represent models with densities values in the range $10^2 \leq n_H \leq 9 \times 10^2 \text{ cm}^{-3}$, decreasing from right to left. 102
- 3.15 Observed $[C II]_{158} / [O I]_{63}$ versus $[O I]_{63} / [O I]_{145}$ ratios, with uncertainties, compared to models with differing cosmic ray ionization rates. The coloured circles represents models with cosmic ray ionization rates of $\zeta = 5 \times 10^{-15} \text{ s}^{-1}$ (green circle), $\zeta = 5 \times 10^{-16} \text{ s}^{-1}$ (claret circle) and $\zeta = 5 \times 10^{-17} \text{ s}^{-1}$ (blue circle). . . 103
- 3.16 Observed $[C II]_{158} / [O I]_{63}$ versus $[O I]_{63} / [O I]_{145}$ ratios, with uncertainties. The observations do not take into account the likely percentage of $[C II]$ coming from H II regions. The coloured points represent represent models with radiation field strengths in the range $10 \leq G_0 \leq 2 \times 10^4$ and the arrows indicate the direction of the increase of radiation field strength. 105
- 3.17 Observed $[C II]_{158} / [O I]_{63}$ versus $[O I]_{63} / [O I]_{145}$ ratios, with uncertainties. In the observations the estimated contribution to the $[C II]$ flux is taken into account for each source. The coloured points represent represent models with radiation field strengths in the range $10 \leq G_0 \leq 2 \times 10^4$ and the arrows indicate the direction of the increase of radiation field strength. The arrow corresponds to the median shift in the $[C II]_{158} / [N II]_{122}$ ratio, corresponding to 27% of the $[C II]$ emission originating from H II regions. 106
- 3.18 Theoretical oxygen line profiles produced from a 20 pc GMC, observed at a distance of 3.2 Mpc. The dotted line represents the $[O I]_{145 \mu m}$ emission line profile and the solid line represents the $[O I]_{63 \mu m}$ emission line profile. The physical parameters of the UCL_PDR model used for modeling the oxygen line profiles were $\zeta = 5 \times 10^{-17} \text{ s}^{-1}$, $n_H = 10^3 \text{ cm}^{-3}$, $Z/Z_{\odot} = 1$, $200 G_0$ and $t = 10^7 \text{ yrs}$. . . 108

-
- 3.19 Theoretical oxygen line profiles produced from a 5pc GMC, observed at a distance of 3.2 Mpc. The dotted line represents the $[\text{O I}]_{145\mu\text{m}}$ emission line profile and the solid line represents the $[\text{O I}]_{63\mu\text{m}}$ emission line profile. The physical parameters of the UCL_PDR model used for modeling the oxygen line profiles were $\zeta=5\times 10^{-17}\text{s}^{-1}$, $n_H=10^3\text{cm}^{-3}$, $Z/Z_\odot=1$, $200G_0$ and $t=10^7$ yrs. 109
- 3.20 Theoretical $[\text{O I}]_{63\mu\text{m}}$ emission line profile produced from a 5pc GMC, observed at a distance of 3.2 Mpc. The physical parameters of the UCL_PDR model used for modeling the oxygen line profiles were: $\zeta=5\times 10^{-17}$, $n_H=10^3\text{cm}^{-3}$, $Z/Z_\odot=1$ and $2000G_0$, $t=10^7$ yrs. 110
- 3.21 Theoretical $[\text{O I}]_{63\mu\text{m}}$ emission line profile produced from a 5pc GMC, observed at a distance of 3.2 Mpc. The physical parameters of the UCL_PDR model used for modeling the oxygen line profiles were: $\zeta=5\times 10^{-17}$, 10^4cm^{-3} , $Z/Z_\odot=1$ and $200G_0$, $t=10^7$ yrs. 111
- 3.22 Theoretical ionized carbon line profile produced from a 5pc GMC, observed at a distance of 3.2 Mpc. The solid line represents the $[\text{C II}]_{158\mu\text{m}}$ emission line profile. The physical parameters of the UCL_PDR model used for modeling the ionized carbon line profiles were $\zeta=5\times 10^{-17}\text{s}^{-1}$, $n_H=10^3\text{cm}^{-3}$, $Z/Z_\odot=1$, $200G_0$ and $t=10^7$ yrs. 112
- 4.1 An optical image of the Antennae galaxy 120
- 4.2 Representative scheme of the model of the nucleus of NGC 4038. 123
- 4.3 A geometrical representation of the physical conditions used with SMMOL. The beige central area represents the central cavity. The radiation field of the extra external source (Habing flux) is assumed to be the same used as the input for the UCL_PDR grid models. Also, the size of the sphere, z (cm), used in the SMMOL code, is the same as that assumed to model the PDR region. The level populations of the selected species are computed in each radial shell. 133

- 4.4 Model 004: with a computed $[\text{NIII}]_{57}/[\text{NII}]_{122}=13.13$ ratio. The top panel shows the $[\text{C II}]_{158}/[\text{O I}]_{63}$ ratio versus the $[\text{O I}]_{63}/[\text{O I}]_{145}$ ratio, the black triangle (with error bars) represents the observed ISO ratio for NGC 4038 (see Table 4.5) and the coloured circles represent either the contribution from both ionized and photodominated regions or just the contribution from the PDR. The middle panel shows the oxygen emission line profiles computed using the radiative transfer code (SMMOL), the dotted line represents the $[\text{O I}]_{145}$ emission line, while the solid line represents the $[\text{O I}]_{63}$ emission line with oxygen self absorption. The bottom panel is the same as the top panel, however only plotting the models with an age of 10^7 yr, for the PDR, and taking into account the effect of the $[\text{O I}]_{63}$ self absorption. 137
- 4.5 Model 013: with a computed $[\text{NIII}]_{57}/[\text{NII}]_{122}=1.86$ ratio. The top panel shows the $[\text{C II}]_{158}/[\text{O I}]_{63}$ ratio versus the $[\text{O I}]_{63}/[\text{O I}]_{145}$ ratio, the black triangle (with error bars) represents the observed ISO ratio for NGC 4038 (see Table 4.5) and the coloured circles represent either the contribution from both ionized and photodominated regions or just the contribution from the PDR. The middle panel shows the oxygen emission line profiles computed using the radiative transfer code (SMMOL), the dotted line represents the $[\text{O I}]_{145}$ emission line, while the solid line represents the $[\text{O I}]_{63}$ emission line with oxygen self absorption. The bottom panel is the same as the top panel, however only plotting the models with an age of 10^7 yr, for the PDR, and taking into account the effect of the $[\text{O I}]_{63}$ self absorption. 139
- 4.6 Model 019: with a computed $[\text{NIII}]_{57}/[\text{NII}]_{122}=3.82$ ratio. The top panel shows the $[\text{C II}]_{158}/[\text{O I}]_{63}$ ratio versus the $[\text{O I}]_{63}/[\text{O I}]_{145}$ ratio, the black triangle (with error bars) represents the observed ISO ratio for NGC 4038 (see Table 4.5) and the coloured circles represent either the contribution from both ionized and photodominated regions or just the contribution from the PDR. The bottom panel shows the oxygen emission line profiles computed using the radiative transfer code (SMMOL), the dotted line represents the $[\text{O I}]_{145}$ emission line, while the solid line represents the $[\text{O I}]_{63}$ emission line. 140

- 4.7 Model 021: with a computed $[\text{NIII}]_{57}/[\text{NII}]_{122}=3.75$ ratio. The top panel shows the $[\text{C II}]_{158}/[\text{O I}]_{63}$ ratio versus the $[\text{O I}]_{63}/[\text{O I}]_{145}$ ratio, the black triangle (with error bars) represents the observed ISO ratio for NGC 4038 (see Table 4.5) and the coloured circles represent either the contribution from both ionized and photodominated regions or just the contribution from the PDR. The bottom panel shows the oxygen emission line profiles computed using the radiative transfer code (SMMOL), the dotted line represents the $[\text{O I}]_{145}$ emission line, while the solid line represents the $[\text{O I}]_{63}$ emission line. 141
- 4.8 Model 022: with a computed $[\text{NIII}]_{57}/[\text{NII}]_{122}=3.72$ ratio. The top panel shows the $[\text{C II}]_{158}/[\text{O I}]_{63}$ ratio versus the $[\text{O I}]_{63}/[\text{O I}]_{145}$ ratio, the black triangle (with error bars) represents the observed ISO ratio for NGC 4038 (see Table 4.5) and the coloured circles represent either the contribution from both ionized and photodominated regions or just the contribution from the PDR. The bottom panel shows the oxygen emission line profiles computed using the radiative transfer code (SMMOL), the dotted line represents the $[\text{O I}]_{145}$ emission line, while the solid line represents the $[\text{O I}]_{63}$ emission line. 142
- 4.9 Model 023: with a computed $[\text{NIII}]_{57}/[\text{NII}]_{122}=3.65$ ratio. The top panel shows the $[\text{C II}]_{158}/[\text{O I}]_{63}$ ratio versus the $[\text{O I}]_{63}/[\text{O I}]_{145}$ ratio, the black triangle (with error bars) represents the observed ISO ratio for NGC 4038 (see Table 4.5) and the coloured circles represent either the contribution from both ionized and photodominated regions or just the contribution from the PDR. The bottom panel shows the oxygen emission line profiles computed using the radiative transfer code (SMMOL), the dotted line represents the $[\text{O I}]_{145}$ emission line, while the solid line represents the $[\text{O I}]_{63}$ emission line. 143

- 4.10 Model 024: with a computed $[\text{NIII}]_{57}/[\text{NII}]_{122}=2.36$ ratio. The top panel shows the $[\text{C II}]_{158}/[\text{O I}]_{63}$ ratio versus the $[\text{O I}]_{63}/[\text{O I}]_{145}$ ratio, the black triangle (with error bars) represents the observed ISO ratio for NGC 4038 (see Table 4.5) and the coloured circles represent either the contribution from both ionized and photodominated regions or just the contribution from the PDR. The second panel shows the oxygen emission line profiles computed using the radiative transfer code (SMMOL), the dotted line represents the $[\text{O I}]_{145}$ emission line, while the solid line represents the $[\text{O I}]_{63}$ emission line with oxygen self absorption. The third panel shows that $[\text{C II}]_{158}$ is also self absorbed. The bottom panel is the same as the top panel, however only plotting the models with an age of 10^7 yr, for the PDR, and taking into account the effects of $[\text{O I}]_{63}$ and $[\text{C II}]_{158}$ self absorption. 144
- 4.11 Model 025: with a computed $[\text{NIII}]_{57}/[\text{NII}]_{122}=3.73$ ratio. The top panel shows the $[\text{C II}]_{158}/[\text{O I}]_{63}$ ratio versus the $[\text{O I}]_{63}/[\text{O I}]_{145}$ ratio, the black triangle (with error bars) represents the observed ISO ratio for NGC 4038 (see Table 4.5) and the coloured circles represent either the contribution from both ionized and photodominated regions or just the contribution from the PDR. The bottom panel shows the oxygen emission line profiles computed using the radiative transfer code (SMMOL), the dotted line represents the $[\text{O I}]_{145}$ emission line, while the solid line represents the $[\text{O I}]_{63}$ emission line. 145
- 5.1 a) Representation of the adaptive grid used in the UCL_PDR code. The depth step points correspond to a certain value of A_v . The grid size is extremely thin at the first layer; after the H/H₂ transition is fully resolved, the distance between depth-steps points is larger. b) 3D representation of a system of grid cells with multiple ionizing sources. The point indicates the cell of interest and stars representing the ionizing sources. A_{v_A} is the A_v relative to source A and A_{v_B} is the A_v relative to source B. 159
- 5.2 A 3D representation of the computed trajectories of the energy packets. The 3D cubical grid (right) shows the highly improbable scattering of photons within the grid, while the 3D cubical grid (left) shows the expected scattering of photons within the grid. 161

-
- 5.3 The H (turquoise solid line), H₂ (black solid line) and CO (blue solid line) abundances against A_v extinction, in logarithmic scale, obtained running the UCL_PDR code with initial conditions of radiation field 10³ Habing, density 10⁴ cm⁻³ and metallicity 1 Z_⊙ for 170 grid points. The H/H₂ transition occurs at an optical depth of ~0.037, that in terms of extinction is A_v~0.04, after around 62 grid points using the adaptive grid of depth-steps. 162
- 5.4 The H (turquoise solid line), H₂ (black solid line) and CO (blue solid line) abundances against A_v extinction, in logarithmic scale, obtained running the UCL_PDR code with initial conditions of radiation field 10³ Habing, density 10⁴ cm⁻³ and metallicity 1 Z_⊙ for 3 grid points. The H/H₂ transition was occurring further away from Av~3. 163
- 5.5 The H (turquoise solid line), H₂ (black solid line) and CO (blue solid line) abundances against A_v extinction, in logarithmic scale, obtained running the UCL_PDR code with initial conditions of radiation field 10³ Habing, density 10⁴ cm⁻³ and metallicity 1 Z_⊙ for 9 grid points. The H/H₂ transition at higher extinction than Av~3. 164
- 5.6 The H (turquoise solid line), H₂ (black solid line) and CO (blue solid line) abundances against A_v extinction, in logarithmic scale, obtained running the UCL_PDR code with initial conditions of radiation field 10³ Habing, density 10⁴ cm⁻³ and metallicity 1 Z_⊙ for 28 grid points. The H/H₂ transition at higher extinction than Av~3. 165
- 5.7 The H (turquoise solid line), H₂ (black solid line) and CO (blue solid line) abundances against A_v extinction, in logarithmic scale, obtained running the UCL_PDR code with initial conditions of radiation field 10³ Habing, density 10⁴ cm⁻³ and metallicity 1 Z_⊙ for 80 grid points. The H/H₂ transition occurs at Av~0.04. 166

- 5.8 Model 1 of CO (black line), O (cyan line), OH (blue line), O₂ (magenta line), C (green line), HCO⁺ (yellow) and H₃⁺ (red line) fractional abundances versus visual extinction, A_v (mag). The top left panel represents a run with the reduced chemical network and steady state approach, the top right panel represents a run with the reduced chemical network and time dependent approach, the bottom left panel represents a run with the full chemical network and steady state approach, and the bottom right panel represents a run with the full chemical network and time dependent approach. 172
- 5.9 Model 4 of CO (black line), O (cyan line), OH (blue line), O₂ (magenta line), C (green line), HCO⁺ (yellow) and H₃⁺ (red line) fractional abundances versus visual extinction, A_v (mag). The top left panel represents a run with the reduced chemical network and steady state approach, the top right panel represents a run with the reduced chemical network and time dependent approach, the bottom left panel represents a run with the full chemical network and steady state approach, and the bottom right panel represents a run with the full chemical network and time dependent approach. 173
- 5.10 Model 7 of CO (black line), O (cyan line), OH (blue line), O₂ (magenta line), C (green line), HCO⁺ (yellow) and H₃⁺ (red line) fractional abundances versus visual extinction, A_v (mag). The top left panel represents a run with the reduced chemical network and steady state approach, the top right panel represents a run with the reduced chemical network and time dependent approach, the bottom left panel represents a run with the full chemical network and steady state approach, and the bottom right panel represents a run with the full chemical network and time dependent approach. 174
- 5.11 Model 10 of CO (black line), O (cyan line), OH (blue line), O₂ (magenta line), C (green line), HCO⁺ (yellow) and H₃⁺ (red line) fractional abundances versus visual extinction, A_v (mag). The top left panel represents a run with the reduced chemical network and steady state approach, the top right panel represents a run with the reduced chemical network and time dependent approach, the bottom left panel represents a run with the full chemical network and steady state approach, and the bottom right panel represents a run with the full chemical network and time dependent approach. 175

- 5.12 Model 13 of CO (black line), O (cyan line), OH (blue line), O₂ (magenta line), C (green line), HCO⁺ (yellow) and H₃⁺ (red line) fractional abundances versus visual extinction, A_v (mag). The top left panel represents a run with the reduced chemical network and steady state approach, the top right panel represents a run with the reduced chemical network and time dependent approach, the bottom left panel represents a run with the full chemical network and steady state approach, and the bottom right panel represents a run with the full chemical network and time dependent approach. 176
- 5.13 Model 17 of CO (black line), O (cyan line), OH (blue line), O₂ (magenta line), C (green line), HCO⁺ (yellow) and H₃⁺ (red line) fractional abundances versus visual extinction, A_v (mag). The top left panel represents a run with the reduced chemical network and steady state approach, the top right panel represents a run with the reduced chemical network and time dependent approach, the bottom left panel represents a run with the full chemical network and steady state approach, and the bottom right panel represents a run with the full chemical network and time dependent approach. 177
- 5.14 Model 20 of CO (black line), O (cyan line), OH (blue line), O₂ (magenta line), C (green line), HCO⁺ (yellow) and H₃⁺ (red line) fractional abundances versus visual extinction, A_v (mag). The top left panel represents a run with the reduced chemical network and steady state approach, the top right panel represents a run with the reduced chemical network and time dependent approach, the bottom left panel represents a run with the full chemical network and steady state approach, and the bottom right panel represents a run with the full chemical network and time dependent approach. 178
- 5.15 Model 2 (top panel) and model 5 (bottom panel) of the H/H₂ ratio versus visual extinction, A_v (mag). The green line represents the ratio reproduced with the reduced chemical network and steady state approach, the black line represents the ratio reproduced with the reduced chemical network and time dependent approach, the red line represents the ratio reproduced with the full chemical network and steady state approach, and the blue line represents the ratio reproduced with the full chemical network and time dependent approach. 179

-
- 5.16 Model 8 (top panel) and model 11 (bottom panel) of the H/H₂ ratio versus visual extinction, A_v (mag). The green line represents the ratio reproduced with the reduced chemical network and steady state approach, the black line represents the ratio reproduced with the reduced chemical network and time dependent approach, the red line represents the ratio reproduced with the full chemical network and steady state approach, and the blue line represents the ratio reproduced with the full chemical network and time dependent approach. . 180
- 5.17 Model 13 (top panel) and model 16 (bottom panel) of the H/H₂ ratio versus visual extinction, A_v (mag). The green line represents the ratio reproduced with the reduced chemical network and steady state approach, the black line represents the ratio reproduced with the reduced chemical network and time dependent approach, the red line represents the ratio reproduced with the full chemical network and steady state approach, and the blue line represents the ratio reproduced with the full chemical network and time dependent approach. . 181
- 5.18 Model 19 (top panel) and model 21 (bottom panel) of the H/H₂ ratio versus visual extinction, A_v (mag). The green line represents the ratio reproduced with the reduced chemical network and steady state approach, the black line represents the ratio reproduced with the reduced chemical network and time dependent approach, the red line represents the ratio reproduced with the full chemical network and steady state approach, and the blue line represents the ratio reproduced with the full chemical network and time dependent approach. . 182

LIST OF TABLES

3.1	Line flux measurements, in units of 10^{-14} W m ⁻² , for extragalactic sources with ISO-LWS detections of all 3 FIR fine structure emission lines of [C II] and [O I]. For each source, our own line flux measurements are listed in the first row, while literature values, if any, are listed in the second row (Contursi <i>et al.</i> 2002; Bergvall <i>et al.</i> 2000; Colbert <i>et al.</i> 1999; Fischer <i>et al.</i> 1996; Luhman <i>et al.</i> 2003; Malhotra <i>et al.</i> 2001; Negishi <i>et al.</i> 2001; Unger <i>et al.</i> 2000; Brauher <i>et al.</i> 2008). (n.a: not available)	78
3.2	Line flux measurements, in units of 10^{-14} W m ⁻² , for extragalactic sources with ISO-LWS detections of all 3 FIR fine structure emission lines of [C II] and [O I]. For each source, our own line flux measurements ,if any, are listed in the first row, while literature values, are listed in the second row (Contursi <i>et al.</i> 2002; Bergvall <i>et al.</i> 2000; Colbert <i>et al.</i> 1999; Fischer <i>et al.</i> 1996; Luhman <i>et al.</i> 2003; Malhotra <i>et al.</i> 2001; Negishi <i>et al.</i> 2001; Unger <i>et al.</i> 2000; Brauher <i>et al.</i> 2008). (n.a: not available)	84
3.3	Physical and chemical parameters for the UCL.PDR grid. In the grid of models the density and the radiation field parameters are incremented by 2 dex and 1 dex, respectively.	89
3.4	PDR diagnostic transitions. The critical densities for [C II] and [O I] are for collisions with H (Tielens & Hollenbach 1985).	89
3.5	Line flux measurements, in units of 10^{-14} W m ⁻² , for extragalactic sources with ISO-LWS detections of the [N II] 122- μ m emission line, together with the observed [C II] ₁₅₈ /[N II] ₁₂₂ flux ratio. Column 1 is the index number from Table 3.1.	104

4.1	Line flux measurements, in units of 10^{-14} W m ⁻² , for a selection of extra-galactic starburst sources, taken from the galaxy sample studied in the previous Chapter (see Table 3.1), with ISO-LWS detections of all 3 FIR fine structure emission lines of [C II] and [O I]. For each source, our own line flux measurements are listed.	116
4.2	Electron density diagnostic. The critical densities for [O III] 88 and 52 μ m are for collisional de-excitation (Osterbrock & Ferland 2006). All values are calculated for T=10,000 K.	117
4.3	Line flux measurements, in units of 10^{-14} W m ⁻² , for ISO-LWS detections of [O III] 52 and 88 μ m fine structure emission lines. For each source, our own line flux measurements and their ratios are listed.	118
4.4	Electron densities computed with EQUIB06 using the [OIII] 52 μ m/[OIII] 88 μ m ratio, listed in Table 4.3, for an adopted electron temperature of 10,000K. . . .	121
4.5	NGC 4038 ISO lists fine structure emission lines intensities, measured by us, in 10^{-14} W m ⁻² units.	123
4.6	The grid model input parameters of MOCASSIN.	128
4.7	Gas-phase elemental abundances used in the MOCASSIN code. (Relative to total hydrogen nuclei)	129
4.8	The grid model input parameters of UCL_PDR. The incident FUV radiation fields are inputted from the ionization models and represent the radiation field at the ionization front.	130
4.9	The first column lists the computed radiation field at the ionization front. The remaining columns lists the [C II] ₁₅₈ , [O I] ₆₃ and [O I] ₁₄₅ emission lines, and the [N III] ₅₇ /[N II] ₁₂₂ ratio computed from the grid of MOCASSIN models listed in Table 4.6.	134
4.10	[C II] ₁₅₈ , [O I] ₆₃ and [O I] ₁₄₅ emission computed from the grid of UCL_PDR models listed in Table 4.8.	135
4.11	Nitrogen emission lines obtained from the grid of MOCASSIN models. In bold the range of models that minimize the χ^2 with the number of degrees of freedom n , which is listed in the last column.	146
4.12	Results from the gaussian fits derived from spectra of the Antennae galaxy (NGC 4038 nucleus) taken with the CSO telescope (see Tab B2, Bayet <i>et al.</i> 2006). The observed lines are indicated in the first column.	147

4.13	CO rotational emission lines obtained from UCL_PDR for the best fit models listed in bold in Table 4.11 and the calculated χ^2 with the number of degrees of freedom n . The [CI] emission line is also predicted.	148
5.1	Number of grid points used for the benchmark of the adaptive grid and the respective A_v where the H/H ₂ transition occurs.	161
5.2	Species contained in the reduced chemical network of the modified UCL_PDR code.	166
5.3	Grid of 54 UCL_PDR models subdivided by different physical parameters such as density, radiation field, metallicity and cosmic ray ionization rate in a range of visual extinction values ($1 \leq A_v \leq 6$).	169

INTRODUCTION

Naked-eye observations of the sky reveal almost nothing about the real structure of a galaxy. What actually appears empty to us is, in reality, filled with dust and gas and is called the interstellar medium (ISM). Over the past few decades there have been radical changes in the way we view the ISM. Field *et al.* (1969) proposed that the ISM had multiple stable equilibrium phases. This theory was expanded by McKee & Ostriker (1977) who introduced four phases of the ISM and claimed that most space is filled by a hot ionized medium (HIM), while most of the mass is in a cold neutral medium (CNM). Shells of warm neutral medium (WNM) and warm ionized medium (WIM) surround clouds of the CNM (see Fig 1.1).

An understanding of the ISM, of how the interchange between dust and gas plays an important role in the formation of molecules, and of the importance of stellar radiation in controlling the chemical and physical composition of the ISM, is crucial in determining the overall star formation rate of the host galaxy and therefore its global properties. Most of the CNM and all of the WNM are included in what we call photodissociation regions (PDRs), while the WIM is included in what we call photoionization regions. The study of these two regions is very important because it can tell us much about the conditions within star-forming regions. PDRs are responsible for most of the infrared luminosity coming from a galaxy. For example, the COBE 4- μm to 1000- μm spectrum of our Milky Way Galaxy (Wright *et al.* 1991) is dominated by PDR emission (see Fig 1.2 and Fig 1.3 for the [C II]¹ and [N II] maps), with

¹Hereafter, the numeral I is used for spectral lines associated with the neutral element, II for those from the first ionization state, III for those from the second ionization state, and so on. For example, 'C I' denotes lines of neutral carbon, and 'C II' denotes lines arising from the first ionization state, C⁺, of carbon.

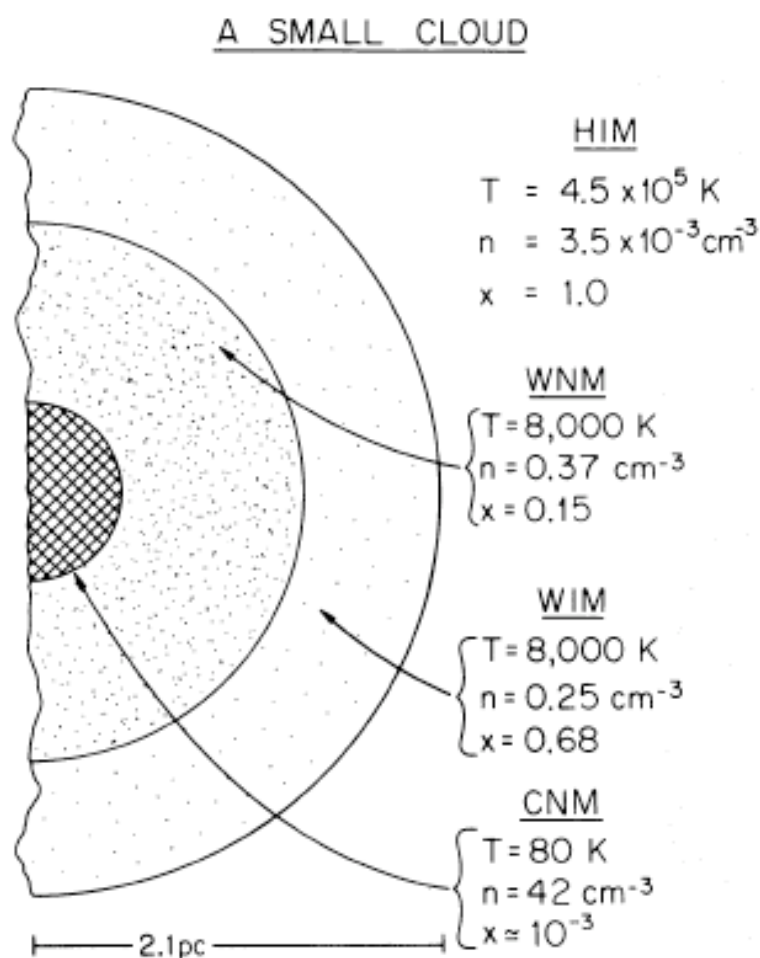


Figure 1.1: Cross section of a characteristic small cloud. The crosshatched region shows the cold core, which gives the usual optical absorption lines. The following region is the WNM with ionization produced by soft X-ray background. The outer layer, WIM, is gas largely ionized by stellar UV background (McKee & Ostriker 1977).

the exception of the [N II] and a fraction of the [C II] fine structure emission, which originate in diffuse H II gas (Hollenbach & Tielens 1997).

Photo-dominated and ionized regions often lie next to each other and they include WNM, WIM, diffuse and translucent clouds, planetary nebulae and proto-planetary discs.

A fundamental aspect in understanding these structures is the investigation of the effect of the ultraviolet and far ultraviolet radiation field coming from a nearby ionising source, on both regions. Traditionally, ionized and photo-dominated regions are associated with ionized gas and atomic gas respectively. In ionized regions almost all the hydrogen is in ionized form, while photodissociation regions include molecular material (mostly H₂ and CO).

COBE FIRAS 158 μm C⁺ Line Intensity

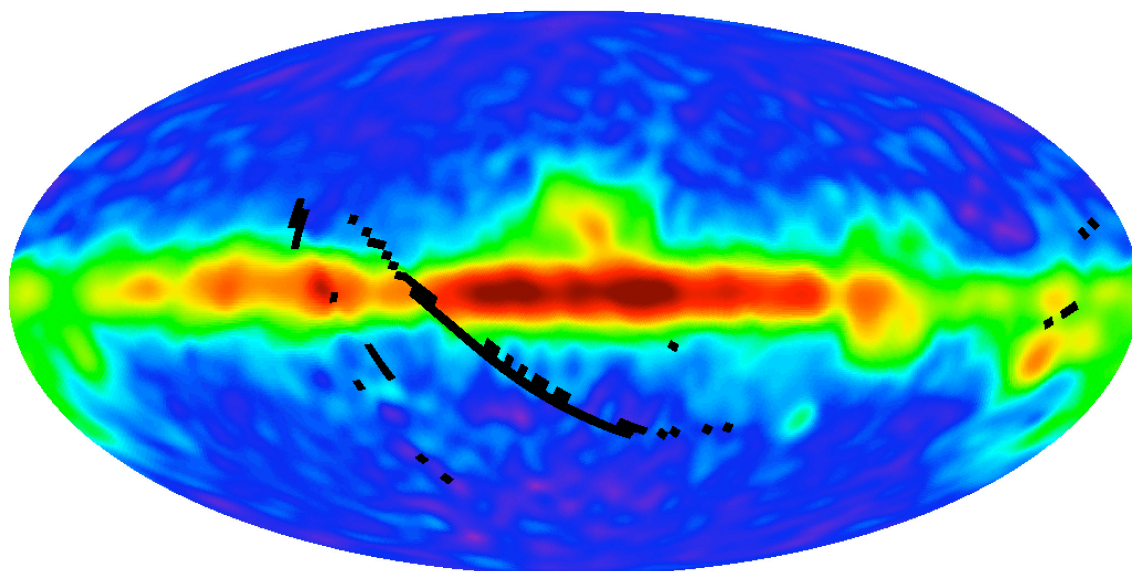


Figure 1.2: The [C II] emission of the galaxy observed by the FIRAS instrument of COBE (Bennett *et al.* 1994). The galactic plane is horizontal with the galactic centre at the centre.

Theoretical models of PDRs have been constructed and developed by several research groups (e.g., Tielens & Hollenbach 1985; Sternberg & Dalgarno 1995; Le Bourlot *et al.* 1993; Koester *et al.* 1994; van Dishoeck & Black 1988; Bell *et al.* 2006*b*) and have successfully interpreted a wide variety of multi-wavelength Galactic and extragalactic emission line data. Several authors have also developed photoionization codes to treat a variety of astrophysical systems (e.g., Péquignot *et al.* 2001; Ercolano *et al.* 2003; Pequignot & Aldrovandi 1986; Ferland *et al.* 1998).

The work presented here is concerned with the study of PDR and ionized regions in extragalactic sources. A detailed description of three codes used throughout my thesis is given in Chapter 2. PDR model tests against extragalactic Infrared Space Observatory Long Wavelength Spectrometer (ISO LWS) data for fine structure emission lines are given in Chapter 3. In Chapter 3 information about oxygen self absorption and the fraction of [C II] emission coming from H II regions are also provided. In Chapter 4 an attempt at a unified model (ionized + PDR regions) of the Antennae starburst galaxy is presented and an investigation of [C II], [O I], [N III], [N II] and CO rotational emission lines is conducted. Chapter 5 is dedicated to the feasibility of coupling a

COBE FIRAS 205 μm N^+ Line Intensity

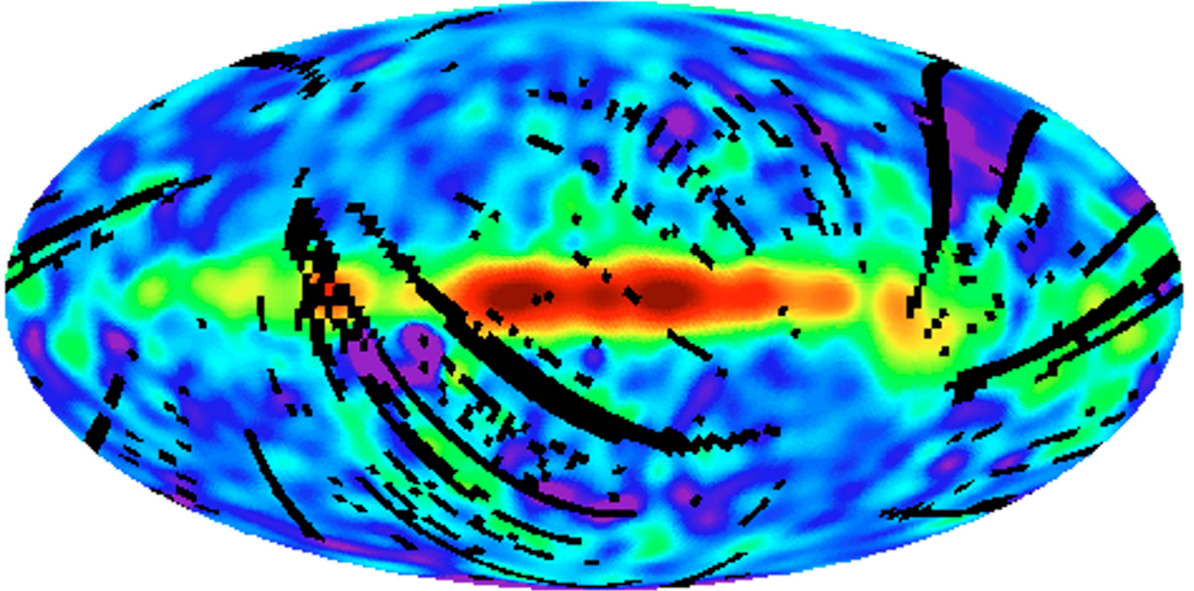


Figure 1.3: The $[\text{N II}]$ emission of the galaxy observed by the FIRAS instrument of COBE (Bennett *et al.* 1994). The galactic plane is horizontal with the galactic centre at the centre.

photoionization code, MOCASSIN, with a PDR code, UCL_PDR, taking into consideration that the ionized and photodissociation regions are linked to each other by the ultraviolet radiation field. The final conclusions and future projects are given in Chapter 6.

1.1 The physics of photoionization regions

Ultraviolet light from stars inside or nearby H II regions provides the source of energy that allows the cloud or nebula to radiate. Usually, it is possible to find one or more OB emitting stars that, by photoionization, transfer energy to the cloud. During this process, photons with energy greater than the hydrogen ionization potential, 13.6 eV, are absorbed and the excess energy, above the ionization potential, of these photons is converted into the kinetic energy of a photoelectron. Collisions among electrons, and between electrons and ions, distribute this energy and maintain a Maxwellian velocity distribution with a temperature in the range $5,000 \text{ K} < T < 20,000 \text{ K}$. They also excite the low lying energy levels of the ion (Osterbrock & Ferland

2006). Downward radiation transitions from these excited levels have very small transition probabilities, but at the typical low densities of ionized regions collisional de-excitation is even less probable. Thermal electrons are recaptured by the ions and the degree of ionization at each point within the H II region is fixed by the equilibrium between photoionization and recombination. The ionization equilibrium can be written as:

$$N_{H^0} \int_{\nu_{H^0}}^{\infty} \frac{4\pi J_\nu}{h\nu} a_\nu(H^0) d\nu = N_e N_p \alpha_A(H^0, T) \quad (1.1)$$

where N_{H^0} , N_e and N_p are the neutral hydrogen, electron and proton densities per unit volume respectively; ν_{H^0} is the ionization frequency threshold of neutral hydrogen; J_ν is the frequency-dependent mean intensity of the radiation field; $a_\nu(H^0)$ is the frequency-dependent photoionization cross-section of neutral hydrogen; and $\alpha_A(H^0, T)$ is the temperature dependent effective recombination coefficient to all levels of H^0 . J_ν has units of energy per unit area per unit solid angle per unit time per frequency interval. The quantity $4\pi J_\nu/h\nu$, therefore, represents the number of incident photons per unit area per unit time per frequency interval. The right hand side of Equation 1.1 represents the total number of recombinations and the left hand side the total number of ionizations. This equation can be used to describe the ionization balance of all other species by substituting N_{H^0} and N_p with N_{X^i} and $N_{X^{i+1}}$ respectively, and using the appropriate photoionization cross-section, $a_\nu(X^i)$, frequency threshold, ν_{X^i} , and total recombination coefficient, $\alpha_\nu(X^i, T)$.

Once emitted, the photoelectrons are quickly thermalized to a Maxwell-Boltzman energy distribution, since the cross-section for elastic collisions between the electrons is much larger than all the recombination cross-sections or the cross-section for any other nebular process involved. The total electron temperature is, therefore, determined by the electron's Maxwellian distribution function and all recombinations and collisional excitations can be assumed to occur at rates fixed by this temperature. During the recombination process photons are emitted creating the H I Balmer and Paschen line spectra observed in most of the photoionization regions (Osterbrock & Ferland 2006).

The total radiation field is the sum of the stellar and the diffuse components. The stellar component consists of photons emitted directly by the ionizing source, whereas the diffuse component is emitted by the gas in the nebula. It is easier to treat the two components separately such that:

$$I_\nu = I_\nu^s + I_\nu^d \quad (1.2)$$

where I_ν , I_ν^s and I_ν^d are the specific intensities of the total, stellar and diffuse radiation fields respectively. The diffuse radiation field is described by the equation of radiative transfer:

$$\frac{dI_\nu^d}{ds} = -N_{H^0}a_\nu I_\nu^d + j_\nu \quad (1.3)$$

where j_ν is the local gas emissivity for ionizing radiation, in units of energy per unit volume per unit time per unit solid angle per unit frequency (Osterbrock & Ferland 2006).

1.1.1 Photoionization

Photoionization occurs when, during the interaction of a photon with an atom or an ion, the photon transfers a part of its energy to one of the bound electrons, which is then able to escape from the ion. In ionized regions any photons emitted with wavelengths lower than the Lyman limit of 912 Å are energetic enough to ionize neutral hydrogen. The gas, where the hydrogen is ionized, becomes a H II region, usually surrounded by neutral hydrogen that is shielded from the UV radiation. The higher the temperature and luminosity of the ionizing stars, the more luminous is the UV radiation and the higher is the ionization degree of the region. Hydrogen is the main constituent of the interstellar gas, hence it is the main component of the H II regions. However, it is possible to find in these regions other heavier elements in ionized states, mainly He, O, N, C and Ne singly or multiply ionized. The photoelectrons released in the ionization process have kinetic energies given by the difference between the energy of the ionizing photons and the ionization potential of hydrogen. These electrons collide with other electrons and ions exciting atoms in the region, which emit in forbidden spectral lines. Since these lines are completely suppressed by collisional de-excitation at normal laboratory densities, it is impossible to detect them. Therefore these lines are referred to as forbidden lines. Since hydrogen accounts for more than 75% of the mass of the region, we can consider the ionization structure of the hydrogen as a first approximation to the global structure of the region. Therefore, approximating the region as a sphere with uniform density and volume $\frac{4}{3}\pi R_s^3$, the flux decreases with the distance to the ionizing star due to geometric dilution and absorption along the path of the photons, until it reaches a level where the ionization and recombination rates are in equilibrium. The radius R_s corresponds to this threshold and it is called the Strömgen Radius (See Chapter 5). Inside this radius, ionizing photons are absorbed, and therefore, the volume of the ionized gas surrounding a hot star, assumed to be spherical and uniform, is proportional to its ionizing luminosity and inversely proportional to the gas density squared. The radius of these regions is limited by the rate of ionizing photons emitted by the stars and not by the size of the

H I cloud. This cloud remains neutral outside the ionized region. These regions are known as ionization bounded regions. However, observations have shown that some regions exist where there is not enough gas to absorb all the ionizing radiation released by the stars. These regions are known as density bounded regions because there is no sharp boundary between the ionized and the neutral regions (Gutiérrez & Beckman 2008).

1.1.2 Nebular continuum emission

The emergent nebular continuum is the sum of the free-free emission (bremsstrahlung), bound-free emission (recombination continuum), and two-photon H I continuum emission contributions, resulting in a complex continuous spectrum crossed by sharp edges. All these three mechanisms are primarily associated with hydrogen and helium, with negligible contributions from metals. The free-bound emission process dominates in the optical region. The continuum radiation is emitted when a free electron with velocity v recombines into an excited level of H I with principal quantum numbers $n \geq n_1$. The energy of the photon is given by energy conservation:

$$h\nu = \frac{1}{2}mv^2 + E_n \quad (1.4)$$

where $h\nu$ is the energy of the photon emitted by recombinations of electrons with velocity v to levels with a binding energy of E_n . The emission coefficient of this continuum radiation is given by:

$$\epsilon_\nu = \sum_{n=n_1}^{\infty} \sum_{L=0}^{n-1} \nu \sigma_{nL}(H^0, v) f(v) h\nu \frac{dv}{d\nu} \quad (1.5)$$

The recombination cross-sections, σ_{nL} , can be derived from the photoionization cross-sections using the Milne Relation that is:

$$\frac{\sigma_{bf}}{\sigma_{fb}} = \frac{1}{2} \left(\frac{mv_e c}{h\nu} \right)^2 \quad (1.6)$$

where σ_{bf} and σ_{fb} are the bound-free and free-bound cross sections.

The free-free emission dominates in the far infrared and it results from electrons scattering off the protons in an encounter that does not result in recombination. The emissivity per unit frequency for free electrons, in Coulomb, colliding with ions of charge Z is given by:

$$\epsilon_\nu = \frac{32Z^2 e^4 h}{3m^2 c^3} \left(\frac{\pi h \nu_0}{3kT} \right)^{1/2} e^{-\frac{h\nu}{kT}} g_{ff}(T, Z, \nu) \quad (1.7)$$

where g_{ff} is a Gaunt factor. The contribution of the He I and He II continua can be similarly calculated. The bound-free and free-free terms are often combined into a single emission

coefficient for the H I recombination continuum. In typical nebulae, He/H is 0.1 (Osterbrock & Ferland 2006). If the He in the nebula is mostly He⁺⁺, the contribution to the continuum from He II will be comparable to the H I continuum. In nebulae where most of the He is He⁺, the contribution to the continuum from He I is about 10% of the strength of the H I continuum. An additional source of continuum emission is the two-photon H I continuum, caused by the decay of the 2²S level of H I. The transition probability for this decay is 8.23 s⁻¹, and the sum of the energies of the two photons is equal to $h\nu_{Ly\alpha}$. The greater the number of scatterings of Ly α within the nebula, the greater the significance of the two-photon continuum, because each scattering electron has a finite probability of shifting from the 2²P level to 2²S level.

1.1.3 Charge transfer

In an ionized gas, electrons are the most abundant, the hydrogen is completely ionized and charge exchange reactions with hydrogen can play an important role in the ionization structure of the gaseous nebula and must be taken into account in the ionization balance calculations of some ions. Charge transfer is a collisional process in which a neutral atom and an ion exchange an electron, as in $H^0 + A^{+2} \rightarrow H^+ + A^+$. Because the heavy element A is usually less abundant, this process has a small effect on the ionization of hydrogen for a solar composition. However, charge transfer can be the dominant ionization or recombination process for the ions of the heavy elements. In particular, charge exchange of neutral oxygen in two body recombination with hydrogen is very important. Charge transfer between atomic hydrogen and oxygen was the first well-studied case (Chamberlain 1956) and is peculiar because the two elements have nearly the same ionization potentials. This reaction can be written as follows



where J is the total angular momentum quantum number. Later, after comparing photoionization models of the planetary nebula NGC 7027 with observations, Pequignot *et al.* (1978) showed that transfer of hydrogen with multiply ionized species must be fast. This behaviour was also predicted by Dalgarno (1954). Today this behavior is well established. Spectroscopic features can be detected through the resulting cascades (Butler *et al.* 1979), as the electron decays to the ground state, thereby providing a potential diagnostic test of the process. Charge transfer occurs when an atom interacts with the Coulomb field of a positive ion, forming a quasi-molecule. For reactions with large rate coefficients, the process is localized at a crossing between the incoming and outgoing potential curves (Ferland 2003). So charge transfer is, by its nature,

treated as a molecular process. Usually, rate coefficients are more difficult to calculate than atomic collision rate coefficients due to the greater difficulty of obtaining accurate molecular interaction potentials. Some charge exchange reactions rate coefficients for oxygen, nitrogen and other heavy ions are listed by Osterbrock & Ferland (2006). For a more complete and up to date listing of all hydrogen charge exchange reaction rate coefficients for the first thirty atomic elements, see Kingdon & Ferland (1996); Stancil *et al.* (1999, 2000). Once the transfer has taken place in a multiply charged system, the system consists of two positively charged ions that are strongly repulsive. These repel each other with an amount of kinetic energy given by the difference in ionization potentials of the relevant levels. This can be a significant heating process for the gas (Kingdon & Ferland 1996).

1.2 The Physics of PDRs

When one talks about the interstellar radiation field, one should consider how the various physical and chemical processes that determine the structure of photon-dominated regions are all connected with the incident far-ultraviolet radiation. Although, the gas is indirectly thermally coupled to the FUV field, the chemistry is driven by photoionization and photodissociation reactions and the radiative transfer of the FUV photons affects the survival of the two most important molecular species, H₂ and CO. The conditions within a PDR can be described using two key parameters: the number density of hydrogen nuclei in the cloud, n , (in cm⁻³) and the flux of photons that strike its surface, G_0 (in erg s⁻¹cm⁻²), but there are many other parameters that can affect this structure. The density range in PDRs varies from $n \sim 0.25$ cm⁻³ in the WNM to $n \geq 10^6$ cm⁻³ in regions of massive star formation. The average flux of the typical Interstellar radiation field (ISRF) (in the wavelength range $912 \text{ \AA} < \lambda < 2400 \text{ \AA}$) has been determined to be 1.6×10^{-3} erg s⁻¹cm⁻² by Habing (1968), who observed O and B stars along many lines of sight. This standard radiation field has been adopted in the calculation of many quantities relevant to the study of PDRs and it is convenient to express the FUV flux in terms of the Habing field, multiplied by some factor G_0 . Alternatively in PDR models the ultraviolet ISRF is also often used for wavelengths less than 2000 Å as given by Draine (1978). This is especially true when determining the rates of photoreactions whose cross sections have been evaluated by integration over the spectral energy distribution (SED) of the Draine field. The average flux of the Draine field is related to that of the Habing field by $\chi = 1.7G_0$. The incident FUV fluxes can range from $G_0 \leq 1$ Habing for clouds illuminated by the local ISRF to $G_0 \geq 10^6$

Habing for PDRs located close to O stars. The radiative transfer of FUV radiation in a dusty medium has been studied in detail for many scenarios (e.g. Hegmann & Kegel 2003; Sternberg & Dalgarno 1995; Goicoechea & Le Bourlot 2007), but for the most part, the assumption of homogeneity and a simplified geometry are sufficient for the modelling of PDRs. The definition of the surface of the PDR is then the point at which the FUV radiation first comes into contact with the neutral gas and is perpendicular to the path the light will take as it permeates the cloud. Flannery *et al.* (1980) solved the radiative transfer equation for plane-parallel slabs of various thicknesses and showed that the mean intensity is given by

$$G_0(A_v, \lambda) = G_0(0) \exp(-\kappa \xi_\lambda A_v), \quad (1.9)$$

where G_0 is the intensity of the unattenuated radiation field at the PDR surface, κ depends on the scattering properties of the dust grains, ξ_λ is the ratio of the extinction at wavelength λ to that in the visual ($\lambda_v \sim 5500 \text{ \AA}$) and A_v is the visual extinction measured from the surface of the slab. To first order, κ is given by the diffusion approximation (Flannery *et al.* 1980),

$$\kappa = \sqrt{3(1 - \omega)(1 - \omega g)} \quad (1.10)$$

in which ω is the albedo of the dust grains and g is the scattering phase function (i.e., the mean cosine of the scattering angle, $\langle \cos \theta \rangle$). The visual extinction is related to the dust properties by

$$A_v = 1.086 \tau_v \int_0^z n_{gr} Q_{ext} \langle \sigma_{gr} \rangle dz'; \quad (1.11)$$

where τ_v is the optical depth in the visual, n_{gr} is the number density of dust grains (in cm^{-3}), Q_{ext} is the ratio of the grain visual extinction cross section to its geometric cross section, $\langle \sigma_{gr} \rangle$ is the average grain geometric cross section (in cm^2) and z is the distance into the slab (in cm), measured from, and perpendicular to, the surface. For thin clouds, a correction factor has to be included in Equation 1.9 to allow photons to penetrate from the far side of the cloud. The intensity of the radiation field inside an interstellar cloud is therefore largely determined by the absorption and scattering properties adopted for the dust grains and, unfortunately, these remain unclear. The ratio of total to selective extinction

$$R_V = \frac{A_V}{E(B - V)} \quad (1.12)$$

is a common measure of the slope of the wavelength-dependent extinction curve in the optical and can be used to determine an approximate extinction law (Cardelli *et al.* 1989). Although observed values of R_V are known to vary quite significantly from one sightline to another, the

typical value of R_V is 3.1 that has been observed for diffuse clouds and varies in a range of 5-6 for dense molecular clouds (Fitzpatrick 1999). Bohlin *et al.* (1978) determining the column densities of atomic and molecular hydrogen, and thus the total column density of hydrogen nuclei, $N_H = N(H) + 2N(H_2)$, using H Lyman- α emission and UV absorption lines of H_2 along lines of sight through diffuse clouds, found:

$$N_H/E(B - V) = 5.8 \times 10^{21} \text{cm}^{-2} \text{mag}^{-1} \quad (1.13)$$

$$N_H/A_v \sim 1.9 \times 10^{21} \text{cm}^{-2} \text{mag}^{-1} \quad \text{for } R_V = 3.1 \quad (1.14)$$

These values are still widely used today to calculate the A_v -depth relation, since $N_H = \int ndz = nz$ for a slab of constant density. One has to be careful when performing such calculation because the observations were limited to diffuse cloud lines of sight and may not be valid for denser molecular clouds.

1.3 The Chemistry of PDRs

One of the most widely recognized functions of grains is the shielding of dense molecular clouds from UV radiation field. This screening effect allows the temperatures of these clouds to become quite low (10-30K) and limits the ionization of species within. This dense, cool cloud in turn can collapse to form new stars. However, as I have already mentioned, FUV radiation is also attenuated by dust grains, which provide the major source of continuum opacity in interstellar clouds as they absorb and scatter light at visible and ultraviolet wavelengths. The attenuation of the FUV flux with distance into the PDR gives rise to a characteristic depth-dependent chemical structure, separated into distinct zones within which the chemistry is controlled by specific sets of gas-phase reactions. These reactions involve atomic species whose ionization potentials lie below the Lyman limit, causing them to be photoionized by incident radiation. As the intensity of radiation decreases, these atoms are able to make the transition from ionic to neutral form. Obviously, because of the high FUV flux, photoreactions are very important as well as reactions with atomic hydrogen. Molecular hydrogen plays a crucial role in PDR chemistry, especially if vibrationally excited. The self-shielding of H_2 is also important. Another species affected by self-shielding is CO: as one moves further into the cloud, fewer H_2 and CO molecules are dissociated by the radiation field. The most important reactions in the chemistry of carbon and oxygen compounds are schematically shown in Fig 1.4 (Sternberg & Dalgarno 1995).

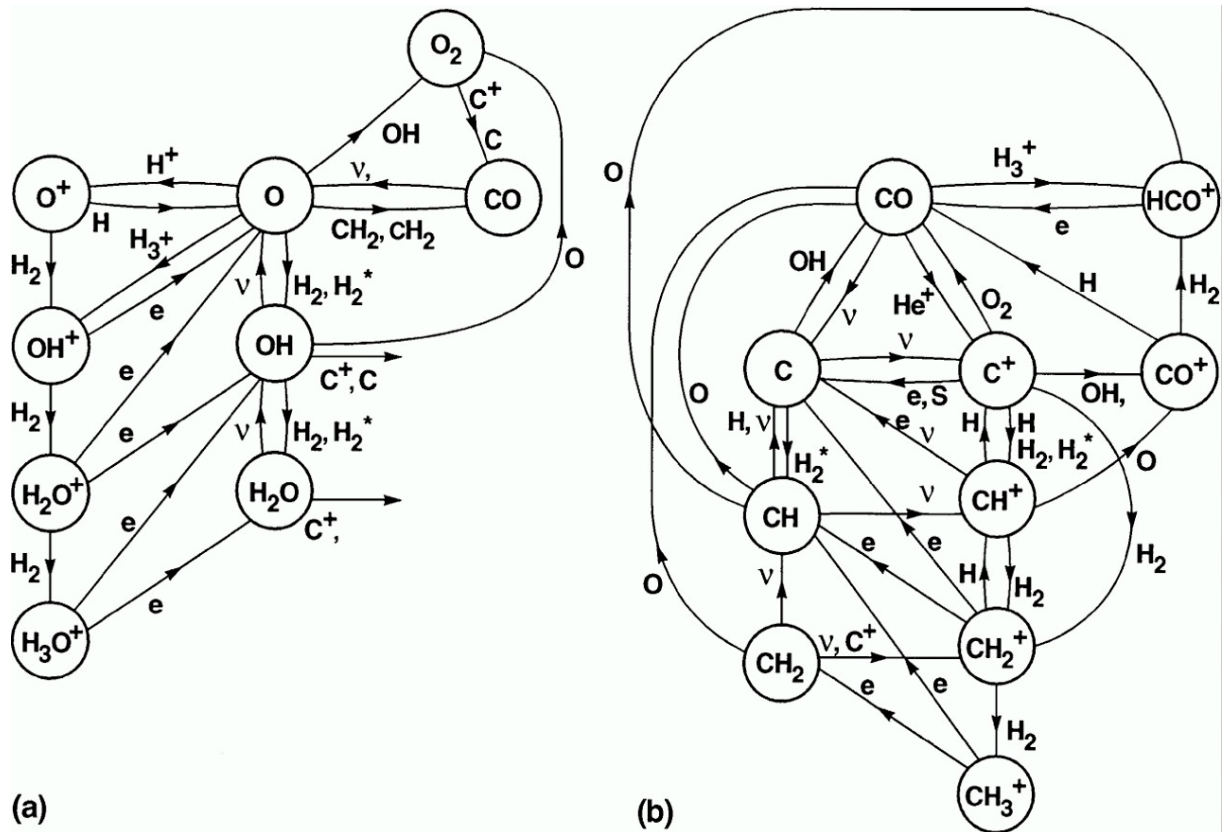


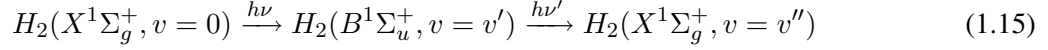
Figure 1.4: The most important reactions in the chemistry of carbon and oxygen compounds. Oxygen-bearing radicals are formed through reactions of O with H_2 , whereas most of OH produced is photodissociated again, but a small fraction reacts with C^+ to form CO^+ and so on (Sternberg & Dalgarno 1995).

In the following sections the principal chemical and physical mechanisms, the formation of H_2 and the distinct characteristic chemical zone in PDRs are presented.

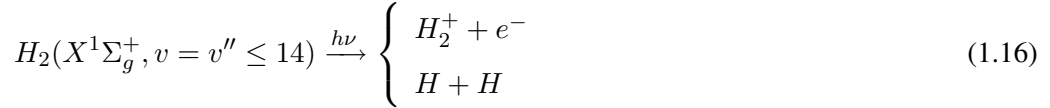
1.3.1 H_2 photodissociation

While H_2 is rapidly destroyed in H II regions, another mechanism is necessary for the photodestruction of H_2 molecule in PDRs. In fact, it was Spitzer (1948) that first claimed that molecular hydrogen is effectively shielded from direct photodissociation in neutral regions, since the photodissociation continuum (14.7 eV) and photoionization continuum (15.4 eV) of H_2 lie above the Lyman limit (13.6 eV). Solomon (1965) proposed a different, but effective route, for the photodissociation of H_2 ; an absorption process, in two steps, via electronic transitions from the ground state ($X^1\Sigma_g^+$) to the Lyman ($B^1\Sigma_u^+$; 11.2 eV) or Werner ($C^1\Pi_u$; 12.3 eV) bands,

followed by radiative decay to the vibrational continuum of the ground electronic state and dissociation of the molecule. Later Stecher & Williams (1967) introduced a formal description of this mechanism and computed its rate. This process can be described by the following equation:



for the case of Lyman band absorption, where v is the vibrational level of the molecule. This process leads to dissociation if $v'' > 14$ (the vibrational continuum). If instead radiative decay leaves the molecule in a vibrationally excited, but bound, level of the ground electronic state ($2 \leq v'' \leq 14$), subsequent absorption of another FUV photon can lead to direct photoionization or photodissociation,



Equation 1.15, showing the spontaneous radiative dissociation mechanism, is believed to dominate the photodestruction of H_2 in neutral interstellar clouds. For the standard Draine ISRF, the total unattenuated photodissociation rate of molecular hydrogen, taking into account all pertinent absorption lines, is $\sim 5 \times 10^{-11} \text{s}^{-1}$. Although the Werner band generally contributes somewhat to the photodissociation rate, absorption in the Lyman band is the dominant process. Increasing the optical depth in the H_2 lines causes a decrease in the rate of dissociation, because this mechanism is initiated by line rather than continuous absorption. In fact, the hydrogen molecules that can be found in the extremities of the cloud shield the hydrogen molecules in the inner regions of the cloud from the dissociating radiation. This self-shielding can, under certain conditions, exceed the attenuation due to scattering and absorption of photons by dust grains. Hollenbach & Salpeter (1971) claimed that the H_2 photodissociation is controlled by the self-shielding function:

$$\theta_i = \frac{\int_{-\infty}^{\infty} \sigma_i(\nu) \exp[-N_i \sigma_i(\nu)] d\nu}{\int_{-\infty}^{\infty} \sigma_i(\nu) d\nu} \quad (1.17)$$

where i refers to a particular transition in the Lyman or Werner systems; $\sigma_i(\nu)$ is the cross section for excitation (in cm^2) and N_i is the column density of molecular hydrogen in the lower state of the transition (in cm^{-2}) along the line of sight to the surface. At the surface of the cloud $\theta_i = 1$ and H_2 is photodissociated by the unattenuated FUV radiation. The radiation field is attenuated in the line and $\theta_i \rightarrow 0$ as $N_i \rightarrow \infty$ as the column density of absorbing molecules

increases, reducing the photodissociation rate accordingly. On the other hand the self-shielding function may be expressed as (Federman *et al.* 1979) :

$$\theta_i = \frac{dW_i}{d(N_i\sigma_i)} \quad (1.18)$$

where W_i is the equivalent width for the i^{th} transition,

$$W_i(N_i) = \int \{1 - \exp[-N_i\sigma_i(\nu)]\} d\nu \quad (1.19)$$

These expressions have been evaluated numerically for the total self-shielding summed over all transitions by a number of groups (van Dishoeck & Black 1986; Draine & Bertoldi 1996; Federman *et al.* 1979) and analytic approximations have been derived to fit the results. This formula is considered quite reliable in most situations. In addition to self-shielding H₂ is also involved in the attenuation of the photodissociation rate. In fact, the overlap of atomic hydrogen lines with the Lyman and Werner bands of H₂ is more important the further inside the cloud one goes, however it is only significant in the line wings. The wavelength range $912 \text{ \AA} \leq \lambda \leq 1110 \text{ \AA}$ contains the Lyman- α , γ , δ , etc. Since PDRs can possess large column densities of atomic hydrogen, these lines may suppress absorption in some of the H₂ lines of atomic hydrogen, at 1025.72 \AA , 972.54 \AA , 949.75 \AA , etc. The calculation of line overlap effects requires that the wavelength-dependent penetration of the radiation field be treated explicitly, through the detailed computation of radiative transfer within the cloud, and this has been examined in detail by a number of authors (van Dishoeck & Black 1986; Draine & Bertoldi 1996; Abgrall *et al.* 1992; Le Bourlot *et al.* 1993; Lee *et al.* 1996). Also, Lee *et al.* (1996) have produced tables of shielding coefficients that can be used to obtain reliable estimates of the H₂ photodissociation rate without the need for computationally expensive radiative transfer calculations.

1.3.2 CO photodissociation

The photodissociation of CO is caused by absorption in predissociating lines to an excited electronic state, followed by transition to a repulsive electronic state and dissociation. Under any circumstances when molecular hydrogen is abundant, the photodissociation rate of CO rapidly declines. In this case, also, the depth of the C II/CI/CO transition layer is linked to that of H/H₂ transition layer when H₂ self-shielding is more important than attenuation by dust. Carbon has an ionization potential of 11.26 eV and so is photoionized by the FUV radiation. CO is subjected to self-shielding effects in the same way as molecular hydrogen, as its photoionization occurs through line absorption. However, its low abundance means that the lines do not become optically

thick, and the contribution of self-shielding to the total shielding is generally small. In addition carbon absorption lines also overlap with those of molecular hydrogen. H_2 therefore provides effective shielding, since its lines become optically thick. The shielding effect due to absorption in the Lyman lines of atomic hydrogen can generally be neglected. The photoionization is able to keep high abundances of singly ionized carbon where the recombination is dominating as the FUV radiation diminishes. The C II/CI/CO transition layer is the point at which recombination becomes the predominant mechanism. At this location the neutral carbon abundance peaks, before declining at greater depths as carbon becomes trapped into the stable CO molecule, through the consumption of CH and CH_2 radicals by atomic oxygen. The total shielding of the FUV radiation appropriate for the photoionization of carbon, including contributions from dust extinction, neutral carbon absorption and overlapping H_2 lines has been computed by Kamp & Bertoldi (2000):

$$\tau = \tau_{uv} + a_C N(C) + 0.9T^{0.27} [N(H_2)/10^{22} \text{cm}^{-2}]^{0.45} \quad (1.20)$$

where τ_{uv} is the dust optical depth in the FUV, $a_C \sim 1.1 \times 10^{-17} \text{cm}^2$ is the FUV-averaged carbon ionization cross section (from Osterbrock & Ferland 2006) T is the gas temperature, and $N(C)$ and $N(H_2)$ are the column densities (in cm^{-2}) of neutral carbon atoms and hydrogen molecules respectively, as measured from the surface of the PDR.

1.3.3 Hydrogen recombination on grain surfaces

Because the following reaction is extremely slow, under typical interstellar conditions:



molecular hydrogen is not formed by the direct radiative association of hydrogen atoms (Gould & Salpeter 1963). This is because the emitted photon that is necessary for stabilising the association of the two ground state atoms, results from a transition that is strongly forbidden (from the repulsive triplet state to the ground electronic state of the H_2 molecule, $(b^3\Sigma_u^+ \rightarrow X^1\Sigma_g^+)$). Usually the fraction of atoms in excited states is small, therefore the radiative recombination of an H atom in the ground state with an H atom in an excited state can proceed via allowed transitions, but can generally be neglected. Also, at number density $n < 10^{10}$ the three-body reaction $3H \rightarrow H_2 + H$ is inefficient, therefore it can be ignored in most PDRs. Molecular hydrogen may be formed in the gas phase by radiative association followed by associative

detachment (McDowell 1961; de Jong 1972):



in which the electron acts as a catalyst. However, this process is only efficient when the electron density is high and the radiation field that dissociates H^- is weak (Dalgarno & McCray 1973). This process only becomes important deep within clouds ($A_v \gg 5$ mag) because the H^- radical, which suffers less attenuation by dust grains than visible light, can be destroyed by near-IR light. The pioneers that first attempted to model the formation of molecular hydrogen, by recombination of H atoms on the surface of interstellar dust grains, were Gould & Salpeter (1963). In this process, the dust grain acts as the stabilising third body that carries away some of the 4.5 eV of excess energy from the formation of the molecule. The excess energy resulting from the formation process is shared between the hydrogen molecule, which is injected into the gas in an excited state with some amount of kinetic energy, and the grain, which carries the energy away through lattice vibrations. The H_2 formation rate per unit volume, averaged over the grain size distribution, that Hollenbach & Salpeter (1971) computed, can be described by the following equation:

$$R_f = S(T, T_d)\eta(T_d)n_{gr}n(H)\langle\sigma_{gr}\rangle\langle v_H \rangle \quad [\text{cm}^{-3}\text{s}^{-1}] \quad (1.23)$$

where $S(T, T_d)$ is the probability that a hydrogen atom with temperature T , colliding with a dust grain of temperature T_d , will stick to the surface (generally called the sticking coefficient), $\eta(T_d)$ is the probability that a trapped H will traverse the grain surface, find another H adatom and recombine, the H_2 molecule subsequently evaporating from the grain surface; n_{gr} is the number density of dust grains in cm^{-3} , $n(H)$ is the number density of H atoms in cm^{-3} , $\langle\sigma_{gr}\rangle$ is the average grain geometric cross section in cm^2 and $\langle v_H \rangle$ is the mean thermal speed of H atoms in the gas in cm s^{-1} . Usually, $n_{gr}\langle\sigma_{gr}\rangle \sim (10^{-21}\text{cm}^2)n$ (n is the number density of hydrogen nuclei), and $\langle v_H \rangle \sim 10^4\sqrt{T} \text{ cm s}^{-1}$, therefore Equation 1.23 becomes

$$R_f \sim 3 \times 10^{-18} S(T, T_d)\eta(T_d)\sqrt{T}n n(H) \quad [\text{cm}^{-3}\text{s}^{-1}] \quad (1.24)$$

Jura (1974) provided observational support for this rate, comparing observed abundances of H and H_2 to derive empirical formation and destruction rates for H_2 computing a formation rate of $R_f \sim 10^{-17} \text{ cm}^{-3}\text{s}^{-1}$ at a temperature of 100 K. Where temperatures are effectively low S and $\eta \sim 1$ both tend to decrease with rising temperature, also H atoms move faster and have a higher probability to bounce off the surface than stick. In fact, the adatoms have a

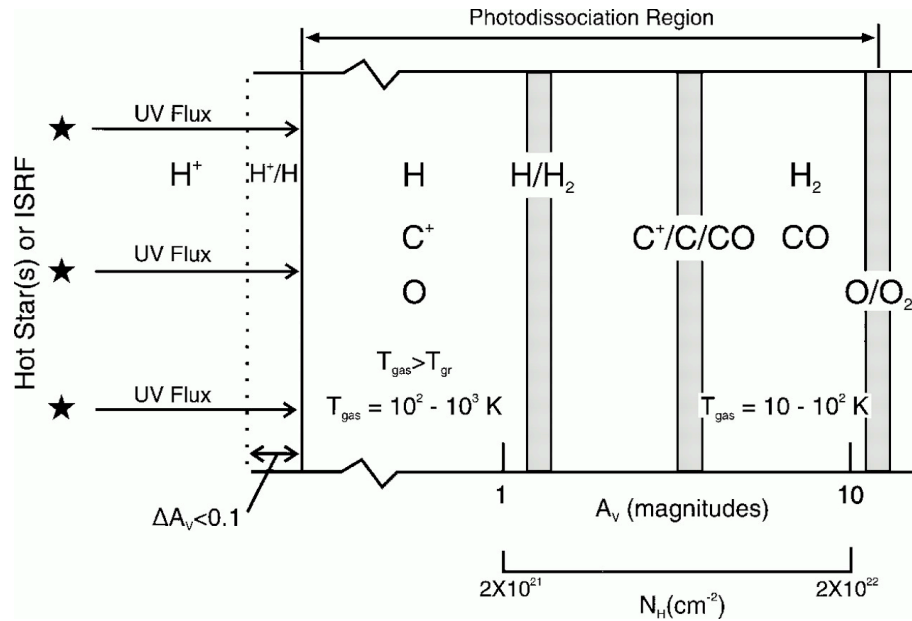


Figure 1.5: A schematic diagram of a photon-dominated region. The PDR is illuminated from the left and extends from the predominantly atomic surface region to the point where O_2 is not appreciably photodissociated ($A_V > 10$) (Hollenbach & Tielens 1997).

shorter residence time and may evaporate before they can recombine. In order to determine a trustworthy formation rate under varying conditions, it is therefore important to estimate the temperature-dependence of S and η . In general, laboratory work supports the feasibility of the H_2 formation mechanism, though there is still some debate about the temperatures for which it is efficient. Although the mechanisms governing H_2 formation on dust grains (Cazaux & Tielens 2004, 2010), at the low temperatures typical of dark clouds, are now well understood, the formation rate at the higher grain temperatures found in PDRs remains rather uncertain (Biham *et al.* 1998).

1.3.4 The H/H_2 layer

PDR regions can be schematically represented as in Fig 1.5. The penetration of the far ultraviolet radiation field influences the chemistry giving rise to the characteristic chemically-distinct zones. At the surface of the PDR when all photons above the Lyman limit are absorbed, ionized hydrogen rapidly recombines, whereas molecular hydrogen is rapidly photodissociated by the FUV radiation (as described in Sec 1.3.1. Therefore, the surface layer consists mainly of atomic hydrogen, with all carbon, sulphur and silicon in singly ionized form (because their ionization

potentials are below the Lyman limit) and all oxygen and nitrogen in atomic form. Further into the cloud, the FUV flux begins to attenuate and the formation of H_2 starts to dominate over photodissociation. Since the dominant form of hydrogen moves from atomic to molecular with increasing depth, an H/H_2 layer appears beyond the H I zone. However, photodissociation and photoionization still maintain large abundances of O, N, C^+ , S^+ and Si^+ . The H/H_2 transition layer plays an important role in the PDR chemistry since further reaction networks are initiated once molecular hydrogen becomes abundant. In dense PDRs the gas in the outer regions can become hot and the combination of high gas temperatures and rising H_2 density initiates a set of endothermic reactions such as:



whose products may subsequently be photodissociated or undergo the reverse reactions or, in the case of CH^+ and SH^+ , suffer dissociative recombination. When the H_2 becomes more abundant, these reactions can produce large quantities of OH and CH^+ in the H/H_2 transition layer, where the high temperatures necessary for the endothermic reactions to proceed efficiently can be maintained. Hydrogen molecules left in vibrationally excited states following FUV absorption, denoted by H_2^* , may also be sufficiently energetic to overcome the endothermicities of these reactions, becoming important in low density PDRs where the temperature is lower (Tielens & Hollenbach 1985). The large values of the OH radical then gives rise to a series of fast ion-molecule reactions that produce the molecular ions SO^+ , CO^+ , HCO^+ and HOC^+ :



and a series of slower neutral-neutral reactions that produce the molecules NO, O_2 and H_2O ,



Subsequently photodissociation contributes to the destruction of these newly formed molecules. In addition, molecular ions can also be destroyed by dissociative recombination or reactions

with H₂, and water can be destroyed by reacting with H to produce H₂ and OH again. CO can be formed efficiently in the outer cloud layers, through the dissociative recombination of HCO⁺ and charge transfer between CO⁺ and H:



In these regions the electron density is high due to photoionization of carbon and sulphur, and hydrogen is still mainly atomic.

1.3.5 The C II/CI/CO layer

The photoionization of atomic carbon by FUV photons,



creates a distinct layer of singly ionized carbon inside the cloud. Because of the self-shielding of H₂, the layer of C II extends to a greater depth than the H I zone. In fact, the H₂ self-shielding allows the layer of C II to survive nearer the cloud surface, producing a zone of C II beyond the H I zone where the carbon is ionized and the hydrogen is in molecular form. Generally, the C II zone extends out to $A_V \leq 2$ mag and it is cooler than the H/H₂ transition layer, hence the usual endothermic reactions that produce OH, CH⁺ and NH near the surface are much less efficient here. C⁺ is quite important in this environment because it is believed to be the starting point of chemical reactions producing carbon-bearing radicals (see Fig 1.4 panel b). CH and CH₂ are destroyed by photodissociation and so reach their peak abundances at the inner (i.e. deeper) edge of the C II zone, where the FUV flux is reduced and the C⁺ density is still large. The deeper we go into the cloud the more the abundances of carbon radicals decrease and so too does the C⁺ density. Carbon radicals are also diminished through important reactions that lead to the formation of complex hydrocarbons,



The hydrocarbons that are produced are susceptible to photodissociation and so their abundances also peak at the inner edge of the C II zone. While the FUV radiation penetrates deeper into the cloud and is more attenuated, the C⁺ undergoes radiative recombination and charge transfer with atomic sulphur,



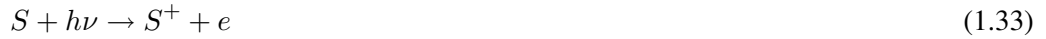
causing the density of neutral atomic carbon to become significant beyond the inner edge of the C II zone. At these depths the UV radiation has now become severely attenuated and carbon makes the transition from a singly ionized state to CO. Between these two states, the carbon is in neutral atomic form and can attain high abundances in the transition layer beyond the C II zone. Photodissociation of CH also contributes to the neutral carbon abundance, which is itself then converted into stable CO molecules via neutral-neutral reactions at depths beyond the C II zone,



At greater depths, carbon is predominantly in the form of CO and the atomic carbon abundance drops rapidly.

1.3.6 The SII layer

Sulphur has a lower ionization potential than carbon (10.4 eV, rather than 11.3 eV) and is less abundant (by over an order of magnitude), so it can remain in ionized form up to a greater depth in the cloud than the C II. In fact photoionization of atomic sulphur by FUV photons maintains a layer of singly ionized sulphur that is directly analogous to that of carbon:



A high density of neutral carbon can be maintained across the transition from the C II to the S II zone thanks to the charge transfer between C^+ and S. Also this charge transfer contributes to the extended layer of ionized sulphur. The S II zone, usually lies between $2 \leq A_V \leq 4$ mag. Beyond the S II zone the sulphur is in neutral form thanks to the photo-destruction of sulphur bearing molecules, radiative recombination of S^+ and charge transfer with silicon. At these depths, the FUV radiation is severely attenuated and the electron density becomes small. At large depths, $A_V \geq 8$ mag, a small fraction of hydrogen is in H_2 , carbon is mostly locked in the stable CO molecules, SO and SO_2 become the dominant forms of sulphur and oxygen forms O_2 via reactions with OH.

1.4 The importance of the thermal balance

Between all the physical processes in PDRs, the thermal balance is one of the most important mechanisms that governs PDR as well as H II regions. In fact, the physical and chemical

properties of these regions are controlled by the incident radiation field photons that both heat the gas and drive the cloud chemistry in sequences initiated by photoionization and photodissociation (Sternberg & Dalgarno 1995). As the names suggest, ionized and photo-dominated regions derive their structure primarily from the penetration of UV and FUV photons into their interiors. The incident radiation field is usually attenuated by dust grains that absorb and scatter the light coming from an ionizing source (see Sec 1.4.2.3. Gas and dust are always coupled together through some mechanisms that help the cloud to be in thermal equilibrium. In order to keep the cloud in thermal equilibrium it is important that internally the thermal balance criteria is satisfied: this happens when the heating and cooling processes are balanced.

In the following sections a description of the most important physical mechanisms in ionized regions are provided.

1.4.1 Thermal Equilibrium in H II region

For an ionized region to be in thermal equilibrium it is necessary that the total heating energy equal the total cooling at every point. The heating is provided by the kinetic energy of the liberated photoelectrons. As already mentioned, when a photon of energy $h\nu$ ionizes a given ion, X^i , which has an ionization potential equal to $h\nu_{X^i}$, where ν_{X^i} is the ionization threshold frequency, the difference between the energy of the absorbed photon and the ionization potential of the ion, $h(\nu - \nu_{X^i})$, is transferred as kinetic energy to the photoelectron; the electrons are quickly thermalised through elastic collisions with other electrons and ions, therefore their initial energy effectively contributes to the local heating. If we consider the simple case of a pure hydrogen nebula, the energy input by photoionization at a given location can be written as:

$$G_{phot}(H) = N_{H^0} \int_{\nu_{H^0}}^{\infty} \frac{4\pi J_{\nu}}{h\nu} a_{\nu}(H^0) h(\nu - \nu_{H^0}) d\nu \quad (1.34)$$

where N_{H^0} is the local density of neutral hydrogen, $\frac{4\pi J_{\nu}}{h\nu}$ is the number of photons per unit area per unit time with frequency in the interval $(\nu, \nu + \delta\nu)$ and $a_{\nu}(H^0)$ is the neutral hydrogen photoionization cross-section at frequency ν , therefore $\frac{4\pi J_{\nu}}{h\nu} a_{\nu}(H^0)$ is the total number of photons absorbed by neutral hydrogen per unit time. The heating due to photoionization at each location in the region must be balanced by the total cooling at the same location. Several channels contribute to the cooling. The most effective cooling mechanism is the emission of collisionally excited lines from common ions, such as O^+ , O^{++} and N^+ . These lines are emitted when the ions, which are collisionally excited by the electrons, cascade back down to the ground level via radiative transitions. The collisional lines are emitted at wavelengths longward of the

Lyman limit and they can therefore escape the region without any further interactions. This means that they cool the gas by removing energy from it. Emission lines from collisionally excited ions of common elements dominate the spectra of ionized regions and provide most of the cooling. However, recombination lines of H I, He I and He II are also contributing but much less than the forbidden lines. The recombination lines are formed when an electron recombines to an excited level of a given ion and then cascades down to the ground level by radiative transitions. The energy loss by recombination is not the dominant cooling when heavy elements are present but in the case of a pure hydrogen nebula this mechanism together with free-free radiation constitute the only cooling channels. The free-free continuum radiation, or Bremsstrahlung, is caused by a collision between a free electron and an ion. Nevertheless, the effects of this process on the thermal equilibrium of the nebula are, in general, very small when cooling by collisionally excited lines is available (Osterbrock & Ferland 2006). Finally, including all cooling channels, the thermal balance equation can be simply written as:

$$G_{phot} = L_c + L_r + L_{ff} \quad (1.35)$$

where L_c is the contribution due to collisional excited radiative cooling and L_r and L_{ff} are the contributions due recombination and free-free radiation, respectively (Osterbrock & Ferland 2006).

1.4.1.1 Recombination

Radiative recombination is the opposite of photoionization, and rate coefficients come directly from photoionization cross sections and the Milne relation (Osterbrock & Ferland 2006, Appendix 1). Mazzotta *et al.* (1998) summarized much of the current recombination data. Radiative recombination rate coefficients can be computed with the same accuracy as photoionization cross sections. A lot of recombination lines are observed such as He⁺⁺. However, the main excitation process responsible for the observed strengths of these lines is the resonance fluorescence by photons, which is less effective for H and He lines because the resonance lines of these more abundant elements have greater optical depth. Unfortunately, this process is insignificant for many ions of the heavy elements at nebular temperatures (~ 100 K). For those species that have at least one electron, before recombining, in the outer shell, dielectronic recombination (DR) is important. The free electron is captured by exciting a bound electron. The energy of the resulting system, with two excited electrons, is greater than the binding energy of the entire system. When this situation is verified, the resulting system is said to be in an autoionizing

state. The DR to auto-ionization (or auto-ionization to DR) process is so fast that these two processes, which are related by detailed balance, can hold the population of the autoionizing level at its LTE value. In this case, the DR rate coefficient is given by the LTE population of the autoionizing level multiplied by the sum of transition probabilities to bound levels (Ferland 2003). At the high temperatures, typical of collisionally ionized plasma, free electrons can reach many autoionizing levels and no one state dominates the process (Burgess 1965). However, at the low temperatures, typical of photoionized gas, the electrons can reach only a small number of auto-ionizing levels. What has a greater effect on the total recombination rate coefficient is their specific energy and whether their population is actually in LTE. Only levels within 10% to 20% of the ionization limit, in photoionization equilibrium, are energetically accessible because the electron kinetic energy is typically around this percentage of the ionization potential. Due to these energies, it is difficult to know whether a calculated level is an autoionizing level that is energetically accessible for DR, or whether the level is actually a bound level below the continuum. Usually, in photoionized plasmas at temperatures $\leq 30,000$ K, these DR resonances dominate the electron-ion recombination rate coefficient. This fact brings the reliability of the DR data, currently used to model plasmas at these temperatures, into doubt. Experimental measurement of DR rate coefficients have become possible within the past few years Savin *et al.* (2002). Typical results are shown in Fig 1.6.

At very low temperatures, radiative recombination dominates if there are no autoionizing states accessible to the electrons. The photoionized zone represents temperatures where this ion will be present in photoionization equilibrium. Here only a few autoionizing levels are available to the free electrons and the theoretical rate coefficients show a large scatter, owing to uncertainties in the energies of these levels. At the high temperatures that are characteristic of collisional ionization equilibrium, the recombination process is dominated by a large number of levels and one would expect that details might tend to average out, but as is clear from Fig 1.6 this is not the case (Savin *et al.* 2002). It is difficult for theory to predict low-temperature rate coefficients that agree with experiments, largely as a result of the uncertainties in the positions of the resonances. So far, experiments have been limited to highly charged species.

1.4.1.2 Collisional excitation and de-excitation

One of the most important sources of radiative cooling in ionized regions is the collisional excitation of low-lying energy levels of common ions, such as O^+ , O^{++} , and N^+ . If an electron collides with an ion and excites it and then another electron comes along and de-excites the ion

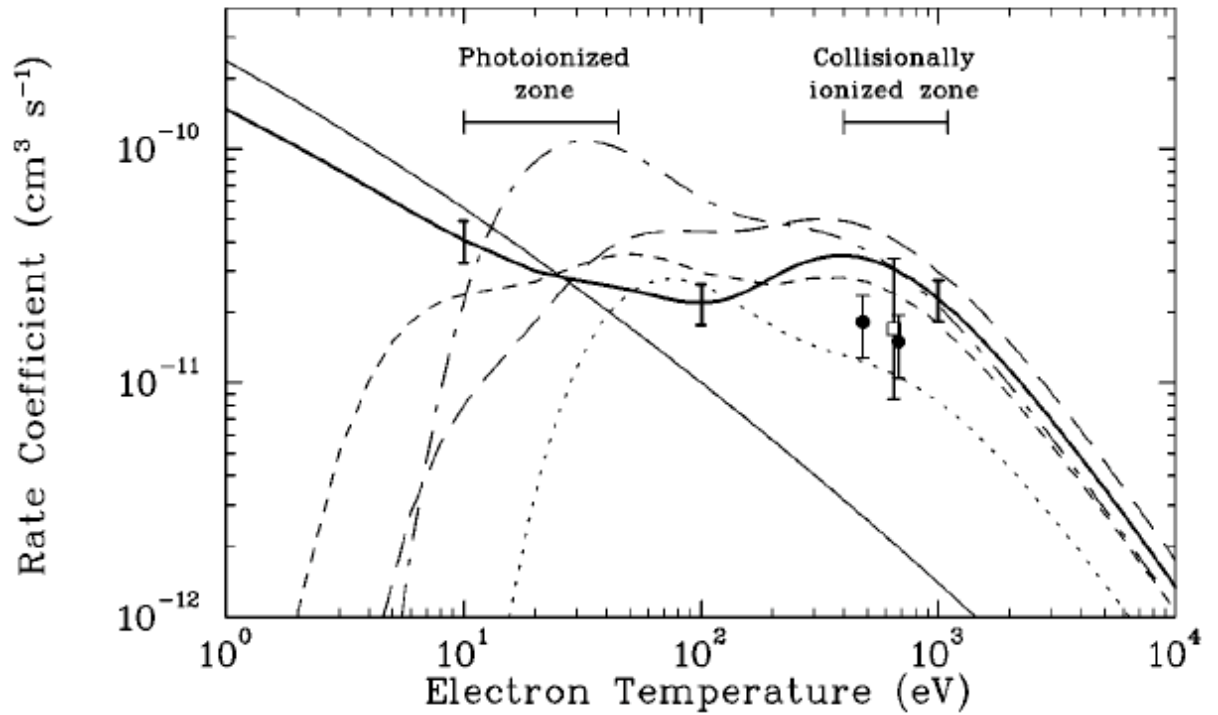


Figure 1.6: Experimental and theoretical recombination rate coefficients as a function of temperature for recombination to produce Fe^{17} . The heavy line gives the experimental dielectronic recombination (DR) rate coefficient, and dotted/dashed lines are the results of various theories. The light solid line is the contribution from radiative recombination. The points-with-error bars are previous experimental measurements, and the error bar on the curve indicates the uncertainty in the heavy line. The collisionally ionized zone marks the temperature range where the kinetic temperature is roughly equal to the ionization potential, whereas the photoionized zone is the range where the temperature is a small percentage of the ionization potential, as is typical of a photoionized gas (Savin *et al.* 2002).

back into its original ground state before it can emit a photon, there is no change in the energy content of the free-electron plasma. However, if the ion can radiatively de-excite before the next collision, it emits a photon that escapes from the nebula, leading to a net loss of energy from the free-electron plasma (i.e., electron kinetic energy is converted into photons that escape). Despite their low abundance, these ions significantly contribute to the cooling as they have energy levels with excitation potentials of the order of kT . On the other hand, H and He, although having much higher excitation potentials, do not contribute at all to the cooling. O^+ , O^{++} , and N^+ can thus be strongly excited by collisions giving rise to collisional excited lines (CELs). For these heavy element ions, the excited level arises from the same electron configurations as the

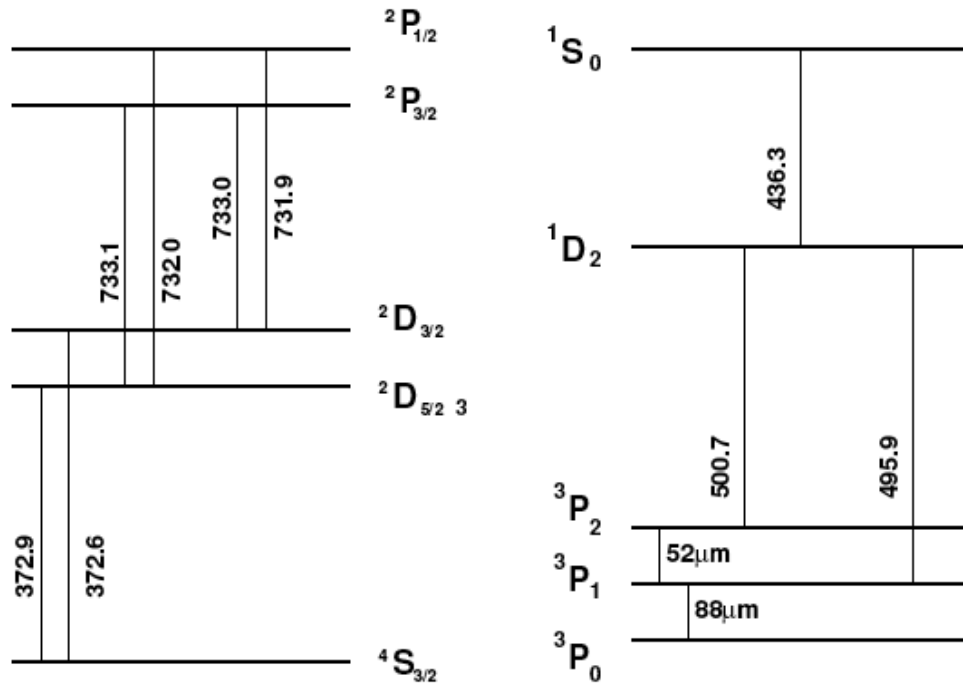


Figure 1.7: Simplified energy-level diagram for O^+ (left) and O^{2+} (right). Unlabelled O^+ and O^{2+} wavelengths are in nm.

ground state and thus a radiative transition back to the ground state is forbidden according to electron dipole selection rules. This is mainly true for visible IR lines, but in the UV some collisional excitations populate levels that emit permitted lines. Before radiative decay occurs, the excited levels have lifetimes of the order of several seconds, which is why they are called metastable. However, in conditions such as an ionized region with a very low density, collisional de-excitation is rare and what appears forbidden in the laboratory, is strongly emitted in this kind of environment. In objects such as planetary nebulae the total flux in forbidden lines of metals exceeds that in the hydrogen lines. For instance, the ionization potential of O^0 , 13.62 eV, is almost the same as that of hydrogen, where hydrogen is ionized oxygen also is ionized. On the other hand, the ionization potential of O^+ is 35.1 eV, which means that only the hotter stars can produce O^{++} . Fig 1.7 shows an example of oxygen forbidden transitions. Since the oscillator strengths are small the probability of a photon from a forbidden transition being re-absorbed is small; these photons readily escape and hence cool the nebula. The efficiency of the collisional excitation compensates the low abundances of metals compared to hydrogen. The collisional

excitation rate from level i to j is:

$$\dot{n}_{ij} = n_e n_i(I) C_{ij}(T_e) \quad [\text{m}^{-3}\text{s}^{-1}] \quad (1.36)$$

where C_{ij} is the rate coefficient for collisional excitation (with typical values of order $\sim 10^{-4}$ - $10^{-2} \text{ m}^3\text{s}^{-1}$), i is the ground level of species I , with number density $n(I)$, and an excited upper level j ; under nebular conditions $n(I) \simeq n(I)_i$.

An estimate of the total cooling by collisionally excited line emission requires computation of the upper level populations for all low-lying levels for each ion present at a given location in the nebula. This is usually done numerically by nebular model codes. At high densities collisional de-excitation completely dominates radiative de-excitation, and we say that the level populations are thermalized.

In general, the cooling due to collisionally excited line emission from a 2-level atom is:

$$4\pi j_{ul} = n_u A_{ul} h\nu_{ul} = n_l \frac{g_u}{g_l} e^{-h\nu_{ul}/kT} \left[1 + \left(\frac{A_{ul}}{n_e q_{ul}}\right)\right]^{-1} A_{ul} h\nu_{ul} \quad (1.37)$$

where the first part of the Equ 1.37, $4\pi j_{ul} = n_u A_{ul} h\nu_{ul}$, is the radiant energy carried off by a given optically thin emission-line, g_u and g_l are the statistical weights of the levels respectively and A_{ul} is the radiative transition probability. In the low-density limit, radiative de-excitation dominates, so that:

$$4\pi j_{ul} \rightarrow n_l n_e q_{ul} h\nu_{ul} \propto n_e^2 \quad (1.38)$$

In the high-density limit, where collisions dominate and the levels thermalize:

$$4\pi j_{ul} \rightarrow n_u A_{ul} h\nu_{ul} \propto n_e \quad (1.39)$$

The dividing line between these limits is the Critical Density for the line, n_{crit} :

$$n_{crit} = \frac{A_{ul}}{q_{ul}} \quad (1.40)$$

As the density increases, the strength of a given collisionally excited line will increase as n^2 until it reaches the critical density, beyond which it will then only increase linearly with n . The overall effect is to collisionally suppress emission from the line at high densities. The maximum cooling provided by a given collisionally-excited line therefore reaches a maximum when the density is at or near the critical density for that line and drops off in effectiveness rapidly above the critical density.

1.4.2 Heating Mechanisms in PDRs

There are two main mechanisms that couple the gas to the FUV photon energy of stars: the photoelectric effect on PAHs (Polycyclic aromatic hydrocarbon) and small dust grains and FUV pumping of H₂ molecules. PAH have been observed in a large variety of sources, including the diffuse interstellar medium, photon-dominated regions, circumstellar envelopes, planetary nebulae and external galaxies (Allamandola *et al.* 1989). More recently, PAH features have also been detected in disks around Herbig Ae/Be and T Tauri stars (Geers *et al.* 2006). In the majority of these sources, the PAHs are electronically excited by ultraviolet (UV) photons. Following internal conversion to a high vibrational level of the electronic ground state, they cool by emission in the primary C-H and C-C stretching and bending modes at the mid-infrared (IR) wavelengths of 3.3, 6.2, 7.7, 8.6, 11.3, 12.8 and 16.4 μm .

Other heating mechanisms play only a limited role in the heating or become important at greater depths in the PDR (Tielens & Hollenbach 1985).

1.4.2.1 Photoelectric heating

The *photoelectric heating* is dominated by the smallest grains present in the ISM; in recent years the role of PAHs as a component of the ISM and their importance in heating has become clearer. In fact, FUV photons absorbed by a grain create energetic electrons that may diffuse through the grain, reach the surface and be injected into the gas phase with excess kinetic energy. Since it is not plausible to directly couple non-ionizing photons with a predominantly neutral gas due the low opacity of the gas, the absorption by interstellar dust grains assumes an important role. It, in fact, transfers energy from the starlight to the gas through the photoelectric ejection of electrons from dust grains and PAHs. Via this mechanism their kinetic energy is subsequently transferred to the gas, providing an important heating source. When the mobile electrons reach the surface, if sufficiently energetic, they overcome the work function W of the grain and any Coulomb potential ϕ_c caused by a positive grain charge in order to be ejected into the gas with excess kinetic energy. The kinetic energy produced will then be converted to thermal energy of the gas via inelastic collisions. The product of the photoelectric yield Y (the probability that an electron will be ejected following the absorption of a photon) and the fraction of photon energy carried away as kinetic energy by the electron, is called the efficiency of the photoelectric effect on a grain, ϵ . The fraction of energy imparted to grains by absorption of FUV photons is what

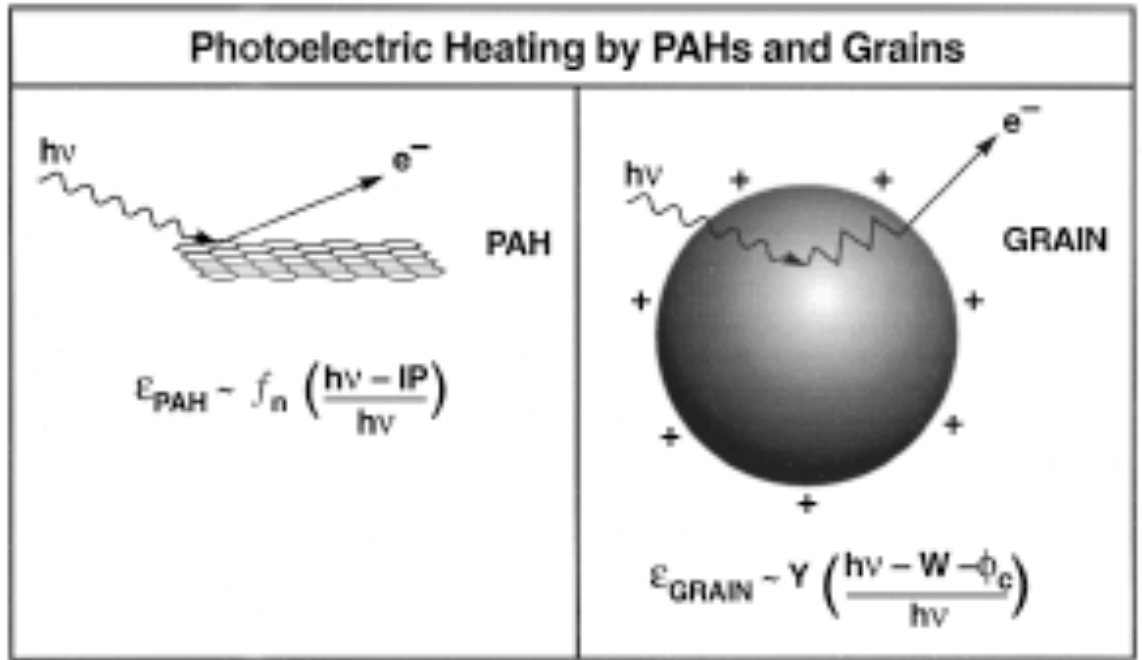


Figure 1.8: The photoelectric heating mechanism: FUV photons are absorbed by interstellar grains and PAHs and energetic electrons are ejected into the gas with excess kinetic energy (Hollenbach & Tielens 1997)

contributes to the gas heating.

$$\epsilon \sim Y(h\nu - W - \phi_c/h\nu) \quad (1.41)$$

Despite some relevant studies, the photoelectric yield Y and efficiency ϵ of the photoelectric effect, still remain somewhat uncertain parameters. In fact, Bakes & Tielens (1994) derived a simple analytical expression for the photoelectric heating efficiency that is dependent only on G_0 , T and n_e . Modelling in detail the photoelectric heating of interstellar gas by PAHs and very small grains (VSGs), in addition to larger grains, they discovered that the heating was dominated by PAHs and small grains. They reached this conclusion, considering a size distribution of graphitic grains extending down into the molecular domain and evaluated the net heating rate, taking into account grain charging, multiple ionization stages of the grains and recombination of electrons with grains.

1.4.2.2 H₂ FUV pumping

Molecular hydrogen is subject to electronic excitation through line absorption of FUV photons in the Lyman and Werner bands (see Fig 1.9). This FUV pumping is followed by spontaneous

UV fluorescence to the vibrational continuum of the ground electronic state and will dissociate 10 – 15% of H₂ or 85 – 90% of molecules left in excited vibrational states in the electronic ground state. At low densities these excited hydrogen molecules can cascade down to the ground vibrational state through the emission of IR photons; this leads to the characteristic far-infrared and near-IR rovibrational spectrum that can be observed throughout many diffuse clouds (Hollenbach & Tielens 1997). At higher densities, instead of radiative decay, collisional de-excitation occurs returning the excited molecules to a thermalised rovibrational state. During this process the gas is heated and this mechanism provides an effective coupling to the FUV photons when H₂ self-shielding exceeds dust extinction such as the case for $G_0/n \leq 0.04$ (Draine & Bertoldi 1996). The rate of collisions with atomic hydrogen, which is the main collision partner of H₂, determines the critical density at which collisional de-excitation becomes important and it ($n_{cr} 10^4\text{-}10^5 \text{ cm}^{-3}$) depends on the gas temperature (Martin & Mandy 1995; Martin *et al.* 1996). The vibrationally excited molecules lose their internal energy through collisions when they are above the critical density, in fact the H atoms transport that energy and transfer it to the thermal energy of the gas. This heating mechanism is most efficient in the atomic H I zone nearest the surface, where the FUV pumping rate is highest and H₂ molecules undergo frequent collisional de-excitation with the abundant H atoms.

1.4.2.3 Other heating mechanisms

Additional heating of the gas can result from collisions with warmer grains, cosmic-ray ionization and excitation, the decay of turbulence within the cloud and pumping of neutral oxygen to excited states by absorption of FIR emission from warm dust. However, the contribution to the total heating rate from these processes is generally small, only becoming important at large depths ($A_V \geq 6$; Tielens & Hollenbach 1985). Overall, photoelectric heating due to small grains and PAHs, and collisional de-excitation of FUV pumped H₂ couple the gas heating to the incident FUV flux and dominate the heating in the outer region of the cloud. High densities lead to effective heating by FUV pumping nearest the surface, whilst photoelectric heating generally peaks slightly deeper into the cloud, since the high electron density at the cloud surface reduces the efficiency with which photoelectrons are ejected.

1.4.3 General cooling mechanisms in PDRs

Cooling is dominated by the far-infrared (FIR) fine structure lines [C II] 158 μm , [O I] 63 and 145 μm , [S III] 35 μm , the near-infrared H₂ rovibrational and molecular rotational lines,

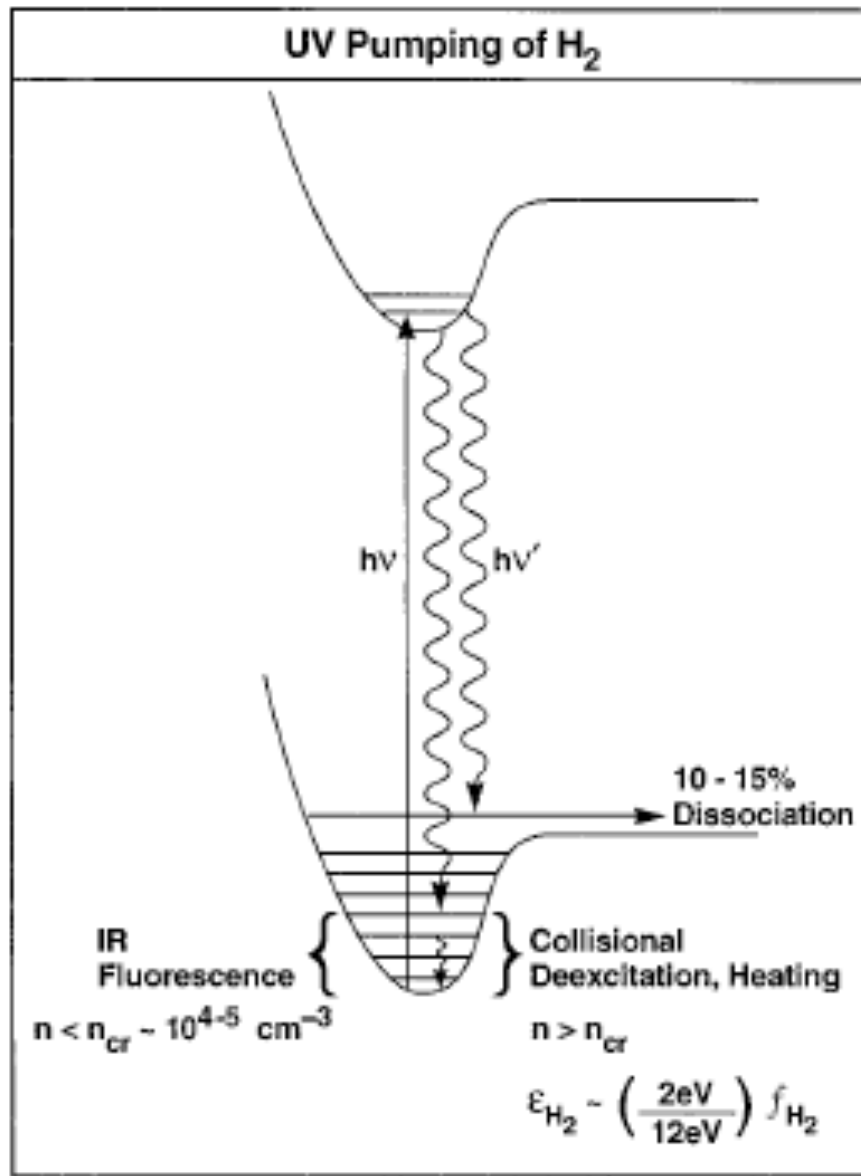


Figure 1.9: The two step photodissociation of H₂: absorption of FUV photons ($912 \text{ \AA} < \lambda < 1118 \text{ \AA}$) in the Lyman and Werner bands, followed by radiative decay to the vibrational continuum of the ground electronic state. This occurs in 10 – 15% of the cases, the majority of decays leading to a vibrationally excited molecule in the ground electronic state (Hollenbach & Tielens 1997).

principally of CO but also of OH and H₂. A temperature above 5000 K can be reached with a high densities and high radiation fields. At these high temperatures significant cooling can also occur in the [Fe II] 1.26 and 1.64 μm , [O I] 6300 \AA , [S II] 6730 \AA , and Lyman- α lines (Burton *et al.* 1990). The cooling of the gas by line emission depends on the atomic and molecular constants as well as on the radiative transfer. At high densities, cooling by collisions with the cooler dust grains and gas particles also contributes to the total cooling. The dust itself cools efficiently through continuum emission in FIR.

1.4.3.1 The most important coolants in PDRs

The FIR fine structure lines of abundant species such as [CII] and [OI] are recognized as one of the most important coolants in the warm interstellar medium (ISM). In particular, the emission from singly ionized carbon [CII] $\lambda=158 \mu\text{m}$ is known to trace warm and dense photodissociation regions because it also traces the gas surrounding active star-forming regions. Carbon is the fourth most abundant element in the Universe and has a lower ionization potential (11.26 eV) than hydrogen. For this reason it is predominantly in the form of [CII] in the surface layers of PDRs, where photoionization of neutral carbon is effective, but can be observed also in ionized regions. [CII] 158 μm line emission arises from PDRs on molecular cloud surfaces. This line is widely observed and is usually optically thin. [CII] 158 μm emission occurs in both ionized and neutral gas and the individual contribution from each component must be determined before the line can be used as a diagnostic of the conditions in the neutral PDR gas. In addition, [CII] 158 μm is reasonably easy to excite, with a transition energy of 92 K. The depth of the [CII] zones is generally determined by dust extinction and often extends to $A_v \geq 4$. Oxygen, because its ionization potential, is found exclusively in neutral regions and first appears just beyond the location of the HII/ HI transition. The incident FUV radiation maintains a significant abundance of atomic oxygen deep into the cloud through photodestruction of CO and O₂. All oxygen not incorporated into CO can remain in atomic form to depths as large as $A_v=10$ mag under strong FUV fluxes (Sternberg & Dalgarno 1995). Oxygen has two fine structure transitions at 63 and 145 μm . The [O I] line at 63 μm has an excitation energy corresponding to 228 K and emits predominantly in warm and dense gas and is the other major coolant of neutral regions. This line is optically thick in some cases. This can be seen comparing it to the [OI] line at 145 μm . The [OI]145 μm line is the hardest to detect in astrophysical environments. The faintness of this line diminishes its capabilities as a robust PDR diagnostic. The lower level of the 145 μm line is not the ground state of O, meaning that [OI] 145 μm emission is usually optically thin

(Abel *et al.* 2007). The $145\mu\text{m}$ line has an excitation energy of 326 K, almost 100 K higher than that of the $63\mu\text{m}$ line, so the ratio of the two line intensities, [OI] at $145\mu\text{m}$ and [OI] at $63\mu\text{m}$, is sensitive to the gas temperature for $T \leq 300$ K. In addition this ratio is found to be a good indicator of optical depth in the $63\mu\text{m}$ line. Since the strength of the FUV radiation field governs the heating of the gas, this line ratio is a diagnostic of the incident FUV flux G_o . The FIR fine structure emission lines can be used as diagnostics to infer physical conditions in the gas, such as temperatures, densities and radiation fields, by comparing with models of photodissociation regions (Tielens & Hollenbach 1985) and HII regions (Rubin *et al.* 1991).

1.5 Far Infrared fine structure emission lines

For several years astronomers have used, as tools for the study of gaseous nebulae, what are called far infrared fine structure emission lines, which are the infrared counterparts of the bright optical forbidden lines. Far Infrared fine structure lines have many properties that make them useful tools for diagnosing astrophysical environments. Interstellar dust does not affect the intensities of these lines and, as interstellar clouds are generally optically thin in fine structure lines, no radiative transfer analysis is required. Ions that have more than one fine structure line are reliable indicators of electron density as the ratio of the strengths of the two fine structure lines provides the electron density of the emitting region even for regions of unknown size. However, one can get useful results when the pair of lines is not saturated. A number of studies have produced models that predict the strength of far-infrared fine structure lines such as [C II] $158\mu\text{m}$, [O I] $145\mu\text{m}$ and [O I] $63\mu\text{m}$ as a function of the density and radiation intensity in PDRs (Tielens & Hollenbach 1985; Wolfire *et al.* 1989; Abel *et al.* 2005), and they act as the primary coolants to the dense, warm, neutral media. Far infrared fine structure emission lines such as [N II] $122\mu\text{m}$, [N III] $57\mu\text{m}$, [O III] $52\mu\text{m}$ and $88\mu\text{m}$ are useful tools for understanding and determining the electron densities and the effective temperature of the ionizing stars in H II regions. The fine structure line ratios are sensitive and accurate probes of density, elemental abundances, and ionization structure. In addition, fine structure emission line profile studies provide valuable information on ionized and photodominated regions. It is well known, by now, that the observed fine structure lines originate in the outer parts of both H II and PDR regions. The only exception are the ionized nitrogen lines that clearly come exclusively from ionized regions because their ionization potential lie above the Lyman limit. Although the diagnostic capabilities of the fine structure lines is reliable, emission lines such as [O I] $63\mu\text{m}$ and [C II]

158 μm are affected by the optical depth.

The Far-Infrared Absolute Spectrophotometer (FIRAS) on the COBE satellite conducted an unbiased survey of the far-infrared emission from our Galaxy. The FIRAS spectral line survey included the emission lines from [C II] 158 μm , [N II] 122 and 205 μm , [C I] 370 and 609 μm and were first reported by Wright *et al.* (1991). Carbon is the fourth most abundant element and has a lower ionization potential (11.26 eV) than hydrogen. For this reason it is predominantly in the form of C⁺ in the surface layers of PDRs, where photoionization of neutral carbon is effective, but can potentially also be excited in ionized regions. Although it is unclear how much [C II] 158 μm comes from ionized gas in diffuse H I and H II regions.

O⁰ is found exclusively in neutral regions and first appears just beyond the location of the HII/HI transition. The incident FUV radiation maintains a significant abundance of atomic oxygen deep into the cloud through photodestruction of CO and O₂. All oxygen not incorporated into CO can remain in atomic form to depths as large as $A_v=10$ mag under strong FUV irradiation (Sternberg & Dalgarno 1995). Atomic oxygen has two fine structure transitions, at 63 and 145 μm . The [O I] transitions are mainly observed in emission but, when spectra are taken with sufficient spectral resolution in a number of sources, this line is seen both in emission and in absorption like in the cases of the ultraluminous infrared galaxy Arp 220 and SgrB2 (Fischer *et al.* 1999; Vastel *et al.* 2002; González-Alfonso *et al.* 2004). In fact, a combination of foreground cold clouds and different velocities can lead, using the relatively broad LWS grating, to the total measured emission being reduced compared to the that expected from pure PDR emission. The [O I] 145 μm line can be harder to detect: in fact, the relative faintness of this line diminishes its capabilities as a robust PDR diagnostic (see Sec 1.4.3.1). Since the strength of the FUV radiation field governs the heating of the gas, this line ratio is also a diagnostic of the incident FUV flux (Tielens & Hollenbach 1985). Neutral nitrogen has an ionization potential of 14.53 eV and it is only found in HII regions. The ground state ³P term of the N⁺ ion is split by the spin-orbit interaction into the three ³P_{2,1,0} levels from which the 121.898 μm (³P₁ – ³P₂) and 205.178 μm (³P₁ – ³P₀) lines arise. The line ratio of these lines is an excellent density probe for low-density ionized gas. The [N II] 205 μm line is of particular interest as it has a critical density that is very close to that of [C II], thus potentially providing complementary information on the origin of the [C II] emission (e.g., Oberst *et al.* 2006). Both of the [N II] lines were strongly detected from the Milky Way by the COBE FIRAS experiment. One of the lines of singly-ionized nitrogen observed by the Infrared Space Observatory (ISO) in external galaxies is the [N II] 122 μm line that has a critical electron density of 3.1x10²cm⁻³. The

COBE and the Kuiper Airborne Observatory (KAO) provided the first astronomical detections of this line (Wright *et al.* 1991). An ionizing energy of 35.12 eV is required to create O^{++} from singly-ionized oxygen. Due to this high ionization potential, the [O III] $52\mu m$ and $88\mu m$ transitions occur in H II regions. The ratio of these two lines can be used to derive the average electron density of these regions, using the method studied by Rubin *et al.* (1991). [N III] has a high ionization potential of 47.45 eV and therefore the transition at $57\mu m$ is only found in the ionized H II regions. The ratio $[N III]_{57\mu m}/[N II]_{122\mu m}$ provides a measure of the effective temperature in ionized regions.

All these lines described above have been observed by several infrared space telescopes, in the following section detailed.

1.5.1 Infrared Space Observatory

The KAO provided early data on the far-infrared fine structure lines that arise in PDR and H II regions in galaxies. The Infrared Space Observatory (ISO) was launched by Ariane in November 1995 and it provided astronomers world-wide with a facility of unprecedented sensitivity and capabilities for a detailed exploration of the Universe at infrared wavelengths.

With the launch of ISO the far-infrared properties of galaxies were observed with greater sensitivity than ever before. The Long Wavelength Spectrometer (LWS) on ISO allowed the large-scale study of far-infrared atomic and molecular lines that supply new insight into the understanding of the interstellar medium. The two spectrometers (SWS and LWS), a camera (ISOCAM) and an imaging photo-polarimeter (ISOPHOT) jointly covered wavelengths from 2.5 to around 240 microns with spatial resolutions ranging from 1.5 arcseconds (at the shortest wavelengths) to 90 arcseconds (at the longer wavelengths). Its 60 cm diameter telescope was cooled by superfluid liquid helium to temperatures of 2-4 K. ISO operated until 1998 and it was the first truly infrared observatory in space. It performed 30,000 scientific observations on more than 6,000 astronomical targets and sky fields, in the wavelength range of 2 to 200 microns. ISO has been a true technological and scientific success. The ISO Data Archive continues to be a treasure trove for astronomical research, with almost 1400 articles having appeared in the refereed literature to date, based on ISO data (Clegg *et al.* 1996; Gry *et al.* 2003). The FIR data used throughout this thesis were obtained from LWS.

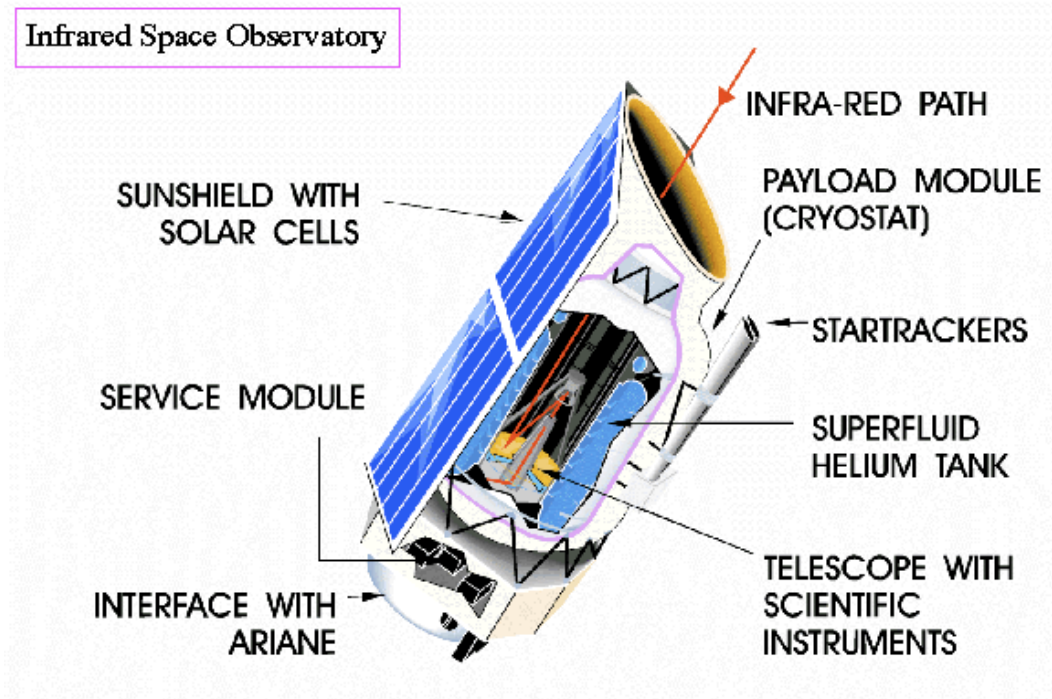


Figure 1.10: A schematic depiction of the Infrared Space Observatory.

1.6 Extragalactic sources and their Infrared emission

Studies of our own Galaxy and observations of external galaxies have suggested that stellar ultraviolet radiation can ionize vast volumes of a galaxy and that far-ultraviolet radiation impinging on neutral cloud surfaces is responsible for a large fraction of the observed far-infrared (FIR) spectral line emission that cools the gas (Crawford *et al.* 1985). The broad features of the relative abundances of molecular species in various standard extragalactic environments share common properties which have many similarities with those observed with much more detail in the Milky Way (Omont 2007). The relative contributions from different gas phases can be estimated from observations of several FIR forbidden lines. Since extragalactic sources cannot be observed easily at high spatial resolution, and hence it is difficult to disentangle their physical properties, it is convenient to utilize FIR fine structure emission lines as a diagnostic of the chemical and physical properties of these sources. One of the most important discoveries from extragalactic observations at mid and far-infrared wavelengths was the identification of Infrared galaxies, so called as they emit predominantly in the infrared ($\sim 5 - 500 \mu\text{m}$) with respect to all other wavelengths combined. The first all sky-survey at infrared wavelengths was carried out in

1983 by the Infrared Astronomical Satellite (IRAS). IRAS data have shown that the infrared spectral energy distributions (SEDs) of Seyfert galaxies and radio quiet QSOs are dominated by thermal dust emission (Sanders *et al.* 1989; Pier & Krolik 1993). In fact, dust emission is one of the three main components contributing to the far-IR spectrum in which dust particles absorb photons from the UV radiation field and re-emit in the far-IR wavelength range. Also, molecular species emit in the far-infrared range. In particular, species responsible for cooling the gas, such as H₂O, OH and CO, have their main spectral contribution in the far-IR. Finally, fine-structure transitions are produced by atomic level splitting, which arises from the magnetic spin-orbit coupling. These transitions are found predominantly in the far-infrared region.

1.6.1 Starburst galaxies

The most luminous galaxies in the universe are over a thousand times more powerful than our Milky Way. These luminous galaxies are not particularly bright in the optical and ultraviolet but they are indeed in the infrared. They appear to be powered by bursts of massive star formation: clusters of massive stars, each star thousands or even tens of thousands of times more luminous than our Sun, and all of them buried in dusty natal clouds of material that block their visible light. Hence, these luminous galaxies are called starburst galaxies, and they are indeed lit up in short bursts of star forming activity. Massive stars, however, are very short-lived, lasting perhaps only tens of millions of years (compared with our Sun's current age of 5 billion years) before exploding as supernovae. M82 is a nearby example of a luminous starburst galaxy.

Starbursts are detected optically by the presence of strong emission lines and blue continuum colours produced by hot stars (Booth & Aalto 1998). Most known starburst galaxies are Ultra Luminous Infrared galaxies (ULIRGs), these galaxies are generally extremely dusty objects. The ultraviolet radiation produced by the obscured star-formation is absorbed by the dust and reradiated in the infrared spectrum at wavelengths of $\sim 100\mu\text{m}$. This explains the extreme red colours associated with ULIRGs. It is not known if the UV radiation is produced purely by star-formation, it is believed that it is partially powered by active galactic nuclei (AGN).

X-ray observations of many ULIRGs that penetrate the dust suggest that many starburst galaxies are double cored systems, lending support to the hypothesis that ULIRGs are powered by star-formation triggered by major mergers. Well-studied ULIRGs include galaxy Arp 220. Although with improved receiver sensitivity many more normal galaxies are detected, the starburst galaxies remain among the galaxies with the highest CO luminosities. In fact, one of the most commonly used tracers of molecular gas is carbon monoxide. Unlike molecular hydrogen, however, CO

readily emits under the conditions typically found in molecular clouds. Observational estimates of CO-to-H₂ conversion factor X_{CO} can be derived for regions of the Milky Way and external galaxies using extinction measurements obtained from star counts to derive N_{H_2} , assuming a constant gas-to-dust relationship, and comparing with observed CO luminosities (Frerking *et al.* 1982). Similarly, far-infrared emission can be used to estimate the cold dust mass and hence, through some assumed gas-to-dust mass ratio, the gas mass, and comparison with CO luminosity can again yield values of X_{CO} (Guelin *et al.* 1995; Boselli *et al.* 2002). This strong correlation, between integrated CO emission and far infrared flux, in nearby galaxies, is shown in Young & Scoville (1991, Fig 7).

1.6.2 Active galactic nuclei

The radiation from an active galactic nuclei (AGN) is believed to be a result of accretion of mass by a supermassive black hole at the centre of the host galaxy.

AGN are the most luminous persistent sources of electromagnetic radiation in the universe, and as such can be used as a means of discovering distant objects. Seyfert galaxies (Sy) are, generally, spiral galaxies with extremely intense active nuclei.

These galaxies comprise two categories: Sy1 and Sy2. Compared to normal galaxies in which it is not easy to detect emission lines, Sy 1 galaxies have broad emission lines that are attributed to ionized gas within 1 pc of the black hole. In addition to the broad wings in the permitted lines, they have narrower forbidden lines. Sy 2 show only narrower emission lines believed to originate from a much larger region around the core. However, they do not appear to have statistically significant differences in their radio luminosities (Booth & Aalto 1998). Another class of galaxies, with similar features to those of Sy 1 and 2, are the low luminosity galaxies with low ionization nuclear emission line regions (LINERs). However, ionization lines such as [O I], [N II] and [S II] are stronger than in their Seyfert 2 counterparts and they can also be distinguished from Sy 2 galaxies by their low values of [O III]/H_β to [N II]/H_α (Osterbrock & Ferland 2006). Some of the most extreme examples of both starburst and Seyfert phenomena are the ultraluminous infrared galaxies detected in the far infrared sky survey with the IRAS satellite (Sanders *et al.* 1989; Pier & Krolik 1993).

1.6.3 Radio galaxies and Quasi stellar objects

Radio galaxies and their relatives, radio-loud quasars and blazars, are types of active galaxy that are very luminous at radio wavelengths (up to 10^{39} W between 10 MHz and 100 GHz). The radio emission is due to the synchrotron process. The observed structure in radio emission is determined by the interaction between twin jets and the external medium, modified by the effects of relativistic beaming. The host galaxies are almost exclusively large elliptical galaxies (Booth & Aalto 1998). Synchrotron radiation is not confined to radio wavelengths: if the radio source can accelerate particles to high enough energies, features which are detected in the radio may also be seen in the infrared, optical, ultraviolet or even X-ray, though in the latter case the electrons responsible must have energies in excess of 1 TeV in typical magnetic field strengths.

Optically Quasi stellar objects (QSOs) are faint blue objects of small diameter, sometimes surrounded by a low surface brightness halo. They have spectra similar to those of Sy 1 galaxies, with very broad lines, except that their stellar absorption features are extremely weak or even absent.

1.7 A unified region: H II/PDR

The majority of all the mass surrounding stars in the galaxy is in PDR regions where hydrogen makes the transition from ionized to atomic and then finally to molecular form. This fact makes the study of PDRs essential to our understanding of the ISM and star forming regions. The classical approach to the study of PDRs is to observe line intensities that are thought to originate in the PDR, many of which are in the infrared. These observations are combined with theoretical calculations that attempt to reproduce the observations by varying the hydrogen density and intensity of the UV radiation field. Calculations of PDRs almost always ignore the radiation $>13.6\text{eV}$, since a PDR is operationally defined to begin where the H II region ends. Some line intensities that are observed in the study of PDRs, however, can also have a significant contribution emerging from the adjacent H II region, which leads to an underestimate of the intensities of these lines. A separate calculation of the H II region is then desired, but calculating the properties of these two regions separately ignores the fact that they are dynamically linked (Ferland *et al.* 1998). H II regions, PDRs, and molecular clouds are not distinct physical problems, but rather a series of layers that are unified by the transport of radiation from hot stars into cold gas and the flow of cold molecular gas into hot ionized regions. In virtue of this, a detailed study of these two regions, which are physically and chemically linked to each

other, has been carried out in this thesis using the far infrared fine structure emission lines that characterize one, the other or both of these regions (see Chapter 3 and 4). Also, the decision to use extragalactic sources aids the study of both ionized and photodissociation regions as it is possible to observe the entire source within the beam size (i.e. H II + PDR). An attempt was also made to provide a model that was able to study the two region as one unified region (see Chapter 5).

THE UCL MODELS

In this chapter I will briefly describe the three principal codes that I used throughout my PhD thesis, UCL_PDR, MOCASSIN and SMMOL. In Chapter 5 I will discuss in greater detail the relevant sections of the UCL_PDR code and the MOCASSIN code that are involved in the computational aspect of my work.

2.1 The Photodissociation code UCL_PDR

In recent years, at UCL, a PDR model has been developed (UCL_PDR). Three people were involved in the development of the UCL_PDR code; initial work was done by S. Viti and W. F. Thi, but it was eventually fully developed by T. Bell. The code has also been benchmarked with several other codes during a workshop held in Leiden (Papadopoulos *et al.* 2002; Bell *et al.* 2005; Röllig *et al.* 2007). The UCL_PDR code models a PDR region as a one-dimensional semi-infinite slab, illuminated from one side. The chemistry and thermal balance are calculated self-consistently at each depth point of the slab and at each time-step, producing chemical abundances, emission line strengths and gas temperatures as a function of depth and time. The full chemical network includes ion-molecule, photoionization and photodissociation reactions. Freeze-out of atoms and molecules onto grains is optional. The gas is assumed to be initially in atomic form. All metals that possess ionization potentials below 13.6 eV are in singly ionized form. At each depth-step, the model calculates the attenuation of the FUV field before beginning an iterative cycle to determine the gas temperature at which the total heating and cooling rates are equal, that is, when the condition of thermal balance is satisfied. For each iteration, the chemistry is first calculated, based on the gas temperature and attenuated FUV flux, after which

the heating and cooling rates are computed, together with the radiative transfer in the emission line, using the revised chemical abundances. The difference between the total heating and cooling rates is then used to derive a new gas temperature. The chemical abundances are then computed at each depth-step by solving the set of ordinary differential equations describing the formation and destruction of each species in the chemical network for the duration of the current time-step. This is repeated at all time-steps and the chemistry of the gas evolves accordingly. All fractional abundances are quoted relative to total hydrogen nuclei. Elemental abundances of all metals are assumed to scale linearly with metallicity (Z/Z_{\odot}). The reaction rates are taken from the UMIST99 database (Le Teuff *et al.* 2000), with some modifications introduced as part of the benchmarking effort (Röllig *et al.* 2007). The following grain surface H_2 formation rate of de Jong (1977) is adopted:

$$R = 3 \times 10^{-18} \sqrt{T} \exp(-T/1000) \quad [cm^3 s^{-1}] \quad (2.1)$$

and it is assumed that the rate scales linearly with metallicity. Extinction within the cloud is calculated assuming an average grain size of $0.1 \mu m$, albedo of 0.7 and mean photon scattering by grains of $g = 0.9$ ($g = \langle \cos \theta \rangle$). The dust-to-gas mass ratio is assumed to scale linearly with metallicity and takes a standard value of 10^{-2} at Solar metallicity (Z_{\odot}). The visual extinction (A_v) and dust optical depth (τ_v) are related by:

$$A_v = 1.086 \tau_v \quad (2.2)$$

The incident FUV radiation is characterised by the standard Draine field (Draine 1978), scaled by a free parameter χ . Attenuation of the radiation field strength with cloud depth is given by:

$$\chi = \chi_0 \exp(-k/A_v) \quad (2.3)$$

where $k=1.38$ and χ_0 is the unattenuated field strength at the surface of the cloud (in units of the Draine field). Self-shielding of H_2 against photodissociation is calculated using the single line approximation of Federman *et al.* (1979). The self-shielding factors of van Dishoeck & Black (1988) are adopted for CO. Neutral carbon shielding includes contributions from H_2 , CO and C II, using the treatment of Kamp & Bertoldi (2000). The gas temperature is determined at each depth point using an iterative process to balance the total heating and cooling rates. Photoejection of electrons from dust grains (Tielens & Hollenbach 1985) and PAHs (Bakes & Tielens 1994), and FUV pumping and photodissociation of H_2 molecules (Hollenbach & McKee 1979) are the dominant heating mechanisms near the cloud surface, whilst cosmic ray heating

(Tielens & Hollenbach 1985) and exothermic reactions become significant deeper into the cloud. Heating by C II photoionization (Kamp & van Zadelhoff 2001), H₂ formation (Kamp & van Zadelhoff 2001), gas-grain collisions (Burke & Hollenbach 1983) and turbulence (Black 1987) are also included in the model. The gas is mainly cooled through emission from collisionally excited atoms and molecules and by interactions with the cooler dust grains. Emission from the [O I], [C I] and [C II] fine structure lines and CO rotational lines, up to $J = 11 \rightarrow 10$, are calculated at each depth point in the code using the escape probability method of de Jong *et al.* (1980) and non-LTE level populations determined using the updated collisional rate coefficients from the PDR benchmarking (Röllig *et al.* 2007). The contribution to the total cooling rate by H₂ emission is calculated using data from Martin *et al.* (1996). Also, H_α and O I 6300Å fine structure line emission are considered. Variation in metallicity is accounted for by assuming that the dust and PAH photoelectric heating rates are directly proportional to Z, in addition to the scaling of the elemental abundances, H₂ formation rate, dust-to-gas mass ratio and grain number density. The calculated integrated intensity lines along the line of sight towards the cloud are then:

$$I = \frac{1}{2\pi} \int \Lambda(z) dz \quad [\text{erg s}^{-1} \text{cm}^{-2} \text{sr}^{-1}] \quad (2.4)$$

where $\Lambda(z)$ is the line emissivity at depth z into the cloud ($\text{erg s}^{-1} \text{cm}^{-3}$) and the factor of $1/2\pi$ accounts for the fact that photons only emerge from the edge of the cloud, rather than over the full 4π steradians. The UCL_PDR code represents a powerful tool for the study of interstellar gas under a wide variety of conditions. Its short computation times and time-dependent capability make it suitable for both parameter space studies and detailed modelling of phenomena that evolve rapidly with time. The code produces a large amount of useful output data, including the abundances and column densities of all the species contained in the chemical network, the line intensities and opacities of the main fine structure and CO rotational transitions, and the gas and dust temperatures, all as a function of time and cloud depth.

2.2 The Photoionization code MOCASSIN

The MOCASSIN code realistically treats a model of photoionized regions, which have arbitrary geometry and density distributions, with both the stellar and diffuse radiation fields treated self-consistently. In addition, the code is able to handle one or more exciting stars located at non-central locations. The region considered is approximated by a cuboidal Cartesian grid

composed of numerous cells. The physical conditions within each grid cell are determined by solving the thermal equilibrium and ionization balance equations. This requires a knowledge of the local primary and secondary radiation fields, which are calculated self-consistently by locally simulating the individual processes of ionization and recombination (Ercolano *et al.* 2003). Inside each grid cell all nebular properties, such as the mass density of the gas, ρ , the electron temperature and density, T_e and N_e , and the frequency dependent gas opacity and emissivity, κ_ν and j_ν , are constant by definition. Thermal balance and ionisation equilibrium are imposed in each grid cell in order to obtain the physical conditions in the local gas.

The MOCASSIN code uses the Monte Carlo approach, in general this method is used to solve various problems by generating suitable random numbers and observing the fraction of the number obeying some property or properties. The method is useful for obtaining numerical solutions to problems that are too complicated to solve analytically and for modeling phenomena with significant uncertainties in inputs.

The main differences from the other models is the radiation field treatment, which is expressed in terms of energy packets, $\varepsilon(\nu)$, which are the calculation quanta. This is a packet consisting of n photons of frequency ν such that $\varepsilon(\nu) = nh\nu$. In addition all packets have constant energy ε_o . Choosing to work with indivisible packets of radiant energy instead of photons is more computationally economic and, also, since they all have the same energy, then those packets emitted in the infrared will contain a larger number of photons that, as a consequence, will not have to be followed individually (Abbott & Lucy 1985). Note that all energy packets are followed until they escape the nebula, including infrared energy packets. The energy packets are created at the position of the ionising source and they all carry the same energy with frequency ν . From the input spectrum of the ionising source the frequency of each individual packet emitted is derived. This calculations are done according to the probability density function:

$$p(\nu) = \frac{F_\nu d\nu}{\int_{\nu_{min}}^{\nu_{max}} F_{\nu'} d\nu'} = \frac{F_\nu d\nu}{L_\star/4\pi R_\star^2} \quad (2.5)$$

where F_ν is the stellar flux, R_\star is the stellar radius and L_\star is the stellar luminosity. This is then the probability of an energy packet being emitted with a frequency lying in the interval $(\nu, \nu + d\nu)$. In order to make sure that the bulk of the radiation is included in the right frequency range, it is necessary to choose properly the upper and lower integration limits (ν_{max}, ν_{min}) that depend on the input spectrum. When a packet of radiant energy $\varepsilon\nu_a = \varepsilon_o$ is absorbed, it is immediately re-emitted with a frequency ν_e , which is determined according to a frequency

distribution set by the gas emissivity of the current cell. The packet emitted, $\varepsilon\nu_e$, will then have the same energy as the absorbed packet, $\varepsilon\nu_a$, meaning that only the number of photons n contained in the packet is changed (Ercolano *et al.* 2003). As the source emits energy isotropically, the direction of travel of each energy packet emitted is chosen randomly. This is done by choosing two random numbers, α and β in the interval $[0, 1]$, and calculating the following quantities:

$$\begin{aligned}
 w &= 2\alpha - 1 \\
 t &= \sqrt{1 - \omega^2} \\
 \theta &= \pi(2\beta - 1) \\
 u &= t \cos \theta \\
 v &= t \sin \theta
 \end{aligned}
 \tag{2.6}$$

The random unit vector in Cartesian coordinates is then (u, v, w) . The choice of the parameters in Equ 2.6 is based on Monte-Carlo simulations of scattering of OVI resonance-line photons from a hot source using numerical models of Raman-line formation in symbiotic systems (see Harries & Howarth 1997). The stellar packet is created at the source and launched into the nebula; this packet undergoes absorptions followed by re-emissions due to bound-free and free-free processes. Its trajectory ends when the packet reaches the edge of the nebula, where it escapes to infinity and contributes to the emergent spectrum, but before it is necessary to follow its path. The method used to track the packets and determine the locations of the absorption events, considering a packet of frequency ν_p , emitted in the direction \hat{u} , is the method suggested by Lucy (1999). This method consists of testing whether an absorption event occurs, on a cell by cell basis (Ercolano *et al.* 2003). Assuming that, within each uniform cell, the random path of a packet between events is given by the following equation:

$$\tau_{\nu p}(l) = -\ln(1 - U_R)
 \tag{2.7}$$

where U_R is a random number in the interval $[0, 1]$. Once $\tau_{\nu p}(l)$ has been calculated then the path length can be directly derived (Harries & Howarth 1997). The physical displacement, l , is given by:

$$\tau_{\nu p}(l) = \kappa_{\nu} \rho l
 \tag{2.8}$$

where κ_{ν} and ρ are the frequency dependent absorption coefficients and the density of the current cell respectively. The method then consists of checking whether the displacement l is large enough to carry the packet out of its current cell. If this is the case, the packet is moved

along its direction of travel, \hat{u} , up to the boundary of the adjacent cell, where a new value for U_R is cast, giving a new $\tau_{\nu p}$ and any further movement of the packet in this new cell is to be followed. Alternatively, if the displacement l is not large enough to carry the energy packet across the next boundary, the packet will be absorbed and then re-emitted at the end-point of the displacement (Ercolano *et al.* 2003).

In order to satisfy the thermal balance implied by the Monte Carlo model, all major emission processes have to be taken into account, including the complete non-ionizing nebular continuum and line emission, since they are part of the energy budget. The non-ionizing radiation generated in the nebula is assumed to escape without further interaction and constitutes the observable spectrum, which can be compared with observations. Procedures in MOCASSIN have been constructed such that only an initial guess at the electron temperature (which is initially set to a constant value throughout the nebula) must be included in the input file (Ercolano *et al.* 2003).

As already remarked for PDR models, the construction of such codes involves a number of choices regarding atomic data, physical assumptions and numerical algorithms; this results in the various codes having many differences, and therefore sometimes returning slightly different answers to the same problems. Therefore benchmarking is a necessity in order to guarantee a certain standard of results. MOCASSIN code has been benchmarked during the workshop held in Lexington (Péquignot *et al.* 2001).

2.3 The Radiative Transfer code SMMOL

The SMMOL code used approximated accelerated lambda-iteration (ALI) that solves the radiative transfer problem in multi-level non-local conditions. It starts by calculating the level populations assuming LTE and takes an adopted radiation field as the input continuum and then recalculates the total radiation field and level populations and repeats the process until convergence is achieved. The main input parameters include molecular data such as the molecular mass, energy levels, radiative and collisional rates and also the dust size distribution and opacity. The model parameters also include the gas and dust temperatures of the object to model, such as the kinetic and dust thermal temperature (Rawlings & Yates 2001).

The radiative transfer problem can be represented by an equation that describes the emission, absorption and movements of photons along a straight line in a medium:

$$\frac{dI_\nu}{ds} = j_\nu - \alpha_\nu I_\nu \quad (2.9)$$

where I_ν is the description of the intensity along a photon path ds at frequency ν and j_ν and α_ν are the emission and the absorption coefficients. The previous equation can also be written as:

$$\frac{dI_\nu}{d\tau_\nu} = S_\nu - I_\nu \quad (2.10)$$

where $S_\nu = j_\nu/\alpha_\nu$ is referred to as the source function (the emissivity of the medium per unit optical depth), and the optical depth τ_ν , is described in differential form as $d\tau_\nu = \alpha_\nu ds$. Equation 2.10 can be written in its full form:

$$I_\nu(\tau) = \int_0^\tau S_\nu(\tau') e^{\tau' - \tau} d\tau' \quad (2.11)$$

The emission and absorption coefficients, for the molecular line transfer problem, are determined by the transition rate between the various rotational and/or vibrational levels of the molecule and the population of these levels. Taking for example, a transition from level i to level j , the upper and lower transition levels respectively, the emission and absorption coefficients are given by:

$$\begin{aligned} j_{ij}(\nu) &= n_i A_{ij} \phi_{ij}(\nu) \\ \alpha_{ij}(\nu) &= (n_j B_{ji} - n_i B_{ij}) \phi_{ij}(\nu) \end{aligned} \quad (2.12)$$

where n_i and n_j , cm^{-3} are the population densities of the upper and lower levels and A_{ij} , B_{ij} and B_{ji} are the Einstein coefficients. The function ϕ_{ij} described what is called the Voigt profile that is the line profile of this transition. The Voigt profile is a combination of a (micro-turbulent) Gaussian and intrinsic Lorentzian line broadening. The relative level populations n_i are determined from the statistical equilibrium equation:

$$\sum_{j>l} [n_j A_{jl} + (n_j B_{jl} - n_l B_{lj}) \bar{J}_{jl}] - \sum_{j<l} [n_l A_{lj} + (n_l B_{lj} - n_j B_{jl}) \bar{J}_{lj}] + \sum_j [n_j C_{jl} - n_l C_{lj}] = 0 \quad (2.13)$$

where $C_{ij} = n_{col} K_{ij}$ with K_{ij} the collisional rate coefficients in $\text{cm}^{-3} \text{s}^{-1}$, n_{col} the density of collision partners and \bar{J}_{jl} is the integrated mean intensity over the line profile. The intensity is proportional to T_{ex} , in the optically thin limit, where T_{ex} is the temperature of the transition between level i and j . In local thermodynamic equilibrium (LTE), T_{ex} equals the local gas temperature, while if T_{ex} is higher or lower, the excitation is super- or sub-thermal. To solve the source function S_{ij} , the intensity $I_\nu(\tau)$, the emission and the absorption coefficients, j_ν and α_ν , the statistical equilibrium equation, and the integrated mean intensity, \bar{J}_{jl} , one must determine the radiation field and the level populations simultaneously. This means that the system must be solved through complete linearization and computing a huge matrix equation involving all

level populations at all spatial positions (van Zadelhoff *et al.* 2002). However, it is possible to compute these parameters using what is called Lambda iteration. This Lambda iteration method has the only disadvantage of converging slowly at high optical depths. Because of this limitation many radiative transfer codes use a hybrid scheme such as the Local Linearization MULTI used by SMMOL. The SMMOL code computes the intensities at each radial grid point in the spherical cloud using a finite difference method to compute the intensities. In fact, at each radial point it generates the level populations and the line source functions. The emergent intensity distributions are then convolved with the telescope beam, so that the model directly predicts the line profiles for a given source as observed with a given telescope. The telescope beam can be approximated by a Gaussian, with a characteristic half-power beam width (HPBW). The SMMOL code uses a convergence criterion of 1×10^{-4} for both the level populations and the mean intensities. SMMOL has been benchmarked for accuracy, van Zadelhoff *et al.* (2002), and expanded to include a more comprehensive dataset of molecular collisional data.

TESTING PDR MODELS AGAINST EXTRAGALACTIC ISO DATA FOR FINE STRUCTURE EMISSION LINES

The work presented in this chapter is based on the paper by Vasta et al. (2010).

The FIR fine structure lines of abundant species, such as [C II] and [O I], have long been recognised as one of the most important coolants in the interstellar medium (ISM). In particular, the emission from singly ionized carbon [C II], at $\lambda=158 \mu\text{m}$, is known to trace warm and dense photodissociation regions (PDRs) and is used to trace the gas surrounding active star-forming regions. In the presence of foreground cold and tenuous gas the [O I] $63\mu\text{m}$ line can show both emission and absorption components (Tielens & Hollenbach 1985). Nevertheless observations of the FIR fine structure emission lines of [O I] and [C II] can be used as diagnostics to infer the physical conditions in the emitting gas, such as temperatures, densities and radiation field strengths, by comparing with models of photodissociation regions (Tielens & Hollenbach 1985) and H II regions (Rubin *et al.* 1991). In the past, several models have been used to interpret infrared, submillimeter and millimeter line observations of neutral gas in our own Galaxy as well as in the central regions of nearby starburst galaxies (e.g. Mao *et al.* 2000; Seaquist & Frayer 2000; Wild *et al.* 1992, and references therein).

In this Chapter I will present the fluxes of fine structure emission lines observed by ISO from 46 sources and we estimate the bulk properties of the gas in these external galaxies using the UCL_PDR model of Bell *et al.* (2005) and the radiative transfer code SMMOL (Rawlings &

Yates 2001). The Chapter is structured as follows: first, I give details of the sources selected and the fine structure emission line fluxes I measured. I describe the UCL_PDR models and evaluate the sensitivity of the UCL_PDR models to variations in the physical parameters. Subsequently, I will consider the contribution of H II regions to fine structure emission lines. The results are given in the final Section, and there I discuss their interpretation in the context of our SMMOL line profile calculations. Concluding remarks are also given.

3.1 The ISO data

All the FIR data included in this paper were acquired using the ISO Long Wavelength Spectrometer (LWS; Clegg *et al.* 1996), which had an estimated FWHM beam size of ~ 80 arcsec. I collected [C II]158 μm , [O I]145 μm and 63 μm emission line fluxes from ISO LWS archival observations for 100 external galaxies, 46 have been published (Table 3.1) and the remaining 54 sources are listed in Table 3.2. The work presented in this Chapter is based only on the study of the 46 extragalactic sources that have been published. The [C II]158 μm , [O I]145 μm , 63 μm emission line fluxes were measured from the spectra using the interactive package SMART (Spectroscopy Modeling Analysis and reduction Tool; Higdon *et al.* (2004).)

3.1.1 Data Reduction

The observational data were obtained from the ISO data archive (IDA) interface (<http://iso.esac.esa.int/ida/>). I retrieved the data by specifying my object identifiers and selecting the Standard data and LWS options. Standard data contains all observations done with Astronomical Observing Templates (AOTs), which are already processed and calibrated. The LWS has four modes for standard data: LWS01 medium resolution wavelength range, LWS02 medium resolution line spectrum, LWS03 high resolution wavelength range and LWS04 high resolution wavelength spectrum. For a given source I chose the scientifically validated data with the best looking spectra and downloaded the Highly Processed Data Products (HPDP). The HPDP are the result of further processing, by hand, beyond the pipeline and/or using new, refined algorithms.

After retrieving the data I used the SMART package to reduce them. SMART has been designed specifically for IRS data, and in particular to extract spectra from observations of faint or extended sources. I checked for the [C II]158 μm , [O I]145 μm and 63 μm emission line detections by identifying the relevant wavelength range and taking into account the effect of

redshift using the following equation:

$$\lambda_{obs} = \lambda_{emit} + \lambda_{emit}z \quad (3.1)$$

where λ_{obs} is the observed wavelength, λ_{emit} is the emitted wavelength and z is the redshift of the given source taken from the NASA/IPAC Extragalactic database (NED). A detection of a spectral line transition is produced when an atom or molecule interacts with a photon which has the right energy to allow a change in the energy state of the system. The line can be seen in emission or absorption depending on the geometry of the gas, the photon source and the observer, and on the temperatures of the photons source and gas. When no detection was found, I fitted the first order polynomial baseline to the appropriate range of the spectrum and I measured the upper limit of the possible detection using the following equation:

$$U_{pplim} = 3 \times rms \times spl \quad (3.2)$$

where rms corresponds to the continuum flux density at the wavelength of the line measured fitting the baseline, and spl is the spectral resolution element equal to $0.29 \mu\text{m}$ for the [O I]63 μm line, and $0.6 \mu\text{m}$ for the [O I]145 μm and [C II]158 μm lines respectively. Otherwise, if the detection was clear I fitted the first order polynomial baseline and measured the flux of the emission line fitting the line profile with a gaussian or a Lorentzian profile. A Gaussian profile is a consequence of the distribution of velocities in the gas. The line will be broader if the temperature of the gas is higher while a Lorentzian profile will appear in all conditions as a consequence of the uncertainty between the life time of an excited state and the precision with which its energy is known. However, with the LWS grating, spectra are of sufficiently low resolution that neither the Lorentian profile nor the natural line width will any influence on the line shape.

3.1.2 Extragalactic ISO data for fine structure emission lines

Table 3.1 lists the emission line fluxes measured by us from the ISO spectra. For 33 of the galaxies, fluxes previously published in the literature were available and these are also listed in Table 3.1, for each source, our own line flux measurements are listed in the first row, while literature values, if any, are listed in the second row. When uncertainties were not listed for these literature fluxes, we have estimated them as 20% for fluxes $\leq 10^{-14} \text{ W m}^{-2}$ and 10% for fluxes $\geq 10^{-14} \text{ W m}^{-2}$. Although the choice of how to estimate the associated errors, when it is not provided, is arbitrary, we used typical uncertainties resulting from calibration and pointing

Table 3.1: Line flux measurements, in units of 10^{-14} W m $^{-2}$, for extragalactic sources with ISO-LWS detections of all 3 FIR fine structure emission lines of [C II] and [O I]. For each source, our own line flux measurements are listed in the first row, while literature values, if any, are listed in the second row (Contursi *et al.* 2002; Bergvall *et al.* 2000; Colbert *et al.* 1999; Fischer *et al.* 1996; Luhman *et al.* 2003; Malhotra *et al.* 2001; Negishi *et al.* 2001; Unger *et al.* 2000; Brauher *et al.* 2008). (n.a: not available)

Index	Source	Radial Vel (km s $^{-1}$)	TDT No. of Observation	[CII] 158 μ m	[OI] 63 μ m	[OI] 145 μ m	[CII] $_{158}$ [OI] $_{63}$	[OI] $_{63}$ [OI] $_{145}$
1	IC 10	-348	45700609	0.966 \pm 0.034	0.591 \pm 0.025	0.0217 \pm 0.0032	1.64 \pm 0.13	27.23 \pm 5.17
2	Haro 11	6175	54900720	0.763 \pm 0.021	0.65 \pm 0.02	0.024 \pm 0.004	1.17 \pm 0.07	27.08 \pm 5.34
3	NGC 253	243	56901708	0.0410 \pm 0.0022	0.0954 \pm 0.0041	<0.0086	0.43 \pm 0.04	n.a
				0.039 \pm 0.001	0.092 \pm 0.018	0.003 \pm 0.001	0.42 \pm 0.09	30.6 \pm 16.2
				4.618 \pm 0.126	3.47 \pm 0.16	0.461 \pm 0.074	1.33 \pm 0.09	7.53 \pm 1.55
				5.19 \pm 1.04	3.76 \pm 0.75	0.52 \pm 0.11	1.38 \pm 0.55	7.23 \pm 2.97
4	NGC 520	2281	77702295	0.2188 \pm 0.0045	0.29 \pm 0.015	0.0133 \pm 0.0028	0.75 \pm 0.05	21.80 \pm 5.72
				0.28 \pm 0.06	0.21 \pm 0.04	0.02 \pm 0.01	1.33 \pm 0.54	10.5 \pm 7.3
5	Maffei 2	-17	85800682	1.072 \pm 0.051	0.512 \pm 0.051	0.071 \pm 0.021	2.09 \pm 0.31	7.21 \pm 2.85
				1.21 \pm 0.24	0.53 \pm 0.11	0.05 \pm 0.01	2.28 \pm 0.93	10.6 \pm 4.3
6	NGC 1068	1137	60500401	1.881 \pm 0.062	1.416 \pm 0.043	0.1522 \pm 0.0024	1.33 \pm 0.08	9.30 \pm 0.43
				2.13 \pm 0.43	1.60 \pm 0.32	0.09 \pm 0.02	1.33 \pm 0.54	17.8 \pm 7.5
7	IC 342	31	64600302	0.3146 \pm 0.0097	<0.117	0.0202 \pm 0.0049	n.a	n.a
				n.a	n.a	n.a	n.a	n.a
8	NGC 1482	1916	79600984	0.571 \pm 0.022	0.362 \pm 0.025	<0.057	1.58 \pm 0.17	n.a
				0.655 \pm 0.013	0.318 \pm 0.063	n.a	2.06 \pm 0.45	n.a
9	NGC 1569	-104	64600489	0.652 \pm 0.027	0.657 \pm 0.025	0.0085 \pm 0.0019	0.99 \pm 0.08	77.3 \pm 20.2
				0.674 \pm 0.134	0.589 \pm 0.119	n.a	1.14 \pm 0.46	n.a

Index	Source	Radial Vel (km s ⁻¹)	TDT No. of Observation	[CII] 158 μ m	[OI] 63 μ m	[OI] 145 μ m	[CII] ₁₅₈ [OI] ₆₃	[OI] ₆₃	[OI] ₁₄₅
10	NGC 1614	4778	85501010	0.1953±0.0067	0.346±0.016	0.0179±0.0026	0.56±0.05	0.56±0.05	19.33±3.70
				0.226±0.010	0.343±0.016	n.a	0.65±0.05	0.65±0.05	n.a
11	NGC 2146	893	67900165	2.479±0.078	1.756±0.091	0.164±0.023	1.41±0.12	1.41±0.12	10.70±2.06
				2.62±0.52	1.73±0.35	0.10±0.02	1.51±0.61	1.51±0.61	17.3±6.7
12	NGC 2388	4134	71802360	0.1473±0.0073	0.0954±0.0058	0.0032±0.0010	1.54±0.17	1.54±0.17	29.81±11.13
				0.191±0.038	0.097±0.019	n.a	1.97±0.77	1.97±0.77	n.a
13	M 82	203	65800611	13.02±0.30	16.70±0.59	1.366±0.056	0.78±0.05	0.78±0.05	12.23±0.93
				12.79±2.59	16.94±3.38	1.46±0.29	0.75±0.31	0.75±0.31	11.60±4.62
14	NGC 3256	2804	25200456	1.124±0.044	1.178±0.033	<0.032	0.95±0.03	0.95±0.03	n.a
				1.37±0.27	1.28±0.26	n.a	1.07±0.43	1.07±0.43	n.a
15	IRAS 10565+2448	12921	20200453	0.0551±0.0076	0.0848±0.0069	<0.011	0.65±0.14	0.65±0.14	n.a
				0.047±0.009	0.076±0.008	n.a	0.61±0.18	0.61±0.18	n.a
16	NGC 3620	1680	27600981	0.173±0.012	0.152±0.093	<0.046	1.14±0.77	1.14±0.77	n.a
				0.249±0.049	0.164±0.029	0.029±0.006	1.52±0.57	1.52±0.57	5.65±2.17
17	NGC 3690	3121	18000704	0.755±0.028	0.895±0.084	0.074±0.012	0.84±0.11	0.84±0.11	12.09±3.10
				0.86±0.17	0.83±0.17	0.05±0.005	1.03±0.41	1.03±0.41	16.6±5.1
18	NGC 4039/9	1641	25301107	0.378±0.011	0.412±0.079	0.0211±0.0041	0.92±0.20	0.92±0.20	19.53±7.54
				0.37±0.01	0.34±0.07	n.a	1.09±0.25	1.09±0.25	n.a

Index	Source	Radial Vel (km s ⁻¹)	TDT No. of Observation	[CII] 158 μ m	[OI] 63 μ m	[OI] 145 μ m	[CII] ₁₅₈ [OI] ₆₃	[OI] ₆₃ [OI] ₁₄₅
19	NGC 4102	846	19500584	0.322±0.012	0.341±0.022	0.0141±0.0041	0.944±0.096	24.18±8.59
				0.289±0.049	0.269±0.049	0.022±0.004	1.07±0.38	12.22±4.45
20	NGC 4151	995	35800185	0.0551±0.0043	0.401±0.032	0.0331±0.0047	0.14±0.02	12.11±2.71
			35300163	0.074±0.006	0.376±0.029	n.a	0.19±0.031	n.a
21	NGC 4194	2501	19401369	0.2094±0.0073	0.267±0.010	<0.0057	0.78±0.06	n.a
				0.217±0.008	0.28±0.02	0.013±0.003	0.77±0.08	21.53±6.50
22	NGC 4449	207	23400120	0.2383±0.0086	0.151±0.046	0.0187±0.0044	1.58±0.53	8.07±4.36
				0.278±0.008	0.133±0.013	n.a	2.09±0.26	n.a
23	NGC 4490	565	20501578	0.430±0.014	0.333±0.017	<0.0063	1.29±0.11	n.a
				0.423±0.084	0.328±0.065	0.011±0.002	1.29±0.51	29.81±11.33
24	NGC 4670	1609	58000205	0.0954±0.0083	0.717±0.075	0.0248±0.0051	0.13±0.03	28.91±8.97
				0.094±0.008	<1.13	<0.17	n.a	n.a
25	NGC 4945	563	28000446	3.547±0.075	1.82±0.061	0.38±0.021	1.95±0.11	4.79±0.43
				3.52±0.70	1.93±0.39	0.34±0.07	1.82±0.73	5.67±2.31
26	Cen A	547	63400464	2.764±0.085	1.757±0.068	0.102±0.0062	1.57±0.11	17.23±1.71
				2.90±0.58	1.92±0.39	0.10±0.02	1.51±0.61	19.2±7.74
27	NW Cen A	547	45400151	2.79±0.22	0.984±0.070	0.0744±0.0058	2.83±0.43	13.22±1.97
				2.43±0.48	0.90±0.18	0.08±0.02	2.7±1.1	11.25±5.06

Index	Source	Radial Vel (km s ⁻¹)	TDT No. of Observation	[CII] 158 μ m	[OI] 63 μ m	[OI] 145 μ m	[CII] ₁₅₈	[OI] ₆₃	[OI] ₁₄₅
28	M 51	600	35100651	0.951 \pm 0.048 1.04 \pm 0.01	0.623 \pm 0.057 0.44 \pm 0.09	0.0268 \pm 0.0038 n.a	1.53 \pm 0.22 2.36 \pm 0.51	23.25 \pm 5.42 n.a	
29	M 83	513	64200513	1.202 \pm 0.051 1.76 \pm 0.35	1.37 \pm 0.29 1.18 \pm 0.24	0.137 \pm 0.032 0.10 \pm 0.02	0.88 \pm 0.22 1.49 \pm 0.60	10.0 \pm 4.45 11.8 \pm 4.8	
30	Circinus	434	10401133	2.61 \pm 0.10 2.65 \pm 0.53	2.170 \pm 0.084 2.30 \pm 0.46	0.1606 \pm 0.023 0.18 \pm 0.05	1.20 \pm 0.09 1.15 \pm 0.46	3.58 \pm 0.27 12.77 \pm 6.10	
31	Mrk 297	4739	62702069	0.227 \pm 0.027 0.21 \pm 0.008	0.291 \pm 0.037 0.225 \pm 0.18	<0.19 <0.18	0.78 \pm 0.19 0.93 \pm 0.78	n.a n.a	
32	NGC 6240	7339	27801108	0.2447 \pm 0.0082 0.29 \pm 0.06	0.651 \pm 0.027 0.69 \pm 0.14	0.0349 \pm 0.0029 0.031 \pm 0.007	0.38 \pm 0.03 0.42 \pm 0.17	18.65 \pm 2.32 22.26 \pm 9.54	
33	NGC 6810	2031	84700610	0.311 \pm 0.014 0.40 \pm 0.08	0.22 \pm 0.031 0.18 \pm 0.04	<0.016 n.a	1.41 \pm 0.26 2.22 \pm 0.93	n.a n.a	
34	NGC 6946	48	45700139	0.876 \pm 0.028 1.03 \pm 0.21	0.611 \pm 0.024 0.59 \pm 0.12	<0.061 0.05 \pm 0.01	1.43 \pm 0.10 1.74 \pm 0.71	n.a 11.8 \pm 4.8	
35	NGC 7673	3408	76601364	0.1061 \pm 0.0041 n.a	0.172 \pm 0.041 n.a	<0.0075 n.a	0.62 \pm 0.17 n.a	n.a n.a	
36	Mrk 331	5541	56500637	0.182 \pm 0.006 0.148 \pm 0.008	0.096 \pm 0.008 0.11 \pm 0.006	0.0076 \pm 0.0018 < 0.13	1.89 \pm 0.22 1.34 \pm 0.14	12.63 \pm 4.03 n.a	

Index	Source	Radial Vel (km s ⁻¹)	TDT No. of Observation	[CII] _{158μm}	[OI] _{63μm}	[OI] _{145μm}	[CII] ₁₅₈	[OI] ₆₃	[OI] ₁₄₅
37	NGC 4151	995	35300163	0.822±0.006	0.445±0.024	<0.042	1.85±0.11	n.a	n.a
				0.074±0.006	0.37±0.029	n.a	0.20±0.03	n.a	n.a
38	NGC 6286	5501	20700509	0.187±0.008	0.087±0.004	0.0094±0.0013	2.15±0.19	9.25±1.70	
				0.168±0.005	0.073±0.009	0.005±0.001	2.30±0.35	14.6±4.7	
39	NGC 6574	2282	70500604	0.436±0.021	0.223±0.034	0.078±0.017	1.95±0.39	2.86±1.05	
				0.44±0.020	0.23±0.041	n.a	1.91±0.42	n.a	
40	NGC 6822	-57	34300915	0.176±0.011	0.128±0.005	0.008±0.002	1.37±0.15	16.5±3.9	
				0.187±0.011	0.143±0.006	<0.05	1.30±0.13	n.a	
41	NGC 7552	1608	36903087	0.583±0.028	0.20±0.04	0.037±0.007	2.92±0.72	5.41±2.10	
				0.64±0.015	0.63±0.023	n.a	1.01±0.06	n.a	
42	NGC 7771	4277	56500772	0.29±0.01	0.141±0.009	0.0187±0.0026	2.06±0.20	7.54±1.52	
				0.298±0.009	0.115±0.013	n.a	2.59±0.37	n.a	
43	NGC 4041	1234	22202506	0.32±0.01	0.38±0.05	<0.14	0.84±0.13	n.a	
				0.348±0.005	0.197±0.016	n.a	1.76±0.16	n.a	
44	NGC 0278	627	59702260	0.72±0.002	<0.03	0.020±0.002	n.a	n.a	
				0.728±0.012	0.347±0.016	<0.021	2.09±0.13	n.a	
45	NGC 0695	9735	63300744	0.137±0.007	0.19±0.01	0.010±0.002	0.72±0.07	19±4.8	
				0.20±0.008	0.118±0.009	n.a	1.69±0.19	n.a	
46	NGC 0986	1974	74300187	0.278±0.009	0.19±0.04	0.013±0.001	1.46±0.35	14.62±4.20	
				0.304±0.011	0.127±0.013	<0.025	2.39±0.33	n.a	

errors in the submillimeter and IR domain (Martín *et al.* 2006; Bayet *et al.* 2004; Israel *et al.* 1995). The percentage uncertainty estimated in this way appears, on average, to be similar to the percentage line flux uncertainties measured by us using the interactive package SMART.

In order to show that our measurements are in good agreement with the fluxes collected from the literature we have plotted our measurements versus literature values in Fig 3.1. We have plotted the ratio of the literature value of $[\text{C II}]_{158}/[\text{O I}]_{63}$ over our own measured $[\text{C II}]_{158}/[\text{O I}]_{63}$ value, with respective error bars (open triangles), as well as the ratio of the literature value of $[\text{O I}]_{63}/[\text{O I}]_{145}$ over our own value of $[\text{O I}]_{63}/[\text{O I}]_{145}$, with respective error bars (filled triangles). The horizontal line in Fig 3.1 represents the case in which the literature ratios and our own measured ratios are in perfect agreement. Flux ratios of two lines of the same species, such as $[\text{O I}]_{145}/[\text{O I}]_{63}$ can provide information about nebular conditions such as temperature (or radiation field strength). In addition, a ratio such as $[\text{O III}]_{88}/[\text{O III}]_{52}$ can provide information on the electron density. In addition by using ratios, rather than fitting the line intensities directly, the beam filling factors of the two emission lines cancel out, assuming that they come from the same regions and are the same size.

Fig 3.2 shows the $[\text{C II}]_{158}/[\text{O I}]_{63}$ ratio versus the $[\text{O I}]_{63}/[\text{O I}]_{145}$ ratio for the 28 sources, out of the 46 listed in Table 3.1, that showed $\geq 4\sigma$ detections in all three lines.

3.2 The UCL_PDR models

We used the **UCL_PDR** time and depth-dependent PDR code (Bell *et al.* 2006a) which solves the chemistry, thermal balance and radiative transfer self-consistently within a cloud. The range of parameter values input to the code are listed in Table 3.3, including the mean grain radius and grain number density adopted for grain surface reactions. The FUV grain opacity properties adopted by UCL_PDR are listed by Bell *et al.* (2006b). The outputs of the code are the abundances of each species included in the chemical network, their column densities, the emissivities and integrated intensities of the emission lines involved in the cooling, and the gas and dust temperatures. All of these quantities are functions of depth and time. We use a grid of 1702 PDR models, already computed and partially used in previous works (Bell *et al.* 2006a,b, 2007) spanning a large range of densities, metallicities and cosmic ray ionization rates. Amongst the range of parameter values covered by the grid of models (see Table 3.3), we do not consider variations of the turbulent velocity parameter in our attempts to fit the observed emission from each galaxy, since the line ratios are believed to be fairly insensitive to small

Table 3.2: Line flux measurements, in units of $10^{-14} \text{ W m}^{-2}$, for extragalactic sources with ISO-LWS detections of all 3 FIR fine structure emission lines of [C II] and [O I]. For each source, our own line flux measurements, if any, are listed in the first row, while literature values, are listed in the second row (Contursi *et al.* 2002; Bergvall *et al.* 2000; Colbert *et al.* 1999; Fischer *et al.* 1996; Luhman *et al.* 2003; Malhotra *et al.* 2001; Negishi *et al.* 2001; Unger *et al.* 2000; Brauher *et al.* 2008). (n.a: not available)

Index	Source	Radial Vel (km s^{-1})	[CII] $158\mu\text{m}$	[OI] $63\mu\text{m}$	[OI] $145\mu\text{m}$
1	Eso 317-G023	2892	n.a	n.a	n.a
			0.10 ± 0.01	0.0680 ± 0.01	n.a
2	NGC 0693	1567	n.a	n.a	n.a
			0.167 ± 0.03	0.07 ± 0.01	n.a
3	NGC 1022	1453	n.a	n.a	n.a
			0.127 ± 0.02	0.191 ± 0.03	n.a
4	UGC 02238	6560	n.a	n.a	n.a
			0.222 ± 0.04	0.073 ± 0.01	n.a
5	NGC 1155	4644	n.a	n.a	n.a
			0.034 ± 0.01	0.035 ± 0.01	n.a
6	NGC 1156	375	n.a	n.a	n.a
			0.186 ± 0.03	0.07 ± 0.01	n.a
7	NGC 1222	2448	0.189 ± 0.006	0.233 ± 0.014	n.a
			0.206 ± 0.04	0.25 ± 0.05	n.a
8	NGC 1317	1941	n.a	n.a	n.a
			0.074 ± 0.01	0.041 ± 0.01	n.a
9	NGC 1326	1360	n.a	n.a	n.a
			0.148 ± 0.02	0.076 ± 0.01	n.a
10	LEDA 90327	25701	n.a	n.a	n.a
			0.0223 ± 0.004	n.a	n.a
11	NGC 4414	716	n.a	n.a	n.a
			0.78 ± 0.16	0.32 ± 0.06	n.a
12	LEDA 3183	4706	n.a	n.a	n.a
			0.29 ± 0.06	0.270 ± 0.05	n.a
13	ESO 173-15	2918	n.a	n.a	n.a
			0.53 ± 0.11	0.400 ± 0.08	n.a

14	NGC 5937	2807	n.a	n.a	n.a
			0.40±0.08	0.15±0.03	n.a
15	NGC 6156	3263	n.a	n.a	n.a
			0.41±0.08	0.18±0.04	n.a
16	NGC 7582	1575	n.a	n.a	n.a
			0.42±0.08	0.30±0.07	n.a
17	NGC 891	528	n.a	n.a	n.a
			0.77±0.15	0.19±0.04	n.a
18	NGC 6824	3386	n.a	n.a	n.a
			0.18±0.04	0.08±0.02	n.a
19	NGC 3683	1716	n.a	n.a	n.a
			0.376±0.0752	0.17±0.034	n.a
20	NGC 3885	1952	n.a	n.a	n.a
			0.137±0.0274	0.11±0.022	n.a
21	NGC 5713	1899	n.a	n.a	n.a
			0.454±0.0908	0.265±0.053	n.a
22	IC 4595	3419	n.a	n.a	n.a
			0.244±0.0488	0.069±0.0138	n.a
23	NGC 6753	3169	n.a	n.a	n.a
			0.288±0.0576	0.081±0.0162	n.a
24	NGC 7418	1450	n.a	n.a	n.a
			0.123±0.0246	n.a	n.a
25	NGC 7218	1658	n.a	n.a	n.a
			0.18±0.036	0.076±0.0152	n.a
26	IC 2554	1397	n.a	n.a	n.a
			0.36±0.07	0.23±0.05	n.a
27	NGC 4027	1671	n.a	n.a	n.a
			0.287±0.0574	0.328±0.0656	n.a
28	NGC 1052	1510	n.a	n.a	n.a
			0.012±0.002	0.148±0.0296	n.a
29	Iras 05189-2554	12760	n.a	n.a	n.a
			0.0133±0.002	n.a	n.a
30	LEDA 84586	30000	n.a	n.a	n.a
			0.288±0.0576	0.081±0.0162	n.a

31	ESO 148-2	13371	n.a	n.a	n.a
			0.288±0.0576	0.081±0.0162	n.a
32	NGC 1266	2194	n.a	n.a	n.a
			0.038±0.007	0.054±0.0108	n.a
33	Arp 220	5434	n.a	n.a	n.a
			0.0999±0.019	-0.0635±0.01	n.a
34	LEDA 90429	19331	n.a	n.a	n.a
			0.0132±0.002	0.0126±0.002	n.a
35	Mrk 273	11326	n.a	n.a	n.a
			0.0524±0.010	0.0470±0.009	n.a
36	NGC 5128	547	n.a	n.a	n.a
			2.90±0.58	1.92±0.39	0.10±0.02
37	NGC 5430	2961	n.a	n.a	n.a
			0.16±0.03	0.10±0.02	n.a
38	IC 4662	302	n.a	n.a	n.a
			0.244±0.048	0.143±0.0286	n.a
39	NGC 1385	1499	n.a	n.a	n.a
			0.511±0.102	0.243±0.0486	n.a
40	NGC 1546	1284	n.a	n.a	n.a
			0.27±0.054	0.062±0.0124	n.a
41	Iras 17208-0014	12834	n.a	n.a	n.a
			0.068±0.0136	0.0653±0.013	0.10±0.02
42	NGC 6764	2416	n.a	n.a	n.a
			0.011±0.02	0.11±0.03	n.a
43	Iras 19254-7254	18500	n.a	n.a	n.a
			0.0271±0.005	n.a	n.a
44	NGC 1097	1284	n.a	n.a	n.a
			0.71±0.14	0.39±0.08	n.a
45	LEDA 90354	>30000	n.a	n.a	n.a
			0.0065±0.001	n.a	n.a
46	ESO 286-19	12890	n.a	n.a	n.a
			0.0351±0.007	0.05±0.01	n.a
47	NGC 7714	2798	n.a	n.a	n.a
			0.20±0.04	0.23±0.05	n.a

48	Mrk 231	12642	n.a	n.a	n.a
			0.0351±0.007	0.0289±0.005	n.a
49	NGC 1365	1636	n.a	n.a	n.a
			1.10±0.22	0.55±0.11	n.a
50	NGC 7469	4892	n.a	n.a	n.a
			0.23±0.5	0.25±0.05	n.a
51	IC 0883	6985	n.a	n.a	n.a
			0.088±0.0176	0.12±0.024	n.a
52	NGC 6052	4739	0.169±0.007	0.291±0.037	0.017±0.006
			n.a	n.a	n.a
53	NGC 0625	4892	0.097±0.007	n.a	n.a
			n.a	n.a	n.a
54	NGC 4449	207	0.24±0.008	0.151±0.046	0.018±0.004
			n.a	n.a	n.a

changes in the turbulent velocity (Wolfire *et al.* 1989).

3.3 Sensitivity of model results to parameter variations

We attempted to find the range of physical parameters which best reproduced the observations, such as visual extinction, metallicity, cosmic ray ionization rate and UV radiation field strength. The influence of changing the number density of hydrogen nuclei (n_H), the visual extinction (A_v), the incident radiation field strength (G_o), the cosmic ray ionization rate ζ and the metallicity (Z) is considered individually by varying only one of these parameters at a time. The age of the modeled regions was set to a value of 10^7 yrs, owing to the fact that clouds with ages $\geq 10^7$ yrs do not undergo significant changes in their predicted chemical profiles, even though, in some cases, the chemistry only reaches its final steady state somewhat later (Bell *et al.* 2006b).

When one parameter was varied the remainder were held constant at the reference parameter values listed in the final column of Table 3.3.

In Figs 3.3 through 3.17 we overplot our model predictions against flux ratios from the [C II] $158\mu\text{m}$ and [O I] $63\mu\text{m}$ and $145\mu\text{m}$ ISO LWS fluxes. Table 3.4 lists these 3 important PDR cooling transitions, their wavelengths, upper energy levels E_{upper} , and critical densities n_{cr} . In this section we will only discuss the sensitivity of the ratios to changes in the input

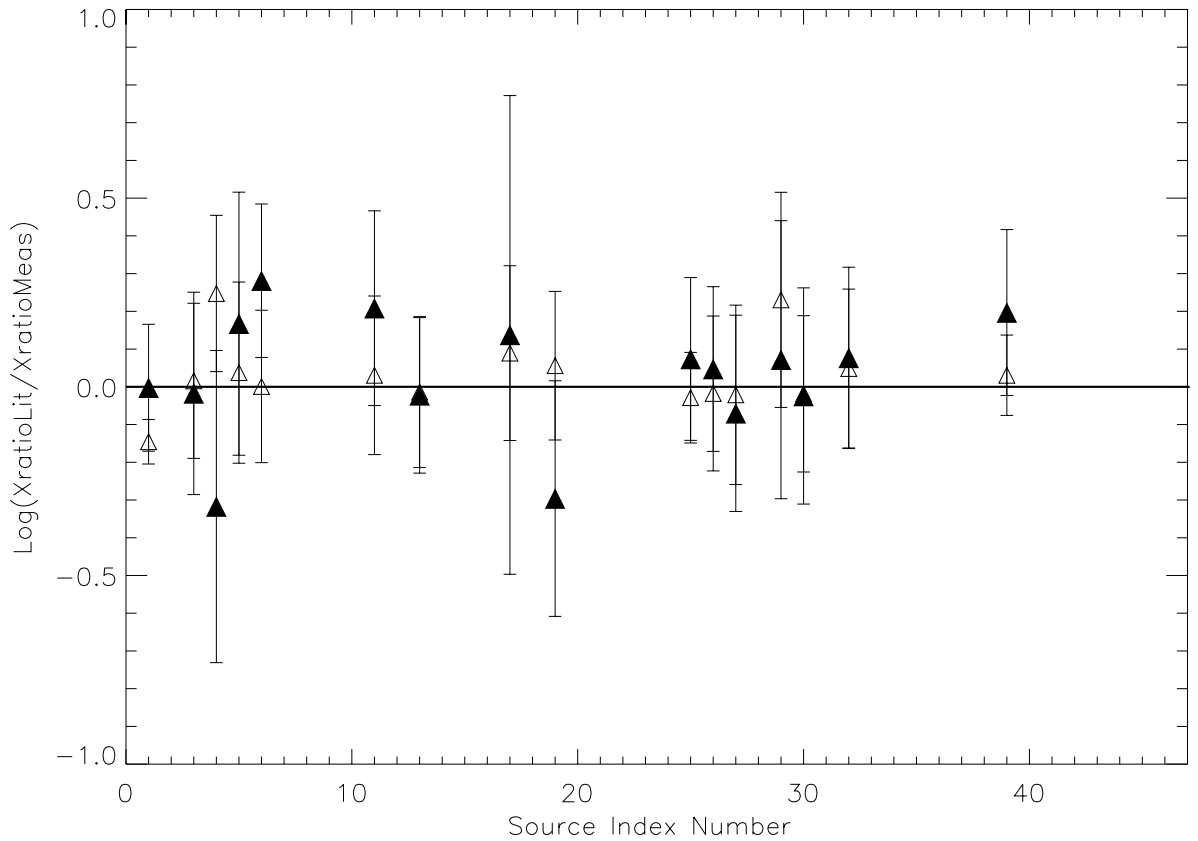


Figure 3.1: $[C II]_{158}/[O I]_{63}$ and $[O I]_{63}/[O I]_{145}$ ratios. Filled triangles represent the ratio of the literature value of $[O I]_{63}/[O I]_{145}$ over our own measured $[O I]_{63}/[O I]_{145}$ ratio, with respective error bars. Open triangles represent the ratio of the literature value of $[C II]_{158}/[O I]_{63}$ over our own measured $[C II]_{158}/[O I]_{63}$ ratio with respective error bars. The horizontal line represents the case in which literature ratios and our own measured ratios are perfectly matched. The source index numbers and galaxy identifications are listed in Table 3.1.

parameters. The comparison with observations will be made in Section 3.5.

3.3.1 Visual Extinction

PDRs derive their properties primarily from the penetration of FUV photons into their interiors. Dust grains provide the major source of continuum opacity and attenuate the incident radiation field by selectively absorbing and scattering light at visible and ultraviolet wavelengths. This means that there is a strong correlation between visual extinction and the chemistry of PDRs. We examined models for different visual extinction values in the range $1 \leq A_v \leq 10$.

From Fig 3.3 and Fig 3.4 one can see that there is no significant change in the emission line

Table 3.3: Physical and chemical parameters for the UCL_PDR grid. In the grid of models the density and the radiation field parameters are incremented by 2 dex and 1 dex, respectively.

Parameter	Range of values	Reference parameter values
Cloud density (cm^{-3})	$10^2 \leq n_H \leq 10^5$	$n_H = 10^3$
Incident FUV flux (Habing)	$10 \leq G_0 \leq 10^5$	$G_0 = 10$
Age of the cloud (yr)	$10^4 \leq t \leq 10^8$	$t = 10^7$
Cloud size (mag)	$0 \leq A_v \leq 10$	$A_v = 10$
Metallicity	$Z/Z_\odot = 5, 4, 3, 2, 1, 0.5$ $0.1, 0.25, 0.01$	$Z = Z_\odot$
C.R. ionization rate (s^{-1})	$\zeta = 5x, 50x, 500x 10^{-15}$ $5x, 50x, 500x 10^{-16}$ $5x, 50x, 500x 10^{-17}$	$\zeta = 5x 10^{-17}$
Turbulent velocity (km s^{-1})	$v_{turb} = 1.5$	$v_{turb} = 1.5$
Carbon elemental abundance	$1.4x 10^{-4} n_H$	Sofia & Meyer (2001)
Oxygen elemental abundance	$3.2x 10^{-4} n_H$	Sofia & Meyer (2001)
Grain radius	$0.1 \mu\text{m}$	$0.1 \mu\text{m}$
Grain number density n_g	$2x 10^{-12} Z n \text{ cm}^{-3}$	$2x 10^{-9} \text{ cm}^{-3}$

Table 3.4: PDR diagnostic transitions. The critical densities for [C II] and [O I] are for collisions with H (Tielens & Hollenbach 1985).

Species	Transitions	Wavelength (μm)	E_{upper}/k (K)	n_{cr} (cm^{-3})
[C II]	$^2P_{3/2} - ^2P_{1/2}$	157.74	92	$3x 10^3$
[O I]	$^3P_1 - ^3P_2$	63.18	228	$4.7x 10^5$
[O I]	$^3P_0 - ^3P_1$	145.53	326	$1x 10^5$

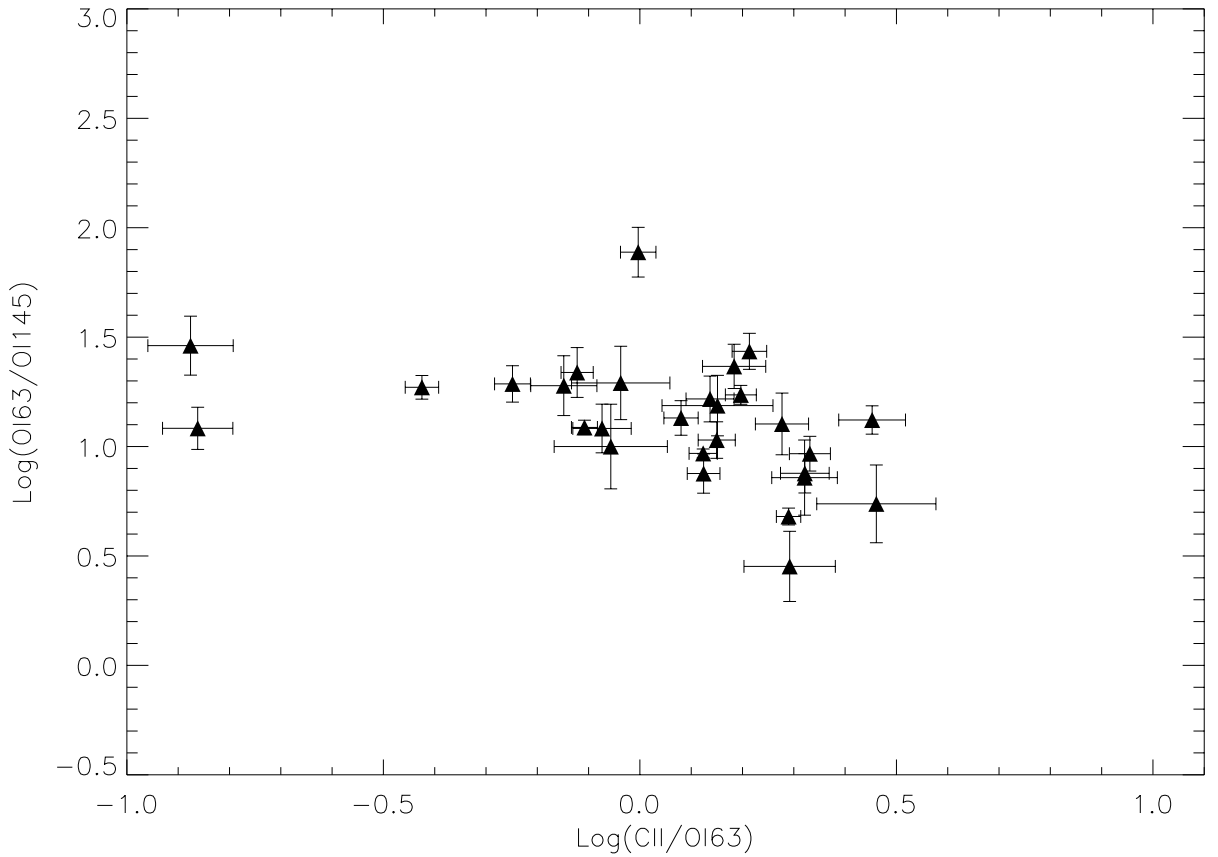


Figure 3.2: The observed $[\text{C II}]_{158} / [\text{O I}]_{63}$ ratios versus the $[\text{O I}]_{63} / [\text{O I}]_{145}$ ratios for detections $\geq 4\sigma$, with error bars.

ratios from $A_v=1$ (black circle) to $A_v=10$ (green circle). This trend implies that the majority of the line fluxes arise from $1 \leq A_v \leq 2$ and is consistent with the C^+ abundance because, for values of A_v larger than 2, this ion recombines to form C^0 and subsequently forms CO. Indeed C^+ is a tracer of the edge of PDRs. This implies that the C^+ fine structure emission lines that are observed are coming predominantly from regions with low visual extinction. Although neutral oxygen is still present at higher visual extinctions, it is somewhat reduced beyond $A_v=1$ because a fraction of oxygen combines with C to form CO (see Röllig *et al.* 2007). We fixed $A_v=10$ as the most appropriate depth range to fit our sample of sources, since Fig 3.3 and Fig 3.4 show that we cannot distinguish between models with optical depths in the range of $1 \leq A_v \leq 10$.

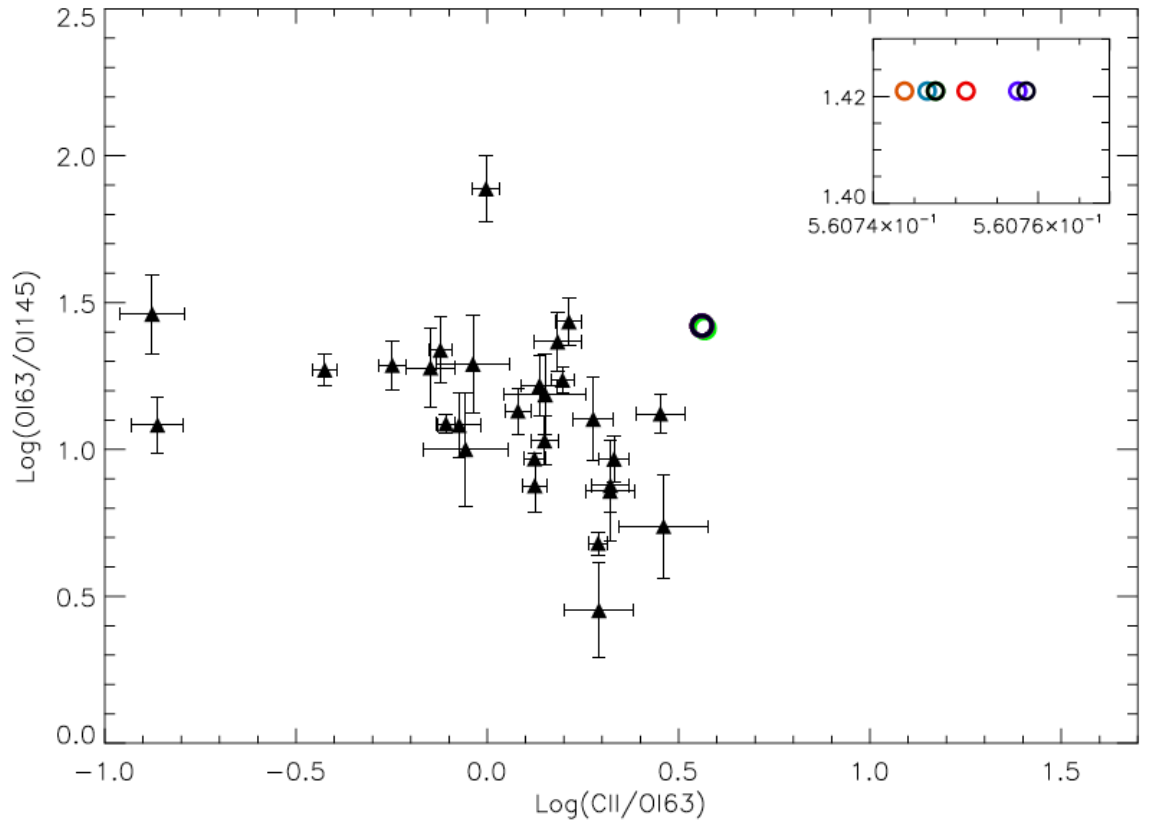


Figure 3.3: $[C II]_{158} / [O I]_{63}$ versus $[O I]_{63} / [O I]_{145}$ ratios with error bars, compared with models of varying visual extinctions. The insert shows a zoomed-in region of the overlapping coloured circles corresponding to differing visual extinction values.

3.3.2 Radiation field

Radiation field strengths incident upon a gas cloud can vary from the standard interstellar field ($\chi = \text{Draine}$) up to $\chi \sim 10^7$ Draines (Draine 1978) in regions of intense star formation (see Hollenbach & Tielens 1997). The FUV field may be also expressed in terms of the Habing parameter (Habing 1968). The FUV flux expressed in this way is determined by the parameter $G_0 = \chi / 1.7$. We adopt a range of $10 \leq G_0 \leq 500000$ Habings for consideration in this study, but we only plot the significant results. From Fig 3.5 to Fig 3.8, $[C II]_{158} / [O I]_{63}$ versus $[O I]_{63} / [O I]_{145}$ appears to be sensitive to variations in the radiation field strength. As the radiation field strength increases so does the $[O I]_{63} / [O I]_{145}$ ratio, while the $[C II]_{158} / [O I]_{63}$ ratio decreases. The energy required to excite the $[O I]_{63}$ transition is somewhat higher than that for $[C II]_{158}$, hence the line intensity ratio $[O I]_{63} / [C II]_{158}$ is expected to increase with gas temperature and hence higher FUV flux. PDR models predict that for $n_H > 10^3 \text{ cm}^{-3}$ the line ratio will increase

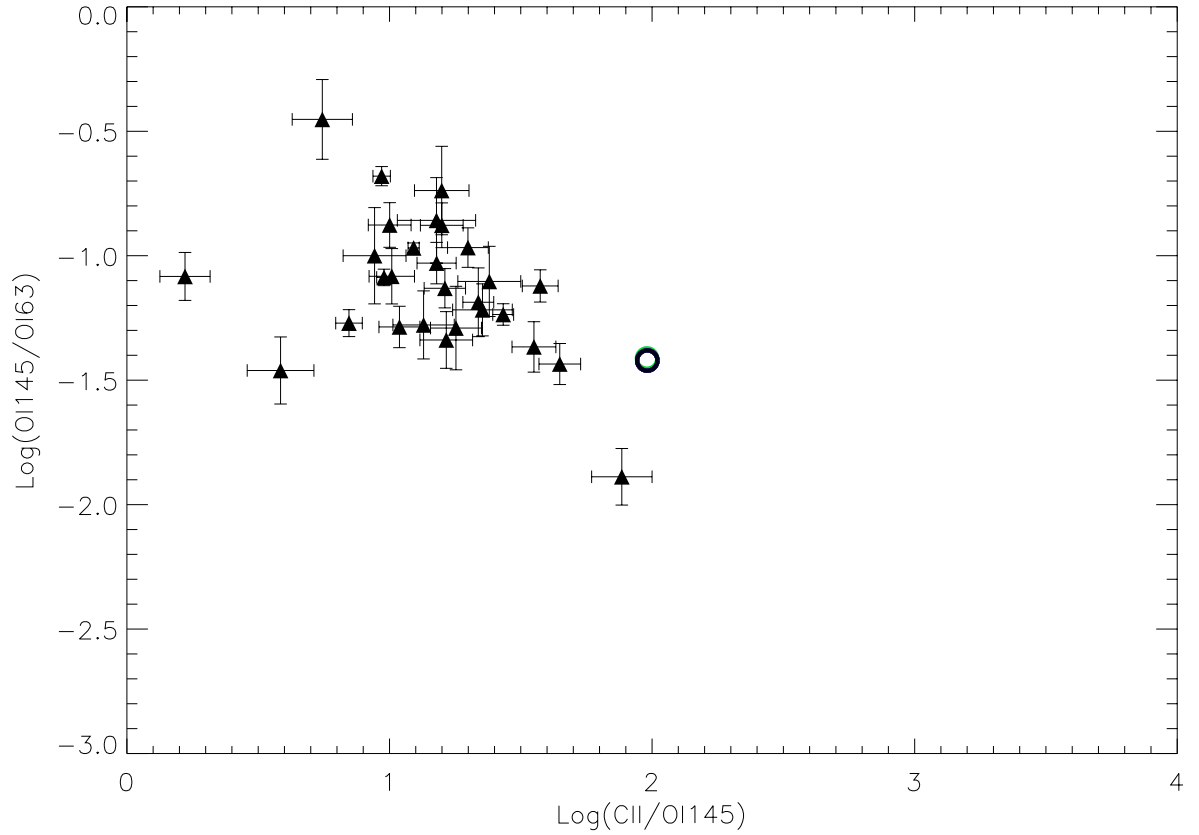


Figure 3.4: $[\text{C II}]_{158}/[\text{O I}]_{145}$ versus $[\text{O I}]_{145}/[\text{O I}]_{63}$ ratios (right), with error bars, compared with models of varying visual extinctions.

with both G_0 and n_H , due to the different critical densities of the two transitions (Wolfire *et al.* 1990).

3.3.3 Metallicity

Metallicities significantly below solar are observed in Local Group galaxies, including the Small Magellanic Cloud, as well as in more distant dwarf galaxies, with I Zw 18's metallicity of 1/40 being amongst the lowest known (Izotov & Thuan 1999). The metallicity-dependence appears in several key processes in the UCL_PDR code. Elemental abundances of all metals are assumed to scale linearly with metallicity (Z/Z_\odot); the dust-to-gas mass ratio is also assumed to scale linearly with metallicity and takes a standard value of 10^{-2} at Solar metallicity. The formation rate of H_2 on grain surfaces and the grain photoelectric heating rate are assumed to scale linearly with metallicity.

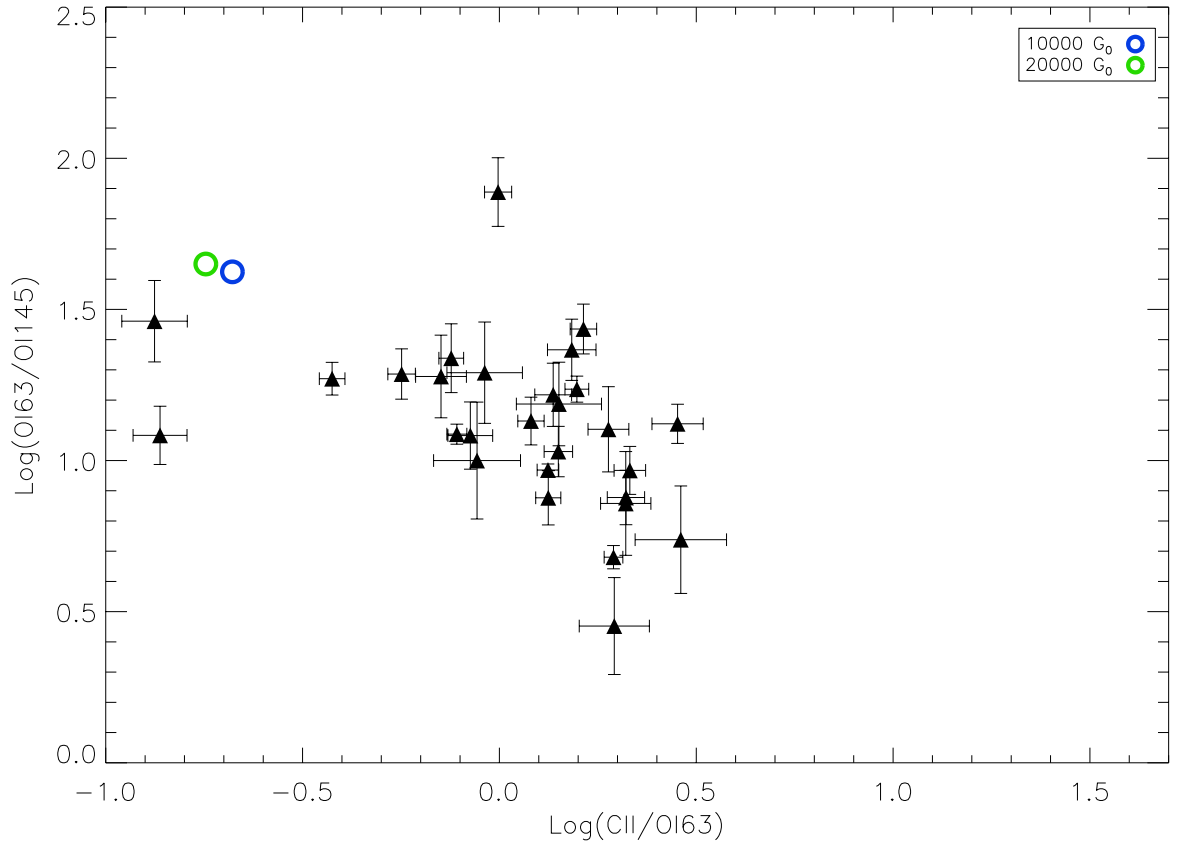


Figure 3.5: The observed $[C II]_{158} / [O I]_{63}$ versus $[O I]_{63} / [O I]_{145}$ ratios, with uncertainties. The coloured points represent models with radiation field strengths in the range $10^4 \leq G_0 \leq 2 \times 10^4$.

We investigated a metallicity range of $0.01 \leq Z/Z_{\odot} \leq 5$ for this study, with the adopted solar neighbourhood carbon and oxygen elemental abundances listed in Table 3.3. Metallicity affects the total abundances of carbon and oxygen bearing species, and hence can influence the chemical and thermal structure of PDRs in galaxies.

In Fig 3.9 we show our model results for metallicities of 0.01 (light green circle), 0.25 (claret circle) and 0.5 (light blue circle), with remaining symbols representing values of 1, 2, 3, 4 and 5 times solar metallicity respectively. The C/O ratios for the Sun, the Large Magellanic Cloud (LMC) and the Small Magellanic Cloud (SMC) are all ~ 0.5 within the uncertainties, but for lower metallicities than the SMC C/H decreases faster than O/H. We tried to reproduce this trend by changing carbon and oxygen elemental abundances with metallicity. In Fig 3.10 we show our model results for a metallicity of $Z/Z_{\odot} = 1$, with $C/O = 0.53$ (Asplund *et al.* 2005), then we scaled all the elemental abundances with Z/Z_{\odot} down to $Z/Z_{\odot} = 0.25$. Below $Z/Z_{\odot} = 0.25$ the

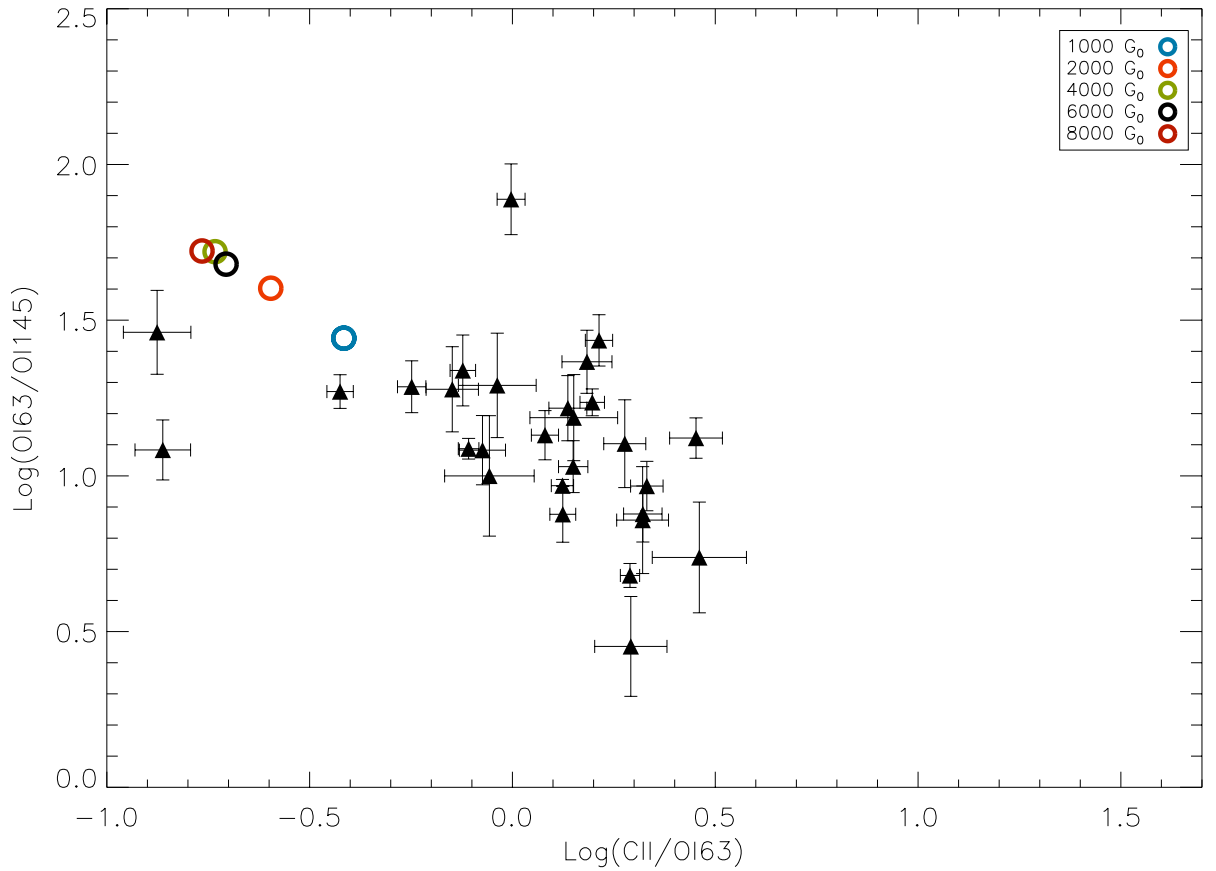


Figure 3.6: The observed $[\text{C II}]_{158} / [\text{O I}]_{63}$ versus $[\text{O I}]_{63} / [\text{O I}]_{145}$ ratios, with uncertainties. The coloured points represent models with radiation field strengths in the range $10^3 \leq G_0 \leq 8 \times 10^3$.

C/O ratio was scaled from 0.53 to 0.16 as Z/Z_{\odot} was reduced from 0.25 to 0.03 (Izotov & Thuan 1999).

The very large jump from 0.01 to the next step in Z/Z_{\odot} in Fig 3.9 and from 0.03 to the next step in Z/Z_{\odot} in Fig 3.10 can at least partly attributed to the metallicity-dependence that appears in several key processes in the UCL_PDR code. However, as expected, the $[\text{O I}]_{63} / [\text{O I}]_{145}$ ratio is not sensitive to variations of metallicity whereas the $[\text{C II}]_{158} / [\text{O I}]_{63}$ ratio would appear at first sight to be a good tracer of metallicity.

3.3.4 Density

We have considered the sensitivity of the fine structure emission line intensities to H-nuclei densities in the range $10^2 \leq n_H \leq 10^5 \text{ cm}^{-3}$. In Fig 3.11– 3.14 we show our model results for different values of density. The $[\text{C II}]_{158} / [\text{O I}]_{63}$ and $[\text{O I}]_{63} / [\text{O I}]_{145}$ ratios are both sensitive to

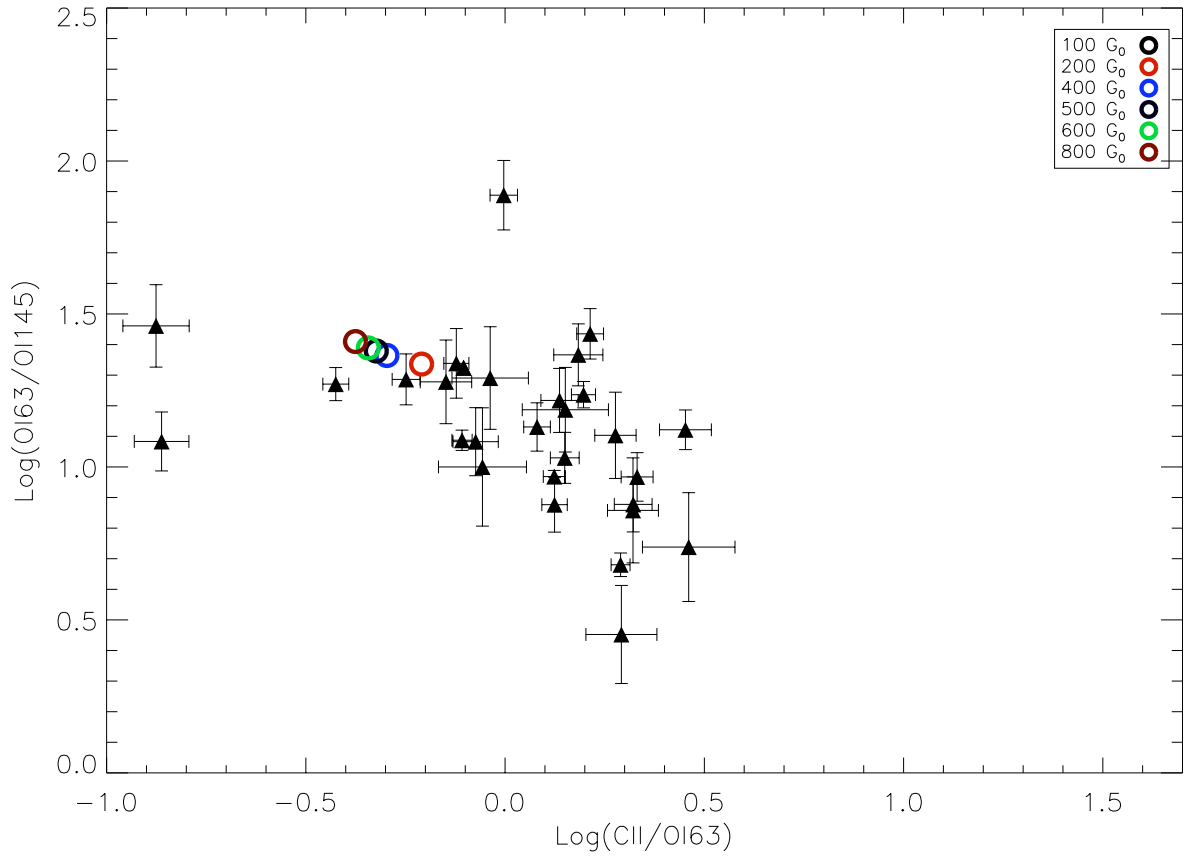


Figure 3.7: The observed $[\text{C II}]_{158}/[\text{O I}]_{63}$ versus $[\text{O I}]_{63}/[\text{O I}]_{145}$ ratios, with uncertainties. The coloured points represent models with radiation field strengths in the range $10^2 \leq G_0 \leq 8 \times 10^2$.

density, however there is a higher sensitivity for the $[\text{C II}]_{158}/[\text{O I}]_{63}$ ratio. As expected, there is a substantial decline in the $[\text{O I}]_{63}/[\text{O I}]_{145}$ ratio as the density decreases from $n_H \sim 10^5 \text{ cm}^{-3}$ to $n_H \sim 9 \times 10^3 \text{ cm}^{-3}$, and a steady decline in the $[\text{O I}]_{63}/[\text{O I}]_{145}$ ratio as the density decreases from $n_H \sim 9 \times 10^3$ while the model $[\text{C II}]_{158}/[\text{O I}]_{63}$ ratios increase initially with decreasing density until the density reaches a value of $n_H \sim 10^3 \text{ cm}^{-3}$ and then decrease as the density decreases further. Clearly, the changes in the $[\text{O I}]_{63}/[\text{O I}]_{145}$ ratio at 10^5 cm^{-3} are partly due to the critical density of the two lines (see Table 3.4). Similarly, the decrease in the $[\text{C II}]_{158}/[\text{O I}]_{63}$ ratio as the density decreases is partially due to the density falling below the critical density of the $[\text{C II}]_{158}$ line.

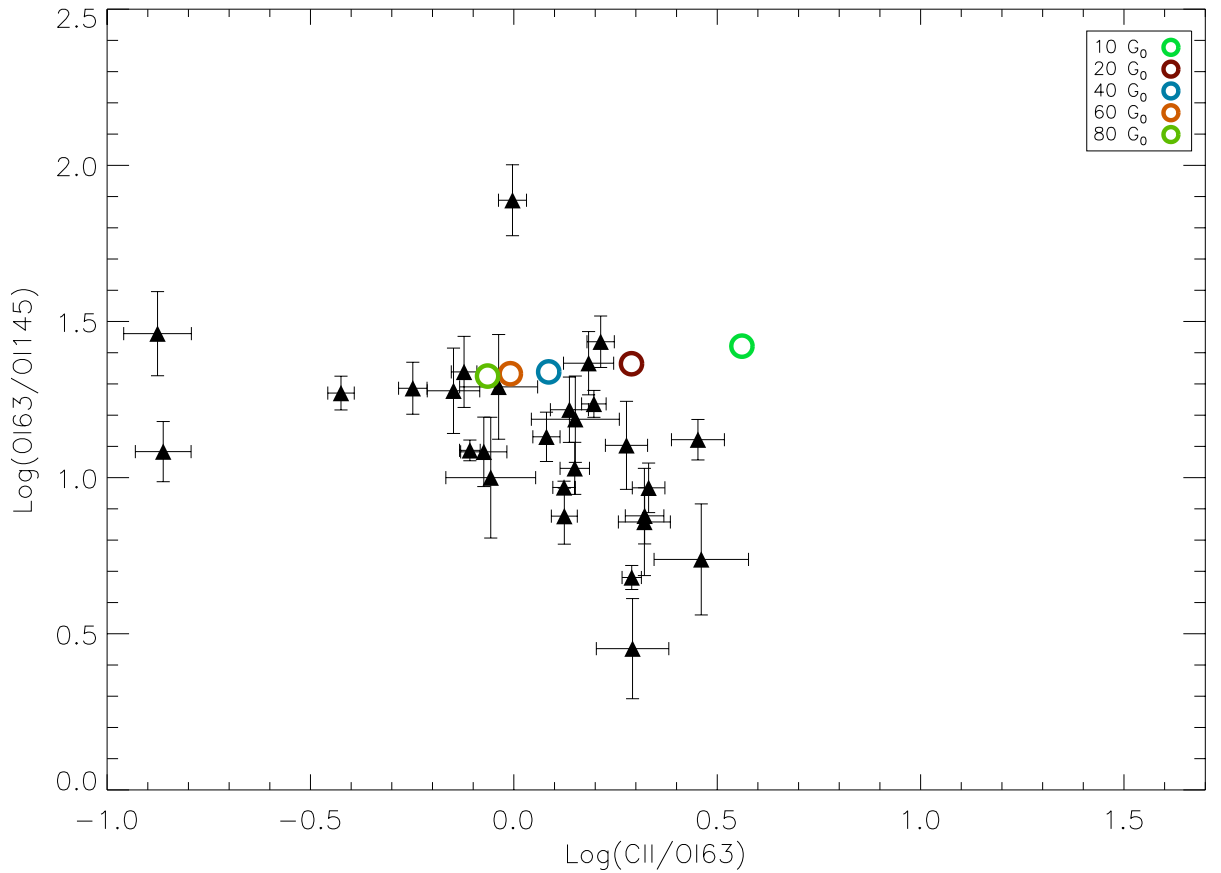


Figure 3.8: The observed $[\text{C II}]_{158} / [\text{O I}]_{63}$ versus $[\text{O I}]_{63} / [\text{O I}]_{145}$ ratios, with uncertainties. The coloured points represent models with radiation field strengths in the range $10 \leq G_0 \leq 80$.

3.3.5 Cosmic ray ionization rate

The cosmic ray flux is known to vary by over an order of magnitude in the Milky Way (Schilke *et al.* 1993). Magnetic field lines can channel cosmic rays away from dense molecular cores; alternatively, the flux of particles in star forming regions can be many times higher than the canonical rate (Schilke *et al.* 1993). The UCL_PDR code does not have a separate treatment for X-ray Dominated Region (XDR) effects that may be important in some galaxies (see Meijerink *et al.* 2006). However to a first approximation one may use an enhanced cosmic ray ionization rate to mimic the effects of XDRs (Bell *et al.* 2006a). In Fig 3.15 we show our model results for cosmic ray ionization rates in the range $5 \times 10^{-15} \leq \zeta \leq 5 \times 10^{-17} \text{ s}^{-1}$. The higher end of our range can represent a higher ionization rate (see e.g. McCall *et al.* 2003) or the effect of additional ionization due to X-rays. There is a substantial decline in the $[\text{O I}]_{63} / [\text{O I}]_{145}$ ratio as the cosmic ray ionization rate decreases from $\zeta = 5 \times 10^{-15} \text{ s}^{-1}$ (green circle) to $\zeta = 5 \times 10^{-16} \text{ s}^{-1}$ (claret

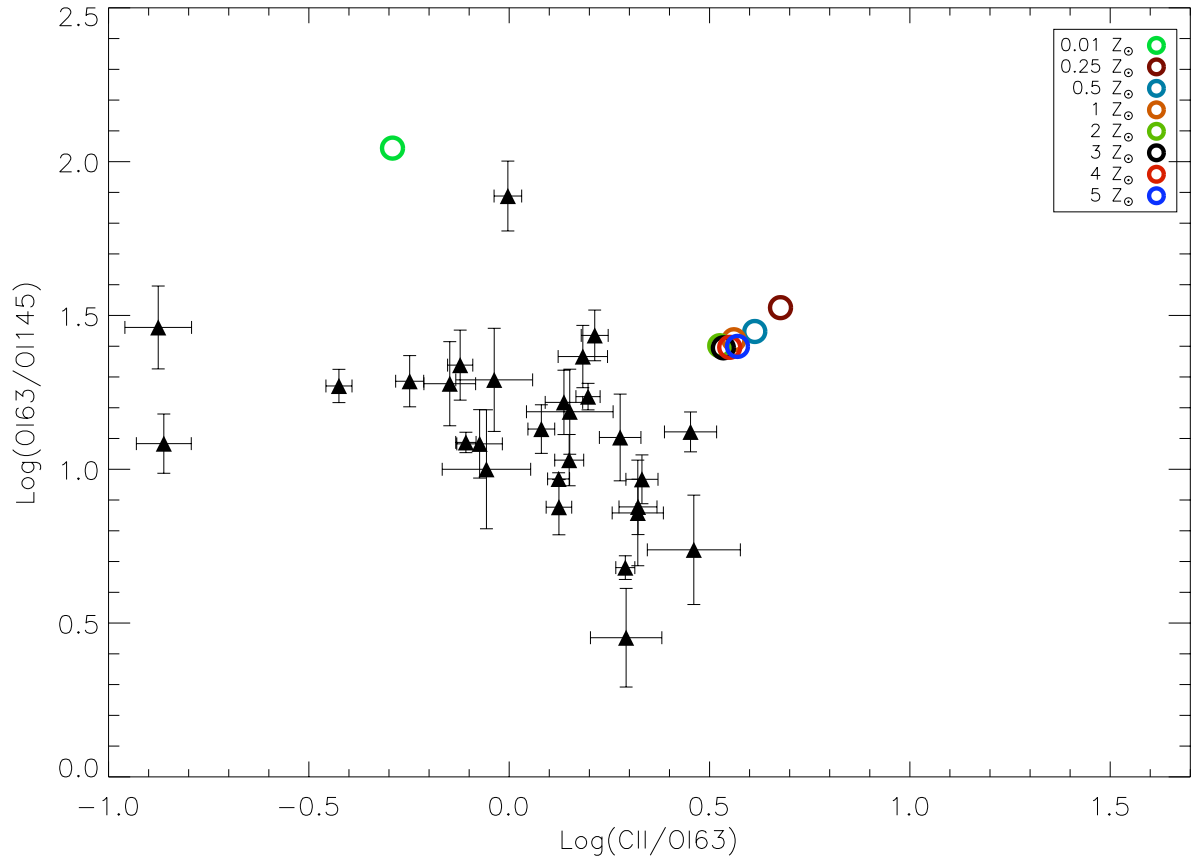


Figure 3.9: Observed $[C II]_{158} / [O I]_{63}$ versus $[O I]_{63} / [O I]_{145}$ ratios, with uncertainties, compared to models of differing metallicity. The coloured circles represent models with different values of metallicity, ranging from 0.01 (light green circle), 0.25 (claret circle) and 0.5 (light blue circle) up to 5 times solar metallicity.

circle) and it then decreases slightly for $\zeta = 5 \times 10^{-17} \text{s}^{-1}$ (blue circle); the $[C II]_{158} / [O I]_{63}$ ratio decreases significantly from $\zeta = 5 \times 10^{-15} \text{s}^{-1}$ (green circle) to $\zeta = 5 \times 10^{-16} \text{s}^{-1}$ (claret circle) and then remains constant. In fact both the $[C II]$ and $[O I]_{63}$ fluxes decrease with a decrease in ionization rate, with $[O I]_{63}$ decreasing at a faster rate.

3.4 Using [N II] fluxes to estimate the ionized gas contribution to [C II] fluxes

Several studies have been made that show that significant $[C II]$ emission can arise from H II regions (Heiles 1994; Abel *et al.* 2005; Kaufman *et al.* 2006; Abel 2006). Since the ionization

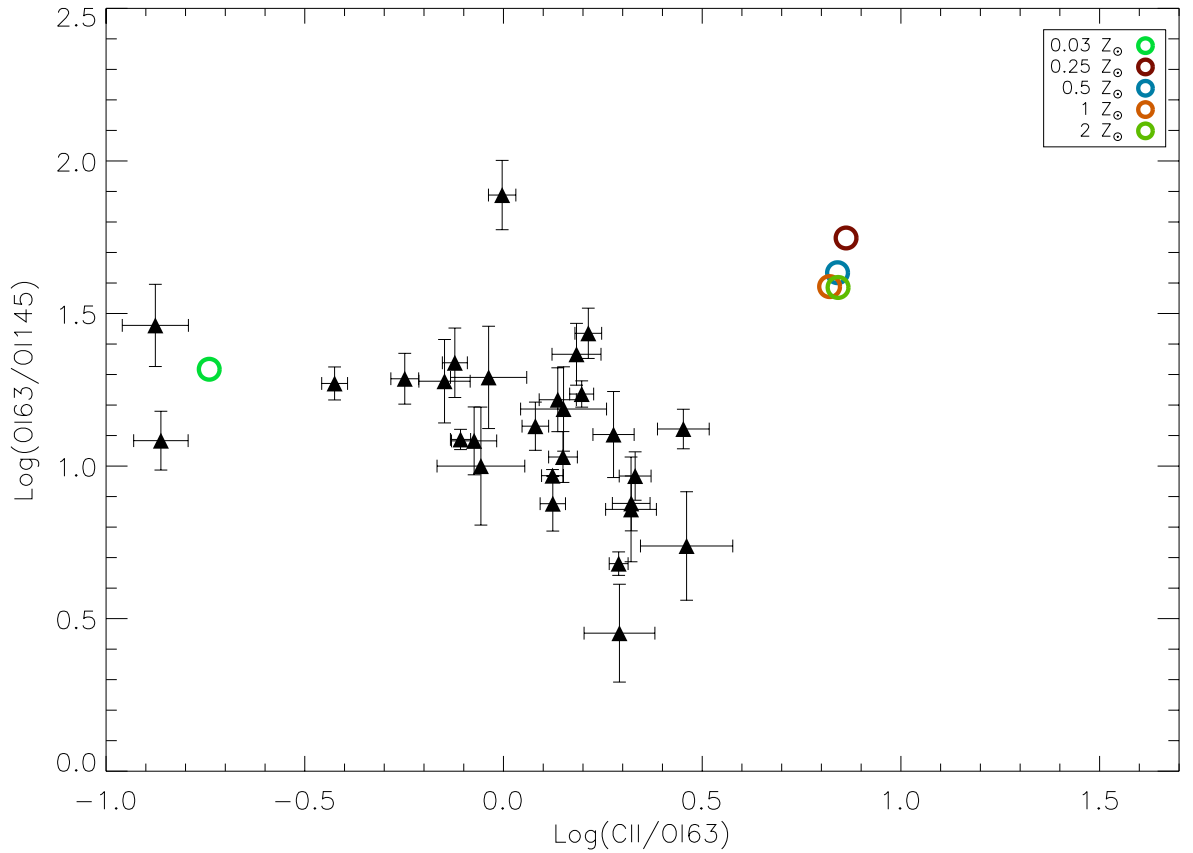


Figure 3.10: Observed [C II]₁₅₈ / [O I]₆₃ versus [O I]₆₃ / [O I]₁₄₅ ratios, with uncertainties, compared to models of differing metallicity, with the C/O ratio adopted to be 0.53 for metallicities of 0.25 and above, but dropping to 0.16 as metallicities decrease to 0.03. The coloured circles represent models with different values of metallicity, ranging from 0.03 (light green circle), 0.25 (claret circle) and 0.5 (light blue circle) up to twice solar metallicity.

potential from C⁺ to C²⁺ is 24 eV, the [C II] 158 μm ²P_{3/2} to ²P_{1/2} line can be formed over a substantial part of a H II region and according to Aannestad & Emery (2003) may contribute up to 1/3 of the total intensity in the line.

More recent work has indicated that approximately 25% of the observed [C II] 158 μm emission may come from ionized regions (Abel 2006). This is particularly true where low-density H II regions are adjacent to PDRs (Heiles 1994; Abel *et al.* 2005; Kaufman *et al.* 2006; Abel *et al.* 2007). This effect can hamper the use of [C II] emission as a pure PDR diagnostic in cases where ionized and PDR emission are observed in a single spectrum. Therefore, the contribution of [C II] emission from the ionized gas must be estimated. Such an estimate requires a separate model of the H II region, although in recent years computational methods exist that

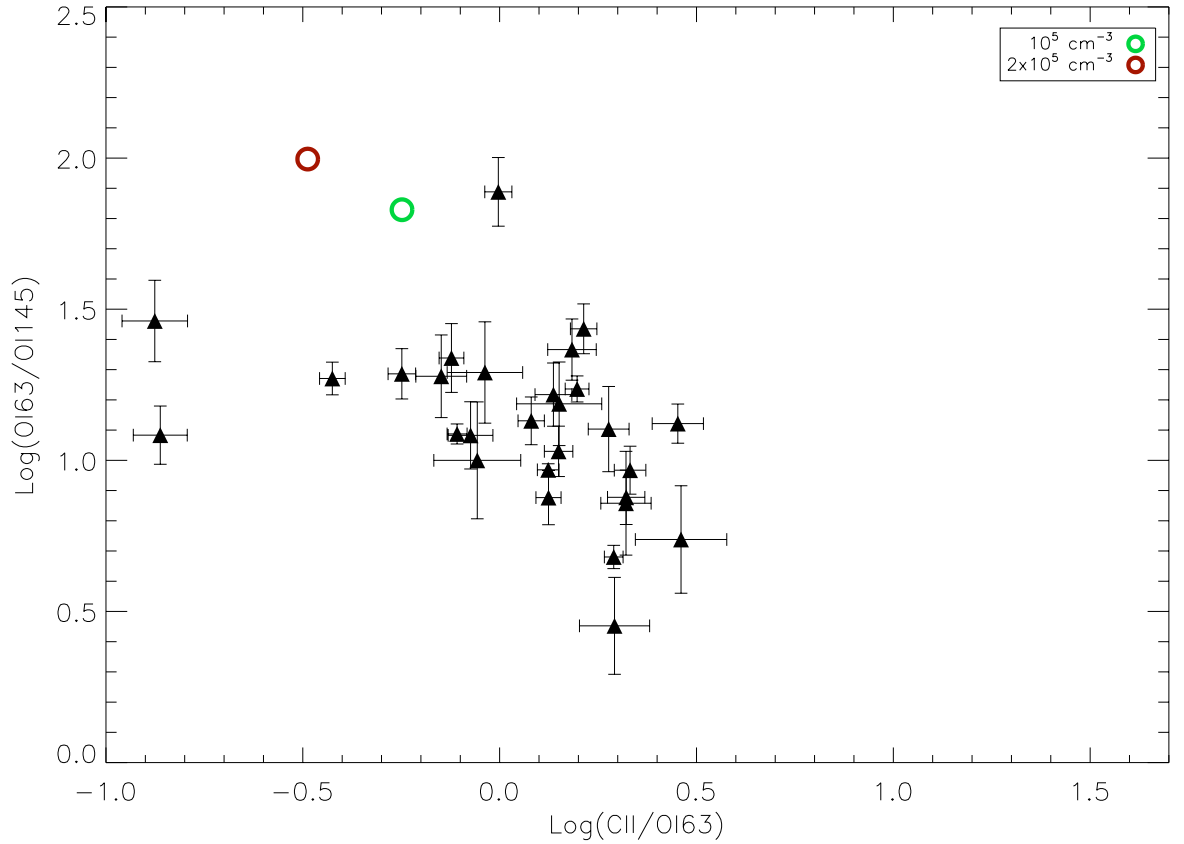


Figure 3.11: Observed $[C II]_{158} / [O I]_{63}$ versus $[O I]_{63} / [O I]_{145}$ ratios, with uncertainties, compared to models of differing densities. The colored points represent models with densities in the range $10^5 \leq n_H \leq 2 \times 10^5 \text{ cm}^{-3}$ decreasing from left to right.

allow the H II region and PDR spectrum to be calculated self-consistently (Abel *et al.* 2005; Kaufman *et al.* 2006). A study of S125 by Aannestad & Emery (2003) found that $\sim 40\%$ of the $[C II]$ and $\sim 20\%$ of the $[O I]$ 63- μm line intensities come from the ionized regions. Therefore, even though $[C II]$ emission is widely observed and is usually optically thin, its dependence on the properties of the H II region can diminish its use as a PDR diagnostic. The possibility that some of the $[C II]$ flux may come from H II regions is not explicitly taken into account by the UCL_PDR models.

While ionized carbon, because of its ionization potential, can be found in both neutral gas and ionized gas clouds, species such as ionized nitrogen, N^+ , requiring an ionization potential of 14.53 eV, can arise only from H II regions. Along with the $[C II]$ 158 μm emission line, the $[N II]$ 122- μm and 205- μm lines are the brightest emission lines contributing to the total far-infrared

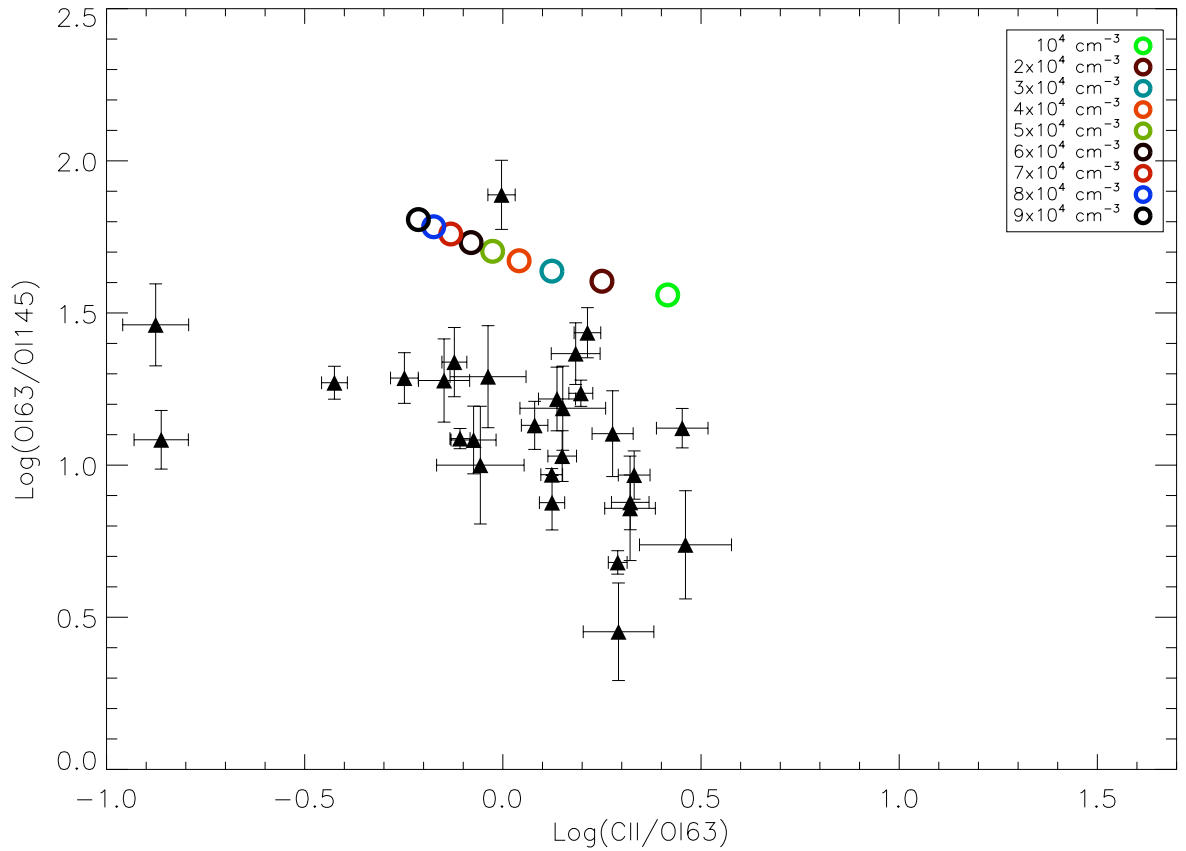


Figure 3.12: Observed $[C II]_{158} / [O I]_{63}$ versus $[O I]_{63} / [O I]_{145}$ ratios, with uncertainties, compared to models of differing densities. The colored points represent models with densities values in the range $10^4 \leq n_H \leq 9 \times 10^4 \text{ cm}^{-3}$, decreasing from left to right.

emission from our Galaxy (Wright *et al.* 1991). The ground state 3P term of the N^+ ion is split into the three $^3P_{2,1,0}$ levels from which the $122 \mu\text{m}$ and $205 \mu\text{m}$ lines arise. Therefore if a predicted H II region value for the $[C II]_{158} / [N II]_{122}$ flux ratio is available, the observed $[N II]_{122}$ - μm flux could be used to indicate the amount of $[C II]_{158}$ - μm emission arising from H II regions that are in the telescope beam.

The COBE FIRAS Galactic Plane spectral measurements yielded an integrated value of $[N II]_{122} / [N II]_{205} = 1.5$ (Wright *et al.* 1991). The same $[N II]_{122} / [N II]_{205}$ flux ratio was measured by Oberst *et al.* (2006) for the Great Carina nebula, which has $N_e \sim 30 \text{ cm}^{-3}$. They used photoionization models for the Carina nebula to estimate $[C II]_{158} / [N II]_{122} = 1.6$ for the H II region. Table 3.5 lists the $[N II]_{122}$ - μm emission line fluxes measured by us from the ISO LWS spectra of 12 out of the 46 sources listed in Table 3.1 that showed a detection, together

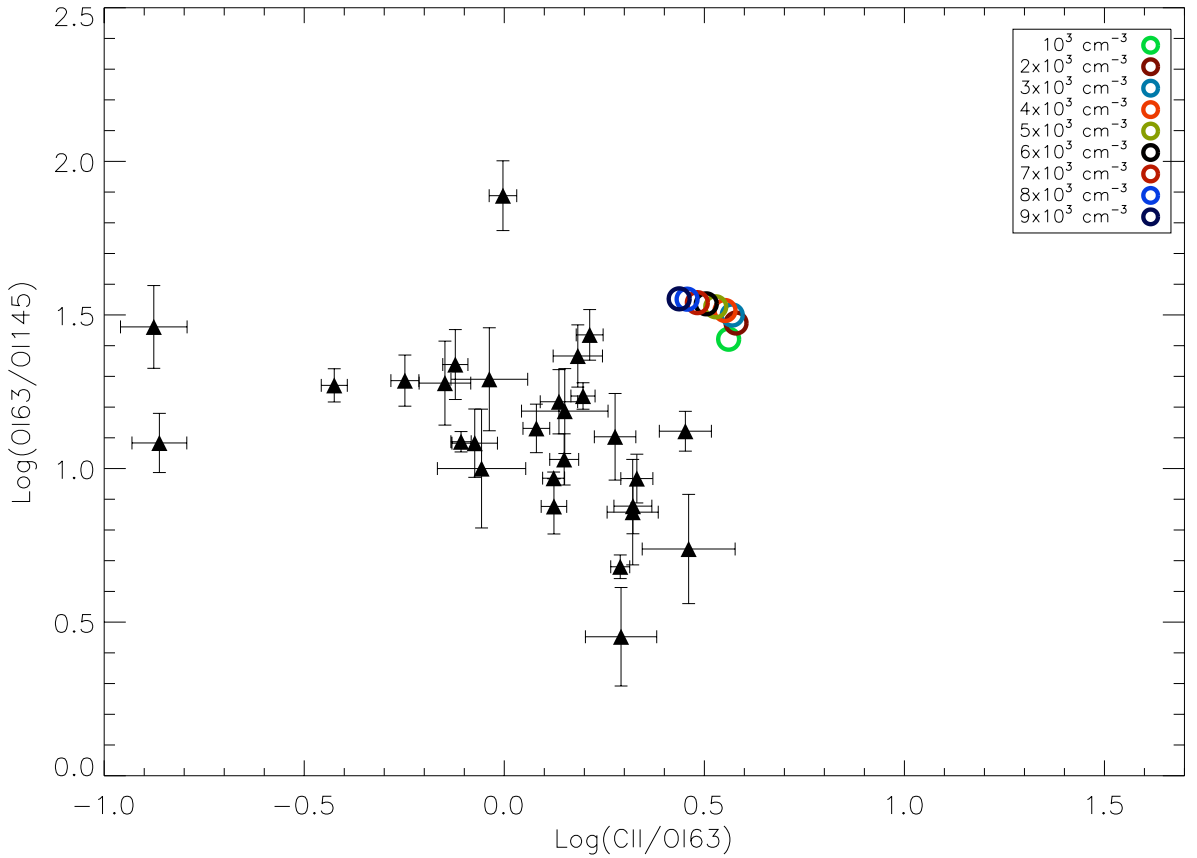


Figure 3.13: Observed $[C II]_{158} / [O I]_{63}$ versus $[O I]_{63} / [O I]_{145}$ ratios, with uncertainties, compared to models of differing densities. The colored points represent models with densities in the range $10^3 \leq n_H \leq 9 \times 10^3 \text{ cm}^{-3}$ decreasing from left to right.

with the relative $[C II]_{158} / [N II]_{122}$ ratios and the estimated percentage of $[C II]_{158}$ coming from the H II region. The 12 sources that have detections of both $[C II]_{158} \mu\text{m}$ and $[N II]_{122} \mu\text{m}$ have mean and median $[C II]_{158} / [N II]_{122}$ flux ratios of 10.2 and 5.9 respectively. A H II region $[C II]_{158} / [N II]_{122}$ ratio of 1.6 implies that H II regions contribute only 16% (mean case) and 27% (median case) of the overall $[C II]_{158} \mu\text{m}$ flux that is observed.

We used the above predicted H II region $[C II]_{158} / [N II]_{122}$ ratio of 1.6 along with the observed $[N II]_{122} \mu\text{m}$ fluxes, to correct the observed $[C II]_{158} \mu\text{m}$ flux of these 12 sources for H II region contributions. In Fig 3.16– 3.17 we overplot our model results, with the same physical parameters used in Fig 3.5– 3.8, on the observations. In Fig 3.17 the observations have been corrected for the predicted H II region contribution to the $158 \mu\text{m}$ fluxes using the measured $[N II]_{122} \mu\text{m}$ fluxes. As shown in Fig 3.17, the model results appears to fit the corrected observations better, compared to Fig 3.5– 3.8, because the observations have been

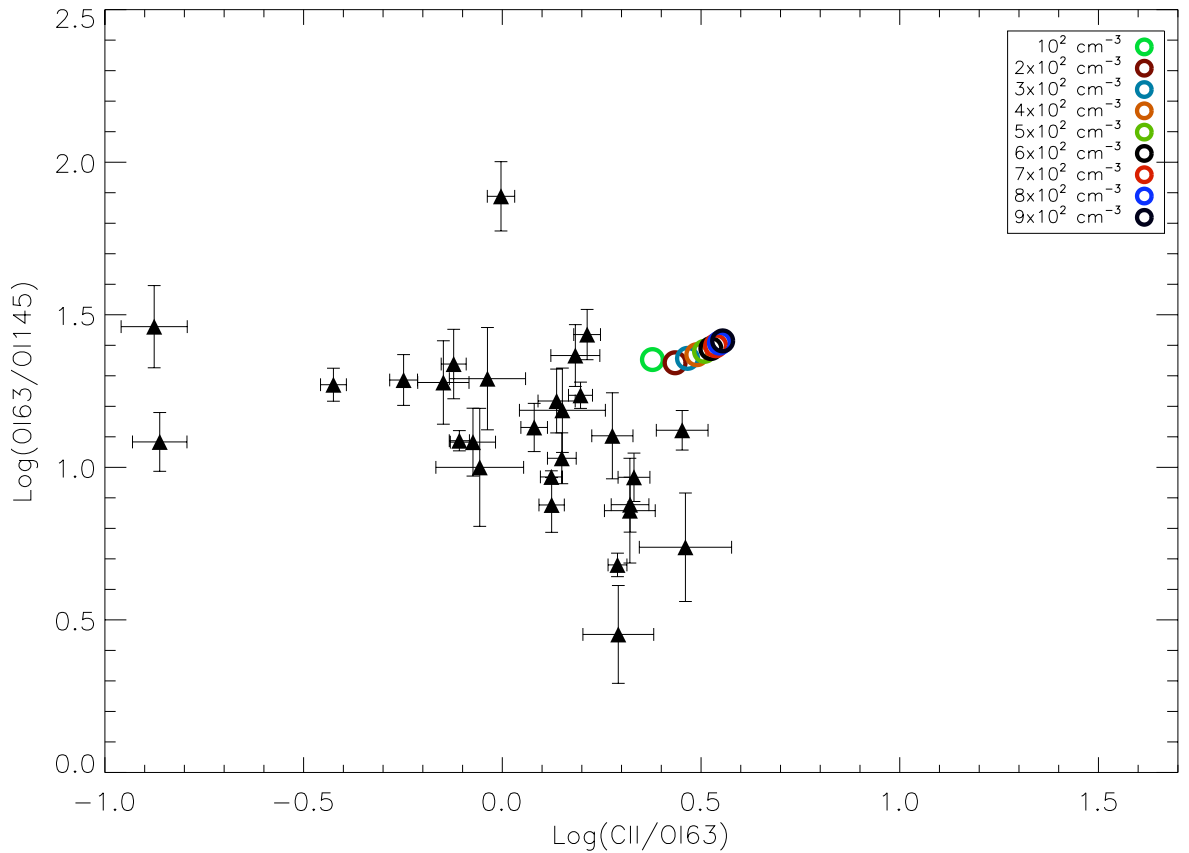


Figure 3.14: Observed $[\text{C II}]_{158} / [\text{O I}]_{63}$ versus $[\text{O I}]_{63} / [\text{O I}]_{145}$ ratios, with uncertainties, compared to models of differing densities. The colored points represent models with densities values in the range $10^2 \leq n_H \leq 9 \times 10^2 \text{ cm}^{-3}$, decreasing from right to left.

shifted to lower values of $[\text{C II}]_{158} / [\text{O I}]_{63}$. The remaining discrepancy is attributed to $[\text{O I}]_{63}$ - μm self-absorption, as discussed in Section 3.5 below.

3.5 Fitting the observations

The clear discrepancy between the location of the observations and our models in Figures 3.13 and 3.14 can at least be partly attributed to self absorption in the $[\text{O I}]_{63}$ - μm line. This is consistent with what Liseau *et al.* (2006) found: namely that $\sim 65\%$ of observed $[\text{O I}]_{63} / [\text{O I}]_{145}$ emission line ratios from Milky Way PDRs are lower than can be explained by current models, which they attributed to optical depth effects in the $[\text{O I}]_{63}$ - μm line. They partially attributed the low observed ratios to absorption by cold foreground O^0 in front of the 63 - μm -emitting region, although other explanations such as very optically thick $[\text{O I}]$ line emission could not be

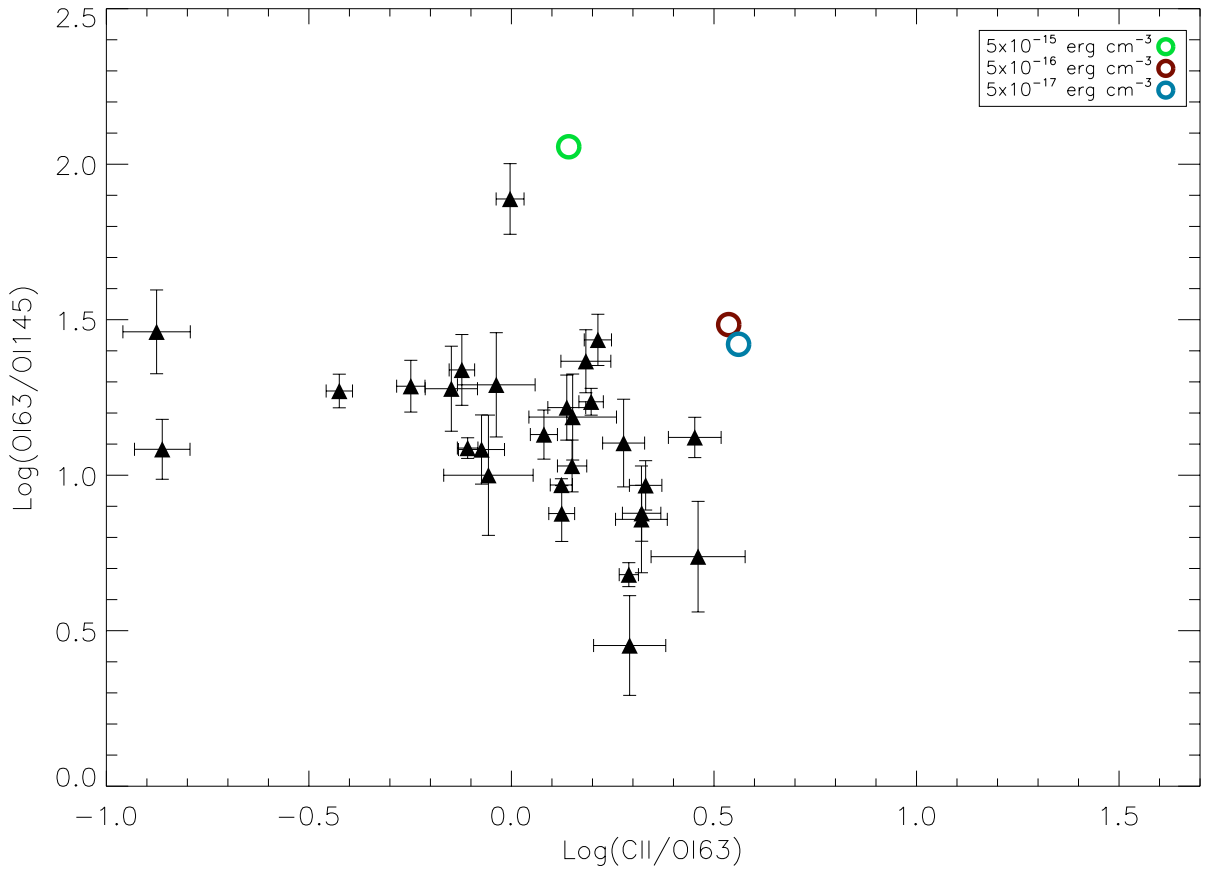


Figure 3.15: Observed $[C II]_{158} / [O I]_{63}$ versus $[O I]_{63} / [O I]_{145}$ ratios, with uncertainties, compared to models with differing cosmic ray ionization rates. The coloured circles represents models with cosmic ray ionization rates of $\zeta = 5 \times 10^{-15} \text{ s}^{-1}$ (green circle), $\zeta = 5 \times 10^{-16} \text{ s}^{-1}$ (claret circle) and $\zeta = 5 \times 10^{-17} \text{ s}^{-1}$ (blue circle).

ruled out.

The overall conclusion of Liseau *et al.* (2006) was that because this ratio depends sensitively on models, $[O I]$ emission has a limited diagnostic value. In fact most PDR models calculate the emergent flux from a plane-parallel slab of gas illuminated from one side. A galaxy has many PDRs at all orientations, and optical depth effects are non-negligible. In the approximation that the densest PDRs correspond to the shells of molecular clouds and that the $[C II]$ line emission and far-IR dust continuum emission are optically thin, while the $[O I]$ 63- μm line is optically thick, then the $[O I]$ 63- μm line will be seen only from the front side of each cloud while the $[C II]$ line arises from both the front and the rear sides. The velocity dispersion from cloud to cloud, however, allows most $[O I]$ 63- μm photons that have escaped their parent cloud to escape

Table 3.5: Line flux measurements, in units of $10^{-14} \text{ W m}^{-2}$, for extragalactic sources with ISO-LWS detections of the [N II] 122- μm emission line, together with the observed $[\text{C II}]_{158}/[\text{N II}]_{122}$ flux ratio. Column 1 is the index number from Table 3.1.

Index	Source	TDT No. of Observation	[N II] 122 μm	$[\text{C II}]_{158}$ [N II] ₁₂₂	$[\text{C II}]_{158}$ from H II
3	NGC 253	56901708	1.72 ± 0.18	2.7 ± 0.4	$\sim 60\%$
5	Maffei 2	85800682	0.188 ± 0.014	5.7 ± 0.7	$\sim 28\%$
6	NGC 1068	60500401	0.356 ± 0.026	5.3 ± 0.6	$\sim 30\%$
10	NGC 1614	85501010	0.021 ± 0.004	9.7 ± 2.5	$\sim 17\%$
11	NGC 2146	67900165	0.152 ± 0.006	16.3 ± 6.4	$\sim 10\%$
13	M 82	65800611	2.20 ± 0.17	5.9 ± 0.6	$\sim 27\%$
18	NGC 4039/9	25301107	0.0468 ± 0.0049	8.08 ± 1.09	$\sim 20\%$
26	Cen A	63400464	0.170 ± 0.019	16.2 ± 2.4	$\sim 10\%$
27	NW Cen A	45400151	0.097 ± 0.011	28.8 ± 5.7	$\sim 5.5\%$
28	M 51	35100651	0.228 ± 0.027	4.2 ± 0.7	$\sim 38\%$
29	M 83	64200513	0.231 ± 0.066	5.2 ± 1.7	$\sim 31\%$
30	Circinus	10401133	0.213 ± 0.019	12.2 ± 1.5	$\sim 13\%$

the galaxy entirely. This scenario implies that we should observe only a fraction of the [O I] flux and all of the [C II] flux expected from PDR models (Malhotra *et al.* 2001).

The observed $[\text{C II}]_{158}/[\text{O I}]_{63}$ and $[\text{O I}]_{63}/[\text{O I}]_{145}$ ratios, in the selected range, do not appear to be traced properly by our UCL_PDR model results although there is a common trend in the behaviour of these ratios, indicating that the observations are off-set compared to our model results. At first glance the model in Fig 3.8, where we varied the radiation field strength, appears to show the best fit to the observations. However, taking into account the effects of [O I] self-absorption and the [C II] contribution from H II regions, the models in Fig 3.7 could also probably provide a fit to the observations. In fact both these effects would shift the models downwards and to the right relative to the observations. A similar trend could be found when we varied the density. Although at first glance the models in Fig 3.12 do not appear to show a good fit to the observations, if one takes into account the effects of [O I]₆₃ self-absorption, which will shift observations downwards and to the left relative to the models, due to the decrease in the [O I] 63- μm flux, these models will probably provide a better fit to the observations. The

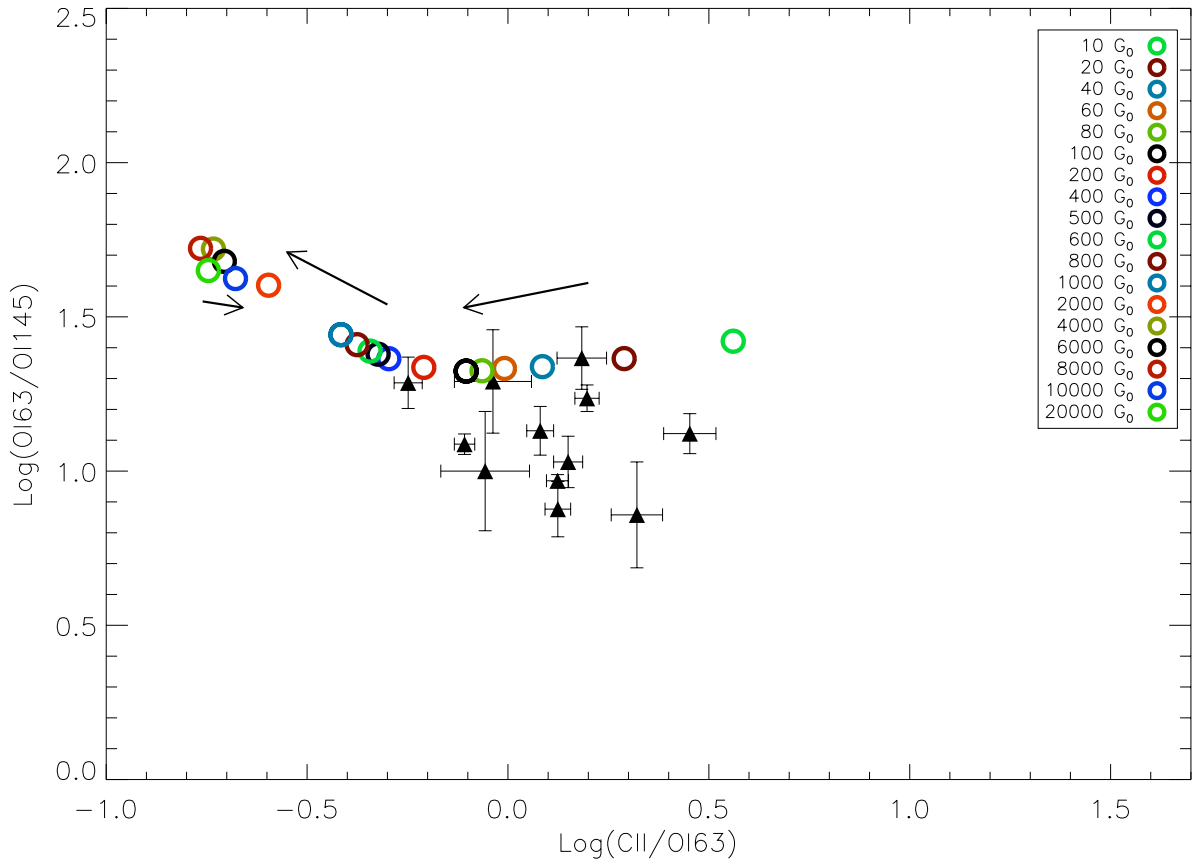


Figure 3.16: Observed $[\text{C II}]_{158} / [\text{O I}]_{63}$ versus $[\text{O I}]_{63} / [\text{O I}]_{145}$ ratios, with uncertainties. The observations do not take into account the likely percentage of $[\text{C II}]$ coming from H II regions. The coloured points represent represent models with radiation field strengths in the range $10 \leq G_0 \leq 2 \times 10^4$ and the arrows indicate the direction of the increase of radiation field strength.

models will be shifted downwards and to the right relative to the observations. Unfortunately the results obtained varying the cosmic ray ionization rate and the metallicity suggest that the $[\text{C II}]_{158} / [\text{O I}]_{63}$ versus $[\text{O I}]_{63} / [\text{O I}]_{145}$ ratio is not a good tracer for these parameters. We identified the best parameter values of our source sample as $10^4 \leq n_H \leq 9 \times 10^4 \text{ cm}^{-3}$ and $60 \leq G_0 \leq 8 \times 10^2$, $A_v = 10$. These values were chosen while taking into account the effects of absorption in the $[\text{O I}]$ 63- μm line and the contribution to $[\text{C II}]$ 158- μm from H II regions.

3.5.1 $[\text{O I}]$ 63- μm self-absorption

The intensity of the $[\text{O I}]$ 63 μm line can be suppressed through self-absorption (e.g. González-Alfonso *et al.* 2004). The $^3\text{P}_1$ state, the upper level of the $[\text{O I}]$ 63- μm line, is 228 K above

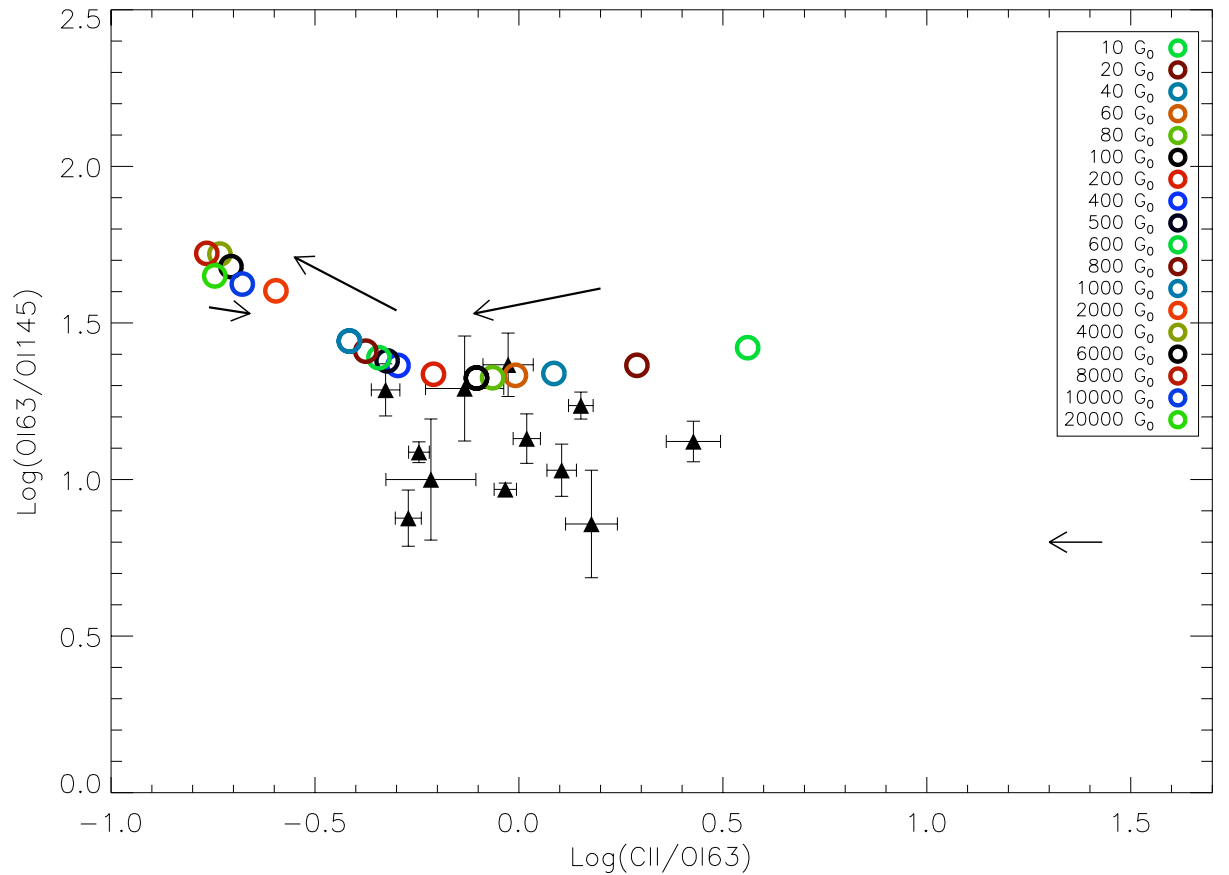


Figure 3.17: Observed $[\text{C II}]_{158} / [\text{O I}]_{63}$ versus $[\text{O I}]_{63} / [\text{O I}]_{145}$ ratios, with uncertainties. In the observations the estimated contribution to the $[\text{C II}]$ flux is taken into account for each source. The coloured points represent represent models with radiation field strengths in the range $10 \leq G_0 \leq 2 \times 10^4$ and the arrows indicate the direction of the increase of radiation field strength. The arrow corresponds to the median shift in the $[\text{C II}]_{158} / [\text{N II}]_{122}$ ratio, corresponding to 27% of the $[\text{C II}]$ emission originating from H II regions.

the ground state and its critical density is $n_{crit} = 4.7 \times 10^5 \text{ cm}^{-3}$ (Tielens & Hollenbach 1985). Because of this, at typical interstellar cloud temperatures all oxygen atoms occupy the lowest level of their ground state, with $J=2$. This means that $[\text{O I}]$ 63- μm emission, originating from collisional excitation in a warm medium, could be absorbed by the abundant reservoir of ground state neutral oxygen that exists within the galaxy along the line of sight. The 63- μm line can also be absorbed by cold foreground material but this is less likely in the case of a face-on galaxy, where the neutral oxygen column density will be less along the line of sight than for an edge-on galaxy. For our sample of sources the majority are not edge-on galaxies, therefore we attribute most of the suppression of the $[\text{O I}]$ 63- μm line to self-absorption in the PDRs in

which the emission is excited.

3.5.1.1 The [O I] 63- μ m line profile

In an attempt to investigate the effect of [O I] 63- μ m self-absorption on the observations we have developed a new version of the Spherical Multi-Mol code (SMMOL, Rawlings & Yates 2001). Originally SMMOL only considered a sphere of material illuminated by the standard ISRF at the outer boundary of the sphere: we have now implemented the ability to insert a central illuminating source with an arbitrary SED. SMMOL uses an accelerated Λ -iteration (ALI) method to solve multilevel non-LTE radiative transfer problems of gas inflow and outflow. The code computes the total radiation field and the level populations self-consistently. At each radial point, SMMOL generates the level populations, the line source functions and the emergent spectrum from the cloud surface. This can then be convolved with the appropriate telescope beam. A detailed description of the SMMOL radiative transfer model can be found in the appendix of Rawlings & Yates (2001). The coupling between the UCL_PDR code and the radiation transfer code has been performed through an interface ¹ that will be presented in a forthcoming paper (Bayet et al. 2010, in prep). We used the physical parameters from one of the UCL_PDR models² and we chose an arbitrary distance of 3.2 Mpc for the clouds modeled. In Fig 3.18– 3.19 we show the SMMOL [O I] emission line profiles for a PDR with a diameter of 20 pc and a PDR with a diameter of 5 pc respectively. In Fig 3.18 and Fig 3.19 the effect of self-absorption is clearly seen in the [O I]_{63 μ m} line profile (solid line) while there is no trace of self-absorption in the [O I]_{145 μ m} line profile (dotted line). The [O I]_{63 μ m} emission line is still significantly brighter than the [O I]_{145 μ m} emission line, consistent with current observations. The line profile from a single 20 pc GMC exhibits extremely strong [O I] 63- μ m self-absorption. Without self-absorption in the [O I] 63- μ m line, the 63/145 flux ratio would be 46.2. With self-absorption, the flux ratio is found to be 8.5, a reduction of 0.73 dex. The effect is smaller for the 5 pc model; the 63/145 flux ratio is reduced from 12.6 to 7.9, i.e. by 0.20 dex. The $\log(63/145) \sim 0.9$ flux ratios predicted by both SMMOL models are in reasonable agreement with the observed ratios in e.g. Fig 3.17. Although our 20 pc and 5 pc diameter SMMOL models produce similar final 63- μ m and 145- μ m fluxes, their relative masses (1.0×10^5 and $1.6 \times 10^3 M_{\odot}$, respectively) would seem to make an ensemble of the smaller clouds more

¹See website: [https://www.astro.uni-koeln.de/projects/schilke/sites/www.astro.uni-koeln.de.projects.schilke/files/Viti_Cologne09.pdf](https://www.astro.uni-koeln.de/projects/schilke/sites/www.astro.uni-koeln.de/projects/schilke/files/Viti_Cologne09.pdf)

²Model result listed in Fig 3.7: $\zeta=5 \times 10^{-17} \text{ s}^{-1}$, 10^3 cm^{-3} , $Z/Z_{\odot}=1$, $200G_0$ and $t=10^7 \text{ yrs}$ (red circle).

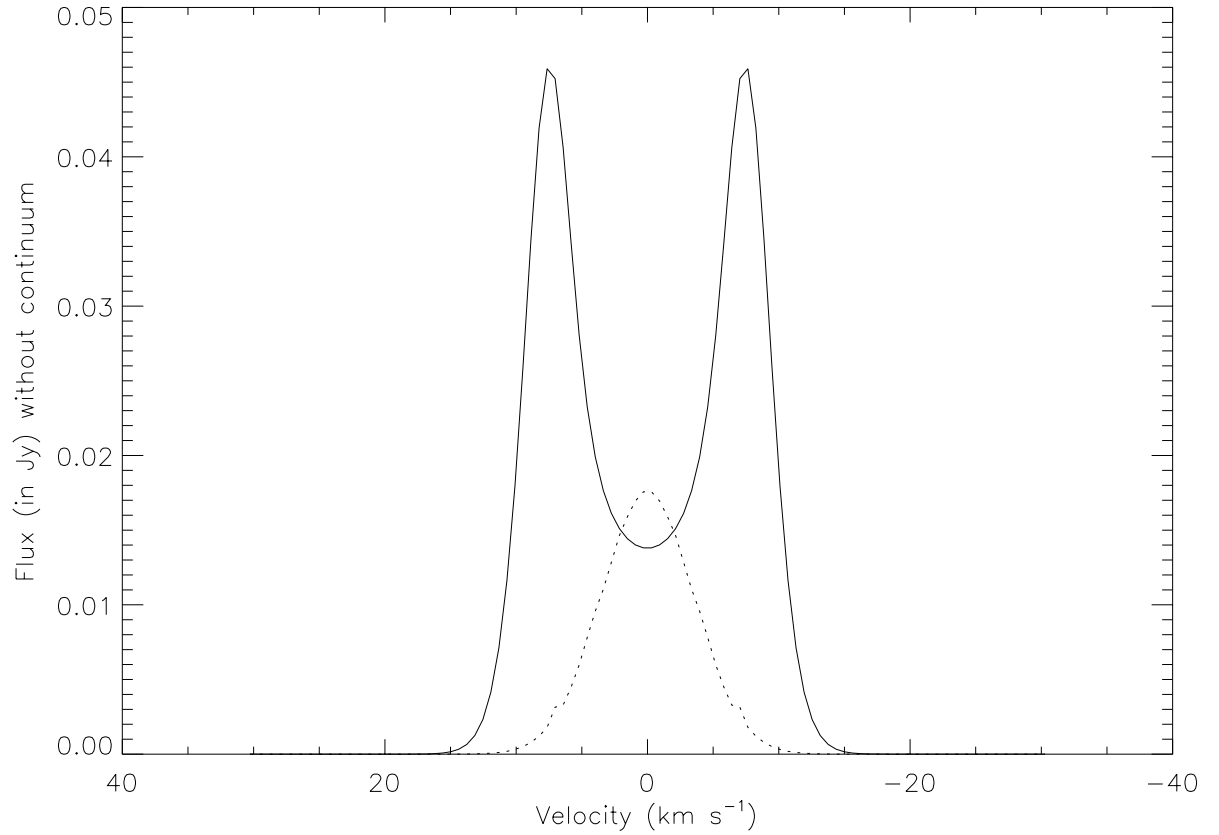


Figure 3.18: Theoretical oxygen line profiles produced from a 20 pc GMC, observed at a distance of 3.2 Mpc. The dotted line represents the $[\text{O I}]_{145\mu\text{m}}$ emission line profile and the solid line represents the $[\text{O I}]_{63\mu\text{m}}$ emission line profile. The physical parameters of the UCL_PDR model used for modeling the oxygen line profiles were $\zeta=5\times 10^{-17}\text{s}^{-1}$, $n_H=10^3\text{cm}^{-3}$, $Z/Z_\odot=1$, $200G_0$ and $t=10^7$ yrs.

plausible for matching the observed ratios.

Note that although all profiles in Fig 3.18– 3.19 have been modeled with the same physical parameters, the difference between the two $[\text{O I}]_{63\mu\text{m}}$ emission line profiles is due to the difference between the inner and outer temperatures of the two clouds. The 20 pc GMC is approximately 100 K cooler than the 5 pc GMC at the centre. This is because the 20 pc GMC extends to $A_v=19$ mag, while the 5 pc GMC has a visual extinction of ~ 5 mags. These differences account for the much stronger $[\text{O I}]_{63\mu\text{m}}$ self-absorption in Fig 3.18. The $[\text{O I}]_{145\mu\text{m}}$ line, on the other hand, is approximately the same for both GMCs.

In order to qualitatively understand the behaviour of $[\text{O I}]_{63\mu\text{m}}$ self-absorption in PDRs, we investigated its sensitivity to variations in the density and radiation field strength. In Fig 3.20

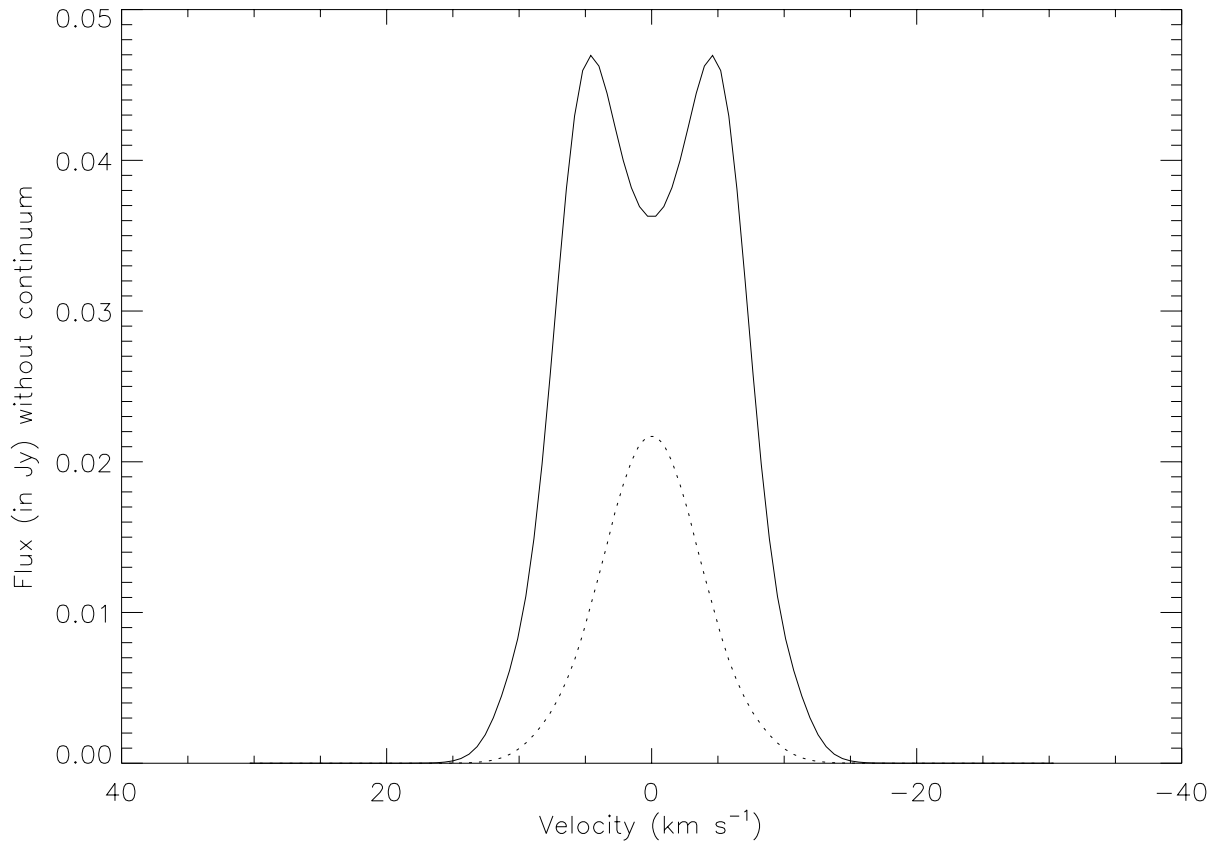


Figure 3.19: Theoretical oxygen line profiles produced from a 5pc GMC, observed at a distance of 3.2 Mpc. The dotted line represents the $[\text{O I}]_{145\mu\text{m}}$ emission line profile and the solid line represents the $[\text{O I}]_{63\mu\text{m}}$ emission line profile. The physical parameters of the UCL_PDR model used for modeling the oxygen line profiles were $\zeta=5\times 10^{-17}\text{s}^{-1}$, $n_H=10^3\text{cm}^{-3}$, $Z/Z_\odot=1$, $200G_0$ and $t=10^7\text{yrs}$.

and Fig 3.21 we reproduce the $[\text{O I}]_{63}$ emission line profile increasing the radiation field strength and the density by an order of magnitude with respect to the previous model (See footnote 1). We find that an order of magnitude increase in the radiation field strength causes the inner and outer temperatures to be twice as high as those in the models plotted in Fig 3.18– 3.19. This produces a higher flux and an increase in self-absorption in the $[\text{O I}]_{63\mu\text{m}}$ line. Increasing the density by one order of magnitude causes an increase in the optical depth of the cloud, so that the degree of $[\text{O I}]_{63\mu\text{m}}$ self-absorption is larger than in Fig 3.19, while the overall flux is reduced by an order of magnitude. We underline here that we are not attempting to model the actual line profiles that may be exhibited by these galaxies: in order to do so one would need to consider density gradients, multiple sources and the geometry of the galaxy. Our theoretical line

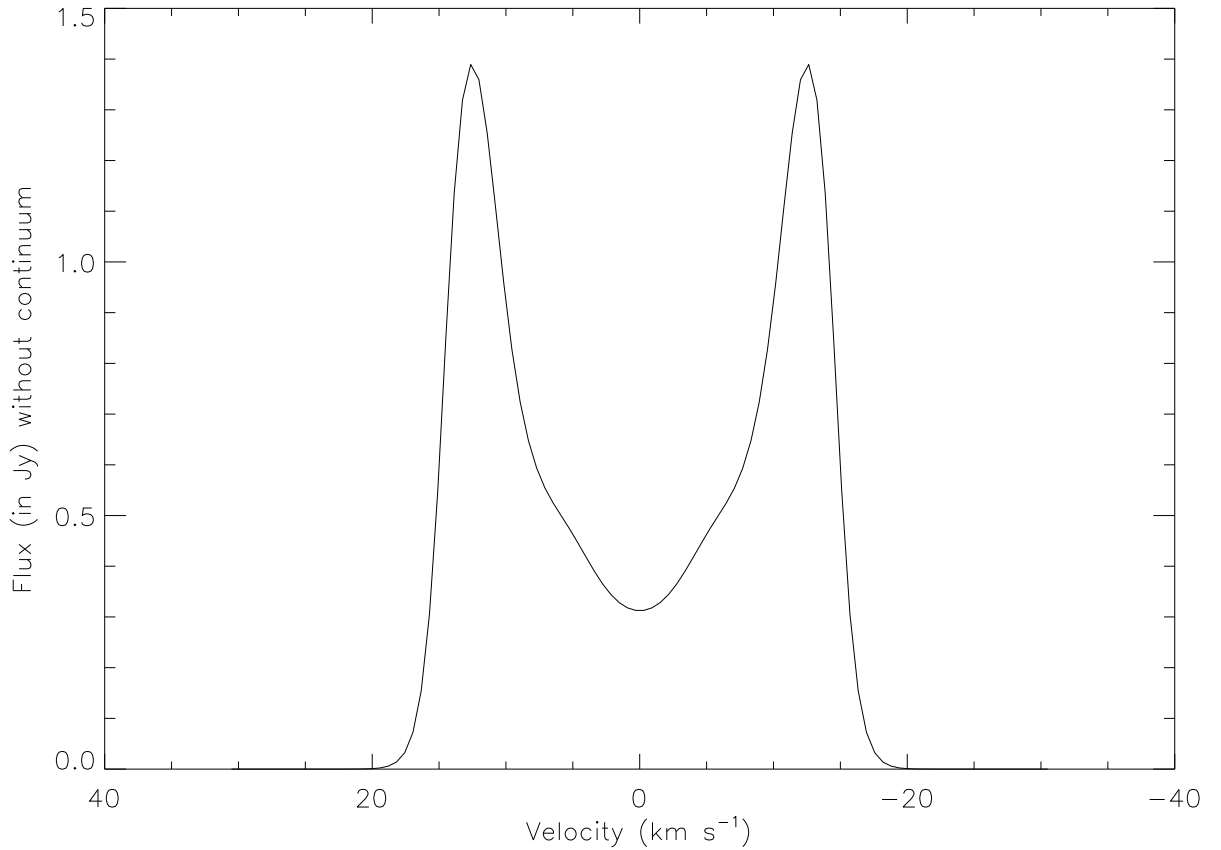


Figure 3.20: Theoretical $[\text{O I}]_{63\mu\text{m}}$ emission line profile produced from a 5pc GMC, observed at a distance of 3.2 Mpc. The physical parameters of the UCL_PDR model used for modeling the oxygen line profiles were: $\zeta=5\times 10^{-17}$, $n_H=10^3 \text{ cm}^{-3}$, $Z/Z_\odot=1$ and $2000G_0$, $t=10^7$ yrs.

profiles simply demonstrate the effect of the initial conditions on the degree of self-absorption in the $[\text{O I}]_{63\mu\text{m}}$ line.

The $[\text{O I}]_{63/145}$ flux ratios predicted by our SMMOL models shift them downwards by 0.2-0.7 dex relative to the UCL_PDR predictions, bringing them into quite good agreement with the observed ratios plotted in Fig 3.16– 3.17. However, allowance for the 0.2-0.7 dex reduction in the $[\text{O I}]_{63-\mu\text{m}}$ line strength caused by self-absorption would also move the UCL_PDR $[\text{C II}]/[\text{O I}]_{63\mu\text{m}}$ model ratios in those figures to larger values. We ran SMMOL for the case of C^+ and we found (see Fig 3.22), as expected, that the $[\text{C II}]_{158\mu\text{m}}$ emission line profile did not show self-absorption in any of the models. However, the $[\text{C II}]$ line is relatively easy to excite, so that the line can efficiently cool the warm neutral gas. Depending on the density in this layer, the line may be self-absorbed. Recently, studies of many bright galaxies showed that the $[\text{C II}]_{158}$ line is deficient compared to the total FIR luminosity. Non detection or weak detection have

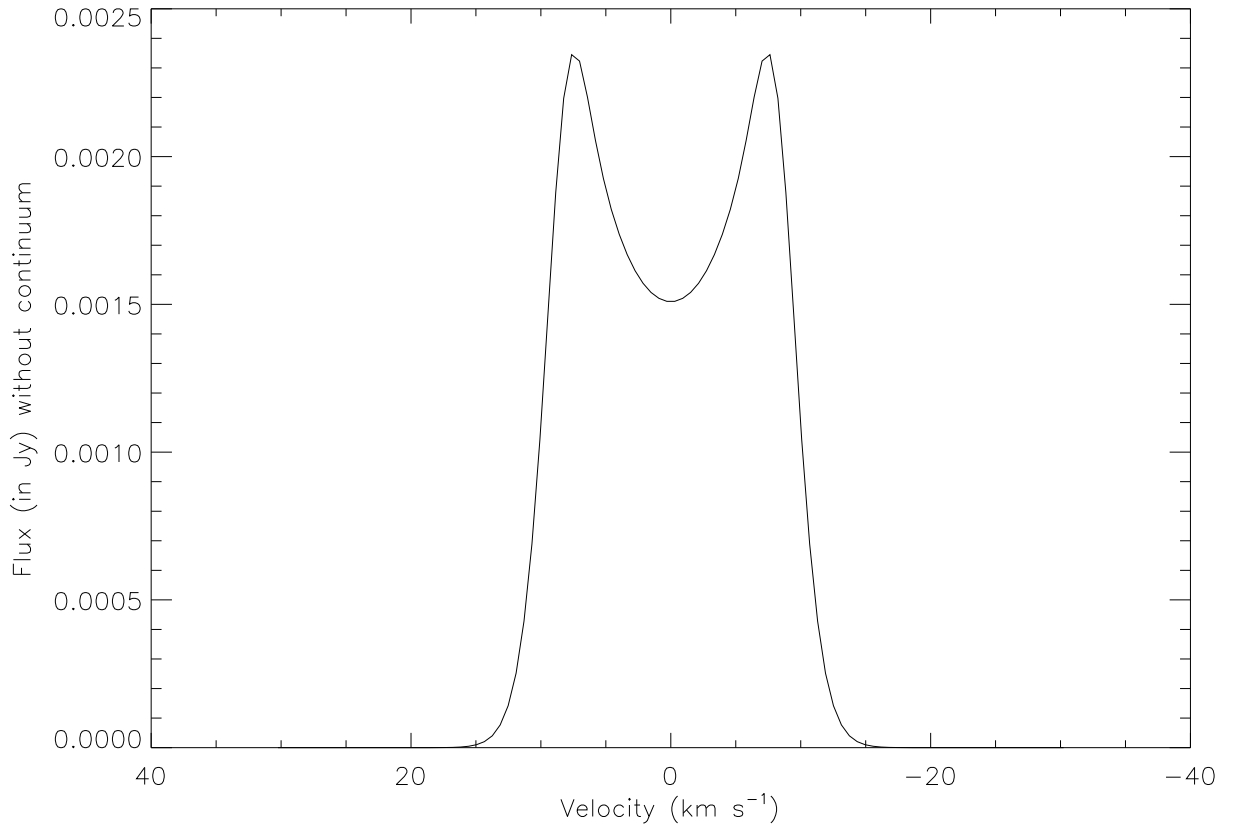


Figure 3.21: Theoretical $[\text{O I}]_{63\mu\text{m}}$ emission line profile produced from a 5pc GMC, observed at a distance of 3.2 Mpc. The physical parameters of the UCL_PDR model used for modeling the oxygen line profiles were: $\zeta=5\times 10^{-17}$, 10^4 cm^{-3} , $Z/Z_{\odot}=1$ and $200G_0$, $t=10^7$ yrs.

been highlighted toward FIR bright galaxies (see Luhman *et al.* 2003; Malhotra *et al.* 2001). However the decrement in C^+ luminosity within the LWS resolution element can be due to absorption by ISM material at different velocities. In fact, the spectra could reveal both emission and absorption components present in the C^+ profile. This strengthens the idea that under certain conditions the C^+ line could be optically thick in the direction of large star-forming complexes or in the nuclei of galaxies (see Vastel *et al.* 2002; Polehampton *et al.* 2005).

In summary, we find that 20-80% of the intensity of the $[\text{O I}]_{63\mu\text{m}}$ line can be suppressed through absorption, with the percentage depending strongly on the physical parameters of the PDR region. Comparing with the model trends shown in Fig 3.17, it would seem that a combination of high radiation field strengths and allowance for $[\text{O I}]_{63\mu\text{m}}$ self-absorption could provide the best match to the observed line ratios. $[\text{O I}]$ line profile observations from the *PACS Herschel Space Observatory* should allow a greater degree of discrimination amongst

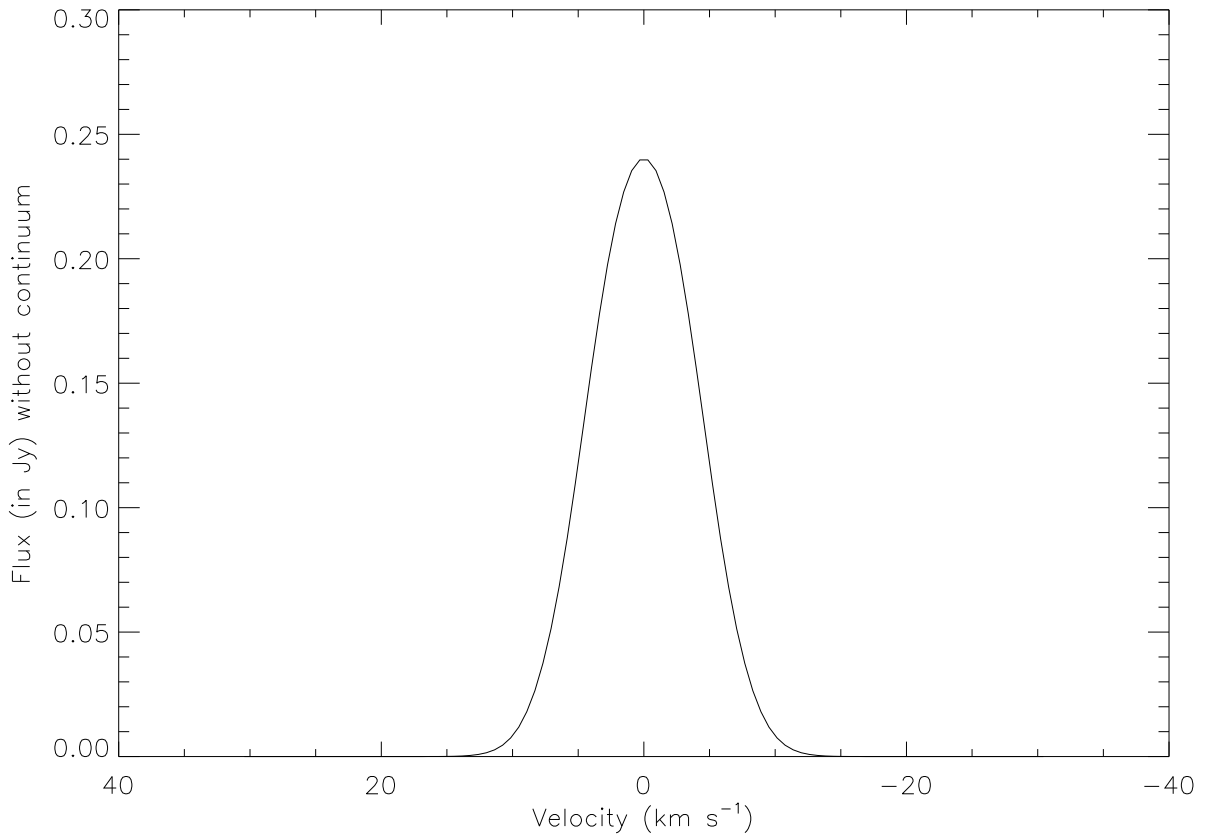


Figure 3.22: Theoretical ionized carbon line profile produced from a 5pc GMC, observed at a distance of 3.2 Mpc. The solid line represents the $[\text{C II}]_{158\mu\text{m}}$ emission line profile. The physical parameters of the UCL_PDR model used for modeling the ionized carbon line profiles were $\zeta=5\times 10^{-17}\text{s}^{-1}$, $n_H=10^3\text{ cm}^{-3}$, $Z/Z_\odot=1$, $200G_0$ and $t=10^7$ yrs.

possible models.

3.6 Conclusions

To fit the observed $[\text{C II}]_{158\mu\text{m}}$, $[\text{O I}]_{63\mu\text{m}}$ and $[\text{O I}]_{145\mu\text{m}}$ emission line fluxes for 28 extragalactic sources, measured from archival ISO-LWS spectra, we used a grid of 1702 PDR models from the UCL_PDR code spanning a large range of densities, radiation field strengths, metallicities and cosmic ray ionization rates. We took into account the contribution to the observed $[\text{C II}]$ fluxes from H II regions, using expected $[\text{C II}]_{158}/[\text{N II}]_{122}$ ratios for H II regions to correct the $[\text{C II}]_{158}$ fluxes of the 12 sources that had $[\text{N II}]_{122}$ μm detections.

We found that the best fitting PDR models had $10^4 \leq n_H \leq 9 \times 10^4\text{ cm}^{-3}$ and $60 \leq G_0 \leq 8 \times 10^2$.

Consistent with the conclusions of Liseau *et al.* (2006), we found that the persistent discrepancy between the observed and modelled line flux ratios can at least partly be attributed to self-absorption in the [O I] 63- μm line. We used the SMMOL code to predict oxygen emission line profiles for several PDR models and found clearly self-absorbed [O I] 63- μm profiles, with 20-80% of the intensity suppressed, depending on the physical parameters of the PDR regions. A combination of high radiation field strengths and [O I] self-absorption would appear to provide the best explanation for the observed [C II] 158 μm , [O I] 63 μm and [O I] 145 μm line flux ratios.

MODELLING NGC 4038: AN ATTEMPT AT A UNIFIED MODEL.

In this chapter I will present an attempt to model one of the nuclei of the Antennae starburst galaxy, NGC 4038, using the ionization MOCASSIN code, the photodissociation UCL_PDR code, an interface between the two and SMMOL. The selected NGC 4038 galaxy was chosen between a sample of starburst galaxies after measuring their electron densities using the $[OIII] 52\mu m/[OIII] 88\mu m$ ratio.

The aim of this project is to continue with the study of the far infrared fine structure emission lines analysed in the previous chapter. The contribution of $[C II] 158 \mu m$, $[O I] 63$ and $145 \mu m$ coming from the H II region will be studied using the 3D ionization MOCASSIN code. Subsequently, the computed radiation field at the ionization front, which links the H II and the PDR regions, will be used as an input for the UCL_PDR code. Similarly to the previous chapter, I will investigate the oxygen self absorption by computing the emission line profiles using the SMMOL code and compare the CO emission rotational lines with observations. However, due to lack of time, this work is still ongoing. Future developments will involve more PDR runs spanning a different range of densities and metallicities.

4.1 Starburst galaxy sample

Observations of gas-phase atoms and molecules in galaxies allow us, in principle, to study the physical characteristics of environments that are quite different from those found in our own Galaxy, e.g. lower abundances of heavy elements, stronger radiation fields, etc. However, one

of the difficulties in observing molecular species in even the nearest galaxies is that the lines are quite weak, which limits one to observing only the most abundant species and only a few lines from each species. There is growing evidence that the properties of the molecular gas in the nuclei of starburst galaxies may be very different from those seen in Galactic star forming regions and that a high kinetic temperature in the molecular gas may lead to a non-standard initial mass function in the next generation of stars (Spinoglio & Malkan 1992). Burst of star formation (called Starburst) consumes much faster the gas reservoir than in a normal spiral quiet galaxy. As a consequence, the star formation rate (SFR) is much higher and the gas depletion time scale is shorter. Essentially to ignite a starburst, it is necessary to concentrate a large amount of cool molecular gas in a small volume. Such concentrations and perturbations are strongly suspected to cause global starburst phenomena in major galaxy mergers, although the exact mechanisms are not fully understood. Bursts of massive star formation can dramatically alter the structure of their host galaxies by injecting large amounts of energy and mass into the ISM via strong stellar winds and repeated supernova explosions.

In the next section the electric density, n_e , of this sample of starburst galaxies will be computed using far infrared oxygen emission lines. Starbursts can occur in disk galaxies, and irregular galaxies often exhibit knots of starburst, which can be spread throughout the gas.

Examples of starburst galaxies are: Blue compact galaxies (BCGs), these galaxies are often low mass, low metallicity, dust-free objects; Luminous infrared galaxies (LIRGs) or Ultra-luminous Infrared Galaxies (ULIRGs), these galaxies are generally extremely dusty objects; Wolf-Rayet galaxies, galaxies where a large portion of the bright stars are Wolf-Rayet stars (WR). Infrared photometry and later infrared spectroscopy provide powerful diagnostics to distinguish between the main emission mechanisms in Starburst galaxies.

Starburst galaxies are characterized by uncommonly high star formation efficiencies (i.e. $SFE = M_{gas}/SFR$), but it remains unclear what physical conditions in the molecular gas produce this high efficiency. Invariably, high star formation efficiency is associated with high column densities of molecular material (e.g the Kennicutt-Schmidt law Schmidt 1959; Kennicutt 1998). Much of the interest in starburst galaxies arises from the fact that some galaxies, and often very small regions within their nuclei, manage to effectively convert a large amount of gas into stars in a very short time. Often there is plenty of molecular gas (observed via CO emission), so it is not a fuelling question so much as a collection puzzle.

It is important to take advantage of the bright emission lines in these types of galaxies in order to investigate the mechanisms that are taking place in the regions where these lines are found.

Table 4.1: Line flux measurements, in units of 10^{-14} W m $^{-2}$, for a selection of extragalactic starburst sources, taken from the galaxy sample studied in the previous Chapter (see Table 3.1), with ISO-LWS detections of all 3 FIR fine structure emission lines of [C II] and [O I]. For each source, our own line flux measurements are listed.

Index	Source	Radial Vel (km s $^{-1}$)	[CII] 158 μ m	[OI] 63 μ m	[OI] 145 μ m
1	IC 10	-348	0.966 \pm 0.034	0.591 \pm 0.025	0.0217 \pm 0.0032
2	NGC 253	243	4.618 \pm 0.126	3.47 \pm 0.16	0.461 \pm 0.074
3	NGC 520	2281	0.2188 \pm 0.0045	0.29 \pm 0.015	0.0133 \pm 0.0028
4	NGC 1614	4778	0.1953 \pm 0.0067	0.346 \pm 0.016	0.0179 \pm 0.0026
5	M 82	203	13.02 \pm 0.30	16.70 \pm 0.59	1.366 \pm 0.056
6	NGC 3256	2804	1.124 \pm 0.044	1.178 \pm 0.033	<0.032
7	NGC 4039/9	1641	0.378 \pm 0.011	0.412 \pm 0.079	0.0211 \pm 0.0041
8	NGC 4194	2501	0.2094 \pm 0.0073	0.267 \pm 0.010	<0.0057
9	NGC 4449	207	0.2383 \pm 0.0086	0.151 \pm 0.046	0.0187 \pm 0.0044
10	NGC 4670	1609	0.0954 \pm 0.0083	0.717 \pm 0.075	0.0248 \pm 0.0051
11	NGC 4945	563	3.547 \pm 0.075	1.82 \pm 0.061	0.38 \pm 0.021
12	M 83	513	1.202 \pm 0.051	1.37 \pm 0.29	0.137 \pm 0.032
13	NGC 6240	7339	0.2447 \pm 0.0082	0.651 \pm 0.027	0.0349 \pm 0.0029
14	NGC 6810	2031	0.311 \pm 0.014	0.22 \pm 0.031	<0.016
15	NGC 6946	48	0.876 \pm 0.028	0.611 \pm 0.024	<0.061
16	Cen A	547	2.764 \pm 0.085	1.757 \pm 0.068	0.102 \pm 0.0062
17	NGC 1569	-104	0.652 \pm 0.027	0.657 \pm 0.025	0.0085 \pm 0.0019
18	NGC 6052	4739	0.169 \pm 0.007	0.291 \pm 0.037	0.017 \pm 0.006

I selected a sample of starburst galaxies from Table 3.1 where the main fine structure emission lines, measured by us, were provided. Table 4.1 lists the sample of starburst galaxies involved in this project.

4.1.1 Oxygen emission lines as diagnostic of the electron density

In this section I will explain how it is possible to measure the electron density (n_e), and subsequently the hydrogen density (n_H) using the ratio of two far infrared fine structure emission lines. In addition, I will select the starburst galaxy that best represents the hydrogen density of our sample to model its ionized and photodominated regions.

Far infrared fine structure emission lines can measure the density and ionization of the gas: the ratio of lines with similar critical density, but different ionization potential, measures the ionization, while the ratio of lines with similar ionization potential, but different critical density, measures the density (Spinoglio & Malkan 1992). Table 4.2 lists [O III] 88 and 52 μm transitions and their critical densities calculated for $T=10,000$ K (see Osterbrock & Ferland 2006). These far infrared lines have much smaller excitation potentials than optical lines such as $^3P_2 - ^1D_2$ $\lambda 5007$. Thus a ratio like $j_{\lambda 5007}/j_{\lambda 88\mu\text{m}}$ depends strongly on temperature but, since the 3P_2 level has a much lower critical electron density than the 1D_2 does, it also will depend on density.

On the other hand, the ratio $j_{\lambda 52\mu\text{m}}/j_{\lambda 88\mu\text{m}}$ will hardly depend on the temperature at all (since both excitation potentials are so low in comparison with typical nebular temperatures), but does depend strongly on density (since the two upper levels have different critical densities). Hence by measuring two [O III] ratios, we can determine the average values of the two parameters, T and n_e (Osterbrock & Ferland 2006).

Table 4.3 lists the [O III] 88 and 52 μm emission lines and their ratios, measured by us, from the ISO LWS archive of our sample of starburst galaxies.

Table 4.2: Electron density diagnostic. The critical densities for [O III] 88 and 52 μm are for collisional de-excitation (Osterbrock & Ferland 2006). All values are calculated for $T=10,000$ K.

Species	Transitions	Wavelength (μm)	n_{cr} (cm^{-3})
[O III]	$^3P_0 - ^3P_1$	88.536	5.1×10^2
[O III]	$^3P_1 - ^3P_2$	51.814	3.6×10^3

Table 4.3: Line flux measurements, in units of $10^{-14} \text{ W m}^{-2}$, for ISO-LWS detections of [O III] 52 and $88\mu\text{m}$ fine structure emission lines. For each source, our own line flux measurements and their ratios are listed.

Index	Source	[OIII] $52\mu\text{m}$	[OIII] $88\mu\text{m}$	$\frac{[\text{OIII}]_{52}}{[\text{OIII}]_{88}}$
1	IC 10	2.11 ± 0.26	1.416 ± 0.005	1.49 ± 0.19
2	NGC 253	0.52 ± 0.11	1.14 ± 0.25	0.456 ± 0.196
3	NGC 520	0.081 ± 0.003	0.14 ± 0.03	0.5714 ± 0.1438
4	NGC 1614	0.253 ± 0.046	n.a	n.a
5	M 82	10.3 ± 0.5	8.6 ± 0.4	1.197 ± 0.114
6	NGC 3256	0.361 ± 0.067	0.60 ± 0.13	0.6022 ± 0.2421
7	NGC 4038	0.491 ± 0.029	0.471 ± 0.013	1.0425 ± 0.0905
8	NGC 4194	n.a	0.185 ± 0.017	n.a
9	NGC 4449	0.24 ± 0.10	n.a	n.a
10	NGC 4670	0.10 ± 0.02	0.157 ± 0.012	0.64 ± 0.18
11	NGC 4945	n.a	0.75 ± 0.16	n.a
12	M 83	n.a	1.76 ± 0.35	n.a
13	NGC 6240	0.097 ± 10^{-7}	0.0321 ± 10^{-7}	3.0218 ± 0.00006
14	NGC 6810	0.128 ± 0.081	0.1678 ± 0.0129	0.767 ± 0.541
15	NGC 6946	n.a	0.121 ± 0.03	n.a
16	Cen A	0.70 ± 0.14	0.72 ± 0.144	0.972 ± 0.388
17	NGC 1569	1.611 ± 0.102	2.491 ± 0.084	0.646 ± 0.062
18	NGC 6052	0.20 ± 0.046	0.10 ± 0.02	2.1 ± 0.9

In order to measure the electron density through the [OIII] 52 μm /[OIII] 88 μm ratio I used the program EQUIB06 (originally written by I. D. Howarth and S. Adams), which solves the equations of statistical equilibrium to obtain level populations and hence line strengths. Using the flux ratio of the 52 μm transition and the 88 μm [OIII] transition, and an adopted 10,000 K electron temperature, a range of electron densities corresponding to the flux ratio error limits was calculated for each starburst source, and these are given in Table 4.4. The electron density was estimated using the [O III] 52/88 μm ratio that was measured for 12 of the 18 selected starburst galaxies. In the attempt to study starburst galaxy properties using bright fine structure emission lines coming from both ionised and photodissociated regions, I selected, among the sample of galaxies where the electron density was measured, the starburst galaxy NGC 4038. The electron density, $n_e=190\pm_{12}^{16}$, of the chosen source NGC 4038, represents the density in the ionised region, which will be used to calculate the hydrogen density, n_H , necessary to model the H II region with the MOCASSIN code. In fact, the relation between n_H and n_e is given by $n_H = n_e/1.08$ (from ionised hydrogen plus the fraction of singly ionised helium) (Osterbrock & Ferland 2006).

4.2 Antennae galaxy

The Antennae galaxies, NGC 4038/39 (Arp 244), are arguably the best known example of interacting galaxies. The Antennae are undergoing a galactic collision. Most galaxies probably undergo at least one significant collision in their lifetimes. This is likely the future of our Milky Way when it collides with the Andromeda Galaxy. The two galactic nuclei of NGC 4038 and NGC 4039, and the dust obscured overlap region in between, exhibit one of the most stunning examples of starburst activity in the nearby universe (Brandl *et al.* 2009). With a luminosity just below $10^{11} L_{\odot}$ the Antennae does not classify as a luminous infrared galaxy (LIRG). The distance to the Antennae has been a subject of recent controversy but the best assumed value seems to be 19.2 Mpc (Bastian *et al.* 2006). The first high signal-to-noise mid-IR images of the Antennae were made by ISO. ISOCAM observations at angular resolutions of 5'' - 8'' showed that the overlap region contributes more than half of the total luminosity observed in the 12.5–18 μm range (Vigroux *et al.* 1996). Observations at the longer far-IR, submillimeter and radio wavelengths generally agree with the mid-IR picture. The early work of Hummel & van der Hulst (1986) with the VLA at 1.465 GHz and 4.885 GHz found thermal radio knots, which account for about 35 percent of the total emission, coinciding with peaks in



Figure 4.1: An optical image of the Antennae galaxy

Table 4.4: Electron densities computed with EQUIB06 using the [OIII] $52\mu\text{m}$ /[OIII] $88\mu\text{m}$ ratio, listed in Table 4.3, for an adopted electron temperature of 10,000K.

Index	Source	Electron Density (n_e)
1	IC 10	$390 \pm_{0.36}^{2.33}$
2	NGC 253	$1.467 \pm_{0.30}^{31}$
3	NGC 520	$1.98 \pm_{0.40}^{56}$
4	NGC 1614	n.a
5	M 82	$257 \pm_{0.50}^{0.50}$
6	NGC 3256	$13 \pm_{10}^{96}$
7	NGC 4038	$190 \pm_{12}^{16}$
8	NGC 4194	n.a
9	NGC 4449	n.a
10	NGC 4670	$26.30 \pm_{25}^{71}$
11	NGC 4945	n.a
12	M 83	n.a
13	NGC 6240	$1259 \pm_{0.0001}^{0.0002}$
14	NGC 6810	$77.27 \pm_{76}^{226}$
15	NGC 6946	n.a
16	Cen A	$160.7 \pm_{154}^{156}$
17	NGC 1569	$30.20 \pm_{24}^{27}$
18	NGC 6052	$700 \pm_{300}^{450}$

H_α emission associated with recent star formation. During the mapping of the Antenna galaxy in the [C II] $158\mu\text{m}$ cooling line, at angular resolution of $55''$, it was found that the starburst activity is confined to small regions of high SFE (Nikola *et al.* 1998). Wilson *et al.* (2003) found an excellent correlation between the strengths of the CO emission and the $15\mu\text{m}$ broad band emission seen by ISO, and determined masses of $3-6 \times 10^8 M_\odot$ for the largest molecular complexes, typically an order of magnitude larger than the largest structures found in the disks of more quiescent spiral galaxies. The bulk of the current massive star formation in an interacting system, which extends over tens of kpc, is confined to just two compact regions (Brandl *et al.* 2009). A predominant fraction of the PAH usually arises from the diffuse ISM, heated only by the interstellar radiation field, with only a low fraction rising from PDRs (Draine & Li 2007).

However, in starburst galaxies like the Antennae, the situation is reversed, with most part of the total emission coming from the regions of recent star formation. Both nuclei of NGC 4038 and NGC 4039 are surrounded by regions of moderately active star formation. While the nucleus of NGC 4039 appears more active in terms of the [Ne III], [S VI] emission lines, the lack of [Ne V] and the low [O IV]/[Ne II] ratio can rule out the presence of an AGN in both nuclei (Brandl *et al.* 2009).

4.3 Modelling the nucleus of NGC 4038

Fig 4.2 shows a diagram of our attempt to model the physical parameters of the nucleus of NGC 4038 from a study of its ionized and photodominated regions. The nucleus is chosen in order to reduce contributions from different gas components other than the ionized and photodissociated regions. From the left: I obtained a spectrum from STARBURST 99, a code consisting of a comprehensive set of model predictions for the time-dependent spectrophotometric and related properties of galaxies that have undergone active star formation (SB99, Leitherer *et al.* 1999) and used it as an input for the 3D photoionization code MOCASSIN. The H II region, within the nucleus of NGC 4038, is fully described by MOCASSIN and the full spectral energy distribution (SED) is computed along with the most important far infrared fine structure emission lines (e.g. O I, C II, N III, N II). Through the use of an interface, the radiation field at the ionization front is calculated integrating the MOCASSIN SED in the range $912\text{\AA} \leq \lambda \leq 2400\text{\AA}$. This radiation field (in Habing) is then fed into the plane parallel UCL_PDR code, which describes the physical and chemical conditions of the photodominated region, within the nucleus of NGC 4038, and computes the cooling and rotational emission lines ([C II] 158 μm , [O I] 63 and 145 μm , CO).

[C II] 158 μm , [O I] 63 and 145 μm FIR fine structure emission line contributions are added together and the ratios of [C II]₁₅₈/[O I]₆₃ and [O I]₆₃/[O I]₁₄₅ are used to constrain the physical and chemical parameters of NGC 4038. [C II] 158 μm , [O I] 63 and 145 μm emission line profiles are calculated by the radiative transfer code SMMOL using the chemical abundances, and gas and dust temperatures obtained from the UCL_PDR code. Finally, CO rotational emission lines are computed in order to compare them with Caltech Submillimeter Observatory (CSO) observations Bayet *et al.* (2006). The best fit of our models to the nucleus of NGC 4038 starburst galaxy was at first chosen by attempting to match the [N III]₅₇/[N II]₁₂₂ ratio obtained from MOCASSIN with that measured from LWS ISO observations. An alternative approach was performed by comparing [N III] 57 μm and [N II] 122 μm emission line intensities, calculated by

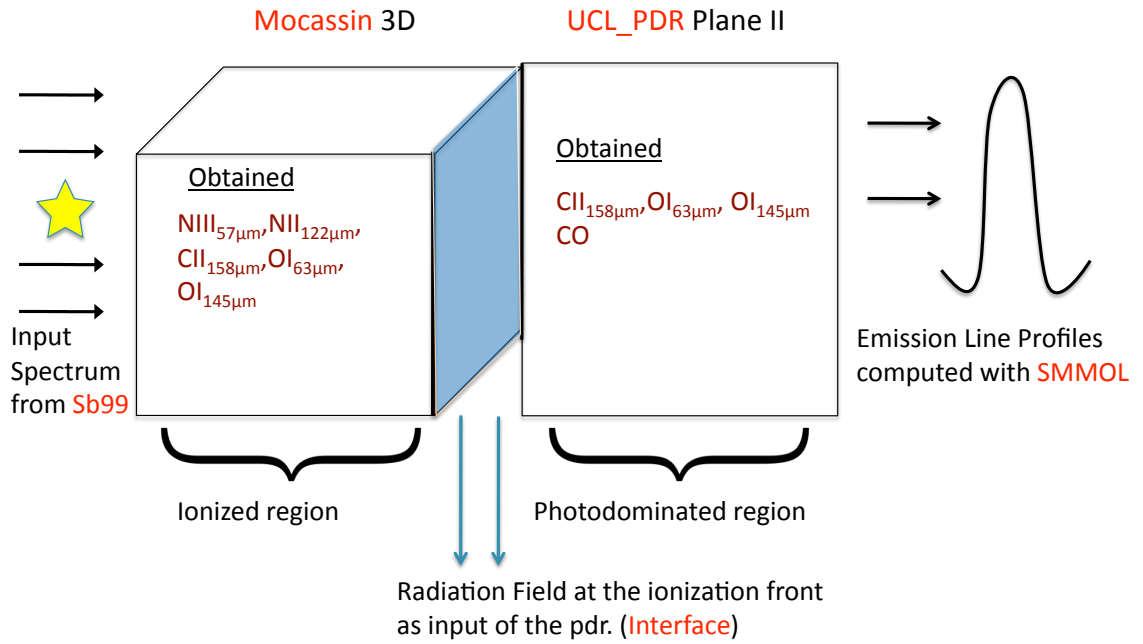


Figure 4.2: Representative scheme of the model of the nucleus of NGC 4038.

MOCASSIN, with the ISO observations.

Table 4.5: NGC 4038 ISO lists fine structure emission lines intensities, measured by us, in $10^{-14} \text{ W m}^{-2}$ units.

Source	NGC 4038
[NII] 122 μm	0.047 \pm 0.0049
[NIII] 57 μm	0.196 \pm 0.039
[OIII] 52 μm	0.491 \pm 0.029
[OIII] 88 μm	0.471 \pm 0.013
[CII] 158 μm	0.378 \pm 0.011
[OI] 63 μm	0.412 \pm 0.079
[OI] 145 μm	0.0211 \pm 0.0041

Table 4.5 lists the far infrared fine structure emission lines, measured by us, from the ISO LWS archive and used throughout this project. Results from each modelling will be presented in Sec 4.4.

Details of each of these steps are provided in the following sections.

4.3.1 Modelling with STARBURST 99

In this section I will describe the first step of this project, which is how the input spectrum used to describe the whole stellar population of the NGC 4038 starburst source has been reproduced in order to be used as an input to model the ionized region. The photoionization MOCASSIN code requires an input spectrum representative of the whole stellar population within the nucleus of NGC 4038, i.e. a spectrum produced by a stellar population synthesis code such as SB99. Using a web-based interface, a user can run specific stellar population models using the latest set of stellar evolution models and atmosphere grids for a range of metallicities, initial mass functions and ages, and retrieve a wide range of model outputs including spectra and equivalent widths of spectral features (Leitherer *et al.* 1999). In order to correctly match the observed ISO LWS FIR fine structure emission lines, a multi-epochal SB99 input spectrum was created based on a young $\sim 2\text{--}5$ Myr old WR population and a ~ 15 Myr population of young massive star clusters in and around NGC 4038, as estimated by Bastian *et al.* (2006). The parameters of the model input spectrum were as follows: A metallicity of $0.5 Z_{\odot}$ was chosen (as estimated by Bastian *et al.* 2006), together with assumptions of an instantaneous burst with a Salpeter initial mass function (IMF) with a total stellar mass produced of $2.5 \times 10^8 M_{\odot}$ (Fischer *et al.* 1996). The models contained Padova tracks (evolutionary tracks and isochrones for low- and intermediate-mass stars, Girardi *et al.* 2000) with thermally pulsing AGB stars included and Pauldrach-Hillier model atmospheres, chosen since they incorporate stars with strong winds, i.e. a stellar population representative of the WR population within NGC 4038. Once read in, MOCASSIN normalises the input spectrum to the specified luminosity of the central star, L_{\star} , and calculates the number of ionising photons per second Q_{phot} (e.g. $Q(H^0)$, the number of hydrogen-ionising photons per second) - therefore, L_{\star} must be changed accordingly until the observed number of ionising photons is matched and consequently the observed nitrogen line ratio is correctly predicted. In the next section a more in-depth explanation of the MOCASSIN grid of input parameters is given.

4.3.2 Modelling gas and dust in the ionized region with the MOCASSIN code

This section will describe the second step of this project, which is the study of the ionized region in the attempt to model NGC 4038. A model is specified to the code via a 3-dimensional cartesian grid (defined in physical size units of cm) with the n_e (or n_H) and chemical abundance specified for each cartesian grid point i.e. each grid cell (see Sec 2.2). Input files containing a

three dimensional density distribution and chemical abundance sets and their specific abundance grid indices are specified to the code, allowing the user to accurately simulate inhomogenous chemical and physical conditions in the object being studied. Table 4.6 presents the grid of MOCASSIN models used for this project. The arbitrary combinations of parameters, in each row, were chosen in order to constrain the observed $[\text{NIII}]_{57}/[\text{NII}]_{122}$ ratio. It was decided that initially a simple gas-only model should be constructed, with dust to be added if necessary to better reproduce the observations once the model was firmly established. In both cases the initial elemental abundances are those listed in Table 4.7.

Structurally, this gas-only model consisted of an ionising source, which in this case was the SB99 input spectrum located at the centre of a symmetrical grid, which aimed to be representative of the stellar population of the nucleus of NGC 4038. The ages chosen for the input stellar population, representing the ionising source, were 2×10^6 yr and 6×10^6 yr. These values were selected because at these time steps there are sufficient photons to ionize the nuclear region. The size and resolution of the grid, n_{xyz} , must be sufficient not to cause loss of detail via blending across the grid cells but it is also limited computationally. Along with T_{eff} , either the luminosity of the central star, L_* (in units of 10^{36} erg s^{-1}), or the number of hydrogen-ionising photons per second, $Q(H^0)$ (in units of $10^{36} s^{-1}$), must be specified as an input parameter. If L_* is defined, $Q(H^0)$ is then derived from it by the code.

As a first approach (see Table 4.6), I decided to use the upper limit of the electron density, $n_e = 190 \pm 12^6 \text{ cm}^{-3}$ (which is related to n_H by $n_H = n_e/1.08$, as calculated in Sec 4.1.1) to compute the Stromgren radius of a symmetrical sphere where the hydrogen is completely ionized, using:

$$R_s = \left(\frac{3Q(H^0)}{4\pi(n_H)^2\alpha_B} \right)^{\frac{1}{3}} \quad (4.1)$$

(Osterbrock & Ferland 2006). In order to calculate the R_s it is necessary to first compute the number of ionising photons using the observed $H\alpha$ emission. The number of ionising photons, $Q(H^0)$, in units of s^{-1} can be calculated using:

$$Q(H^0) = \frac{N(H\alpha)\alpha_B}{\alpha_{eff}^{H\alpha}} \quad (4.2)$$

where α_B is the recombination coefficient summed over all levels above the ground level ($= 2.59 \times 10^{-13}$ at $T_e=10,000$ K) and $\alpha_{eff}^{H\alpha}$ is the effective recombination coefficient for emission of a $H\alpha$ photon ($= 1.167 \times 10^{-13}$ at $T_e=10,000$ K, Storey & Hummer 1995).

$N(H\alpha) = L(H\alpha)/E(H\alpha)$ is the number of $H\alpha$ photons, where $L(H\alpha)$ is the $H\alpha$ luminosity ($L(H\alpha) = 3 \times 10^{40} \text{ erg s}^{-1}$ Hummel & van der Hulst 1986) and $E(H\alpha)$ is the energy of a $H\alpha$ photon ($E(H\alpha) = 3.018 \times 10^{-12} \text{ erg}$). The computed $Q(H^0) = 2.21 \times 10^{52}$ leads to a radius, $R_s = 8.27 \times 10^{19} \text{ cm}$, which was set to the R_{out} parameter for models 001 to 013 (see Table 4.6). For models 014 to 017 the density was decreased and therefore a value of $R_s = 8.69 \times 10^{19} \text{ cm}$ was used for the R_{out} parameter. Subsequently, since the choice of $R_s = R_{out}$ was not producing the expected values of the observed ISO $[NIII]_{57}/[NII]_{122}$ ratio, (as the Stromgren radius does not actually reproduce the end of the H II region), a radius of $\sim 350 \text{ pc}$ ($\sim 1.08 \times 10^{21} \text{ cm}$) was set to the R_{out} parameter for models 018 to 024. This new R_{out} is the radius out to which the $H\alpha$ emission is seen in the nucleus of NGC 4038 (Hummel & van der Hulst 1986). For all choices of R_{out} , the $Q(H^0)$ computed cannot be matched exactly to the measured value ($Q(H^0) = 2.21 \times 10^{52}$). In our grid of models I assumed that a typical WR stellar temperature ranges between $3-5 \times 10^4 \text{ K}$. A grid size of 15^3 cells was chosen, and a uniform $N_{bin} = 600$ was adopted, after noting that changing the number of cells (see Table 4.6 model 003-004-008) and number of bins (see Table 4.6 model 007) did not affect the results. From models 014 to 024, $n_e = 190 \text{ cm}^{-3}$ was chosen, because the previous upper limit value used ($n_e = 206 \text{ cm}^{-3}$) did not reproduce the physical conditions of the nucleus of NGC 4038 as expected.

We found that no matter how we varied the physical parameters, a gas only model did not reproduce the ISO LWS observations. MOCASSIN includes a fully self-consistent treatment of dust radiative transfer (RT) within a photoionised region (Ercolano *et al.* 2005). The inclusion of dust within a H II region is essential when attempting to recreate radiative transfer and physical conditions within it. Dust grains compete with the gas for absorption of the UV photons, whose energy they reradiate in the infrared, contributing to the observed SED. The code successfully establishes the dust and gas phase coupling by incorporating interactions in the RT such as scattering, absorption and re-emission. In addition to the emission line spectrum, ionisation, T_e and N_e structure of the H II region, the code can also determine accurate dust temperatures and spectral energy distributions (SEDs). This is achieved by allowing the specification of discrete grain sizes and different grain species separately, rather than having a single grain as a representation of an ensemble of grains (as in e.g. DUSTY, Ivezić & Elitzur 1997). Firstly, a dust composition is specified, consisting of a set of optical constants that encompass the wavelength range from the UV to the FIR where dust absorption, emission or scattering are important. Secondly, the grain size distribution is supplied, which is derived from a_{min} and a_{max} , the minimum and maximum grain radii in μm , and ρ , the power-law exponent of the

size distribution found by Mathis *et al.* (1977), which typically lies in the range -3.3– -3.6. Mie scattering is used to calculate the absorption and scattering efficiencies, $Q_{abs}(a, \lambda)$ and $Q_{sca}(a, \lambda)$, at each wavelength, λ , and the grain radius a . Separate temperatures are derived for each grain radius and species. The necessity for the independent treatment of all grain sizes and species was demonstrated by van Hoof *et al.* (2004), who showed using CLOUDY that approximating a grain mixture with a composite grain species can yield misleading results. The most influential parameter on the level of IR emission by dust is the dust to gas mass fraction, $\frac{M_d}{M_g}$. By constraining this parameter, an estimate can be made of the dust mass required to match the IR flux levels. I used either a silicates or a graphite grain species and a dust composition with a $\frac{M_d}{M_g}=0,75 \times 10^{-6}$ (as used in Aannestad & Emery 2003) throughout the grid of models with dust included. When the $\frac{M_d}{M_g}$ was used, the dust consisted of an mixture silicates-graphite dust grain species with the standard grain size distribution of Mathis *et al.* (1977). This ‘MRN’ grain size distribution has dust parameters of $a_{min}=0.0156 \mu\text{m}$, $a_{max}=0.25 \mu\text{m}$ and a power-law size distribution exponent of -3.5 (Aannestad & Emery 2003).

In the following section I will discuss the physical input parameters used in the UCL_PDR code and the interface used to link the MOCASSIN and UCL_PDR radiation fields.

4.3.3 Modelling the chemistry in PDRs with the UCL_PDR code

PDRs can be found surrounding, or nearby, H II regions and they are linked through the radiation field, which influences the chemical and physical conditions within these regions (see Sec 1.1 and 1.2). In virtue of this link, I created an interface between the MOCASSIN and the UCL_PDR code. The interface consists in computing the radiation field at the ionization front by integrating the SED, outputted from MOCASSIN, in the range $912\text{\AA} \leq \lambda \leq 2400\text{\AA}$. Finally, the integrated SED is converted to Habing units ($1 \text{ Habing} = 1.6 \times 10^{-3} \text{ erg s}^{-1} \text{ cm}^{-2}$) and inputted into the UCL_PDR code. Table 4.8 lists the input parameters of the UCL_PDR code run in time dependent mode. We assumed a constant standard cosmic ray ionization rate, $5 \times 10^{-17} \text{ s}^{-1}$, a standard metallicity of $1 Z/Z_{\odot}$ and a turbulent velocity of 1.5 km s^{-1} , throughout the grid. n_H is chosen according to that used in the grid of MOCASSIN input parameters. The second column of Table 4.8 lists the incident FUV radiation field obtained through the use of the interface and represents the radiation field, attenuated by dust, at the ionization front of the H II region. The grain radius and the grain number density assumed are those mentioned in Table 3.3. Also a silicate grain species and a dust composition with a $\frac{M_d}{M_g} = 0.01$ was used. All models were run up to $A_v=10$.

Table 4.6: The grid model input parameters of MOCASSIN.

Index	n_H	Input	n_{xyz}	L_{star}	Q_{phot}	T_{star}	N_{bin}	R_{out}	Dust	Md/Mg
	cm^{-3}	Spectrum		(E^{36})	(E^{36})			cm	Type	
001	190	2e6 yr	15	2.59e7	1.99e17	40000	600	8.27e19	X	X
002	190	6e6 yr	15	2.59e7	2.19e16	40000	600	8.27e19	X	X
003	190	2e6 yr	30	2.59e7	1.99e17	40000	600	8.27e19	X	X
004	190	2e6 yr	30	3.30e6	2.53e16	40000	600	8.27e19	X	X
005	190	2e6 yr	15	2.59e6	1.99e16	40000	600	8.27e19	X	X
006	190	2e6 yr	15	2.59e6	1.99e16	40000	600	8.27e19	silicates	X
007	190	2e6 yr	15	2.59e6	1.81e16	40000	1200	8.27e19	silicates	X
008	190	6e6 yr	30	2.59e7	2.19e16	40000	600	8.27e19	X	X
009	190	6e6 yr	15	2.59e6	2.20e15	40000	600	8.27e19	silicates	X
010	190	6e6 yr	15	2.59e7	2.17e16	40000	600	8.27e19	silicates	X
011	190	2e6 yr	15	2.59e6	1.99e16	40000	600	8.27e19	graphite	X
012	190	2.2e7 yr	15	1.19e6	2.29e16	40000	600	8.27e19	graphite	X
013	190	6e6 yr	15	2.59e7	2.17e16	50000	600	8.27e19	graphite	X
014	175.92	6e6 yr	15	2.59e7	2.19e16	40000	600	8.69e19	X	X
015	175.92	6e6 yr	15	2.59e7	2.17e16	40000	600	8.69e19	silicates	X
016	175.92	6e6 yr	15	2.59e7	2.19e16	30000	600	8.69e19	silicates	X
017	175.92	6e6 yr	15	2.59e7	2.19e16	50000	600	8.69e19	silicates	X
018	175.92	6e6 yr	15	2.32e7	1.97e16	50000	600	1.08e21	X	X

Index	n_H	Input	n_{xyz}	L_{star}	Q_{phot}	T_{star}	N_{bin}	R_{out}	Dust	Md/Mg
	cm^{-3}	Spectrum		(E^{36})	(E^{36})			cm	Type	
019	175.92	2e6 yr	15	2.59e6	1.99e16	50000	600	1.08e21	X	X
020	175.92	6e6 yr	15	2.42e7	2.03e16	50000	600	1.08e21	silicates	X
021	175.92	2e6 yr	15	2.42e6	1.85e16	40000	600	1.08e21	silicates	X
022	175.92	2e6 yr	15	2.42e6	1.85e16	50000	600	1.08e21	silicates	X
023	175.92	2e6 yr	15	2.42e6	1.85e16	50000	600	1.08e21	graphite	X
024	175.92	6e6 yr	15	2.42e7	2.03e16	40000	600	1.08e21	graphite& silicates	0.75e-6
025	175.92	2e6 yr	15	2.42e6	1.83e16	40000	600	1.08e21	graphite& silicates	0.75e-6

Table 4.7: Gas-phase elemental abundances used in the MOCASSIN code. (Relative to total hydrogen nuclei)

He	7.5×10^{-2}	C	1.4×10^{-4}	N	6.5×10^{-5}
O	3.2×10^{-4}	Na	8.8×10^{-7}	Mg	5.1×10^{-6}
Si	8.2×10^{-7}	S	1.4×10^{-6}	Cl	1.1×10^{-7}
Ca	5.7×10^{-10}	Fe	3.6×10^{-7}		

Table 4.8: The grid model input parameters of UCL_PDR. The incident FUV radiation fields are inputted from the ionization models and represent the radiation field at the ionization front.

Index	Incident FUV Flux G_0	n_H cm^{-3}	Cloud size A_v (mag)	Metallicity Z/Z_\odot	C.R. ionization rate ζ (s^{-1})	Grain number density n_g (cm^{-3})	Turbulent velocity v_{turb} (km s^{-1})	Dust Type	Md/Mg
001	18145.6	190	10	1	5×10^{-17}	2×10^{-12}	1.5	silicates	0.01
002	20906.4	190	10	1	5×10^{-17}	2×10^{-12}	1.5	silicates	0.01
003	18153.6	190	10	1	5×10^{-17}	2×10^{-12}	1.5	silicates	0.01
004	2429.1	190	10	1	5×10^{-17}	2×10^{-12}	1.5	silicates	0.01
005	1912.2	190	10	1	5×10^{-17}	2×10^{-12}	1.5	silicates	0.01
006	1893.3	190	10	1	5×10^{-17}	2×10^{-12}	1.5	silicates	0.01
007	1892.6	190	10	1	5×10^{-17}	2×10^{-12}	1.5	silicates	0.01
008	20957.4	190	10	1	5×10^{-17}	2×10^{-12}	1.5	silicates	0.01
009	2066.7	190	10	1	5×10^{-17}	2×10^{-12}	1.5	silicates	0.01
010	20667.6	190	10	1	5×10^{-17}	2×10^{-12}	1.5	silicates	0.01
011	1900.4	190	10	1	5×10^{-17}	2×10^{-12}	1.5	silicates	0.01
012	312.7	190	10	1	5×10^{-17}	2×10^{-12}	1.5	silicates	0.01
013	20600.6	190	10	1	5×10^{-17}	2×10^{-12}	1.5	silicates	0.01
014	20899.2	175.92	10	1	5×10^{-17}	2×10^{-12}	1.5	silicates	0.01
015	20625.5	175.92	10	1	5×10^{-17}	2×10^{-12}	1.5	silicates	0.01
016	20626.1	175.92	10	1	5×10^{-17}	2×10^{-12}	1.5	silicates	0.01
017	20491.1	175.92	10	1	5×10^{-17}	2×10^{-12}	1.5	silicates	0.01
018	106.6	175.92	10	1	5×10^{-17}	2×10^{-12}	1.5	silicates	0.01

Index	Incident FUV Flux G_0	n_H cm^{-3}	Cloud size A_v (mag)	Metallicity Z/Z_\odot	C.R. ionization rate ζ (s^{-1})	Grain number density n_g (cm^{-3})	Turbulent velocity v_{turb} (km s^{-1})	Dust Type	Md/Mg
019	10.44	175.92	10	1	5×10^{-17}	2×10^{-12}	1.5	silicates	0.01
020	110.5	175.92	10	1	5×10^{-17}	2×10^{-12}	1.5	silicates	0.01
021	9.92	175.92	10	1	5×10^{-17}	2×10^{-12}	1.5	silicates	0.01
022	9.81	175.92	10	1	5×10^{-17}	2×10^{-12}	1.5	silicates	0.01
023	9.91	175.92	10	1	5×10^{-17}	2×10^{-12}	1.5	silicates	0.01
024	110.77	175.92	10	1	5×10^{-17}	2×10^{-12}	1.5	silicates	0.01
025	10.06	175.92	10	1	5×10^{-17}	2×10^{-12}	1.5	silicates	0.01

In the following section the oxygen emission line profiles computed from the UCL_PDR code will be investigated by the use of the radiative transfer code SMMOL.

4.3.4 Modelling the oxygen emission line profiles with the radiative transfer SMMOL code

As found in Chapter 3 we believe that neutral oxygen, in particular $[\text{O I}]_{63}$, can be self absorbed and that, of course, this self absorption changes the result of the predicted observations (see Sec 3.5.1). We take into account such self absorption by using the radiative transfer model SMMOL.

SMMOL needs to re-grid the output data obtained by the UCL_PDR code, such as chemical abundances, gas and dust temperature, turbulent velocity and size of the cloud. In order to perform this task, an Interface between the SMMOL and UCL_PDR codes was used (Bayet et al in prep). In fact, the interface transforms a 1D semi-plane parallel slab into a sphere of the same size as the cloud modelled by UCL_PDR, it also defines circular shells within the sphere, regularly spaced, in which the radiative transfer calculations are performed. The oxygen emission line profiles were generated, through the interface, using the entire size of the cloud modelled by UCL_PDR, with the geometry and physical conditions shown in Fig 4.3. SMMOL considers a sphere of material illuminated at the outer boundary by the standard ISRF. In addition, the option to consider an additional illuminating source, located outside the sphere, using a flux in Habing units was employed. The assumed Habing flux corresponds to the radiation field used, for each model, as an input for the UCL_PDR code (see Table 4.8). A cavity inside the sphere was also included.

4.4 Results

In this section I will discuss MOCASSIN and UCL_PDR results for the $[\text{C II}]_{158}$, $[\text{O I}]_{63}$ and $[\text{O I}]_{145}$ emission lines. Also, the $[\text{N III}]_{57}/[\text{N II}]_{122}$ ratio that will be used, as a first approach, to constrain the physical parameters of the H II region is computed and listed in Table 4.9.

In this work, the important role of PAH is not included, their inclusion could strongly affects the results as they are believed to be the dominating agent of the process where C^+ ions are excited by photoelectrons ejected from grains heated by the UV radiation.

As already mentioned (see Sec 3.4), neutral nitrogen has an ionization potential of 14.53 eV. One of the brightest lines of singly ionized nitrogen, the $[\text{N II}]_{122\mu\text{m}}$ line has a critical electron

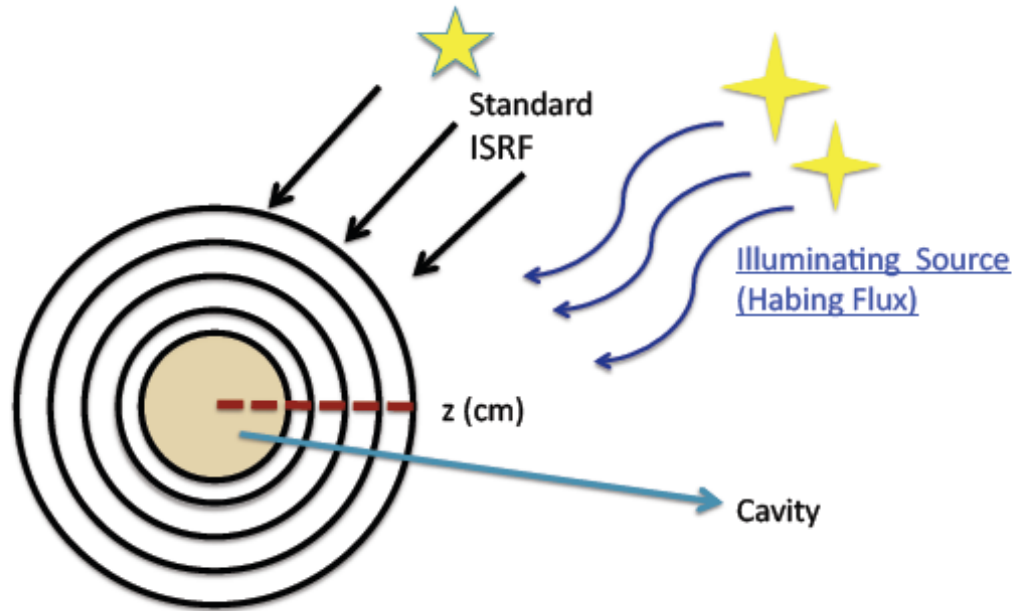


Figure 4.3: A geometrical representation of the physical conditions used with SMMOL. The beige central area represents the central cavity. The radiation field of the extra external source (Habing flux) is assumed to be the same used as the input for the UCL_PDR grid models. Also, the size of the sphere, z (cm), used in the SMMOL code, is the same as that assumed to model the PDR region. The level populations of the selected species are computed in each radial shell.

density of $3.1 \times 10^2 \text{ cm}^{-3}$. The [N II] $122\mu\text{m}$ transition arises only in diffuse, ionized H II regions. N III has a high ionization potential of 47.45 eV, and therefore, the $57\mu\text{m}$ transition of N III is only found in the ionized H II regions.

Table 4.9 lists the [C II] $_{158}$, [O I] $_{63}$ and [O I] $_{145}$ emission lines computed for the grid of MO-CASSIN models listed in Table 4.6. The first column lists the computed radiation field at the ionization front, which is inputted into the UCL_PDR grid. In the last column the [N III] $_{57}$ /[N II] $_{122}$ ratio was computed in order to identify the best fit to the [N III] $_{57}$ /[N II] $_{122}=4.1779 \pm 1.2744$ ratio measured by us from the ISO LWS archive. In fact, because these emission lines are not contaminated by PDRs, matching this ratio with observations implies that we can be confident that the physical parameters adopted are a good representation of the H II region in the nucleus of NGC 4038. From Table 4.9 it appears that the best fit to the observed ISO [N III] $_{57}$ /[N II] $_{122}=4.1779 \pm 1.27435$ ratio lies between models 019 and 025; however a more thorough analysis is required.

Table 4.10 lists the [C II] $_{158}$, [O I] $_{63}$ and [O I] $_{145}$ emission lines computed for the grid of

Table 4.9: The first column lists the computed radiation field at the ionization front. The remaining columns lists the $[\text{C II}]_{158}$, $[\text{O I}]_{63}$ and $[\text{O I}]_{145}$ emission lines, and the $[\text{N III}]_{57}/[\text{N II}]_{122}$ ratio computed from the grid of MOCASSIN models listed in Table 4.6.

Index	Radiation Field (Habing)	[CII] 158μm $\text{erg s}^{-1} \text{cm}^{-2} \text{sr}^{-1}$	[OI] 63μm $\text{erg s}^{-1} \text{cm}^{-2} \text{sr}^{-1}$	[OI] 145μm $\text{erg s}^{-1} \text{cm}^{-2} \text{sr}^{-1}$	$\frac{[\text{NIII}]_{57}}{[\text{NII}]_{122}}$
001	18145.6	3.87e-17	1.15e-21	1.17e-22	5935
002	20906.4	1.47e-14	9.68e-16	9.87e-17	1.85
003	18153.6	3.89e-17	1.21e-21	1.24e-22	5880
004	2429.1	9.01e-15	5.85e-16	5.88e-17	13.13
005	1912.2	8.43e-15	1.02e-15	1.04e-16	12.15
006	1893.3	7.79e-15	9.64e-16	9.77e-17	13.41
007	1892.6	9.73e-15	9.10e-16	9.19e-17	7.13
008	20957.4	1.59e-14	4.33e-16	4.34e-17	1.29
009	2066.7	1.92e-15	1.87e-16	1.90e-17	2.47
010	20667.6	1.44e-14	9.69e-16	9.83e-17	1.92
011	1900.4	7.79e-15	9.67e-16	9.80e-17	13.49
012	312.7	4.74e-17	1.68e-19	1.46e-20	1380
013	20600.6	1.44e-14	9.68e-16	9.81e-17	1.86
014	20899.2	1.60e-14	9.64e-16	9.79e-17	1.81
015	20625.5	1.57e-14	9.71e-16	9.86e-17	1.84
016	20626.1	1.57e-14	9.64e-16	9.79e-17	1.87
017	20491.1	4.40e-17	1.79e-21	1.81e-22	245
018	106.6	3.27e-12	3.81e-14	3.96e-15	2.26
019	10.44	1.84e-12	2.65e-14	2.74e-15	3.82
020	110.5	3.21e-12	3.36e-14	3.49e-15	2.33
021	9.92	1.67e-12	2.65e-14	2.72e-15	3.75
022	9.81	1.65e-12	2.59e-14	2.66e-15	3.72
023	9.91	1.73e-12	2.76e-14	2.85e-15	3.65
024	110.77	1.66e-12	2.92e-14	3.05e-15	2.36
025	10.06	1.63e-12	2.64e-14	2.71e-15	3.73

UCL_PDR models listed in Table 4.8.

At a glance, it is clear that the contribution of these emission lines from the H II region is negligible.

Table 4.10: [C II]₁₅₈, [O I]₆₃ and [O I]₁₄₅ emission computed from the grid of UCL_PDR models listed in Table 4.8.

Index	[CII] 158μm	[OI] 63μm	[OI] 145μm
	erg s⁻¹ cm⁻²sr⁻¹	erg s⁻¹ cm⁻²sr⁻¹	erg s⁻¹ cm⁻²sr⁻¹
001	2.01e-4	1.22e-3	1.36e-5
002	2.12e-4	1.36e-3	1.42e-5
003	1.96e-4	1.11e-3	1.35e-5
004	1.75e-4	5.51e-4	7.74e-6
005	1.56e-4	6.43e-4	7.46e-6
006	1.67e-4	6.02e-4	7.33e-6
007	1.56e-4	6.75e-4	7.45e-6
008	1.66e-4	7.53e-4	7.65e-6
009	1.73e-4	5.03e-4	7.38e-6
010	2.04e-4	1.24e-3	1.41e-5
011	1.55e-4	8.04e-4	7.51e-6
012	1.36e-4	1.66e-4	3.94e-6
013	2.04e-4	1.24e-3	1.41e-5
014	2.00e-4	1.56e-3	1.32e-5
015	1.88e-4	1.30e-3	1.31e-5
016	1.88e-4	1.30e-3	1.31e-5
017	2.00e-4	1.34e-3	1.29e-5
018	8.98e-5	8.58e-5	3.16e-6
019	4.74e-5	1.35e-5	5.25e-7
020	9.51e-5	8.55e-5	2.94e-6
021	4.67e-5	1.26e-5	4.83e-7
022	4.65e-5	1.24e-5	4.76e-7
023	4.67e-5	1.25e-5	4.82e-7
024	9.53e-5	8.59e-5	2.95e-6
025	4.71e-5	1.27e-5	4.92e-7

In the following section, a detailed analysis of the combined results from MOCASSIN and UCL_PDR is provided. In addition, the oxygen emission line profiles are studied using the radiative transfer SMMOL code.

Fig 4.4 through Fig 4.11 show a selection of model results of the combined $[C\ II]_{158}$, $[O\ I]_{63}$ and $[O\ I]_{145}$ emission lines coming from H II and PDR regions. These results were selected to highlight the best and worst fits to the observed $[N\ III]_{57}/[N\ II]_{122}$ ratio. As the UCL_PDR model results were run with the time dependent approach, the contribution from the PDR region takes into account emission from three different ages (10^6 yr, 10^7 yr and 10^8 yr). Therefore, in each plot the contributions from the H II and PDR regions were summed varying the ages only for the PDR part, while the age for the H II part was kept at a constant value of $\sim 10^6$ yr according to the exact age of the input spectrum used. For each model the oxygen emission line profiles were calculated and, where the oxygen self-absorption was present, new results taking into account the percentage of this self-absorption were produced. The oxygen line profiles were computed taking into account the distance from the source.

Fig 4.4 shows the results for model 004 with a computed $[N\ III]_{57}/[N\ II]_{122}=13.13$ ratio. The top panel shows the $[C\ II]_{158}/[O\ I]_{63}$ ratio versus the $[O\ I]_{63}/[O\ I]_{145}$ ratio, the black triangle (with error bars) represents the observed ISO ratio for NGC 4038 (see Table 4.5) and the coloured circles represent either the contribution from both ionized and photodominated regions or just the contribution from the PDR. The middle panel shows the oxygen emission line profiles computed using the radiative transfer code (SMMOL), the dotted line represents the $[O\ I]_{145}$ emission line that, as expected (see Sec 3.5.1), does not show any self absorption, while the solid line represents the $[O\ I]_{63}$ emission line with oxygen self absorption. The $[O\ I]_{63}$ self-absorption varies according to the physical condition adopted to model the cloud. Finally, the bottom panel is the same as the top panel, however only plotting the models with an age of 10^7 yr, for the PDR, and taking into account the effect of the $[O\ I]_{63}$ self absorption by subtracting the percentage of oxygen self-absorbed from the sum of oxygen fluxes coming from both ionised and PDR regions. The choice of the 10^7 yr models was made because it is established that the PDR chemistry has already reached the steady state at this time (See Sec 3). As can be seen from Fig 4.4 none of the models fit the observed ISO ratio. This is expected because a priori the ratio of $[N\ III]_{57}/[N\ II]_{122}$ in the modelled ionized region does not fit the observed ISO ratio ($[N\ III]_{57}/[N\ II]_{122}=4.1779\pm 1.2744$). This clearly illustrates the strong tie between the H II and PDR regions and that if the H II region is not properly modelled, the PDR cannot produce the expected FIR fine structure emission lines.

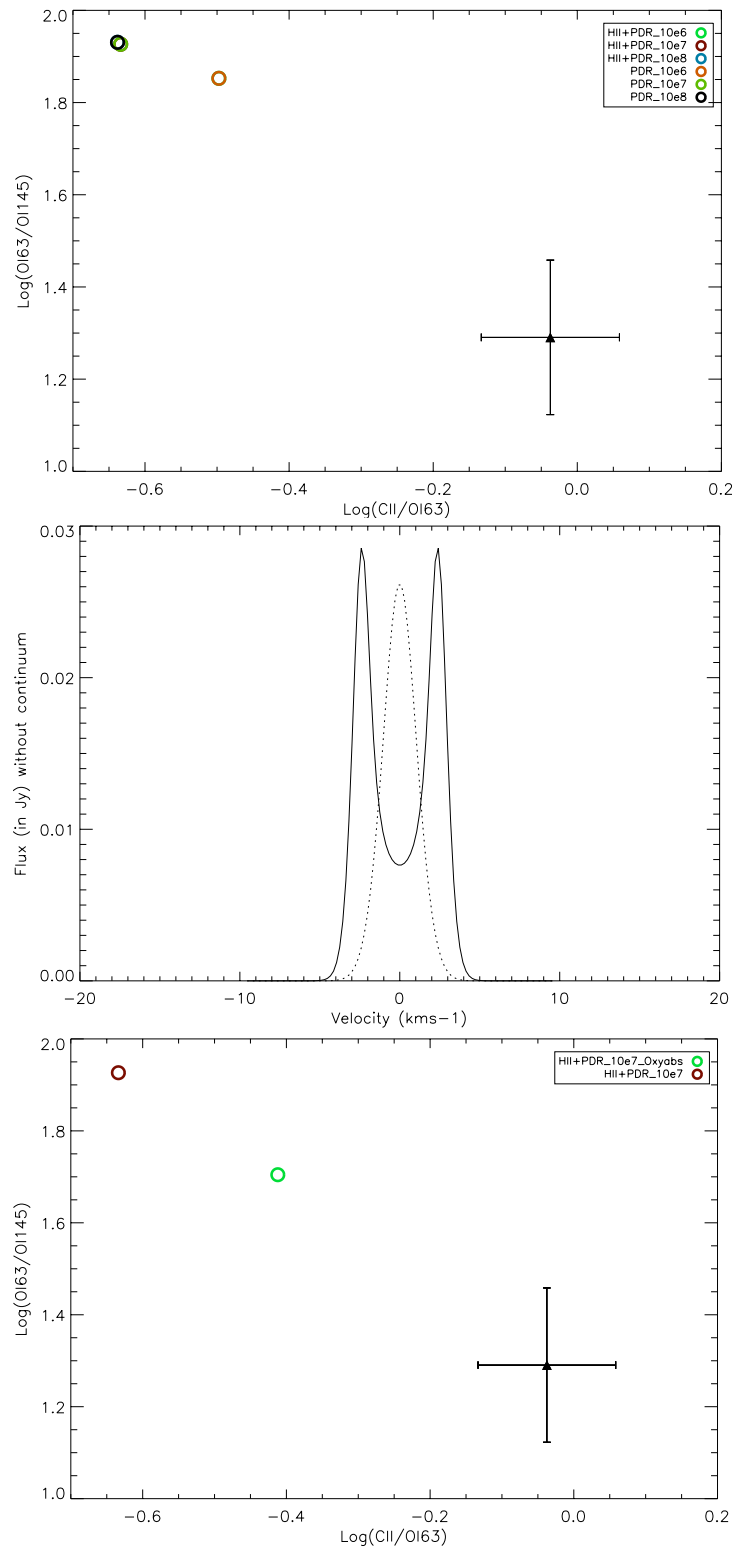


Figure 4.4: Model 004: with a computed $[\text{NIII}]_{57}/[\text{NII}]_{122}=13.13$ ratio. The top panel shows the $[\text{C II}]_{158}/[\text{O I}]_{63}$ ratio versus the $[\text{O I}]_{63}/[\text{O I}]_{145}$ ratio, the black triangle (with error bars) represents the observed ISO ratio for NGC 4038 (see Table 4.5) and the coloured circles represent either the contribution from both ionized and photodominated regions or just the contribution from the PDR. The middle panel shows the oxygen emission line profiles computed using the radiative transfer code (SMMOL), the dotted line represents the $[\text{O I}]_{145}$ emission line, while the solid line represents the $[\text{O I}]_{63}$ emission line with oxygen self absorption. The bottom panel is the same as the top panel, however only plotting the models with an age of 10^7 yr, for the PDR, and taking into account the effect of the $[\text{O I}]_{63}$ self absorption.

Fig 4.5 through Fig 4.11 show the results for models 013–019–021–022–023–024–025 with a range of $3.82 \leq [\text{N III}]_{57}/[\text{N II}]_{122} \leq 1.86$. These models are the closest matches to the observed ISO $[\text{N III}]_{57}/[\text{N II}]_{122}$ ratio. Fig 4.5 shows the same results as those seen in Fig 4.4, but for different physical conditions in both regions, which leads to a value of $[\text{N III}]_{57}/[\text{N II}]_{122} = 1.86$. Fig 4.6, Fig 4.7, Fig 4.8, Fig 4.9 and Fig 4.11, on the other hand, differ from the previous plotted models in that they do not present any oxygen self-absorption. Finally, Fig 4.10 is similar to both Fig 4.5 and Fig 4.4, however the third panel shows that $[\text{C II}]_{158}$ is also self absorbed. This is probably due to optical depth effects. The $[\text{C II}]_{158}$ emission line profile was computed for all models but only plotted for Fig 4.10, since none of the other models exhibit $[\text{C II}]_{158}$ self absorption.

In order to define the best fit for the grid of H II region models, I decided to calculate the χ^2 for the $[\text{N III}]_{57}$ and $[\text{N II}]_{122}$ emission lines, because they only arise from the H II region. The χ^2 was calculated using the following equation:

$$\sum_{i=1}^k = \frac{1}{n} \left(\frac{X_i - \mu_i}{\sigma_i} \right)^2 \quad (4.3)$$

where X_i are the model results, μ_i are the observation measurements and σ_i are the observation errors and n is the number of degrees of freedom. Table 4.11 lists the nitrogen emission lines obtained from the grid of MOCASSIN models and the calculated χ^2 . Listed in bold are the range of models that minimize the χ^2 , which is listed in the last column. From Fig 4.10 and Table 4.11 we find that model 024 is the best fit for both regions. In fact, Fig 4.10 shows the better match to the observations which is confirmed from the calculation of χ^2 listed in Table 4.11. The main reason of this better fit to the observations can be attributed to the inclusion of a grain mixture of silicates and graphite, and Md/Mg ratio in the input parameters. However, looking at the single line emission of $[\text{N III}]_{57}$ and $[\text{N II}]_{122}$ obtained from the MOCASSIN code and comparing the model outputs with the nitrogen ISO observations (see Table 4.5), shows that we have to consider that ISO beam may be bigger than the H II region we modelled. This implies that I need “X” number of H II regions (~ 10 in our case) to better match the ISO observations. In fact, ISO LWS beam is $\sim 80''$ that corresponds to ~ 7 kpc and our modelled H II region is ~ 600 pc. Thus it is plausible to assume that, at least ~ 10 H II regions are within the beam size instead of assuming one big H II region in the ISO LWS beam.

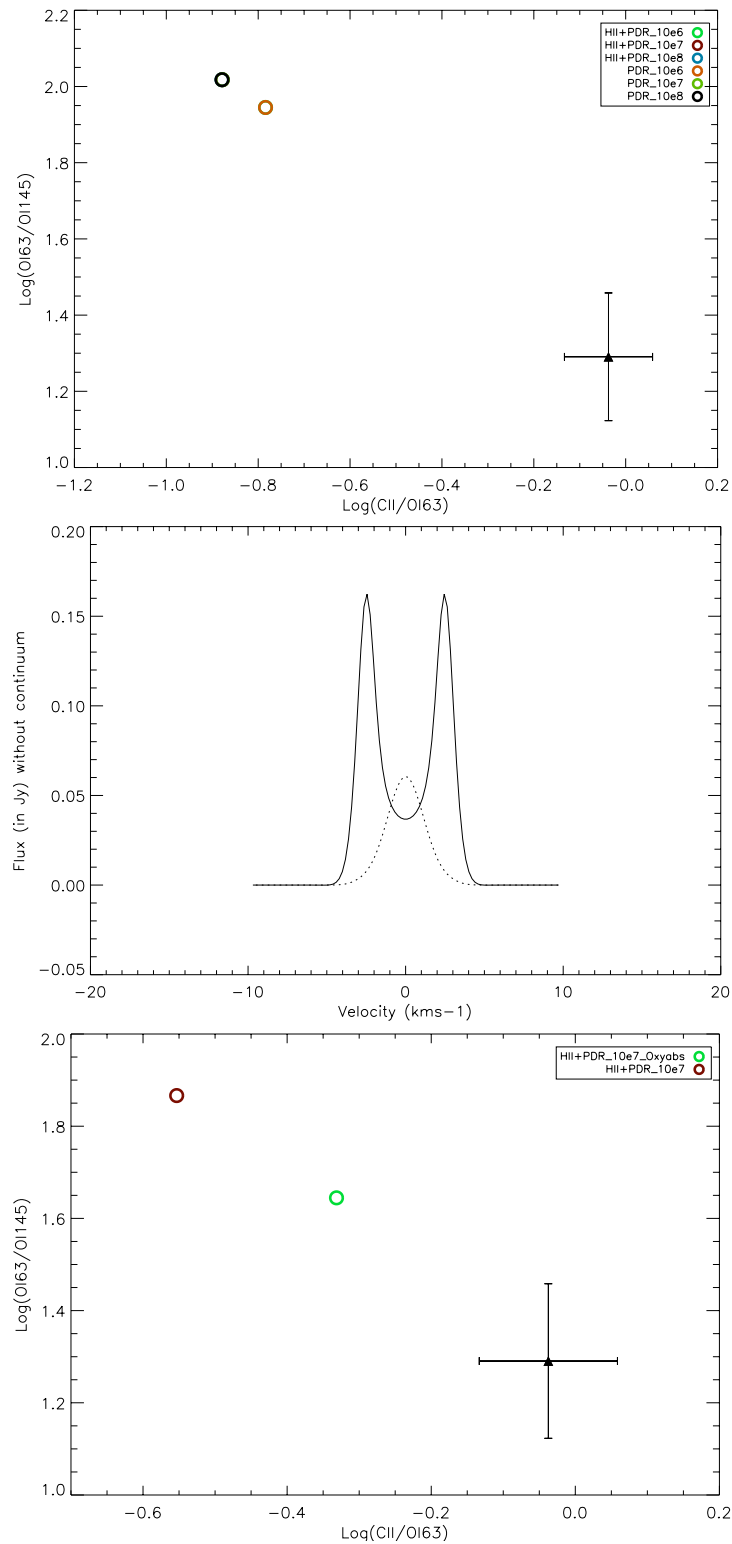


Figure 4.5: Model 013: with a computed $[\text{NIII}]_{57}/[\text{NII}]_{122}=1.86$ ratio. The top panel shows the $[\text{C II}]_{158} / [\text{O I}]_{63}$ ratio versus the $[\text{O I}]_{63}/[\text{O I}]_{145}$ ratio, the black triangle (with error bars) represents the observed ISO ratio for NGC 4038 (see Table 4.5) and the coloured circles represent either the contribution from both ionized and photodominated regions or just the contribution from the PDR. The middle panel shows the oxygen emission line profiles computed using the radiative transfer code (SMMOL), the dotted line represents the $[\text{O I}]_{145}$ emission line, while the solid line represents the $[\text{O I}]_{63}$ emission line with oxygen self absorption. The bottom panel is the same as the top panel, however only plotting the models with an age of 10^7 yr, for the PDR, and taking into account the effect of the $[\text{O I}]_{63}$ self absorption.

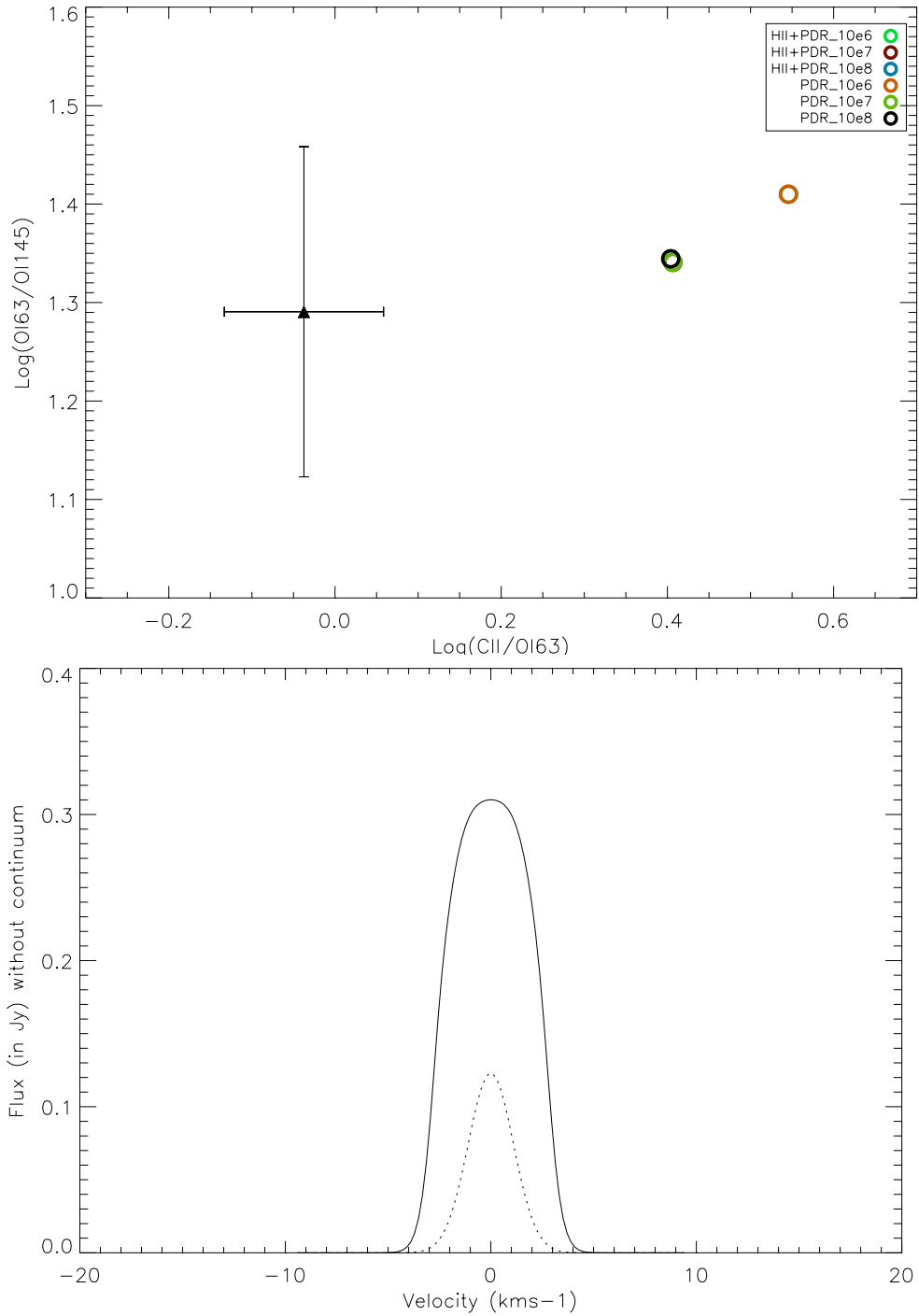


Figure 4.6: Model 019: with a computed $[\text{NIII}]_{57}/[\text{NII}]_{122}=3.82$ ratio. The top panel shows the $[\text{C II}]_{158} / [\text{O I}]_{63}$ ratio versus the $[\text{O I}]_{63}/[\text{O I}]_{145}$ ratio, the black triangle (with error bars) represents the observed ISO ratio for NGC 4038 (see Table 4.5) and the coloured circles represent either the contribution from both ionized and photodominated regions or just the contribution from the PDR. The bottom panel shows the oxygen emission line profiles computed using the radiative transfer code (SMMOL), the dotted line represents the $[\text{O I}]_{145}$ emission line, while the solid line represents the $[\text{O I}]_{63}$ emission line.

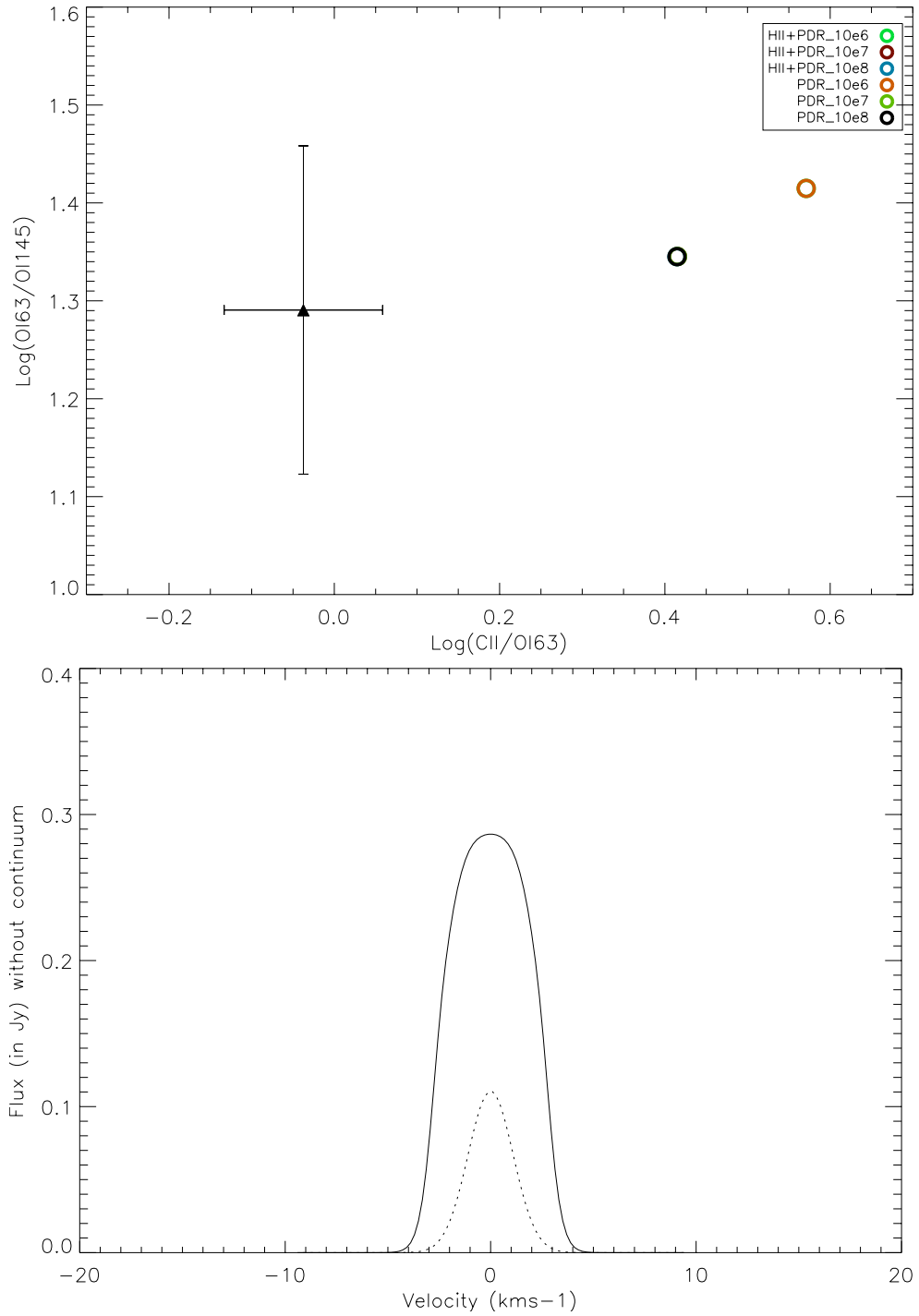


Figure 4.7: Model 021: with a computed $[\text{NIII}]_{57}/[\text{NII}]_{122}=3.75$ ratio. The top panel shows the $[\text{C II}]_{158}/[\text{O I}]_{63}$ ratio versus the $[\text{O I}]_{63}/[\text{O I}]_{145}$ ratio, the black triangle (with error bars) represents the observed ISO ratio for NGC 4038 (see Table 4.5) and the coloured circles represent either the contribution from both ionized and photodominated regions or just the contribution from the PDR. The bottom panel shows the oxygen emission line profiles computed using the radiative transfer code (SMMOL), the dotted line represents the $[\text{O I}]_{145}$ emission line, while the solid line represents the $[\text{O I}]_{63}$ emission line.

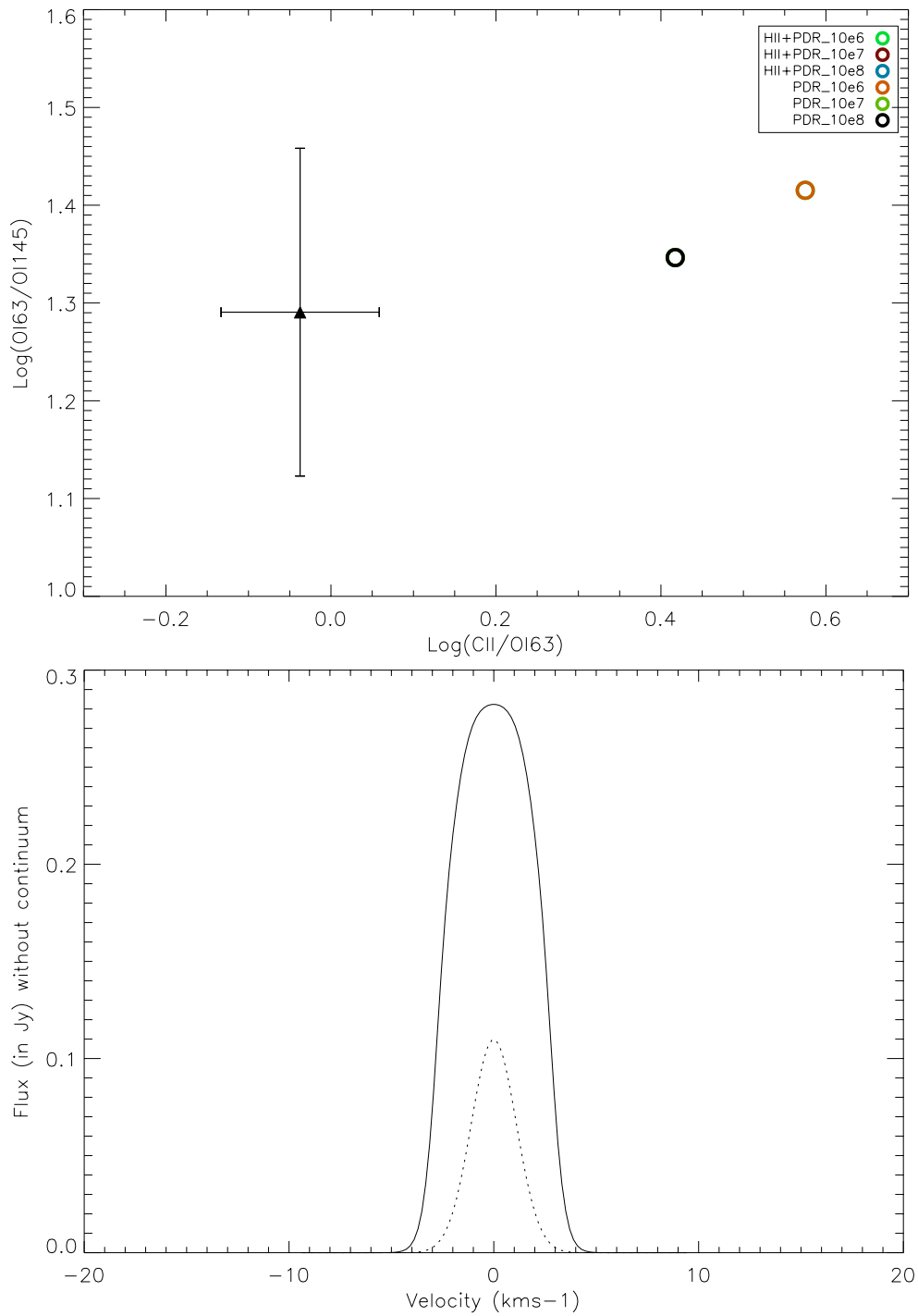


Figure 4.8: Model 022: with a computed $[\text{NIII}]_{57}/[\text{NII}]_{122}=3.72$ ratio. The top panel shows the $[\text{C II}]_{158}/[\text{O I}]_{63}$ ratio versus the $[\text{O I}]_{63}/[\text{O I}]_{145}$ ratio, the black triangle (with error bars) represents the observed ISO ratio for NGC 4038 (see Table 4.5) and the coloured circles represent either the contribution from both ionized and photodominated regions or just the contribution from the PDR. The bottom panel shows the oxygen emission line profiles computed using the radiative transfer code (SMMOL), the dotted line represents the $[\text{O I}]_{145}$ emission line, while the solid line represents the $[\text{O I}]_{63}$ emission line.

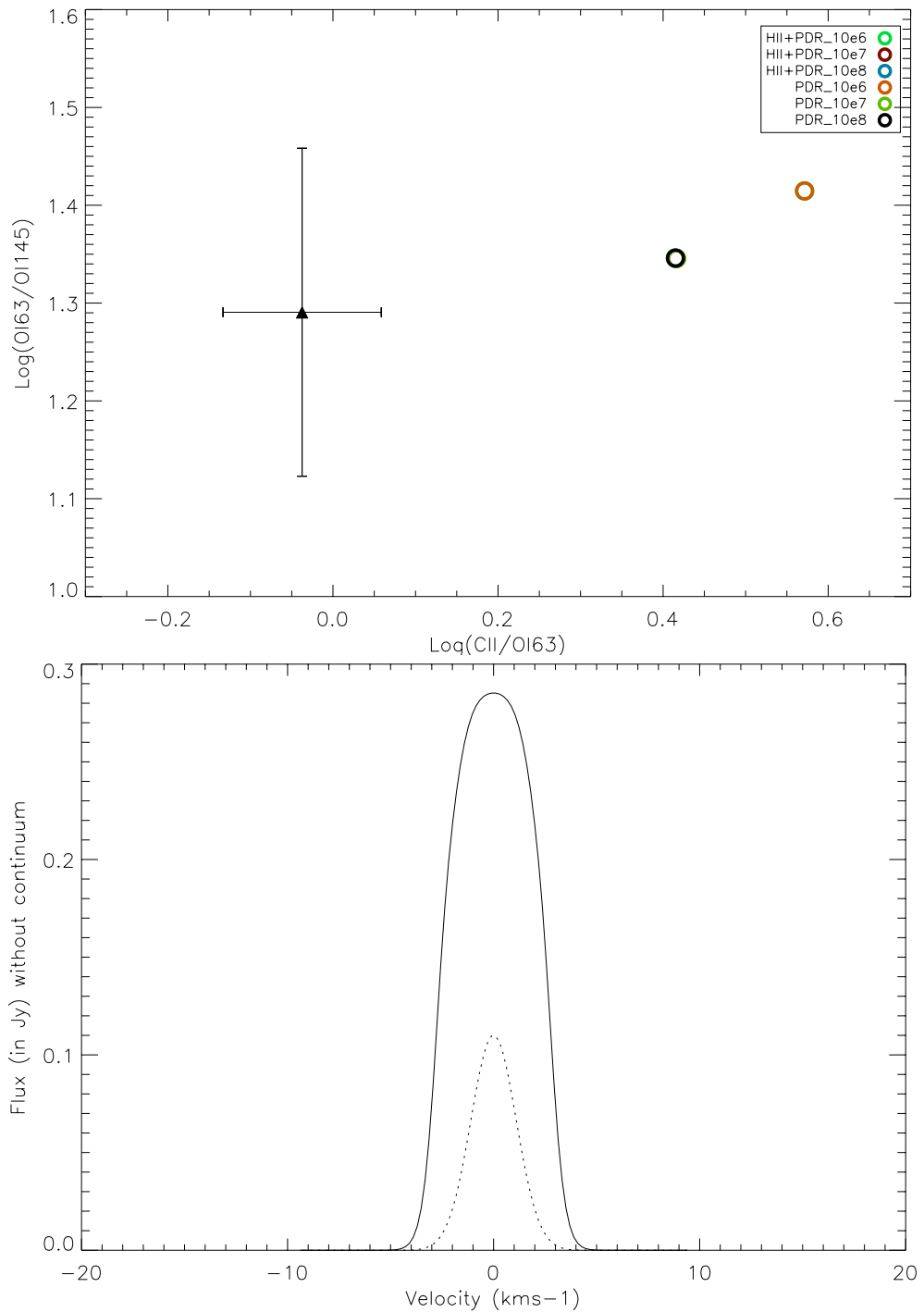


Figure 4.9: Model 023: with a computed $[\text{NIII}]_{57}/[\text{NII}]_{122}=3.65$ ratio. The top panel shows the $[\text{C II}]_{158} / [\text{O I}]_{63}$ ratio versus the $[\text{O I}]_{63}/[\text{O I}]_{145}$ ratio, the black triangle (with error bars) represents the observed ISO ratio for NGC 4038 (see Table 4.5) and the coloured circles represent either the contribution from both ionized and photodominated regions or just the contribution from the PDR. The bottom panel shows the oxygen emission line profiles computed using the radiative transfer code (SMMOL), the dotted line represents the $[\text{O I}]_{145}$ emission line, while the solid line represents the $[\text{O I}]_{63}$ emission line.

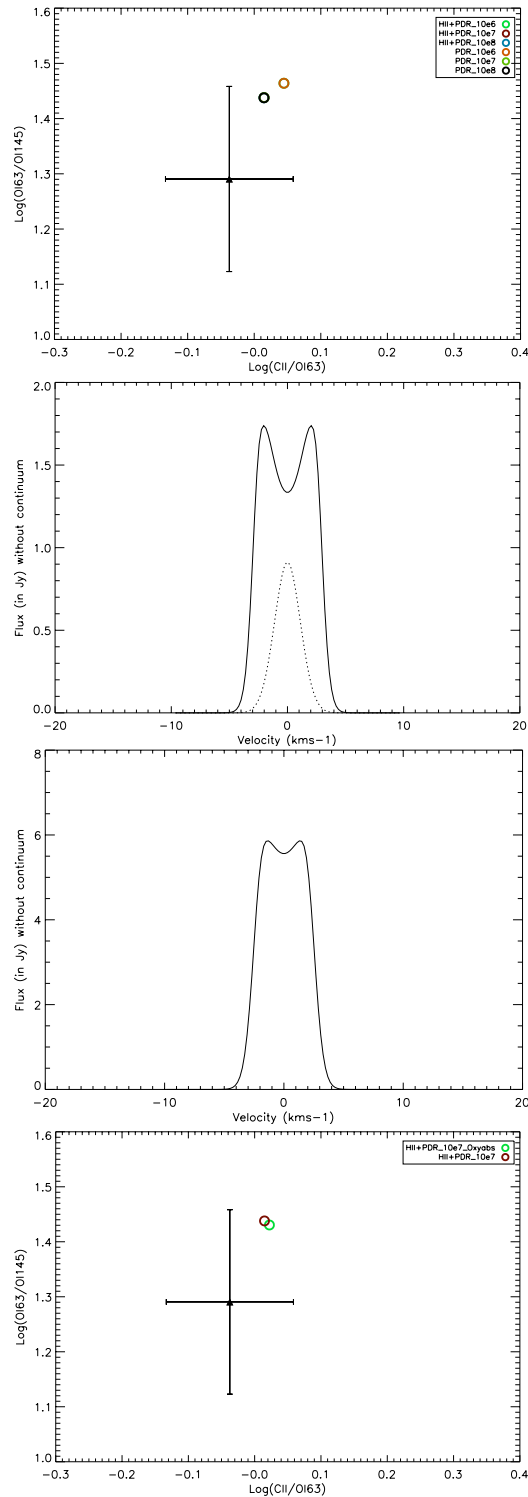


Figure 4.10: Model 024: with a computed $[N III]_{57}/[N II]_{122}=2.36$ ratio. The top panel shows the $[C II]_{158}/[O I]_{63}$ ratio versus the $[O I]_{63}/[O I]_{145}$ ratio, the black triangle (with error bars) represents the observed ISO ratio for NGC 4038 (see Table 4.5) and the coloured circles represent either the contribution from both ionized and photodominated regions or just the contribution from the PDR. The second panel shows the oxygen emission line profiles computed using the radiative transfer code (SMMOL), the dotted line represents the $[O I]_{145}$ emission line, while the solid line represents the $[O I]_{63}$ emission line with oxygen self absorption. The third panel shows that $[C II]_{158}$ is also self absorbed. The bottom panel is the same as the top panel, however only plotting the models with an age of 10^7 yr, for the PDR, and taking into account the effects of $[O I]_{63}$ and $[C II]_{158}$ self absorption.

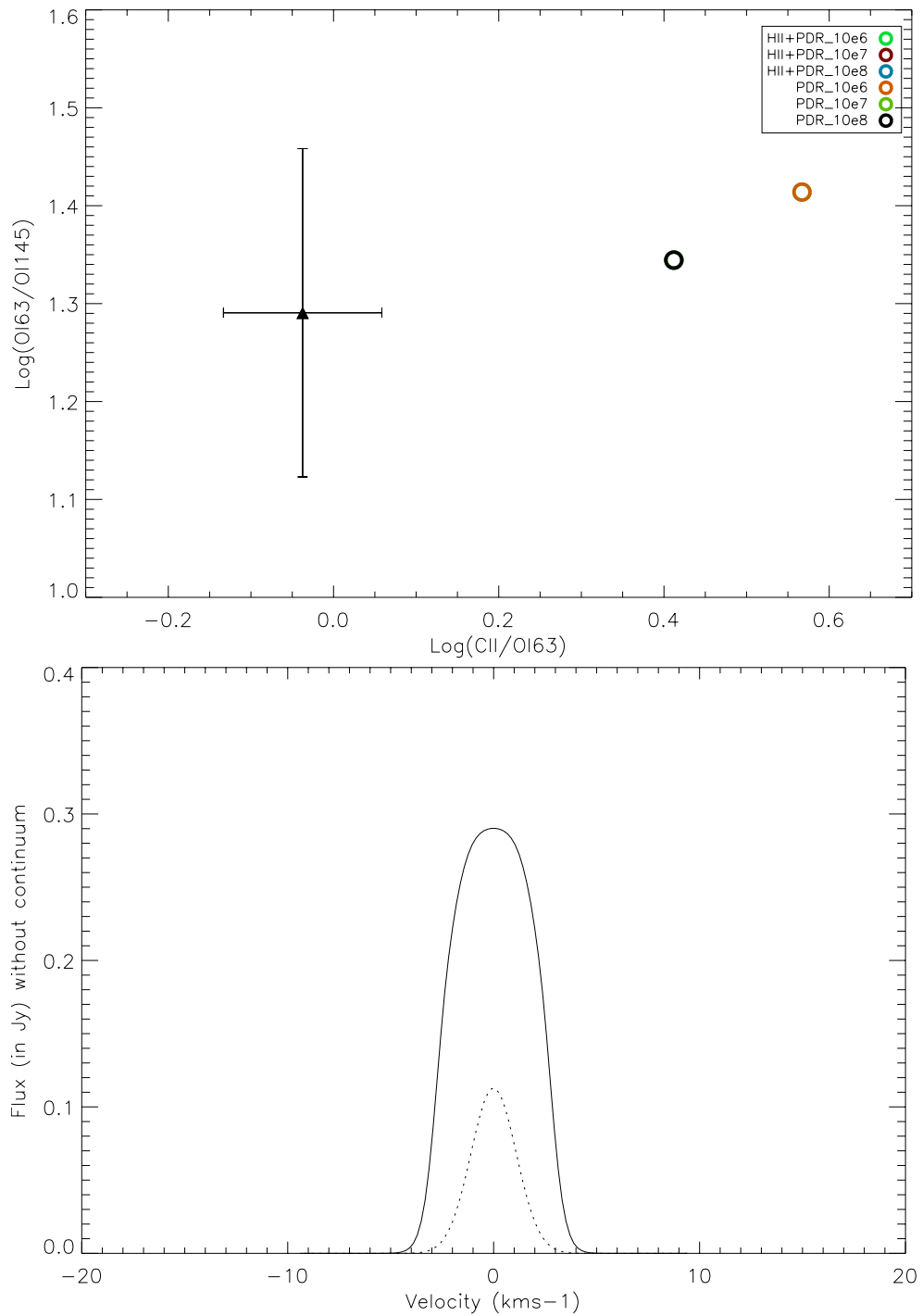


Figure 4.11: Model 025: with a computed $[\text{NIII}]_{57}/[\text{NII}]_{122}=3.73$ ratio. The top panel shows the $[\text{C II}]_{158}/[\text{O I}]_{63}$ ratio versus the $[\text{O I}]_{63}/[\text{O I}]_{145}$ ratio, the black triangle (with error bars) represents the observed ISO ratio for NGC 4038 (see Table 4.5) and the coloured circles represent either the contribution from both ionized and photodominated regions or just the contribution from the PDR. The bottom panel shows the oxygen emission line profiles computed using the radiative transfer code (SMMOL), the dotted line represents the $[\text{O I}]_{145}$ emission line, while the solid line represents the $[\text{O I}]_{63}$ emission line.

Table 4.11: Nitrogen emission lines obtained from the grid of MOCASSIN models. In bold the range of models that minimize the χ^2 with the number of degrees of freedom n , which is listed in the last column.

Index	[NIII] $57\mu\text{m}$ W m^{-2}	[NII] $122\mu\text{m}$ W m^{-2}	χ^2 $n=2$
001	2.92e-15	4.92e-19	48.93
002	3.27e-16	1.76e-16	26.76
003	2.94e-15	5.00e-19	49.06
004	1.47e-15	1.12e-16	27.47
005	1.14e-15	9.38e-17	31.68
006	1.16e-15	8.65e-17	32.73
007	8.13e-16	1.14e-16	30.71
008	2.63e-16	2.04e-16	24.20
009	4.73e-17	1.92e-17	54.34
010	3.35e-16	1.74e-16	26.92
011	1.16e-15	8.60e-17	32.81
012	4.65e-16	3.37e-19	53.28
013	3.24e-16	1.74e-16	27.04
014	3.37e-16	1.87e-16	25.33
015	3.37e-16	1.83e-16	25.81
016	3.44e-16	1.84e-16	25.61
017	6.47e-17	2.64e-19	57.75
018	1.77e-15	7.81e-16	20.26
019	2.70e-15	7.05e-16	13.30
020	1.78e-15	7.66e-16	18.35
021	2.57e-15	6.84e-16	10.76
022	2.56e-15	6.88e-16	11.08
023	2.55e-15	6.98e-16	11.96
024	9.34e-16	3.96e-16	4.6
025	2.54e-15	6.82e-16	10.46

4.5 Comparison of CO and [CI] observations

In the previous Section, we concluded that model 024 best reproduces the observed ISO $[\text{NIII}]_{57}/[\text{NII}]_{122}$ ratio, therefore we decided to investigate if this model is also able to reproduce the CO rotational emission lines and [CI] observed with the CSO by Bayet *et al.* (2006). Observations of CO can provide constraints on the density and temperature of the dense star-forming gas in galaxies, while observations of [C I] trace photon-dominated regions and can provide information on the amount of atomic carbon in molecular clouds. Table 4.12 lists the results from the gaussian fits derived from spectra of the Antennae galaxy (NGC 4038 nucleus) taken with the CSO telescope (see Tab B2, Bayet *et al.* 2006). The observed lines are indicated in the first column.

Table 4.12: Results from the gaussian fits derived from spectra of the Antennae galaxy (NGC 4038 nucleus) taken with the CSO telescope (see Tab B2, Bayet *et al.* 2006). The observed lines are indicated in the first column.

Transition	Freq (GHz)	Beam size(")	Offset position(")	Intensity (W m⁻²sr⁻¹)
C I(³ P ₁ – ³ P ₀)	492.162	21.90	(0,0)	$9.2 \times 10^{-10} \pm 1.5 \times 10^{-10}$
¹² CO(1–0)	115.271	21.90	(0,0)	$7.2 \times 10^{-11} \pm 1.4 \times 10^{-11}$
¹² CO(2–1)	230.538	21.90	(0,0)	$6.4 \times 10^{-10} \pm 1.3 \times 10^{-10}$
¹² CO(3–2)	345.796	21.90	(0,0)	$1.6 \times 10^{-9} \pm 7.2 \times 10^{-11}$
¹² CO(4–3)	461.041	21.90	(0,0)	$2.5 \times 10^{-9} \pm 1.9 \times 10^{-10}$
¹² CO(6–5)	691.473	21.90	(3,3)	$1.1 \times 10^{-8} \pm 1.3 \times 10^{-9}$
¹² CO(7–6)	806.652	21.90	(3,3)	$8.7 \times 10^{-10} \pm 2.4 \times 10^{-10}$

We assumed that the observed CO rotational emission lines listed in Table 4.12 can be reproduced by one gas component (i.e. same physical parameters, only one PDR) as shown in Fig 22 by Bayet *et al.* (2006). We decided to calculate the CO χ^2 for the best fit H II models listed in bold in Table 4.11 to see if they can trace the gas in PDRs. Table 4.13 lists the CO rotational emission lines obtained from the grid of MOCASSIN models and the calculated χ^2 . In the last column the [CI] emission line is also predicted. As seen in Table 4.13 the values of χ^2 are close to each others for all seven model results. The gradient in χ^2 is very low, this implies that we cannot reproduce the PDR gas component with the same physical parameters assumed for the H II regions. In addition, it may be possible that we are trying to compare one modelled

PDR with more than one observed PDR. In fact, the CSO beam is $\sim 22''$ that corresponds to ~ 2 kpc and our modelled PDR region is ~ 45 pc. Thus, it is plausible to assume that, at least ~ 50 PDRs are within the beam size instead of assuming one big PDR in the CSO beam. This is something that future ALMA observations can easily reveal. However, the failure of models to reproduce observations can be also attributed to the low volume density assumed which make difficult to reproduce properly the CO emission line that generally emits in regions with higher density values.

Table 4.13: CO rotational emission lines obtained from UCL_PDR for the best fit models listed in bold in Table 4.11 and the calculated χ^2 with the number of degrees of freedom n . The [CI] emission line is also predicted.

Index	$^{12}\text{CO}(1-0)$ $\text{W m}^{-2}\text{sr}^{-1}$	$^{12}\text{CO}(2-1)$ $\text{W m}^{-2}\text{sr}^{-1}$	$^{12}\text{CO}(3-2)$ $\text{W m}^{-2}\text{sr}^{-1}$	$^{12}\text{CO}(4-3)$ $\text{W m}^{-2}\text{sr}^{-1}$	$^{12}\text{CO}(6-5)$ $\text{W m}^{-2}\text{sr}^{-1}$	$^{12}\text{CO}(7-6)$ $\text{W m}^{-2}\text{sr}^{-1}$	χ^2 $n=6$	$\text{C I}(^3\text{P}_1-^3\text{P}_0)$ $\text{W m}^{-2}\text{sr}^{-1}$
019	9.19×10^{-12}	4.37×10^{-11}	2.77×10^{-11}	1.27×10^{-11}	3.00×10^{-11}	3.41×10^{-11}	128.79	1.96×10^{-9}
020	6.64×10^{-12}	2.76×10^{-11}	1.43×10^{-11}	5.57×10^{-12}	2.14×10^{-11}	2.57×10^{-11}	129.70	2.12×10^{-9}
021	9.19×10^{-12}	4.36×10^{-11}	2.76×10^{-11}	1.26×10^{-11}	2.90×10^{-11}	3.28×10^{-11}	128.81	1.95×10^{-9}
022	9.18×10^{-12}	4.36×10^{-11}	2.76×10^{-11}	1.25×10^{-11}	2.88×10^{-11}	3.26×10^{-11}	128.82	1.94×10^{-9}
023	9.19×10^{-12}	4.37×10^{-11}	2.76×10^{-11}	1.25×10^{-11}	2.90×10^{-11}	3.28×10^{-11}	128.82	1.98×10^{-9}
024	6.58×10^{-12}	2.72×10^{-11}	1.41×10^{-11}	5.54×10^{-12}	2.14×10^{-11}	2.57×10^{-11}	130.87	2.11×10^{-9}
025	9.19×10^{-12}	4.37×10^{-11}	2.76×10^{-11}	1.26×10^{-11}	2.92×10^{-11}	3.31×10^{-11}	128.81	1.95×10^{-9}

4.6 Conclusions and future work

This chapter discusses the attempt to model the nucleus of NGC 4038 using the ionization MOCASSIN code, the photodissociation UCL_PDR code and an interface between the two. I investigated the contribution of [C II] 158 μm , [O I] 63 and 145 μm coming from the H II region, using the 3D MOCASSIN code. I then computed the radiation field at the ionization front, which links the H II and the PDR regions, and used it as an input for the UCL_PDR code. The nucleus is chosen in order to reduce contributions from different gas components other than the ionized and photodissociated regions. I proceeded to analyse step by step the best fit model to, first, the H II region and, subsequently, the PDR region.

- I measured the electron density (n_e) and subsequently the hydrogen density (n_H) using the ratio of [O III] 88 and 52 μm far infrared fine structure emission lines obtained measuring the ISO LWS spectra.
- Using SB99, (Leitherer *et al.* 1999) I provided a representation of the stellar population

- in NGC 4038 as an input for the 3D photoionization code MOCASSIN. The H II region, within the nucleus of NGC 4038, is fully described by MOCASSIN and the full spectral energy distribution (SED) is computed along with the most important far infrared fine structure emission lines (e.g. O I, C II, N III, N II). Through the use of an interface, the radiation field at the ionization front is calculated integrating the MOCASSIN SED in the range $912\text{\AA} \leq \lambda \leq 2400\text{\AA}$. This radiation field (in Habing) is then fed into the plane parallel UCL_PDR code, which describes the physical and chemical conditions of the photodominated region, within the nucleus of NGC 4038, and computes the cooling and rotational emission lines ([C II] $158\mu\text{m}$, [O I] 63 and $145\mu\text{m}$, CO).
- A grid of 25 H II region models and 25 PDR region models were computed and used to investigate the best fit to the observed ISO $[\text{NIII}]_{57}/[\text{NII}]_{122}$ ratio and the $[\text{C II}]_{158}/[\text{O I}]_{63}$ ratio versus the $[\text{O I}]_{63}/[\text{O I}]_{145}$ ratio respectively. A detailed analysis of the combined results from MOCASSIN and UCL_PDR was provided. In addition, the oxygen emission line profiles were studied using the radiative transfer SMMOL code.
 - Finally, the χ^2 for the $[\text{NIII}]_{57}$ and $[\text{NII}]_{122}$ emission lines was computed, because these emission lines arise only from the H II region and can better constrain the physical conditions within it. This led to the conclusion that model 024 is the best fit to the observed ISO $[\text{NIII}]_{57}/[\text{NII}]_{122}$ ratio. The main reason of this better fit to the observations can be attributed to the inclusion of a grain mixture of silicates and graphite, and Md/Mg ratio in the input parameters. However, comparing individual single emission lines of $[\text{NIII}]_{57}$ and $[\text{NII}]_{122}$ from MOCASSIN with ISO observations (see Table 4.5), indicates that within the ISO beam multiple H II regions are present. We estimate that about 10 are needed to better match the ISO observations.
 - In addition, we also calculated the CO χ^2 for the best fit H II models listed in bold in Table 4.11 to see if they can trace the gas in PDRs. Table 4.13 shows that the values of χ^2 are quite large for all seven model results; this implies that we cannot reproduce the PDR gas component with the same physical parameters assumed for the H II regions. This may be explained by the fact that we are trying to compare one modelled PDR with more than one observed PDR. We estimate that about 50 PDRs are needed to better match the CSO observations.

Future tasks will be to run more PDR models spanning a different range of densities and metallicities, as the parameters used throughout the UCL_PDR grid consider only standard

physical conditions in these regions. In fact, the failure of models to reproduce observations can be also attributed to the low volume density assumed which make difficult to reproduce properly the CO emission line that generally emits in regions with higher density values. In addition, it will be interesting to investigate if CO rotational emission lines can trace more than one gas component. Future observations with ALMA and PACS we will be able to constrain the physical and chemical characteristics of galaxy such as the Antennae.

COUPLING OF THE UCL_PDR AND MOCASSIN CODES

Generally when we think about H II and PDR regions we consider them as two separate entities. This is partially true since the physical and chemical conditions are indeed quite different. However, they are both regulated by the ultraviolet radiation field coming from OB stars. The OB stars, either found embedded within molecular clouds or at the edge of a molecular cloud, also provide the ionizing flux that governs the transition between atomic hydrogen and molecular hydrogen.

The gas in H II regions is in atomic form and the hydrogen is completely ionised, while the gas in PDRs is predominantly in molecular form as the hydrogen makes the important transition from H to H₂. Despite these differences, these two regions are dynamically linked by a continuous flow (Abel *et al.* 2007); the gas is in fact coupled together with the radiation field and the physical properties of the PDRs are a consequence of the transport of gas and interstellar radiation through the H II regions.

It is also known that some of the brightest PDR emission lines can be strengthened by contributions coming from H II regions (Abel *et al.* 2007).

From this evidence and work performed in previous chapters, we were compelled to test the feasibility of producing a unique code able to model both the physical and chemical conditions in objects where emission is dominant in both PDRs and H II regions.

This chapter will highlight the computational aspects of the UCL_PDR and MOCASSIN codes, which have been briefly described in Chapter 2, that are relevant to this feasibility test. We will discuss what we need in order to couple the two codes such as compatibility of chemical

networks, escape probability treatments and heating and cooling mechanisms. Finally we will also present the issues we faced while trying to couple the two codes such as the use of adaptive grids and the multiple dimensions.

5.1 The UCL_PDR code

The UCL_PDR code is comprised of several computational components, each of which plays an important role in the analysis of a PDR region. In this section I will describe the components that are most relevant to my work.

- The escape probability approximation: The interstellar gas is cooled by collisional excitation of the atomic, molecular and ionic components of the gas followed by radiative decay. Those photons that are not absorbed elsewhere in the cloud carry away energy and cool the cloud. To calculate the cloud cooling efficiency, the UCL_PDR code uses the method from de Jong *et al.* (1980) where the equations of statistical equilibrium to find the level populations as a function of depth z into the cloud are solved. The cooling by excitation of the fine structure levels of C^+ and C , and the rotational levels of CO in collisions with electrons, hydrogen atoms and hydrogen molecules are computed. The cooling rate due to a radiative transition from level i to levels j of some atomic or molecular system is given by:

$$\Lambda_{ij}(z) = h\nu_{ij}n_i(z)\beta(\tau_{ij})A_{ij}\left\{\frac{S_{ij}(z) - P_{ij}(T_B)}{S_{ij}(z)}\right\} \quad (5.1)$$

where ν_{ij} is the transition frequency, $n_i(z)$ is the population of level i , β is the escape probability of photons at the optical depth τ_{ij} corresponding to the depth z into the cloud, A_{ij} is the spontaneous transition probability, $S_{ij}(z)$ is the line source function and $P_{ij}(T_B)$ is the Planck function at the background temperature $T_B = 2.7$ K (de Jong *et al.* 1980). The escape probability β equals 1 at the surface of the layer so that the radiation field in the line reduces to the ambient blackbody radiation field at temperature T_B . The assumption made is that the level populations along any ray from the surface to z are equal to the level populations at z . (See Appendix B de Jong *et al.* (1980) for more details.)

- The adaptive grid: In order to properly solve the H/H_2 transition, it was necessary to adopt an adaptive grid close to the transition front. Inside a small grid step, an emission line is not expected to be optically thick and the step between the grid points has to be

small enough in order to avoid variations in the physical parameters. In fact, all the escape probabilities are set to 1 at this depth. A more thorough description of the adaptive grid is provided in Sec 5.3.2.

- The ordinary differential equations (ODEs): A solution of a system of ordinary differential equations can be of the form: $\dot{Y}(i) = f(Y(1), Y(2), \dots, Y(n))$, where this expression describes the time rate of change of the abundances of all species in solid and gas phase. The code takes the initial elemental abundances that are then used, in each depth step, to calculate the fractional abundances from the ODEs (see Sec 5.3.3).
- The chemical network: Different chemical networks can be employed using different approaches of steady state or time dependency. The chemical network in the UCL_PDR code contains 128 species including nitrogen and sulphur-bearing molecules with over 1700 reactions, including the ion-molecule, photoionization and photodissociation reactions. The reaction rates are taken from the UMIST99 database with some modifications (Le Teuff *et al.* 2000). A study of the how the use of steady state approximation affects the chemistry compared to a full time dependent model has been carried out by Bell *et al.* (2006b) and a new comparison is presented in Sec 5.3.4.

5.2 The MOCASSIN code

In a similar way to the UCL_PDR code, the MOCASSIN code encompasses various computational components that facilitate the analysis of an ionized region. In this section I will describe the components that are the greatest source of complication for the coupling.

- The Monte Carlo radiative transfer approximation: The Monte Carlo approach is used to solve the radiative transfer problem in order to iteratively determine the temperature and ionisation stratification for a spherically symmetric photoionised nebula of uniform density (Lucy 1999).
- The parallelization: The main limitation in MOCASSIN is imposed by the computer power available. This implies the need for a system with multi-processing capabilities in order to accelerate the computation time. Thus, to improve the working of MOCASSIN a MPI (Message Passing Interface) formalism was chosen, which permits information to be passed from one processor to another and, therefore, does not necessitate a system with shared memory facilities. The presence of MPI, however, imposes that any additional

subroutines need to also be parallelized in order not to slow down the processing speed of the code.

- The dimensionality and the grid cells: The geometry of the MOCASSIN code is approximated by a cuboidal grid. Within each uniform cell, thermal balance and ionization equilibrium are imposed and the path of energy packets, inside each cell, is completely random.
- The multiple sources: the code has the ability to position multiple exciting stars at non-central positions in the nebula.

5.3 The Feasibility of the coupling

In this section the first approach for the feasibility test is provided including the necessary steps to implement the coupling of the codes. Computationally speaking the MOCASSIN code is faster than the UCL_PDR code and, as I remarked earlier, MOCASSIN is the first 3 dimensional Monte Carlo radiation transfer code. Our original aim was the development of a new code based on the highly computational techniques used in the MOCASSIN code, coupled with the fundamental subroutines of molecular chemistry reactions computed in the UCL_PDR code. In order to couple the two codes I needed to test the feasibility of the coupling with the following approach:

- Update the opacity, which in MOCASSIN only includes dust, to insert molecules.
- After having calculated the packet's energy and its trajectories, the dust and gas thermal balance and gas ionization balance need to be satisfied. MOCASSIN stops the calculations at a point in the ionization front beyond which the neutral fraction rises, so the processes in the neutral zone beyond the ionization front are not yet treated. Many of the far-infrared fine structure lines observed from a nebula originate predominantly from the neutral photodissociation region surrounding the ionized gas (Liu *et al.* 1995), so the processes that dominate the heating and cooling within the neutral zone need to be incorporated. In both MOCASSIN and UCL_PDR, the gas temperature is determined using an iterative process to balance the total heating and cooling rates. The implicit assumption made in this approach is that the gas has to reach thermal equilibrium.
- Compute CO rotational lines and fine structure emission lines, which are the most

- important cooling mechanism, using the escape probability formalism provided by the radiative transfer code of Spaans (1996).
- Insert the molecular chemical network which needs to include reactions among O, C, N, S, H, He species for A_v up to 3 mags, because at this A_v the FUV is almost totally attenuated by the dust.
 - The final step would be the testing and benchmarking of the new MOCASSIN code after having decided its criterium of convergence. Since a criterium of convergence for ionized regions already exists (that is, if $n(\text{H}^+)/n(\text{H}) < 0.05$, then we are in ionized region), it is necessary to have a similar criterium for PDRs.

Initial work involved the testing of the current version of MOCASSIN by running the established gas-only benchmark models. MOCASSIN can be run either on a single computer or on multiple processors via the before mentioned MPI routines. The code was compiled and run on *Keter*, a SUN Microsystems SunFire V880/V890 cluster. The cluster is comprised of 3 subclusters. The following sections describes of the main issues that arose, such as the escape probability formalism, the adaptive grid, the ordinary differential equations and the time dependent vs steady state approaches.

5.3.1 Escape probability formalism

This section describes the main concept of escape probability and the importance of using the right computational approach for treating this method in the coupling.

The cooling of the gas by line emission depends on atomic and molecular data as well as on the radiative transfer. Within an arbitrary source, the frequency, ν , and direction, \vec{k} , of an individual photon can be specified. The photon, which we are considering, is emitted at the point \vec{r} following its creation with a collisionally excited ion. This photon is emitted from the upper level of an assumed two-level atom and after that, if it encounters another such two-level atom in the course of its flight, it will be absorbed and may be re-emitted in a different direction and with a different frequency. The probability of its absorption is proportional to the atomic absorption coefficient $\alpha(\nu)$. The atom may be collisionally de-excited or otherwise perturbed before the re-emission, so that the emission probability must include a factor $1 - \epsilon$, where ϵ is the destruction probability that the photon is lost in the scattering event. The effective escape probability is the possibility that a photon emitted at point \vec{r} , with frequency ν , in the direction \vec{k} , will ultimately escape from the source, irrespective of the number of scatterings encountered

before escape. The problem in the escape probability treatment is how to decouple the radiative transfer calculations from the calculations of the level populations. A common approximation to the radiative transfer problem is the assumption of escape probabilities for the cooling lines (de Jong *et al.* 1980).

We need to properly identify where the HII region meets the PDR for measuring the right amount of radiation field contributing to the resultant spectra. Also, the concept of photon escape probability is fundamental to solve the Voigt profile of an emission line. The Voigt profile is a convolution of a Lorentz profile and a Gaussian profile in which a spectral line is broadened by two types of mechanisms, one of which alone would produce a Gaussian profile (usually, as a result of the Doppler broadening), and the other would produce a Lorentzian profile.

The first escape probability method was devised by Sobolev (1960) for solving line transfer problems in rapidly expanding stellar atmospheres. The basic idea was to use an arbitrary factor that determines the chance that a photon at some position in the cloud can escape the system. Sobolev (1960) derived the following general result for the escape probability:

$$\beta_s = \frac{1}{4\pi} \int d\Omega \frac{1 - e^{-\tau_s}}{\tau_s} \quad (5.2)$$

which gives the probability that a photon, emitted at an optical depth τ_s , escapes the spherical system. When β_s is expressed in terms of the optical depth τ in the direction of the observer, the projected one dimensional escape probability can be estimated as:

$$\beta_s = \frac{1 - e^{-\tau_s}}{\tau_s} \quad (5.3)$$

This form is called the Sobolev or large velocity gradient (LVG) approximation. When in a plane parallel medium the probability to escape is given by the expression:

$$\beta_s = \frac{1 - e^{-3(\tau_s)}}{3\tau_s} \quad (5.4)$$

One can choose the appropriate escape probability method depending on the condition of the system. UCL_PDR uses an approximation of the 1D Sobolev escape probability. Unfortunately it would have been taken a substantial amount of time to transform this escape probability approximation into a 3D escape probability approximation for the coupling (see Sec 5.1). The following section will describe the escape probability method that we decided to use for the feasibility test.

5.3.1.1 Computational complications of including the escape probability method.

In order to include the right escape probability formalism I used the Poelman & Spaans (2005) radiative transfer code which calculates the escape probability in 3 dimensions. In fact, this code has a newly developed escape probability method combined with the inhomogeneous numerical code of Spaans (1996), which calculates the transfer of line-radiation of ortho- and para-H₂O in a homogeneous 3-dimensional spherical cloud by use of an escape probability approximation. The Spaans (1996) code employs a Monte Carlo method to calculate the chemical structure and the thermal balance in PDRs, as well as the distribution of water abundance and molecular hydrogen density simultaneously. The calculation of the escape probability in the Poelman & Spaans (2005) code uses the Takahashi *et al.* (1983) approximations in which the mean radiation intensity is computed with the following equation:

$$\langle J_\nu \rangle_{ul} = (1 - \epsilon_{ul})S_L + (\epsilon_{ul} - \eta_{ul})B(T_d) + \eta_{ul}I^* \quad (5.5)$$

where S_L is the frequency independent line source function, $B(T_d) = B_{\nu_{ul}}(T_d)$ is the Planck function at the dust temperature T_d , $I^* = I_{\nu_{ul}}^*$ and I^* is assumed isotropic. The probability that a photon escapes line absorption, ϵ_{ul} , is described by:

$$\epsilon_{ul} = \delta_{ul} + \int \frac{d\Omega}{4\pi} \int_0^\infty d\nu \phi_\nu \frac{t_L}{t_L + t_d} e^{-(t_L - t_d)} \quad (5.6)$$

where t_L and t_d are line and dust optical depth, respectively, δ_{ul} is the probability per scattering that a photon will be absorbed by dust and η_{ul} is the probability that a photon escapes dust absorption as well as line absorption, and therefore contributes to the line emission observed by a distant observer. Therefore, Poelman & Spaans (2005) applied Eq 5.5 and Eq 5.6 to their code with the only difference that the probability for a photon to escape in a point, $p(x, y, z)$, equals the sum of the escape probabilities over all directions such as $\beta_{ij}(x, y, z) = \sum_k \beta_{ij}(x, y, z, \mathbf{k})$, where \mathbf{k} is the direction of the photon escaping the cloud. The number of directions is arbitrary, but a 6-ray approximation is implemented for the 3D models. In this approximation the calculation of the probability for a photon to escape along 6 directions is computed. The sum of the 6 probabilities gives the total escape probability.

The MOCASSIN code is parallelized and this implies that in order to maintain the same computational speed we needed to parallelize the part of the Poelman & Spaans (2005) code in which the escape probability is being treated. While attempting to parallelize the code, it came to our attention that this would have only been possible through fundamentally rewriting the entire code. This is due to the fact that the piece of the code that we required was embedded

in the central loop, meaning that in order to parallelize this piece we would have had to either parallelize the entire code or to adapt that formalism to our code. Both of these options were too time consuming for the purpose of this project.

5.3.2 Adaptive grid and H₂ self shielding

The main characteristic of photodissociated regions is that they have several distinct zones. These areas consist of multiple layers where atoms are taking molecular form or where molecules are photodissociated. All these zones are regulated by processes that may vary according to depth into the cloud. Since transitions such as H/H₂ can occur in different parts of the cloud and are very sensitive to the physical parameters, from a computational point of view, it is necessary to resort to an adaptive grid in order to accurately solve this transition. For the purpose of convergence, the first layer has to be very thin and the grid has to be finer than the scale-length of variation of the physical parameters in the cloud (see Fig 5.1 (a)).

For instance, we do not expect an emission line to easily become optically thick inside the layer nor do we expect the UV flux to diminish. Generally we refer to the adaptive grid in terms of depth step points or grid points. The grid size step is very important, in fact the first layer has to be extremely thin to obtain the right temperature. One can artificially set all escape probabilities to 1 at this depth. The next few layers should also be optically thin at least for the C II line, then the step size can be broadened so that the extinction increases. Because of the strong dependence of heating on the extinction, a step size lower than the typical extinction $\exp(-2.5A_v)$, has to be applied in order to obtain a physical output. It is necessary to carefully follow the H/H₂ and CII/CI/CO front to avoid non-physical results. The adaptive grid of depth-steps is used such that the variation in the H₂ self-shielding function is small between depth points (10%). This is fundamental for solving the H/H₂ transition accurately. In fact, after the H/H₂ transition is fully resolved, the distance between depth-steps points is increased. The increasing A_v is calculated using a variable maximum step size in order to increase the depth step after reaching the H/H₂ transition. In order to speed up the code for depths well beyond the critical H/H₂ transition transition region, the less constrictive convergence criterion of 80% variation in the H₂ self-shielding factor (that is $n(\text{H}_2)/n(\text{H}) > 0.8$) was imposed. Before this point is reached the stricter criterion of 20% variation in the H₂ self-shielding factor is imposed. The column density of H₂ is considered to be similar to that at the previous depth step and the column density computed at the depth-1 (see Fig 5.1 (a)) is used as a guess for the H₂ column density at the new depth step. This analytical approximation, depending on the H₂ column density, is a requirement

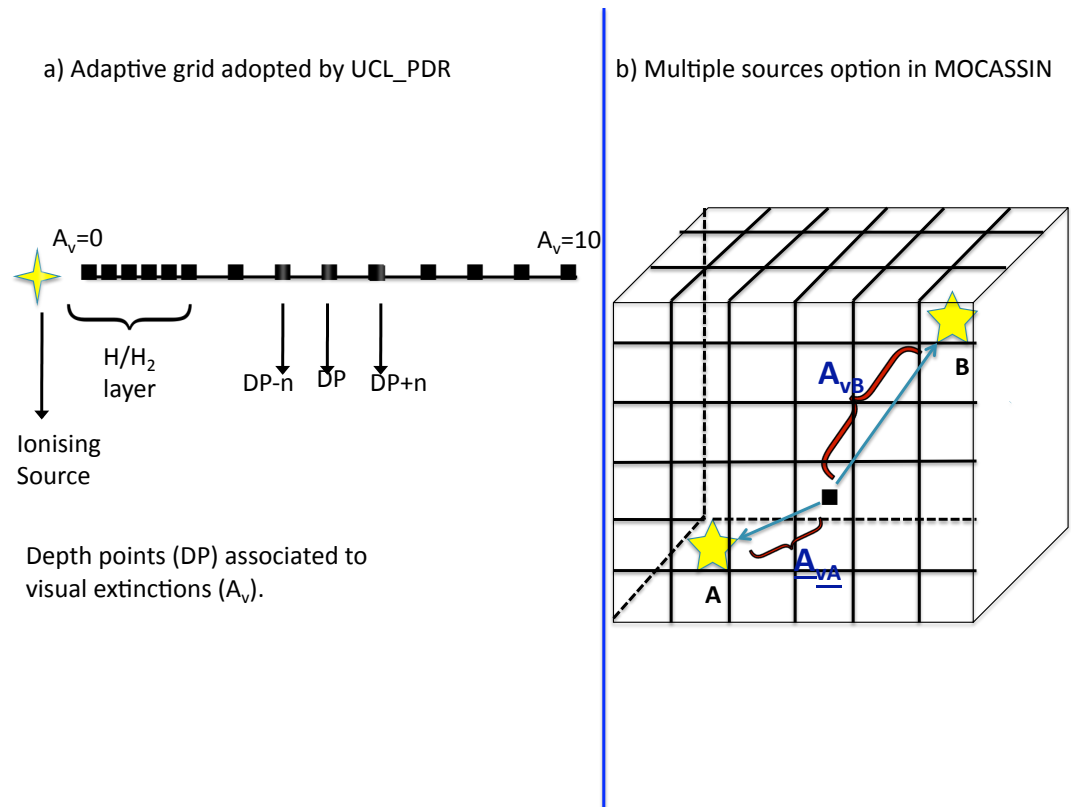


Figure 5.1: a) Representation of the adaptive grid used in the UCL_PDR code. The depth step points correspond to a certain value of A_v . The grid size is extremely thin at the first layer; after the H/H₂ transition is fully resolved, the distance between depth-steps points is larger. b) 3D representation of a system of grid cells with multiple ionizing sources. The point indicates the cell of interest and stars representing the ionizing sources. A_{vA} is the A_v relative to source A and A_{vB} is the A_v relative to source B.

of the adaptive grid that allows the H₂ single line to stay optically thin across a grid cell. If this is not the case then the entire calculation of the H₂ self shielding is not physically correct. Therefore the H₂ self shielding factor, calculated according to the approximation of Draine & Bertoldi (1996)[Eq.37], is computed only when the photodestruction rates are calculated. The correlation between the H₂ self shielding factor and the analytical approximation of the H₂ column density together with the refinement of the grid to reach the H/H₂ transition, makes the presence of the adaptive grid essential.

Also, the use of the adaptive grid in the UCL_PDR code is related to the visual extinction parameter that, indeed, in the MOCASSIN structure is completely irrelevant. This is because the visual extinction is only significant when there is a starting point such as $A_v=0$, with respect

to the radiating source, and from this point it is possible to increase A_v . In a three dimensional system the ionising sources can be positioned anywhere, therefore in a given grid cell the visual extinction could be equal to zero relative to one source and equal to ten relative to another source considering a system of multiple ionising sources (see Fig 5.1 (b)).

Dust is the main source of attenuation of the radiation field and this is already taken into account by MOCASSIN by providing the attenuated radiation field in each cell.

5.3.2.1 Benchmark of the adaptive grid

The use of the adaptive grid implies, especially at the beginning of the grid, the necessity to have closer depth points (in MOCASSIN these depth points are 3D cells). The purpose of the benchmark was to fully resolve the H/H₂ transition, at the right A_v in a maximum of 3 cells close to each other. Fig 5.2 shows how, in a 3D system, it is difficult to have more than 3 cells (or even 2) on the same line, as required by the adaptive grid. In fact, because of the Monte Carlo radiative transfer approximation, the probability that an energy packet transverses 2 adjacent cells is very low. Therefore, the benchmark was computed with the hope of showing that, as the radiation field is already attenuated in MOCASSIN, the requirements adapted by UCL_PDR in the adaptive grid are negligible. In addition, we tried to obtain a correct H/H₂ transition without using adjacent cells. The benchmark is performed as follows:

I tested the feasibility of employing the adaptive grid formalism into the MOCASSIN structure by simulating a fake coupling. I ran the steady state version of the UCL_PDR code with initial conditions of radiation field 10^3 Habing, density 10^4 cm^{-3} and metallicity $1 Z_{\odot}$ for 170 grid points. In Fig 5.3 one can see that for these conditions the H/H₂ transition occurs at an optical depth of ~ 0.037 , which in terms of extinction is $A_v \sim 0.04$, after around 62 grid points using the adaptive grid of depth-steps.

Afterwards, I inputted the optical depth and the attenuated radiation field from the steady state run into the UCL_PDR code and took out the A_v dependence in the calculation of the coefficient rate (hereafter I will refer to this modification in the UCL_PDR code as the modified UCL_PDR code). With the aim of obtaining the H/H₂ transition in as few points as possible (preferably less than 3), the adaptive grid points have been imposed using an input file with a defined number of depth-points. This is possible because the code no longer needs to attenuate the radiation field as it was already an input. Regardless of the number of depth points used, the H/H₂ transition occurred at high extinction ($A_v \sim 3$). In order to have an accurate H/H₂ transition (i.e at low A_v) I ran several models varying the number of grid points to investigate

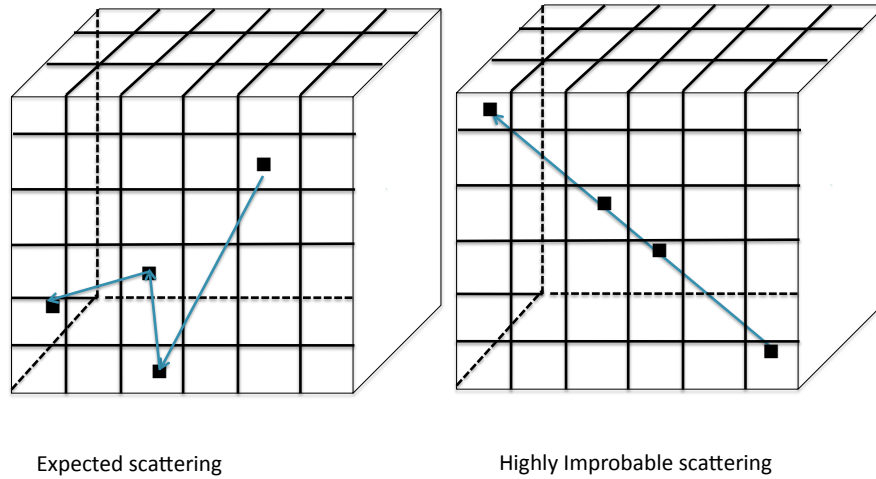


Figure 5.2: A 3D representation of the computed trajectories of the energy packets. The 3D cubical grid (right) shows the highly improbable scattering of photons within the grid, while the 3D cubical grid (left) shows the expected scattering of photons within the grid.

Table 5.1: Number of grid points used for the benchmark of the adaptive grid and the respective A_v where the H/H_2 transition occurs.

Number Points	H/H_2 Transition
170 pt.	$A_v \sim 0.04$
3 pt.	$A_v \sim 3.2$
9 pt.	$A_v \sim 3.1$
28 pt.	$A_v \sim 2.09$
80 pt.	$A_v \sim 0.04$

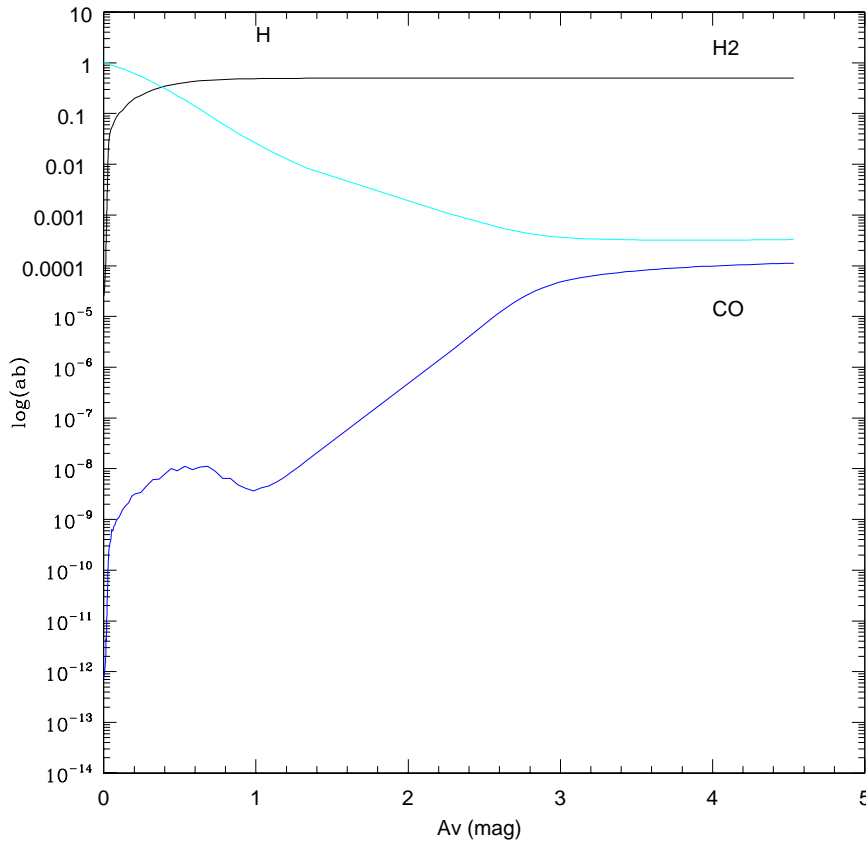


Figure 5.3: The H (turquoise solid line), H_2 (black solid line) and CO (blue solid line) abundances against A_v extinction, in logarithmic scale, obtained running the UCL_PDR code with initial conditions of radiation field 10^3 Habing, density 10^4 cm^{-3} and metallicity $1 Z_\odot$ for 170 grid points. The H/ H_2 transition occurs at an optical depth of ~ 0.037 , that in terms of extinction is $A_v \sim 0.04$, after around 62 grid points using the adaptive grid of depth-steps.

the minimum number of depth points required. I reduced the number of grid points from 170 to 3 grid points, (see Table 5.1). In Fig 5.4 is clear that the H/ H_2 transition is at a higher extinction than $A_v \sim 0.04$, as I expected considering the UCL_PDR run with 170 grid points. I subsequently ran this UCL_PDR version again for 9 and 28 grid points in an attempt to get the H/ H_2 transition at the right A_v . This is shown in Fig 5.5 and Fig 5.6. The H/ H_2 transition again occurred at A_v greater than 3, indicating a much finer grid was needed to solve the H/ H_2 transition properly. In fact by increasing the number of grid points it was clear that the H/ H_2 transition was occurring closer to the value of A_v obtained running the unmodified version of the UCL_PDR code with 170 grid points.

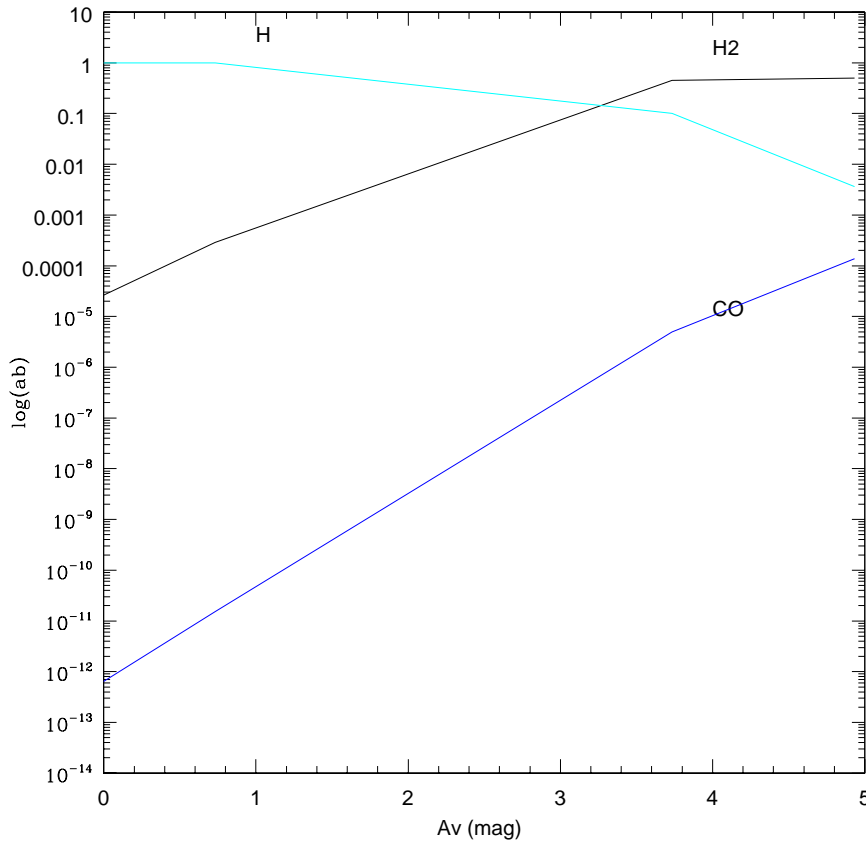


Figure 5.4: The H (turquoise solid line), H₂ (black solid line) and CO (blue solid line) abundances against A_v extinction, in logarithmic scale, obtained running the UCL_PDR code with initial conditions of radiation field 10^3 Habing, density 10^4 cm⁻³ and metallicity $1 Z_{\odot}$ for 3 grid points. The H/H₂ transition was occurring further away from $A_v \sim 3$.

I then ran the modified version of the code with 80 grid points (Fig 5.7) and used the output of the old version of the UCL_PDR code (run for 170 grids point) as the attenuated radiation field input as before. In the end, the H/H₂ transition occurred at an optical depth of ~ 0.037 . This means that, with the initial parameters used for this test, for solving the chemistry and the H/H₂ transition accurately, at least 80 closely spaced grid points were needed in a range of optical depth from 5.7×10^{-5} to 2. If we want to extend the calculation of the chemistry beyond this value of optical depth, a high resolution grid will no longer be needed.

After the benchmarking of the adaptive grid, we reached the conclusion that the coupling was still possible as long as the MOCASSIN code could provide at least 80 grid points inside the PDR regions. These 80 points could be within one cell or shared among several cells. It

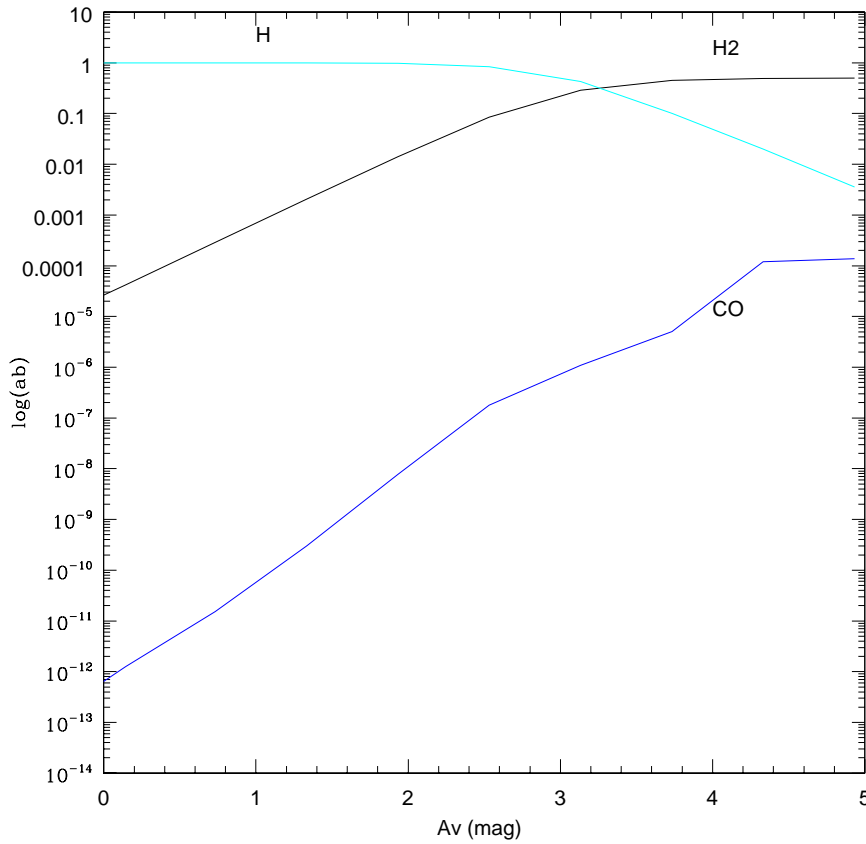


Figure 5.5: The H (turquoise solid line), H₂ (black solid line) and CO (blue solid line) abundances against A_v extinction, in logarithmic scale, obtained running the UCL_PDR code with initial conditions of radiation field 10^3 Habing, density 10^4 cm^{-3} and metallicity $1 Z_{\odot}$ for 9 grid points. The H/H₂ transition at higher extinction than $A_v \sim 3$.

should be noted that these 80 points would only be necessary for the initial conditions used in this test as this number could vary depending on the physical parameters used. In each of the grid points the attenuated radiation field value and the optical depth need to be known. It is also required that these grid points are all in the same line; this means that it is not possible to work with the value of the attenuated radiation field obtained from the scattering or absorption inside the cell, unless there is only one scattering or absorption in each cell. However, since a 3 dimensional cartesian grid is adopted, it is impossible to obtain an 80 grid point system in which the absorption and the scattering of the photon packets occurs along a path in the same direction. This is because, in MOCASSIN the direction of scattering and absorption inside each cell is completely randomised (Fig 5.2). In addition, one cannot be sure that a fixed number (80

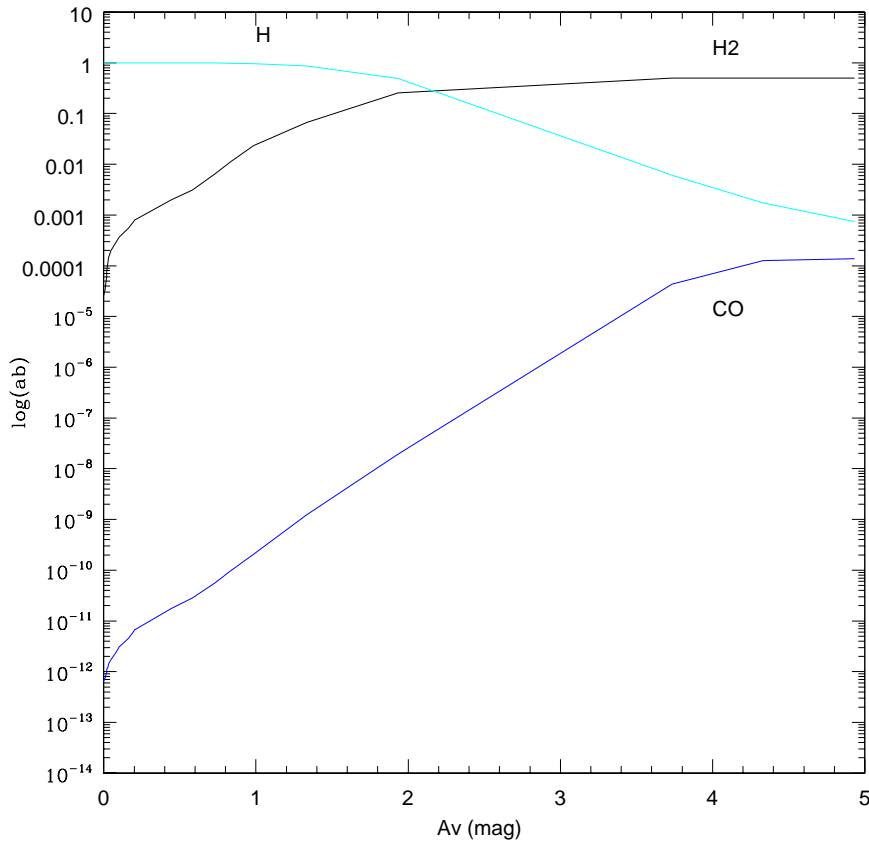


Figure 5.6: The H (turquoise solid line), H₂ (black solid line) and CO (blue solid line) abundances against A_v extinction, in logarithmic scale, obtained running the UCL_PDR code with initial conditions of radiation field 10^3 Habing, density 10^4 cm^{-3} and metallicity $1 Z_{\odot}$ for 28 grid points. The H/H₂ transition at higher extinction than $A_v \sim 3$.

in our case) of grid points encompass the photodissociated region and that beyond this fixed number one cannot change the cell size. Therefore, there remains the issue of resolving the H/H₂ transition without using an adaptive grid.

5.3.3 Chemical Network and Ordinary Differential Equations

For the purpose of testing the feasibility of the coupling I created a new chemical network that contains only the 32 basic chemical species involved in the molecular cloud reactions listed in Table 5.2.

This has been done in order to speed up the computation of the chemistry. The UCL_PDR code makes use of an integrator, called LSODE, to solve the ordinary differential equations

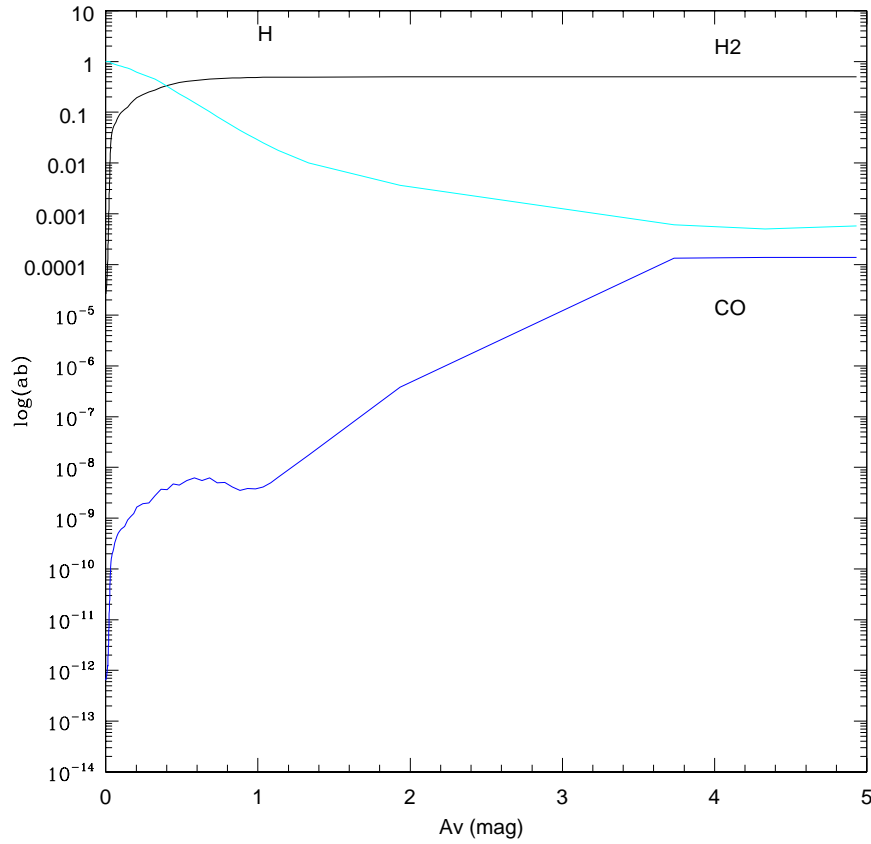


Figure 5.7: The H (turquoise solid line), H_2 (black solid line) and CO (blue solid line) abundances against A_v extinction, in logarithmic scale, obtained running the UCL_PDR code with initial conditions of radiation field 10^3 Habing, density 10^4 cm^{-3} and metallicity $1 Z_\odot$ for 80 grid points. The H/ H_2 transition occurs at $A_v \sim 0.04$.

Table 5.2: Species contained in the reduced chemical network of the modified UCL_PDR code.

Reduced chemical network species.							
H_3^+	He^+	Mg	H_2^+	CH_5^+	CH_4^+	O_2	O^+
OH^+	Mg^+	C	CO^+	C^+	H^+	O_2^+	H
He	OH	CO	H_2O^+	CH_4	H_3O^+	CH_3	HCO^+
CH_2	H_2O	O	H_2	CH_2^+	CH^+	CH	CH_3^+

(ODEs) that contain terms of destruction and formation of chemical species involved in the network, and contained in the master rate file.

A system of stiff ordinary differential equations is used to calculate the abundances of the chemical species. A problem is stiff if the numerical solution has its step size limited more severely by the stability of the numerical technique than by the accuracy of the technique. Frequently, these problems occur in systems of differential equations that involve several components that are decaying at widely differing rates. For a stiff problem, solutions can change on a time scale that is very short compared to the interval of integration, but the solution of interest changes on a much longer time scale. Methods not designed for stiff problems are ineffective on intervals where the solution changes slowly because they use time steps small enough to resolve the fastest possible change. If the problem is stiff, sudden changes in the variables can occur; for example in PDRs the rate equations depend on the abundances in small time intervals. This means that one cannot use simple iteration because this leads to an unacceptable restriction of the stepsize and functional iteration fails to converge.

In order to still use this approach in the coupling, it is necessary that the MOCASSIN code is able to make the cells chemically linked to each other in the finest part of the grid. Irrespective of the accuracy of the attenuated radiation field in each of the grid points, the interpolation between cells is essential. This is because the H₂ and CO shielding are estimated using column densities calculated from the abundances at the previous depth-steps. At each depth-step, the same input abundances are used (at time step=0) and the final abundances, at the final time step, are calculated using the LSODE ODE-solver. So, only the calculation of the input abundances at time step >1 depends on the previous time-step output abundances from the ODE solver (interpolated between nearest depth-steps). The use of the ODEs are strictly linked with the adaptive grid, which cannot be adopted due to the uncertainties in the direction of absorption and scattering in the cells. Also, the necessity to have, at least before the H/H₂ transition front, a system of chemically linked cells for the computation of the H₂ and CO shielding, makes this method not compatible for the purpose of the coupling.

5.3.4 Steady state vs time dependent with the reduced chemical network

Since the MOCASSIN code is not time dependent the initial idea of the coupling was based on inserting the part of the code related to the chemistry in a steady state approximation. Therefore, I have been working on testing the precision in the calculation of abundances, emissivities, brightnesses, and dust and gas temperatures of the steady state approximation versus the time

dependent version with the reduced and the full chemical network. The decision of using a steady state or time dependent approach in order to study certain kinds of objects or environments is totally arbitrary. Even now it is still debated which approach is best to use and which is the more accurate to physically and chemically represent an extragalactic or a galactic source.

The choice of which type of method to use can depend on the type, for instance, of molecules that one wants to study and therefore which type of medium (dense or diffuse) one wants to investigate. Taking as an example a high- z galaxy, the steady state model is suitable as long as we are interested in the bulk average physical and chemical properties. On the other hand, when treating a nearby source one would like to disentangle the various gaseous components taking into account the effects of the age and metallicity, which are time dependent.

In order to investigate the accuracy of the steady state approach, I created a small grid of 54 PDR models and starting with a standard model I varied the physical parameters (such as density, radiation field, metallicity, cosmic ray ionization rate) one at a time. The grid of 54 models is listed in Table 5.3. These models were run up to A_v of 6 mag. The same 54 models have been run for steady state and time dependent conditions with the full chemical network and with the reduced chemical network.

In the following sections I evaluate the effect of the steady state approximation on the H/H₂ transition and on the fractional abundances of different species, as well as on the use of a reduced network.

5.3.4.1 Fractional abundances

Chemically speaking, when the H₂ density becomes large, some reactions can produce high abundances of OH in the H/H₂ transition layer, where the high temperatures necessary for the endothermic reactions to proceed efficiently can be maintained. The high abundance of the OH radical then gives rise to a series of fast ion-molecule reactions that produce some molecular ions such as HCO⁺, and a series of slower neutral-neutral reactions that produce molecules such as O₂, which can be subsequently destroyed by photodissociation. The molecular ions can also be destroyed by dissociative recombination or reactions with H₂, and water can be destroyed by reacting with H to produce H₂ and OH again. The dissociative recombination of HCO⁺, and charge transfer between CO⁺ and H are important formation routes for CO, which can be formed efficiently in the outer cloud layers, where the electron density is high due to photoionization of carbon and sulphur, and hydrogen is still mainly atomic. The shielding of CO from photodissociation increases with gas density and allows its abundance to reach saturation

Table 5.3: Grid of 54 UCL_PDR models subdivided by different physical parameters such as density, radiation field, metallicity and cosmic ray ionization rate in a range of visual extinction values ($1 \leq A_v \leq 6$).

Index	Density n_H (cm^{-3})	Radiation Field G_0	Metallicity Z_{\odot}	Cosmic Ray Ionization Rate ζ (erg s^{-1})	Turbulent Velocity v_{turb} (km s^{-1})
1	500	50	0.5	5×10^{-17}	1.5
2	10^3	50	0.5	5×10^{-17}	1.5
3	10^4	50	0.5	5×10^{-17}	1.5
4	500	100	0.5	5×10^{-17}	1.5
5	10^3	100	0.5	5×10^{-17}	1.5
6	10^4	100	0.5	5×10^{-17}	1.5
7	500	10^3	0.5	5×10^{-17}	1.5
8	10^3	10^3	0.5	5×10^{-17}	1.5
9	10^4	10^3	0.5	5×10^{-17}	1.5
10	500	50	1	5×10^{-17}	1.5
11	10^3	50	1	5×10^{-17}	1.5
12	10^4	50	1	5×10^{-17}	1.5
13	500	100	1	5×10^{-17}	1.5
14	10^3	100	1	5×10^{-17}	1.5
15	10^4	100	1	5×10^{-17}	1.5
16	500	10^3	1	5×10^{-17}	1.5
17	10^3	10^3	1	5×10^{-17}	1.5
18	10^4	10^3	1	5×10^{-17}	1.5
19	500	50	2	5×10^{-17}	1.5
20	10^3	50	2	5×10^{-17}	1.5
21	10^4	50	2	5×10^{-17}	1.5
22	500	100	2	5×10^{-17}	1.5
23	10^3	100	2	5×10^{-17}	1.5
24	10^4	100	2	5×10^{-17}	1.5
25	500	10^3	2	5×10^{-17}	1.5
26	10^3	10^3	2	5×10^{-17}	1.5
27	10^4	10^3	2	5×10^{-17}	1.5
28	500	50	2	5×10^{-16}	1.5

Index	Density n_H (cm^{-3})	Radiation Field G_0	Metallicity Z_{\odot}	Cosmic Ray Ionization Rate ζ (erg s^{-1})	Turbulent Velocity v_{turb} (km s^{-1})
29	10^3	50	2	5×10^{-16}	1.5
30	10^4	50	2	5×10^{-16}	1.5
31	500	100	2	5×10^{-16}	1.5
32	10^3	100	2	5×10^{-16}	1.5
33	10^4	100	2	5×10^{-16}	1.5
34	500	10^3	2	5×10^{-16}	1.5
35	10^3	10^3	2	5×10^{-16}	1.5
36	10^4	10^3	2	5×10^{-16}	1.5
37	500	50	0.5	5×10^{-16}	1.5
38	10^3	50	0.5	5×10^{-16}	1.5
39	10^4	50	0.5	5×10^{-16}	1.5
40	500	100	0.5	5×10^{-16}	1.5
41	10^3	100	0.5	5×10^{-16}	1.5
42	10^4	100	0.5	5×10^{-16}	1.5
43	500	10^3	0.5	5×10^{-16}	1.5
44	10^3	10^3	0.5	5×10^{-16}	1.5
45	10^4	10^3	0.5	5×10^{-16}	1.5
46	500	50	1	5×10^{-16}	1.5
47	10^3	50	1	5×10^{-16}	1.5
48	10^4	50	1	5×10^{-16}	1.5
49	500	100	1	5×10^{-16}	1.5
50	10^3	100	1	5×10^{-16}	1.5
51	10^4	100	1	5×10^{-16}	1.5
52	500	10^3	1	5×10^{-16}	1.5
53	10^3	10^3	1	5×10^{-16}	1.5
54	10^4	10^3	1	5×10^{-16}	1.5

nearer the surface of the cloud, resulting in stronger emission. The formation of molecular hydrogen represents a significant time-scale in the chemical evolution, since the formation of CO proceeds fairly rapidly once H₂ is dominant.

Fig 5.8- 5.14 show the difference in the accuracy using the two distinct methods with both reduced and full chemical networks of CO (black line), O (cyan line), OH (blue line), O₂ (magenta line), C (green line), HCO⁺ (yellow) and H₃⁺ (red line) fractional abundances versus visual extinction, A_v (mag). In each of the figures, the top left panel represents a run with the reduced chemical network and steady state approach, the top right panel represents a run with the reduced chemical network and time dependent approach, the bottom left panel represents a run with the full chemical network and steady state approach, and the bottom right panel represents a run with the full chemical network and time dependent approach. At a glance the general trend presented in the plots indicates that the total number of species included in the chemistry has some effects on the results, while the type of approach used does not influence the results at all. Without going into the details of the changes of the physical parameters, it is plausible to assume, as a general trend, that for a given set of parameters the O (cyan line), C (green line), O₂ (magenta line) and OH (blue line) fractional abundance are constant. In the steady state and time dependent approaches with the reduced chemical network, species such as, HCO⁺ (yellow line), H₃⁺ (red line) and CO (black line) do not show any remarkable differences in their fractional abundances, whereas their fractional abundances, at the beginning and at the end of the run, are slightly dissimilar using a full chemical network (see comparison between top right panel and bottom right panel). An accurate analysis of the most important species that trace the gas leads us to conclude that, for the purpose of the coupling, we can use a reduced chemical network and the steady state approach.

5.3.4.2 H/H₂ transition

As we have already mentioned, one of the most important features of PDRs is the H/H₂ transition layer. When the amount of molecular hydrogen increases significantly, a network of more complex reactions is set up. Previous work has established the point at which the transition between H and H₂ occurs, and it was found to vary from model to model (Röllig *et al.* 2007). The typical location of the H/H₂ transition layer is still under debate and there is some difference of opinion on the appropriate treatment for reproducing it. The variation in the location of the H/H₂ transition layer and the H and H₂ number densities are affected by the fluctuation in the photorates. We investigated the variation of the H/H₂ ratio, using steady state and time

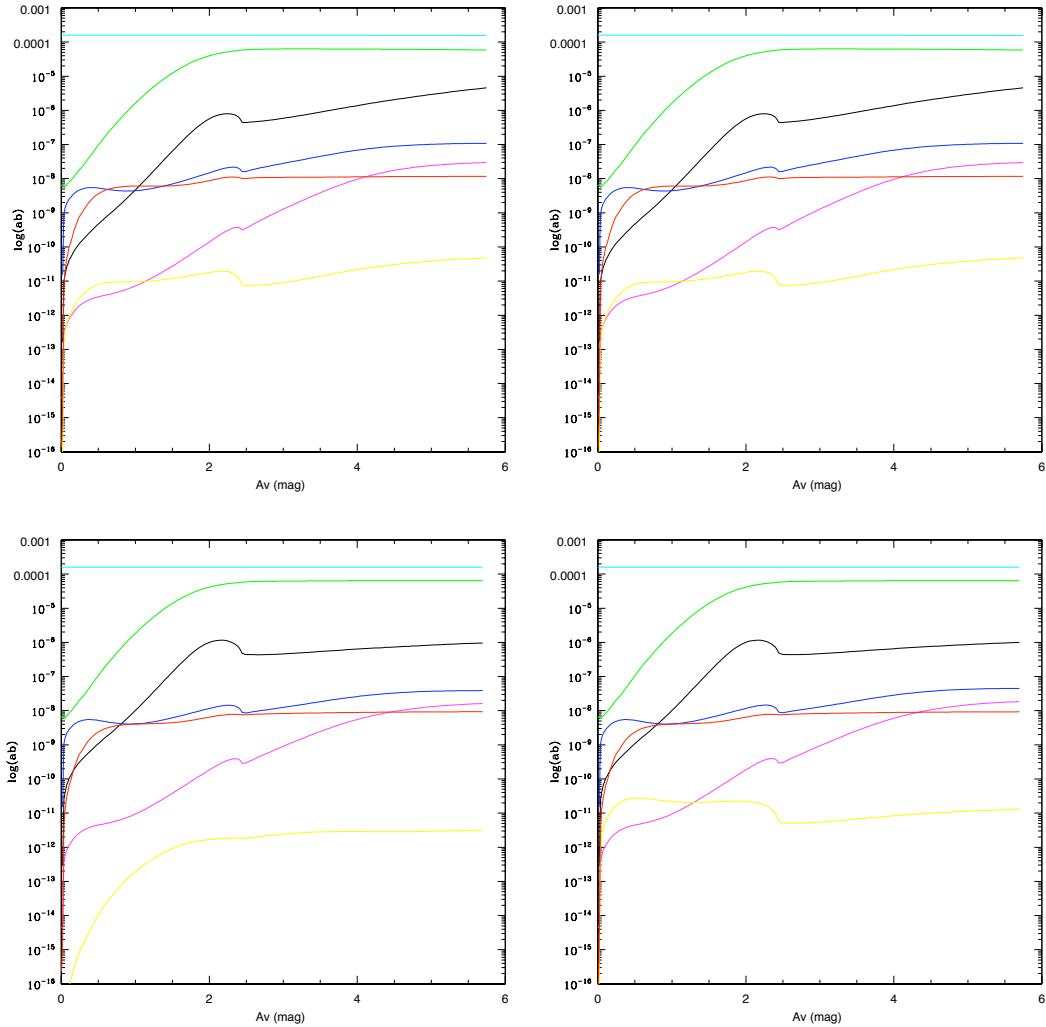


Figure 5.8: Model 1 of CO (black line), O (cyan line), OH (blue line), O_2 (magenta line), C (green line), HCO^+ (yellow) and H_3^+ (red line) fractional abundances versus visual extinction, A_v (mag). The top left panel represents a run with the reduced chemical network and steady state approach, the top right panel represents a run with the reduced chemical network and time dependent approach, the bottom left panel represents a run with the full chemical network and steady state approach, and the bottom right panel represents a run with the full chemical network and time dependent approach.

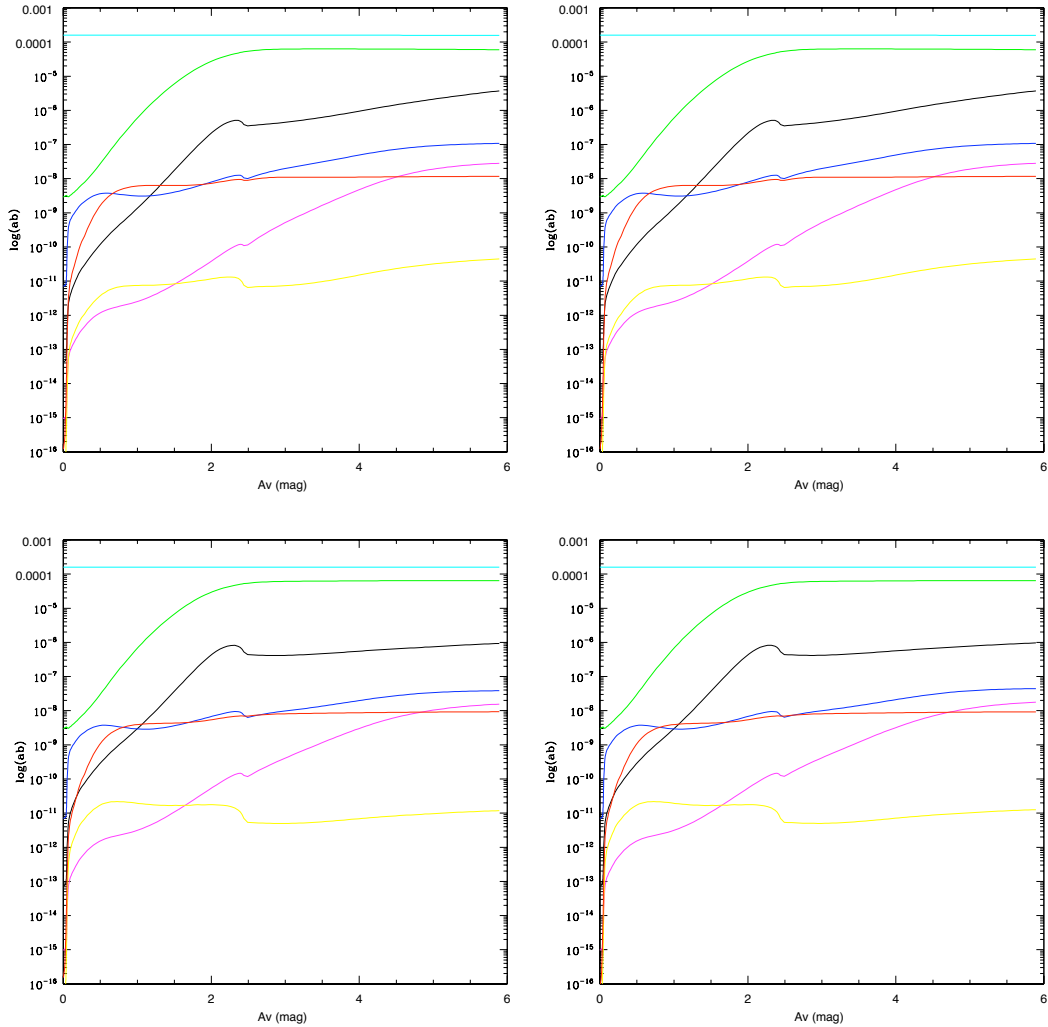


Figure 5.9: Model 4 of CO (black line), O (cyan line), OH (blue line), O₂ (magenta line), C (green line), HCO⁺ (yellow) and H₃⁺ (red line) fractional abundances versus visual extinction, A_v (mag). The top left panel represents a run with the reduced chemical network and steady state approach, the top right panel represents a run with the reduced chemical network and time dependent approach, the bottom left panel represents a run with the full chemical network and steady state approach, and the bottom right panel represents a run with the full chemical network and time dependent approach.

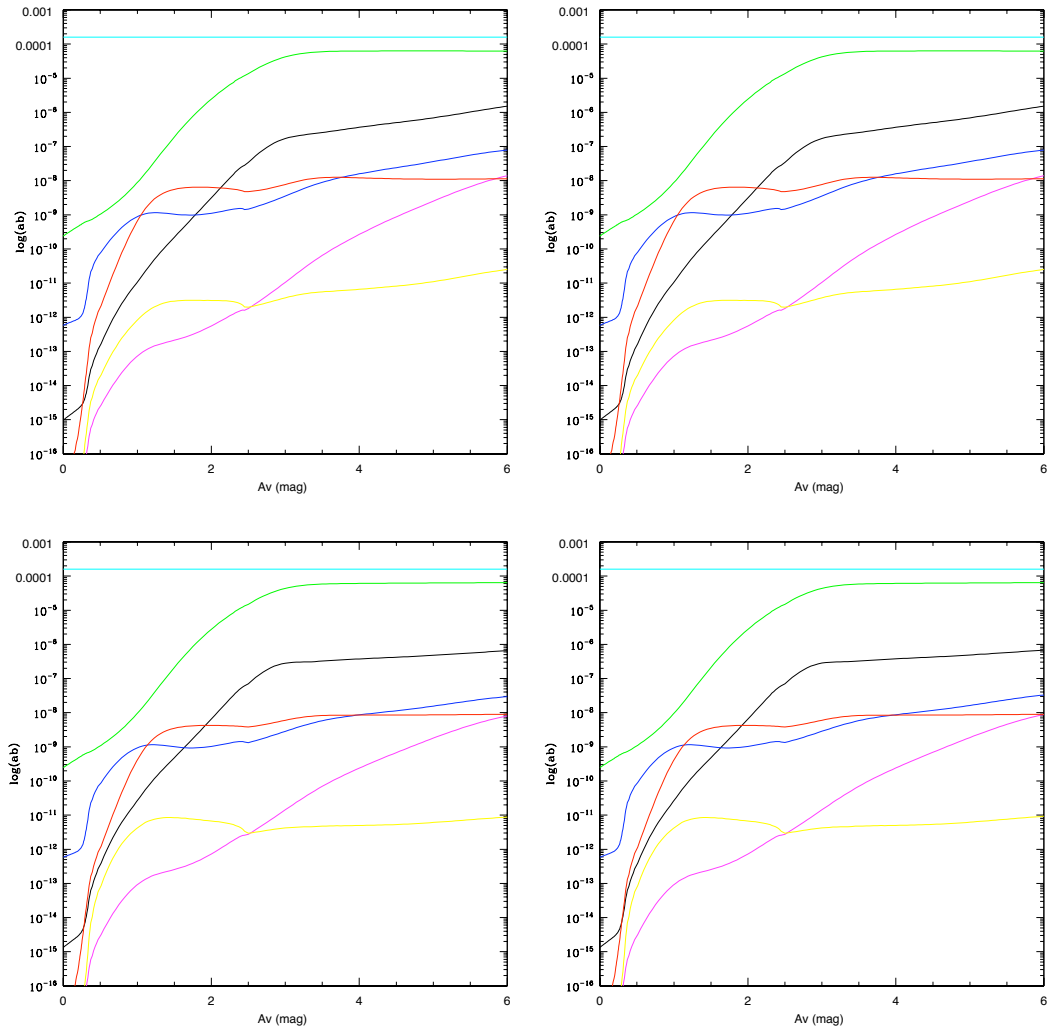


Figure 5.10: Model 7 of CO (black line), O (cyan line), OH (blue line), O₂ (magenta line), C (green line), HCO⁺ (yellow) and H₃⁺ (red line) fractional abundances versus visual extinction, A_v (mag). The top left panel represents a run with the reduced chemical network and steady state approach, the top right panel represents a run with the reduced chemical network and time dependent approach, the bottom left panel represents a run with the full chemical network and steady state approach, and the bottom right panel represents a run with the full chemical network and time dependent approach.

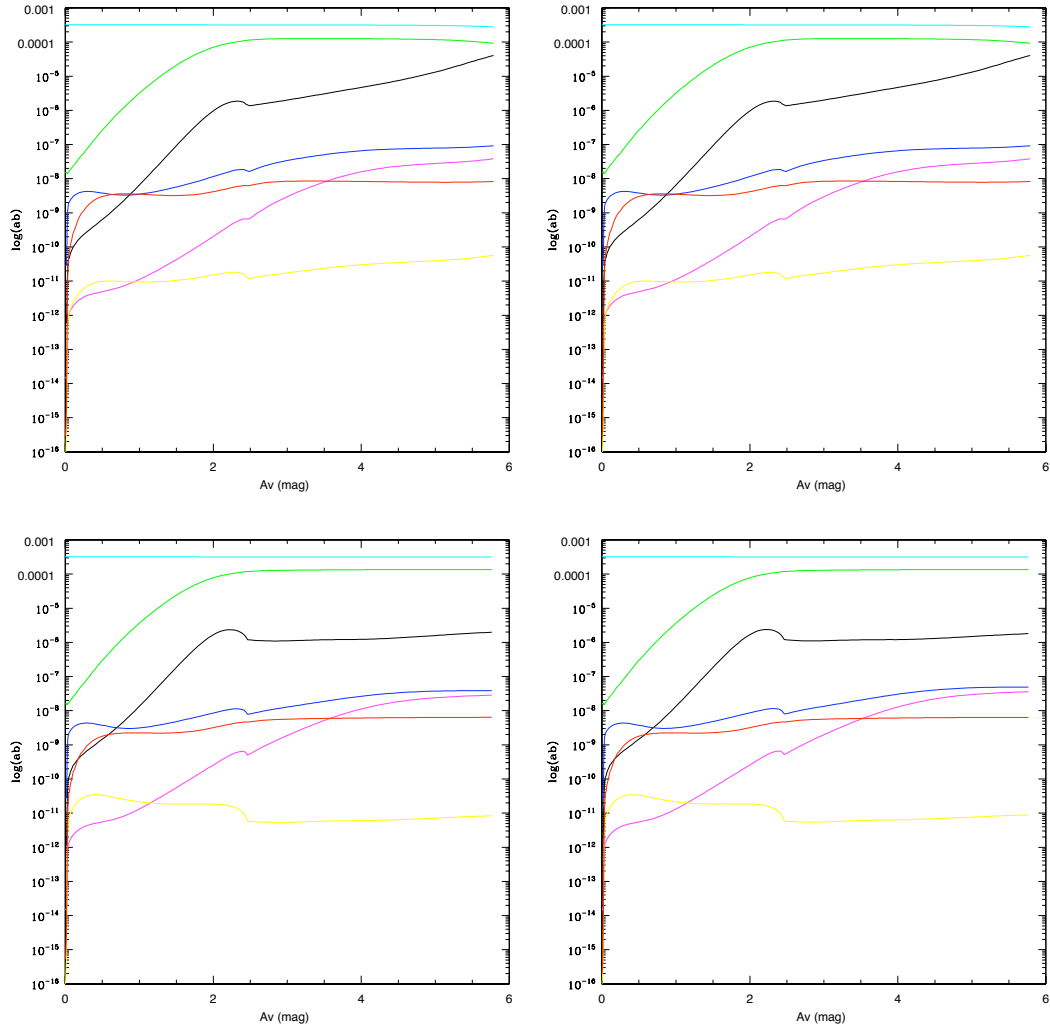


Figure 5.11: Model 10 of CO (black line), O (cyan line), OH (blue line), O_2 (magenta line), C (green line), HCO^+ (yellow) and H_3^+ (red line) fractional abundances versus visual extinction, A_v (mag). The top left panel represents a run with the reduced chemical network and steady state approach, the top right panel represents a run with the reduced chemical network and time dependent approach, the bottom left panel represents a run with the full chemical network and steady state approach, and the bottom right panel represents a run with the full chemical network and time dependent approach.

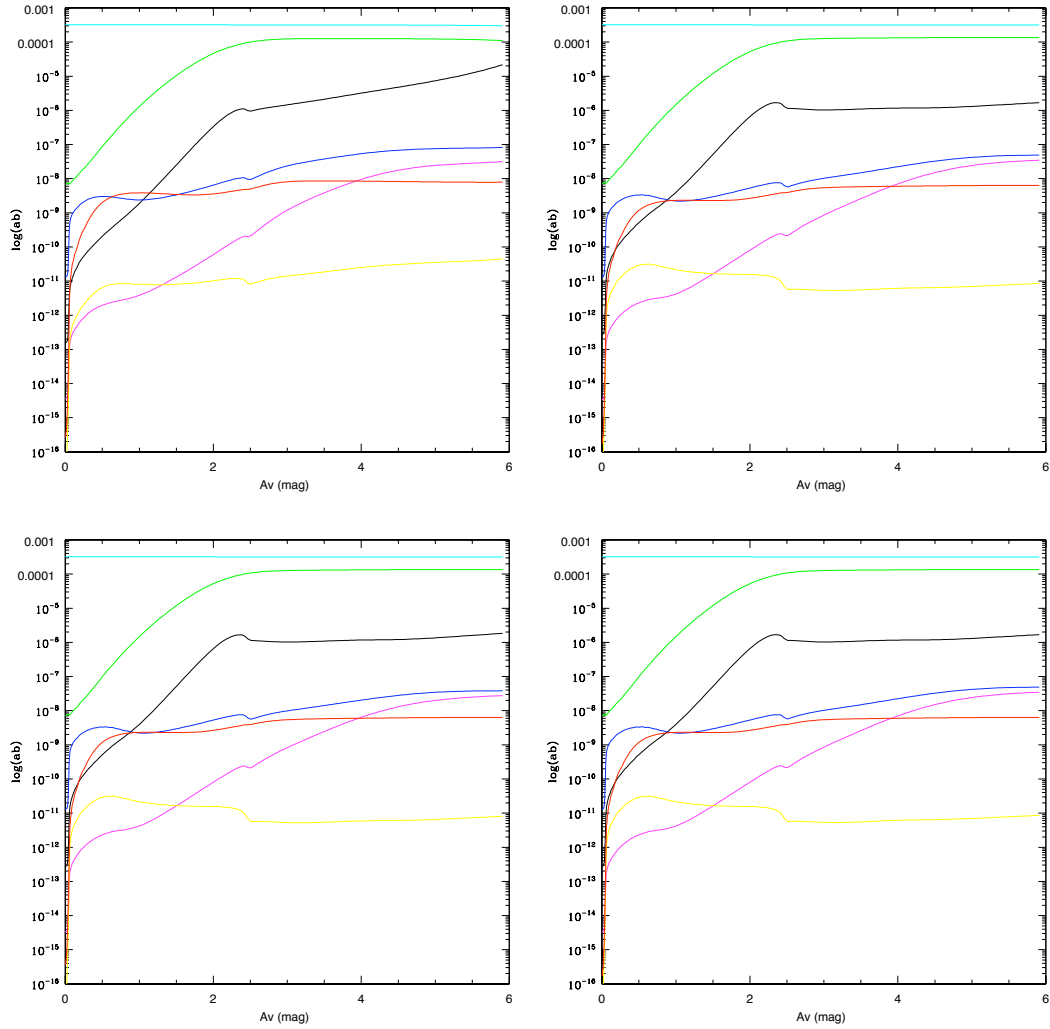


Figure 5.12: Model 13 of CO (black line), O (cyan line), OH (blue line), O₂ (magenta line), C (green line), HCO⁺ (yellow) and H₃⁺ (red line) fractional abundances versus visual extinction, A_v (mag). The top left panel represents a run with the reduced chemical network and steady state approach, the top right panel represents a run with the reduced chemical network and time dependent approach, the bottom left panel represents a run with the full chemical network and steady state approach, and the bottom right panel represents a run with the full chemical network and time dependent approach.

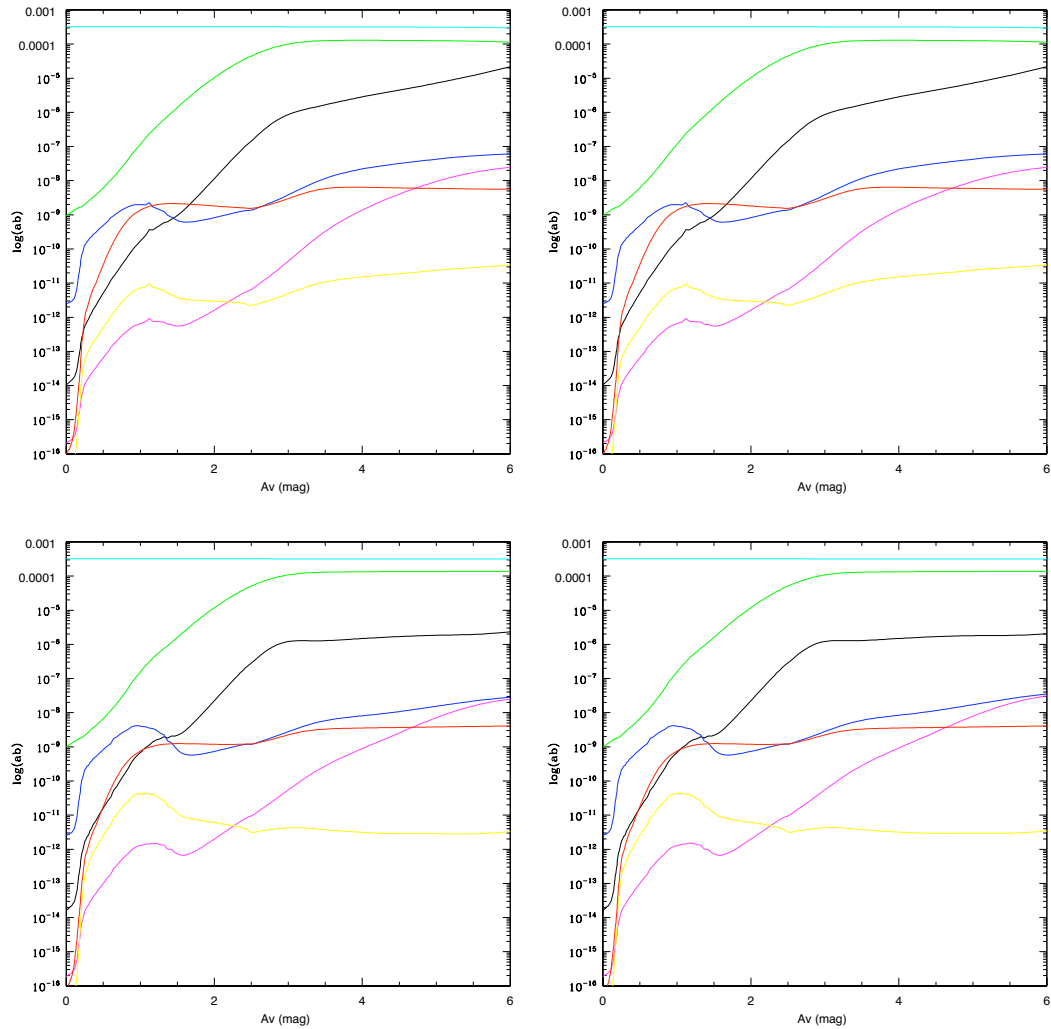


Figure 5.13: Model 17 of CO (black line), O (cyan line), OH (blue line), O₂ (magenta line), C (green line), HCO⁺ (yellow) and H₃⁺ (red line) fractional abundances versus visual extinction, A_v (mag). The top left panel represents a run with the reduced chemical network and steady state approach, the top right panel represents a run with the reduced chemical network and time dependent approach, the bottom left panel represents a run with the full chemical network and steady state approach, and the bottom right panel represents a run with the full chemical network and time dependent approach.

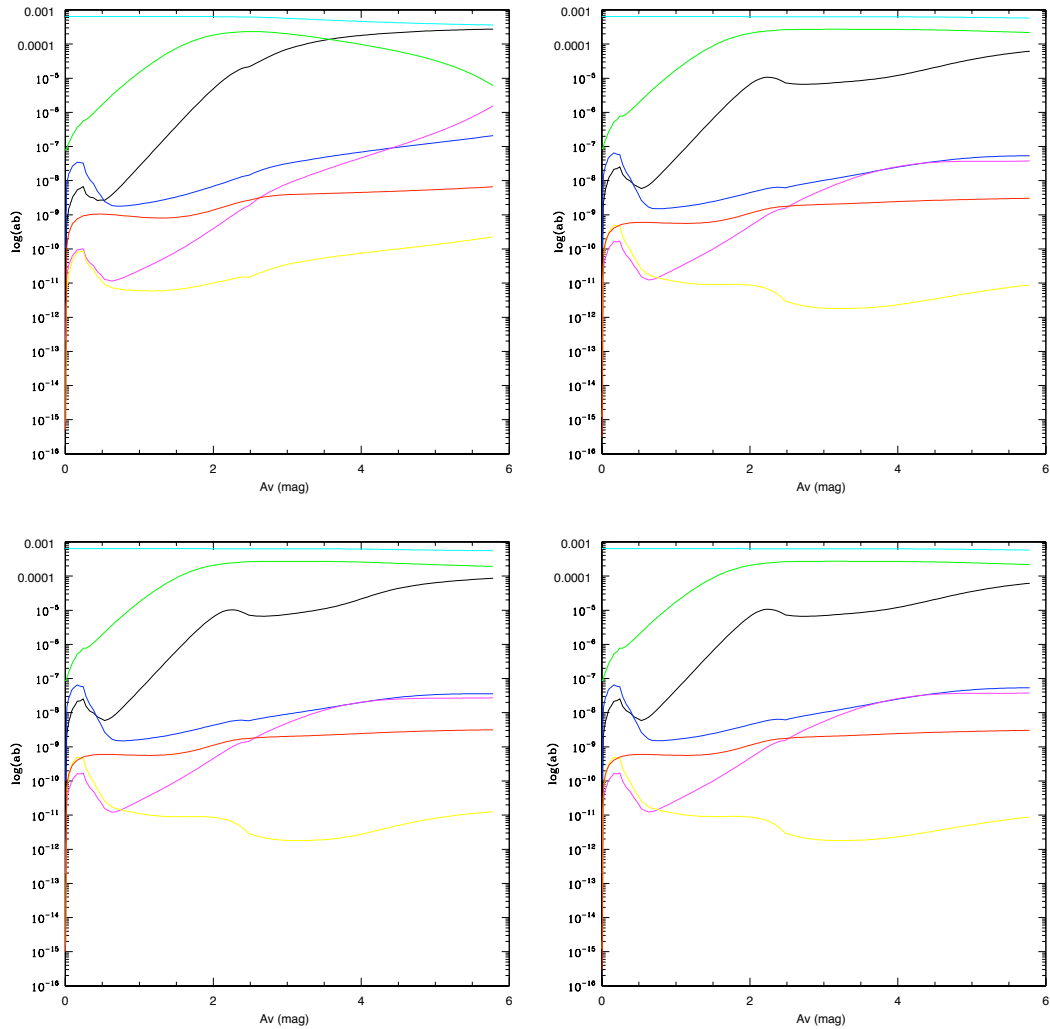


Figure 5.14: Model 20 of CO (black line), O (cyan line), OH (blue line), O₂ (magenta line), C (green line), HCO⁺ (yellow) and H₃⁺ (red line) fractional abundances versus visual extinction, A_v (mag). The top left panel represents a run with the reduced chemical network and steady state approach, the top right panel represents a run with the reduced chemical network and time dependent approach, the bottom left panel represents a run with the full chemical network and steady state approach, and the bottom right panel represents a run with the full chemical network and time dependent approach.

dependent approaches with the full chemical network and with the reduced chemical network.

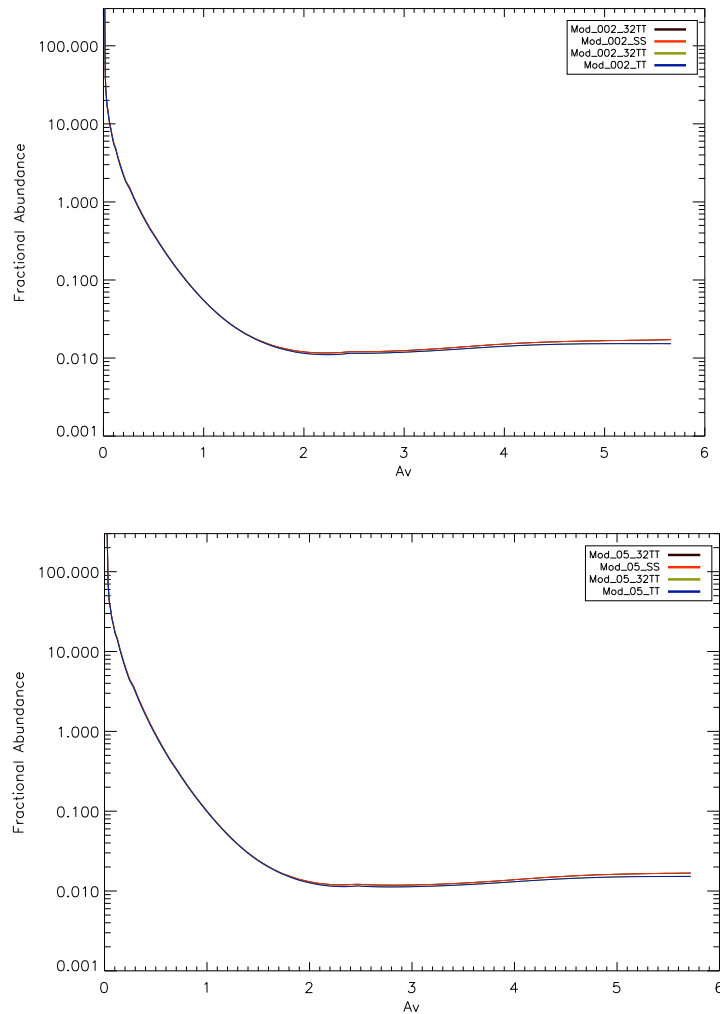


Figure 5.15: Model 2 (top panel) and model 5 (bottom panel) of the H/H_2 ratio versus visual extinction, A_v (mag). The green line represents the ratio reproduced with the reduced chemical network and steady state approach, the black line represents the ratio reproduced with the reduced chemical network and time dependent approach, the red line represents the ratio reproduced with the full chemical network and steady state approach, and the blue line represents the ratio reproduced with the full chemical network and time dependent approach.

Fig 5.15- 5.18 show the H/H_2 ratio versus visual extinction, A_v (mag), for a sample of models. In the plots the green line represents the ratio reproduced with the reduced chemical network and steady state approach, the black line represents the ratio reproduced with the reduced chemical network and time dependent approach, the red line represents the ratio reproduced with the full chemical network and steady state approach, and the blue line represents the ratio

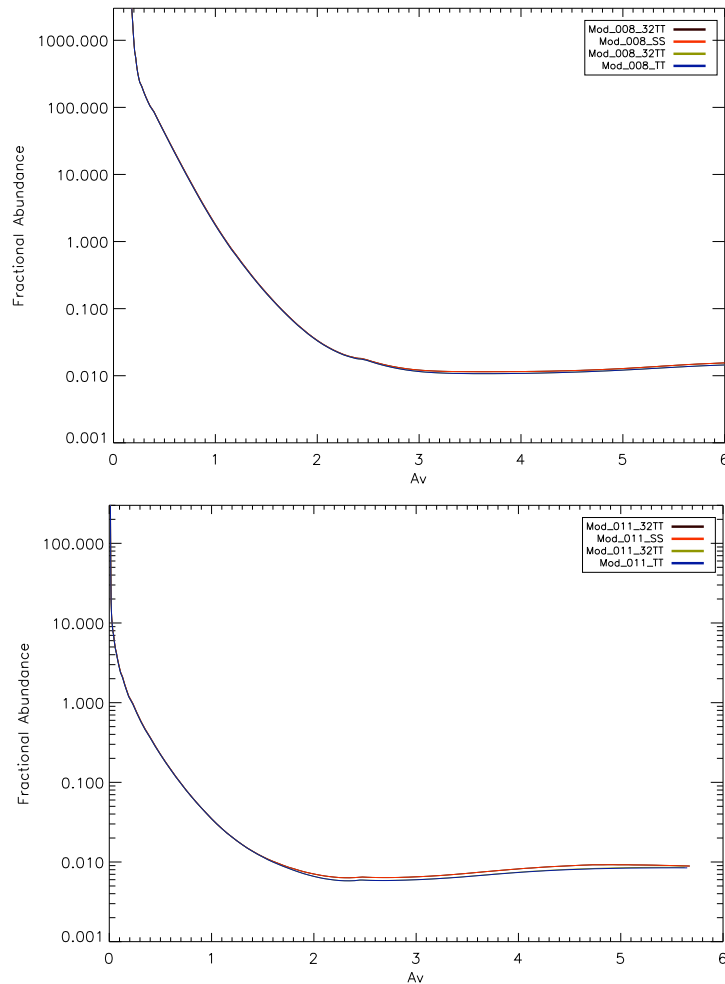


Figure 5.16: Model 8 (top panel) and model 11 (bottom panel) of the H/H_2 ratio versus visual extinction, A_v (mag). The green line represents the ratio reproduced with the reduced chemical network and steady state approach, the black line represents the ratio reproduced with the reduced chemical network and time dependent approach, the red line represents the ratio reproduced with the full chemical network and steady state approach, and the blue line represents the ratio reproduced with the full chemical network and time dependent approach.

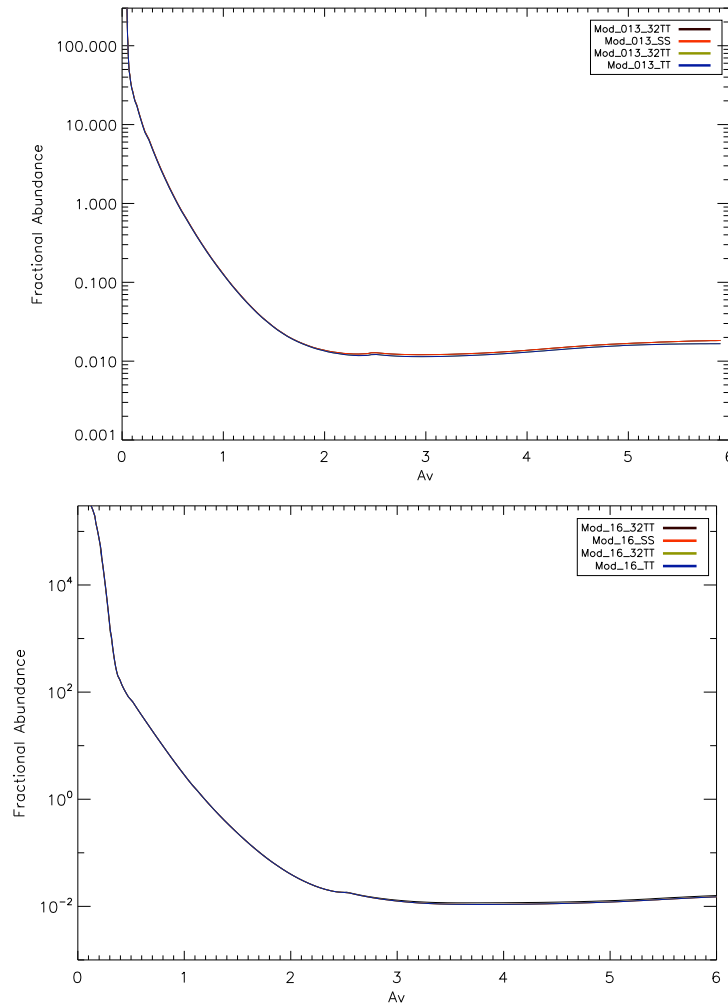


Figure 5.17: Model 13 (top panel) and model 16 (bottom panel) of the H/H_2 ratio versus visual extinction, A_v (mag). The green line represents the ratio reproduced with the reduced chemical network and steady state approach, the black line represents the ratio reproduced with the reduced chemical network and time dependent approach, the red line represents the ratio reproduced with the full chemical network and steady state approach, and the blue line represents the ratio reproduced with the full chemical network and time dependent approach.

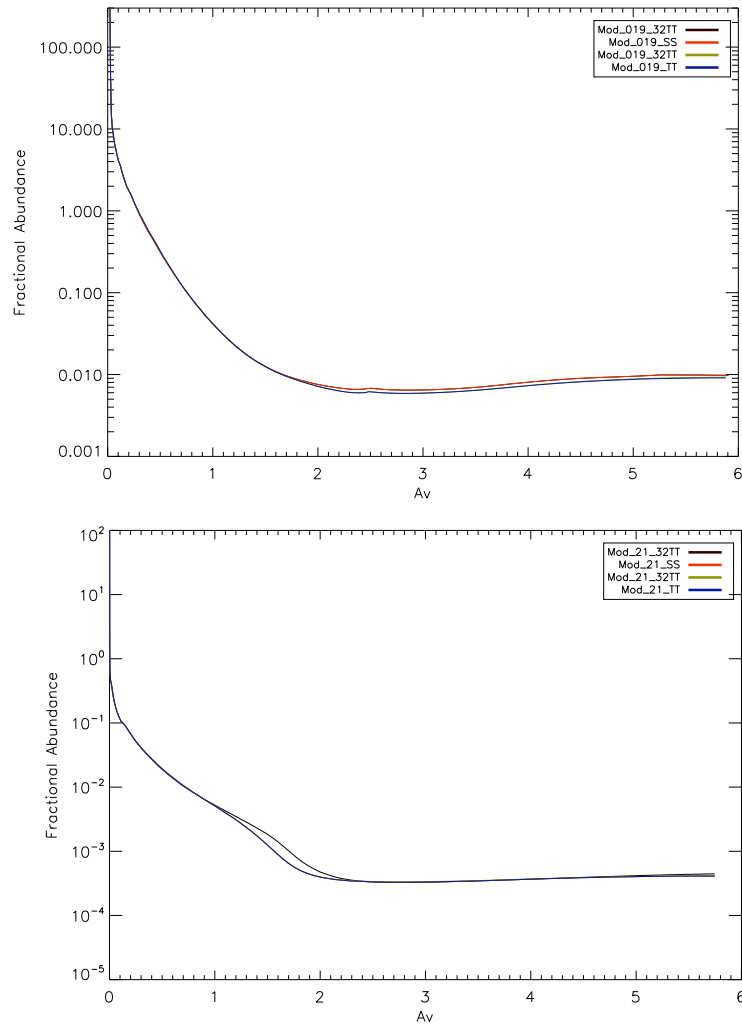


Figure 5.18: Model 19 (top panel) and model 21 (bottom panel) of the H/H_2 ratio versus visual extinction, A_v (mag). The green line represents the ratio reproduced with the reduced chemical network and steady state approach, the black line represents the ratio reproduced with the reduced chemical network and time dependent approach, the red line represents the ratio reproduced with the full chemical network and steady state approach, and the blue line represents the ratio reproduced with the full chemical network and time dependent approach.

reproduced with the full chemical network and time dependent approach. No visible differences can be found among these models, meaning that the steady state approximation and the reduced network are accurate enough to give us the correct H/H₂ transition.

We conclude that for the coupling of the MOCASSIN and PDR codes, a reduced network and the steady state approximation are reliable under the physical conditions assumed. Note that our results are not consistent with those of Bell *et al.* (2006b); this can be attributed to the fact that we used different physical input parameters that lead to a different behaviour in the CO molecule. In fact, higher cosmic ray ionization rate and density values, with respect to the one we used, influence the abundance of CO in gas phase (Tielens 2005).

5.3.5 The dimensionality of the cells

The issue of the dimensionality is a particularly complex problem. The principal difficulty is that the two codes are working with two different dimensionalities: UCL_PDR is a one dimensional code and MOCASSIN is a three dimensional code. As already mentioned, MOCASSIN consists of a three dimensional system of cells in which the energy packets, crossing the surfaces, can be absorbed or reemitted in a different direction. Being a structure in three dimensions means that the direction of reemission of the energy packets cannot be predetermined, because if one defines a direction this becomes a system of straight lines that breaks the three-dimensionality. In the previous sections, the issue of the dimension was always implicit. When discussing PDR regions we introduced the concept of ordinary differential equations and the calculations of molecular abundances, and we refer to a system of equations in which the abundances are computed taking into account the results obtained in the previous point: that is a network of unidimensional concatenated points. In addition, the same problem with the dimensionality of the cells arose when we tried to deal with the H/H₂ transition front without the use of the adaptive grid. Also, the description of the self-shielding used in the UCL_PDR code is not compatible with the notion of three dimensions as it employs the adaptive grid, see Section 5.3.2.

5.4 Conclusion and future work

This chapter discussed the feasibility of the coupling of the ionisation code, MOCASSIN, and the photodissociation code, UCL_PDR. Despite the differences, the two regions are linked to each other through the radiation field. Initially it was thought that the best way forward was to build an interface between the two codes. The creation of an interface would have facilitated

the calculation of the abundances in one dimension, as UCL_PDR was already computing, using MOCASSIN for re-interpolating the results in its grid. I was compelled to test the feasibility of a unique code able to study both physical and chemical conditions in objects such as protoplanetary disks where there is no clear difference between H II and PDR regions and their delineation. The new code would have been the result of the merging of the MOCASSIN code structure and the chemistry subroutine of the UCL_PDR code. I proceeded to analyse step by step the best strategy to couple the two codes. Initial work involved the testing of the current version of MOCASSIN by running the established gas-only benchmark models.

- In order to include the correct escape probability formalism, I tried, unsuccessfully, to parallelize the Poelman & Spaans (2005) code
- I simulated a fake coupling to test the feasibility of employing the adaptive grid formalism into the MOCASSIN structure. Since, in the MOCASSIN structure, the visual extinction parameter is irrelevant and it is not possible to get grid cells close enough to each other, it was necessary to verify if it was possible to get rid of the adaptive grid. We concluded that the coupling is possible as long as the MOCASSIN code can provide at least 80 grid points inside the PDR regions. These 80 points could be within one cell or be shared between several cells. In each of the grid points the attenuated radiation field value and the optical depth need to be known. It is also required that these grid points are all in the same line; this means that it is not possible to work with the value of the attenuated radiation field obtained from the scattering or absorption inside the cell, unless there is only one scattering or absorption in each cell (i.e. problem of dimensionality).
- Looking at the ordinary differential equations method, we concluded that it is necessary for the MOCASSIN code to be able to make the cells chemically linked to each other. Irrespective of the accuracy of the attenuated radiation field in each of the grid points, the interpolation between cells is essential.
- I have been working on testing the precision in the calculation of abundances, emissivities, brightnesses, and dust and gas temperatures of the steady state approximation versus the time dependence with the reduced and the full chemical network, and I investigated the behaviour of some important species that better trace the different gas components, using both approaches. I created a small grid of 54 models and, starting with a standard model, varied the physical parameters one at a time. This study provides information on

the possibility to create a merged code using only a reduced chemical network and the steady state approach. In fact, the benchmark of the fractional abundances and the H/H₂ transition show that the differences in the approaches and chemical networks used are completely negligible.

The basic idea was to try to sidestep these issues without completely changing the way the two codes work. It turned out that the principal difficulty was that the two codes are working with two different dimensionalities: UCL_PDR is a one dimensional code and MOCASSIN is a three dimensional code. The problem that arose was that this method did not allow the use of a system of multiple sources (Section 5.3.2). However, the main conclusion that was reached is that it is necessary to adapt the computational part used in the UCL_PDR code to work in three dimensions without utilising the analytical description of self-shielding. One simple and elegant way would be to attenuate our radiation field at the correct wavelength by resolving the Voigt profile for the H₂ single line. Then we would add an extra opacity source in the radiative transfer for the H₂ and CO self-shielding (Spaans 1996). This would be very easy to implement in the current Monte Carlo treatment and would basically result in an attenuated H₂ and CO shielded radiation field.

CONCLUDING REMARKS AND PROPOSALS FOR FUTURE WORK

The work presented in this thesis describes the study of several far infrared forbidden lines such as [C II] 158 μm , [O I] 145 μm , [O I] 63 μm , [N II] 122 μm and [N III] 57 μm in extragalactic environments. The models (UCL_PDR, MOCASSIN and SMMOL) used to reproduce the Infrared Space Observatory Long Wavelength (ISO LWS) far infrared fine structure emission line observations, have been described in Chapter 2. The majority of all the mass surrounding stars in the galaxy is in PDR regions where hydrogen makes the transition from ionized to atomic and then finally to molecular form. This fact makes the study of PDRs essential to our understanding of the ISM and star forming regions. The classical approach to study PDRs is to observe line intensities that are thought to originate in the PDR, many of which are in the infrared. These observations are combined with theoretical calculations that attempt to reproduce the observations by varying the hydrogen density and intensity of the UV radiation field. Calculations of PDRs almost always ignore radiation $>13.6\text{eV}$, since a PDR is operationally defined to begin where the H II region ends. Some of the line intensities that are observed in the study of PDRs, however, can also have a significant contribution emanating from the adjacent H II region, which leads to an underestimate of the intensities of these lines.

Chapter 3 discusses a fit provided using the UCL_PDR code to the observed [C II] 158 μm , [O I] 63 μm and [O I] 145 μm emission line fluxes for 35 extragalactic sources measured from archival ISO LWS spectra. This study emphasises the importance of taking into account the contribution to the observed [C II] fluxes from H II regions. An attempt to measure this contribution using expected [C II]₁₅₈/[N II]₁₂₂ ratios for H II regions to correct the [C II]₁₅₈

fluxes of the 12 sources that had [N II] 122 μm detections was made. Also, a persistent discrepancy between the observed and modelled line flux ratios was found to be, at least partly, attributed to self-absorption in the [O I] 63- μm line. We estimated that 20-80% of the intensity of the [O I] 63 μm line can be suppressed through absorption, with the percentage depending strongly on the physical parameters of the PDR region. We found that the best fitting PDR models had $10^4 \leq n_H \leq 9 \times 10^4 \text{ cm}^{-3}$ and $60 \leq G_0 \leq 8 \times 10^2$.

Subsequently, to improve the fit to the observations an investigation into the contribution of the far infrared fine structure emission lines coming from both PDR and H II regions was performed in Chapter 4. An attempt to model NGC 4038 using both MOCASSIN and UCL_PDR models, was made. A grid of 25 H II region models and 25 PDR region models were computed and used to investigate the best fit to the observed ISO [NIII]₅₇/[NII]₁₂₂ ratio and the [C II]₁₅₈/[O I]₆₃ ratio versus the [O I]₆₃/[O I]₁₄₅ ratio respectively. The calculated radiation field at the ionization front was used as an input for the photodissociation UCL_PDR code thereby linking the H II and PDR regions, then the cooling and rotational emission lines ([C II] 158 μm , [O I] 63 and 145 μm , CO) was computed. The χ^2 for the [NIII]₅₇ and [NII]₁₂₂ emission lines was computed, because these emission lines arise only from the H II region and can better constrain the physical conditions within it. From Fig 4.10 and Table 4.11 we find that model 024 is the best fit to the observed ISO [NIII]₅₇/[NII]₁₂₂ ratio. In fact, Fig 4.10 shows the better match to the observations which is confirmed from the calculation of χ^2 listed in Table 4.11. The main reason of this better fit to the observations can be attributed to the inclusion of a grain mixture of silicates and graphite, and Md/Mg ratio in the input parameters. However, comparing individual single emission lines of [NIII]₅₇ and [NII]₁₂₂ from the MOCASSIN with ISO observations, indicates that with the ISO beam multiple H II regions are present. We estimate that about 10 are needed to better match the ISO observations. An investigation of oxygen self absorption by computing emission line profiles using the SMMOL code was provided. We also calculated the CO χ^2 for the best fit H II models listed in bold in Tab 4.11 to see if they can trace the gas in PDRs. We estimate that about 50 PDRs are needed to better match the CSO observations. Future tasks will be to run more PDR models spanning a different range of densities and metallicities as the parameters used throughout the UCL_PDR grid consider only standard physical conditions in these regions. In addition, it will be interesting to investigate if CO rotational emission lines can trace more than one gas component.

As claimed throughout these projects, H II regions, PDRs, and molecular clouds are not distinct physical problems, but rather a series of layers that are unified by the transport of

radiation from hot stars into cold gas and the flow of cold molecular gas into hot ionized regions. Then, in Chapter 5, we discuss the feasibility test on the coupling of the two codes (MOCASSIN and UCL_PDR). The main target of this project was to offer the community a useful tool for interpreting observations of star forming regions and to improve physical and chemical predictions by studying regions such as protoplanetary disks or planetary nebulae where ionised and photodissociated regions coexist. This study also provided information on the possibility to create a merged code using only a reduced chemical network and the steady state approach. However, the main conclusion that was reached is that it is necessary to adapt the computational part used in the UCL_PDR code to work in three dimensions without utilising the analytical description of self-shielding. One simple and elegant way would be to attenuate our radiation field at the correct wavelength by resolving the Voigt profile for the H₂ single line. Then we would add an extra opacity source in the radiative transfer for the H₂ and CO self-shielding (Spaans 1996). This would be very easy to implement in the current Monte Carlo treatment and would basically result in an attenuated H₂ and CO shielded radiation field.

The overall conclusion that can be drawn from all of this work is that UCL_PDR, MOCASSIN and SMMOL, combined together, can be used to model several far infrared fine structure emission lines and to infer the physical and chemical conditions in extragalactic sources. The success shown in fitting the observed line [C II]158 μ m, [O I]145 μ m and 63 μ m ratios in the sample of extragalactic sources (Chapter 3) suggests that the relative contributions of the ultraviolet radiation field from different gas phases can be estimated from more accurate observations of these far infrared forbidden lines. High spatial resolutions achievable with the forthcoming ALMA interferometer and the high sensitivity and resolution of PACS (HERSCHEL) will allow external galaxies to be probed on much smaller scales and we will be able to infer the properties of individual molecular clouds, rather than the average properties of large regions. Also, from this work it is found that a potential unified code (H II + PDR) is able to better reproduce physical and chemical conditions in extragalactic environments (see Chapter 4 and 5). Studying far infrared fine structure emission line behaviour with a unified code might help to solve some of the issues that we encounter modelling the two regions separately.

Bibliography

- Aannestad, P. A. & Emery, R. J., 2003, *A&A*, **406**, 155
- Abbott, D. C. & Lucy, L. B., 1985, *ApJ*, **288**, 679
- Abel, N. P., 2006, *MNRAS*, **368**, 1949
- Abel, N. P., Ferland, G. J., Shaw, G. & van Hoof, P. A. M., 2005, *ApJ*, **161**, 65
- Abel, N. P., Sarma, A. P., Troland, T. H. & Ferland, G. J., 2007, *ApJ*, **662**, 1024
- Abgrall, H., Le Bourlot, J., Pineau Des Forets, G., Roueff, E., Flower, D. R. & Heck, L., 1992, *A&A*, **253**, 525
- Allamandola, L. J., Tielens, A. G. G. M. & Barker, J. R., 1989, *ApJS*, **71**, 733
- Asplund, M., Grevesse, N., Sauval, A. J., Allende Prieto, C. & Blomme, R., 2005, *A&A*, **431**, 693
- Bakes, E. L. O. & Tielens, A. G. G. M., 1994, *ApJ*, **427**, 822
- Bastian, N., Emsellem, E., Kissler-Patig, M. & Maraston, C., 2006, *A&A*, **445**, 471
- Bayet, E., Gerin, M., Phillips, T. G. & Contursi, A., 2004, *A&A*, **427**, 45
- Bayet, E., Gerin, M., Phillips, T. G. & Contursi, A., 2006, *A&A*, **460**, 467
- Bell, T. A., Hartquist, T. W., Viti, S. & Williams, D. A., 2006a, *A&A*, **459**, 805
- Bell, T. A., Roueff, E., Viti, S. & Williams, D. A., 2006b, *MNRAS*, **371**, 1865
- Bell, T. A., Viti, S. & Williams, D. A., 2007, *MNRAS*, **378**, 983
- Bell, T. A., Viti, S., Williams, D. A., Crawford, I. A. & Price, R. J., 2005, *MNRAS*, **357**, 961

- Bennett, C. L., Kogut, A., Hinshaw, G., Banday, A. J., Wright, E. L., Gorski, K. M. & Wilkinson, D. T., 1994, *ApJ*, **436**, 423
- Bergvall, N., Masegosa, J., Östlin, G. & Cernicharo, J., 2000, *A&A*, **359**, 41
- Biham, O., Furman, I., Katz, N., Pirronello, V. & Vidali, G., 1998, *MNRAS*, **296**, 869
- Black, J. H., 1987, in D. J. Hollenbach & H. A. Thronson Jr. (ed.), *Interstellar Processes*, volume 134 of *Astrophysics and Space Science Library*, pp. 731–744
- Bohlin, R. C., Savage, B. D. & Drake, J. F., 1978, *ApJ*, **224**, 132
- Booth, R. S. & Aalto, S., 1998, *The Molecular Astrophysics of Stars and Galaxies*, edited by Thomas W. Hartquist and David A. Williams. Clarendon Press, Oxford, 1998., p.437, **4**, 437
- Boselli, A., Lequeux, J. & Gavazzi, G., 2002, *A&A*, **384**, 33
- Brandl, B. R., Snijders, L., den Brok, M., Whelan, D. G., Groves, B., van der Werf, P., Charmandaris, V., Smith, J. D., Armus, L., Kennicutt, R. C. & Houck, J. R., 2009, *ApJ*, **699**, 1982
- Brauher, J. R., Dale, D. A. & Helou, G., 2008, *ApJS*, **178**, 280
- Burke, J. R. & Hollenbach, D. J., 1983, *ApJ*, **265**, 223
- Burton, M. G., Hollenbach, D. J. & Tielens, A. G. G. M., 1990, *ApJ*, **365**, 620
- Butler, S. E., Bender, C. F. & Dalgarno, A., 1979, *ApJL*, **230**, L59
- Cardelli, J. A., Clayton, G. C. & Mathis, J. S., 1989, *ApJ*, **345**, 245
- Cazaux, S. & Tielens, A. G. G. M., 2004, *ApJ*, **604**, 222
- Cazaux, S. & Tielens, A. G. G. M., 2010, *ApJ*, **715**, 698
- Chamberlain, J. W., 1956, *ApJ*, **124**, 662
- Clegg, P. E., Ade, P. A. R., Armand, C., Baluteau, J.-P., Barlow, M. J., Buckley, M. A. & Berges, J.-C., 1996, *A&A*, **315**, L38
- Colbert, J. W., Malkan, M. A., Clegg, P. E., Cox, P., Fischer, J., Lord, S. D., Luhman, M., Satyapal, S., Smith, H. A., Spinoglio, L., Stacey, G. & Unger, S. J., 1999, *ApJ*, **511**, 721

- Contursi, A., Kaufman, M. J., Helou, G., Hollenbach, D. J., Brauher, J., Stacey, G. J., Dale, D. A., Malhotra, S., Rubio, M., Rubin, R. H. & Lord, S. D., 2002, *ApJ*, **124**, 751
- Crawford, M. K., Genzel, R., Townes, C. H. & Watson, D. M., 1985, *ApJ*, **291**, 755
- Dalgarno, A. & McCray, R. A., 1973, *ApJ*, **181**, 95
- de Jong, T., 1972, *A&A*, **20**, 263
- de Jong, T., 1977, *A&A*, **55**, 137
- de Jong, T., Boland, W. & Dalgarno, A., 1980, *A&A*, **91**, 68
- Draine, B. T., 1978, *ApJ*, **36**, 595
- Draine, B. T. & Bertoldi, F., 1996, *ApJ*, **468**, 269
- Draine, B. T. & Li, A., 2007, *ApJ*, **657**, 810
- Ercolano, B., Barlow, M. J. & Storey, P. J., 2005, *MNRAS*, **362**, 1038
- Ercolano, B., Morisset, C., Barlow, M. J., Liu, X.-W. & Storey, P. J., 2003, in S. Kwok, M. Dopita & R. Sutherland (eds.), *Planetary Nebulae: Their Evolution and Role in the Universe*, volume 209 of *IAU Symposium*, p. 397
- Federman, S. R., Glassgold, A. E. & Kwan, J., 1979, *ApJ*, **227**, 466
- Ferland, G. J., 2003, *ArA&A*, **41**, 517
- Ferland, G. J., Korista, K. T., Verner, D. A., Ferguson, J. W., Kingdon, J. B. & Verner, E. M., 1998, *PASP*, **110**, 761
- Field, G. B., Goldsmith, D. W. & Habing, H. J., 1969, *ApJ*, **155**, L149
- Fischer, J., Luhman, M. L., Satyapal, S., Greenhouse, M. A., Stacey, G. J., Bradford, C. M., Lord, S. D., Brauher, J. R., Unger, S. J., Clegg, P. E., Smith, H. A., Melnick, G., Colbert, J. W., Malkan, M. A., Spinoglio, L., Cox, P., Harvey, V., Suter, J.-P. & Streltnitski, V., 1999, *ApSS*, **266**, 91
- Fischer, J., Shier, L. M., Luhman, M. L., Satyapal, S., Smith, H. A., Stacey, G. J. & Unger, S. J., 1996, *A&A*, **315**, L97
- Fitzpatrick, E. L., 1999, *PASP*, **111**, 63

- Flannery, B. P., Roberge, W. & Rybicki, G. B., 1980, *ApJ*, **236**, 598
- Frerking, M. A., Langer, W. D. & Wilson, R. W., 1982, *ApJ*, **262**, 590
- Geers, V. C., Augereau, J., Pontoppidan, K. M., Dullemond, C. P., Visser, R., Kessler-Silacci, J. E., Evans, II, N. J., van Dishoeck, E. F. & Blake, G. A., 2006, *A&A*, **459**, 545
- Girardi, L., Bressan, A., Bertelli, G. & Chiosi, C., 2000, *A&AS*, **141**, 371
- Goicoechea, J. R. & Le Bourlot, J., 2007, *A&A*, **467**, 1
- González-Alfonso, E., Smith, H. A., Fischer, J. & Cernicharo, J., 2004, *ApJ*, **613**, 247
- Gould, R. J. & Salpeter, E. E., 1963, *ApJ*, **138**, 393
- Gry, C., Swinyard, B., Harwood, A., Trams, N., Leeks, S., Lim, T. & Sidher, S., 2003, *The ISO Handbook, Volume III - LWS - The Long Wavelength Spectrometer* (European Space Agency)
- Guelin, M., Zylka, R., Mezger, P. G., Haslam, C. G. T. & Kreysa, E., 1995, *A&A*, **298**, L29+
- Gutiérrez, L. & Beckman, J. E., 2008, in J. H. Knapen, T. J. Mahoney, & A. Vazdekis (ed.), *Pathways Through an Eclectic Universe*, volume 390 of *Astronomical Society of the Pacific Conference Series*, p. 300
- Habing, H. J., 1968, *Bull. Astron. Inst. Netherlands.*, **19**, 421
- Harries, T. J. & Howarth, I. D., 1997, *A&AS*, **121**, 15
- Hegmann, M. & Kegel, W. H., 2003, *MNRAS*, **342**, 453
- Heiles, C., 1994, *ApJ*, **436**, 720
- Higdon, S. J. U., Devost, D., Higdon, J. L., Brandl, B. R., Houck, J. R. & Hall, P., 2004, *PASP*, **116**, 975
- Hollenbach, D. & McKee, C. F., 1979, *ApJS*, **41**, 555
- Hollenbach, D. & Salpeter, E. E., 1971, *ApJ*, **163**, 155
- Hollenbach, D. J. & Tielens, A. G. G. M., 1997, *ArA&A*, **35**, 179
- Hummel, E. & van der Hulst, J. M., 1986, *A&A*, **155**, 151
- Israel, F. P., White, G. J. & Baas, F., 1995, *A&A*, **302**, 343

- Ivezic, Z. & Elitzur, M., 1997, *MNRAS*, **287**, 799
- Izotov, Y. I. & Thuan, T. X., 1999, *ApJ*, **511**, 639
- Jura, M., 1974, *ApJ*, **191**, 375
- Kamp, I. & Bertoldi, F., 2000, *A&A*, **353**, 276
- Kamp, I. & van Zadelhoff, G., 2001, *A&A*, **373**, 641
- Kaufman, M. J., Wolfire, M. G. & Hollenbach, D. J., 2006, *ApJ*, **644**, 283
- Kennicutt, Jr., R. C., 1998, *ApJ*, **498**, 541
- Kingdon, J. B. & Ferland, G. J., 1996, *ApJS*, **106**, 205
- Koester, B., Stoerzer, H., Stutzki, J. & Sternberg, A., 1994, *A&A*, **284**, 545
- Le Bourlot, J., Pineau Des Forets, G., Roueff, E. & Flower, D. R., 1993, *A&A*, **267**, 233
- Le Teuff, Y. H., Millar, T. J. & Markwick, A. J., 2000, *A&AS*, **146**, 157
- Lee, H., Herbst, E., Pineau des Forets, G., Roueff, E. & Le Bourlot, J., 1996, *A&A*, **311**, 690
- Leitherer, C., Schaerer, D., Goldader, J. D., Delgado, R. M. G., Robert, C., Kune, D. F., de Mello, D. F., Devost, D. & Heckman, T. M., 1999, *ApJS*, **123**, 3
- Liseau, R., Justtanont, K. & Tielens, A. G. G. M., 2006, *A&A*, **446**, 561
- Liu, X.-W., Barlow, M. J., Blades, J. C., Osmer, S. & Clegg, R. E. S., 1995, *ApJ*, **276**, 167
- Lucy, L. B., 1999, *A&A*, **344**, 282
- Luhman, M. L., Satyapal, S., Fischer, J., Wolfire, M. G., Sturm, E., Dudley, C. C., Lutz, D. & Genzel, R., 2003, *ApJ*, **594**, 758
- Malhotra, S., Kaufman, M. J., Hollenbach, D., Helou, G., Rubin, R. H., Brauher, J., Dale, D., Lu, N. Y., Lord, S., Stacey, G., Contursi, A., Hunter, D. A. & Dinerstein, H., 2001, *ApJ*, **561**, 766
- Mao, R. Q., Henkel, C., Schulz, A., Zielinsky, M., Mauersberger, R., Störzer, H., Wilson, T. L. & Gensheimer, P., 2000, *A&A*, **358**, 433
- Martin, P. G. & Mandy, M. E., 1995, *ApJL*, **455**, L89

- Martin, P. G., Schwarz, D. H. & Mandy, M. E., 1996, *ApJ*, **461**, 265
- Martín, S., Martín-Pintado, J. & Mauersberger, R., 2006, *A&A*, **450**, L13
- Mathis, J. S., Rumpl, W. & Nordsieck, K. H., 1977, *ApJ*, **217**, 425
- Mazzotta, P., Mazzitelli, G., Colafrancesco, S. & Vittorio, N., 1998, *A&AS*, **133**, 403
- McCall, B. J., Huneycutt, A. J., Saykally, R. J., Geballe, T. R., Djuric, N. & Dunn, G. H., 2003, *Nature*, **422**, 500
- McDowell, M. R. C., 1961, *The Observatory*, **81**, 240
- McKee, C. F. & Ostriker, J. P., 1977, *ApJ*, **218**, 148
- Meijerink, R., Spaans, M. & Israel, F. P., 2006, *ApJ*, **650**, L103
- Negishi, T., Onaka, T., Chan, K.-W. & Roellig, T. L., 2001, *A&A*, **375**, 566
- Nikola, T., Genzel, R., Herrmann, F., Madden, S. C., Poglitsch, A., Geis, N., Townes, C. H. & Stacey, G. J., 1998, *ApJ*, **504**, 749
- Oberst, T. E., Parshley, S. C., Stacey, G. J., Nikola, T., Löhr, A., Harnett, J. I., Tothill, N. F. H., Lane, A. P. & Stark, A. A., 2006, *ApJ*, **652**, L125
- Omont, A., 2007, *Reports on Progress in Physics*, **70**, 1099
- Osterbrock, D. E. & Ferland, G. J., 2006, *Astrophysics of gaseous nebulae and active galactic nuclei* (University Science Books, Mill Valley, CA)
- Papadopoulos, P. P., Thi, W.-F. & Viti, S., 2002, *ApJ*, **579**, 270
- Pequignot, D. & Aldrovandi, S. M. V., 1986, *A&A*, **161**, 169
- Péquignot, D., Ferland, G., Netzer, H., Kallman, T., Ballantyne, D. R., Dumont, A.-M. & Ercolano, B. e. a., 2001, in G. Ferland & D. W. Savin (eds.), *Spectroscopic Challenges of Photoionized Plasmas*, volume 247 of *Astronomical Society of the Pacific Conference Series*, p. 533
- Pequignot, D., Stasińska, G. & Aldrovandi, S. M. V., 1978, *A&A*, **63**, 313
- Pier, E. A. & Krolik, J. H., 1993, *ApJ*, **418**, 673

- Poelman, D. R. & Spaans, M., 2005, *A&A*, **440**, 559
- Polehampton, E. T., Baluteau, J. & Swinyard, B. M., 2005, *A&A*, **437**, 957
- Rawlings, J. M. C. & Yates, J. A., 2001, *MNRAS*, **326**, 1423
- Röllig, M., Abel, N. P., Bell, T., Bensch, F., Black, J., Ferland, G. J., Jonkheid, B., Kamp, I., Kaufman, M. J., Le Bourlot, J. & Le Petit, F., 2007, *A&A*, **467**, 187
- Rubin, R. H., Simpson, J. P., Haas, M. R. & Erickson, E. F., 1991, *ApJ*, **374**, 564
- Sanders, D. B., Phinney, E. S., Neugebauer, G., Soifer, B. T. & Matthews, K., 1989, *ApJ*, **347**, 29
- Savin, D. W., Kahn, S. M., Linkemann, J., Saghiri, A. A., Schmitt, M., Grieser, M. & Repnow, R., 2002, *ApJ*, **576**, 1098
- Schilke, P., Carlstrom, J. E., Keene, J. & Phillips, T. G., 1993, *ApJ*, **417**, L67
- Schmidt, M., 1959, *ApJ*, **129**, 243
- Seaquist, E. R. & Frayer, D. T., 2000, *ApJ*, **540**, 765
- Sobolev, V. V., 1960, *Moving envelopes of stars* (Cambridge: Harvard University Press)
- Sofia, U. J. & Meyer, D. M., 2001, *ApJ*, **554**, L221
- Solomon, P. M., 1965, *The Opacity of Light Molecules in Astrophysics.*, Ph.D. thesis, The University of Wisconsin - Madison.
- Spaans, M., 1996, *A&A*, **307**, 271
- Spinoglio, L. & Malkan, M. A., 1992, *ApJ*, **399**, 504
- Spitzer, Jr., L., 1948, *ApJ*, **107**, 6
- Stancil, P. C., Kirby, K., Gu, J., Hirsch, G., Buenker, R. J. & Sannigrahi, A. B., 2000, *A&AS*, **142**, 107
- Stancil, P. C., Schultz, D. R., Kimura, M., Gu, J., Hirsch, G. & Buenker, R. J., 1999, *A&AS*, **140**, 225
- Stecher, T. P. & Williams, D. A., 1967, *ApJL*, **149**, L29

- Sternberg, A. & Dalgarno, A., 1995, *ApJS*, **99**, 565
- Storey, P. J. & Hummer, D. G., 1995, *MNRAS*, **272**, 41
- Takahashi, T., Silk, J. & Hollenbach, D. J., 1983, *ApJ*, **275**, 145
- Tielens, A. G. G. M., 2005, *The Physics and Chemistry of the Interstellar Medium* (Cambridge University Press)
- Tielens, A. G. G. M. & Hollenbach, D., 1985, *ApJ*, **291**, 747
- Unger, S. J., Clegg, P. E., Stacey, G. J., Cox, P., Fischer, J., Greenhouse, M., Lord, S. D., Luhman, M. L., Satyapal, S., Smith, H. A., Spinoglio, L. & Wolfire, M., 2000, *A&A*, **355**, 885
- van Dishoeck, E. F. & Black, J. H., 1986, *ApJS*, **62**, 109
- van Dishoeck, E. F. & Black, J. H., 1988, *ApJ*, **334**, 771
- van Hoof, P. A. M., Weingartner, J. C., Martin, P. G., Volk, K. & Ferland, G. J., 2004, *MNRAS*, **350**, 1330
- van Zadelhoff, G., Dullemond, C. P., van der Tak, F. F. S. & Yates, J. A., 2002, *A&A*, **395**, 373
- Vasta, M., Barlow, M. J., Viti, S., Yates, J. A. & Bell, T. A., 2010, *MNRAS*, **404**, 1910
- Vastel, C., Polehampton, E. T., Baluteau, J., Swinyard, B. M., Caux, E. & Cox, P., 2002, *ApJ*, **581**, 315
- Vigroux, L., Mirabel, F., Altieri, B., Boulanger, F., Cesarsky, C., Cesarsky, D., Claret, A., Fransson, C., Gallais, P., Levine, D., Madden, S., Okumura, K. & Tran, D., 1996, *A&A*, **315**, L93
- Wild, W., Harris, A. I., Eckart, A., Genzel, R., Graf, U. U., Jackson, J. M., Russell, A. P. G. & Stutzki, J., 1992, *A&A*, **265**, 447
- Wilson, C. D., Scoville, N., Madden, S. C. & Charmandaris, V., 2003, *ApJ*, **599**, 1049
- Wolfire, M. G., Hollenbach, D. & Tielens, A. G. G. M., 1989, *ApJ*, **344**, 770
- Wolfire, M. G., Tielens, A. G. G. M. & Hollenbach, D., 1990, *ApJ*, **358**, 116
- Wright, E. L., Mather, J. C., Bennett, C. L., Cheng, E. S., Shafer, R. A., Fixsen, D. J., Eplee, Jr., R. E., Isaacman, R. B. & Read, S. M., 1991, *ApJ*, **381**, 200

Young, J. S. & Scoville, N. Z., 1991, *ArA&A*, **29**, 581